

57th Scientific Conference for Students of Physics and Natural Sciences

Open Readings 2014

**March 19-21, 2014
Vilnius, LITHUANIA**

Programme and Abstracts

LOCAL ORGANIZING COMMITTEE

Students' Scientific Association, Faculty of Physics, Vilnius University, LITHUANIA:

Jonas Berzinš
Vytautas Butkus
Saulė Abbas
Vytautas Aukštikalnis
Darius Bagdonas
Milda Budreckaitė
Simona Barkauskaitė
Miglius Budriūnas
Justinas Girskis
Martynas Grybauskas
Nerijus Jurkūnas
Gintarė Kuksėnaitė
Mantas Kulnickas
Birutė Leiputė
Evaldas Paulauskas
Vytenis Pranculis
Maria Razgute
Deividas Sabonis
Edvinas Skliutas
Simona Streckaitė
Greta Striokaitė
Laura Šerkšnytė
Rūta Urbonavičiūtė
Rasa Valentinavičienė

Faculty of Physics
Vilnius University
Saulėtekio Ave. 9-III, LT-10222 Vilnius
LITHUANIA

www.ff.vu.lt
www.openreadings.eu

Contents

Conference programme	4
List of poster presentations	7
Oral session 1	15
<i>Laser physics and optical technologies</i>	
Oral session 2	22
<i>Spectroscopy, functional materials and chemistry</i>	
Oral session 3	29
<i>Semiconductor and condensed matter physics</i>	
Oral session 4	36
<i>Material sciences and modern technologies</i>	
Oral session 5	43
<i>Biophysics, medical and environmental physics</i>	
Oral session 6	50
<i>Theoretical physics and astrophysics</i>	
Poster session 1	57
<i>Laser physics and optical technologies</i>	
<i>Spectroscopy, functional materials and derivatives</i>	
<i>Chemistry and chemical physics</i>	
Poster session 2	111
<i>Semiconductor and condensed matter physics</i>	
<i>Material sciences and modern technologies</i>	
<i>Functional materials and derivatives</i>	
Poster session 3	160
<i>Biophysics, medical and environmental physics</i>	
<i>Astrophysics and astronomy</i>	
<i>Theoretical physics</i>	
Author index	211

Conference programme

19 March, WEDNESDAY

INVITED LECTURE

9:00 **Dr. Romas Danielius**, *Light Conversion Ltd., Lithuania*

ORAL SESSION 01

- | | | | |
|-------|--|------|----|
| 10:00 | Dominykas Bričkus, Kasperas Sasnauskas, Aleksej Rodin, Alexander Dement'ev
THERMAL DISTORTIONS IN Nd:YAG CRYSTAL FIBER AMPLIFIER SEEDED BY PICOSECOND PULSES | 01-1 | 16 |
| 10:15 | Eugene Sokolov, Leonid Burov, Alexander Gorbatsevich
SPECTRUM EFFECTS OF POLARIZATION SWITCHING IN VERTICAL CAVITY SURFACE-EMITTING LASERS | 01-2 | 17 |
| 10:30 | Edgaras Markauskas
ULTRAFAST PULSED LASER INDUCED LIFT-OFF PATTERNING OF CZTSe THIN-FILM SOLAR CELLS | 01-3 | 18 |
| 10:45 | Silviu T. Popescu, Adrian Petris, Valentin I. Vlad
PHOTOREFRACTIVE SELF-INDUCED WAVEGUIDES IN LITHIUM NIOBATE FOR INTEGRATED PHOTONICS APPLICATIONS | 01-4 | 19 |
| 11:00 | Linas Jonušauskas, Mangirdas Malinauskas
LASER POLYMERIZATION OF NON-PHOTOSENSITIZED MATERIALS USING VARIOUS FOCUSING CONDITIONS | 01-5 | 20 |
| 11:15 | Sergey Nazarov, Elen Tolstik, Vladimir Mahilny, Rainer Heintzmann, Alexei Tolstik
HOLOGRAPHIC ELEMENTS FOR 3D MICROSCOPY | 01-6 | 21 |

11:30-14:00 POSTER SESSION P1

BREAK

INVITED LECTURE

14:30 **Prof. Markus W. Sigrist**, *ETH Zürich, Switzerland*
LASER-BASED CHEMICAL SENSING

ORAL SESSION 02

- | | | | |
|-------|--|------|----|
| 15:30 | Natalie Tarasenka, Andrei Butsen
LASER ASSISTED TECHNIQUES FOR SYNTHESIS OF COMPOUND NANOPARTICLES IN SOLUTIONS | 02-1 | 23 |
| 15:45 | Krzysztof Ptaszyński, Bartłomiej Grześkiewicz, Michał Kotkowiak
NEAR AND FAR-FIELD OPTICAL PROPERTIES OF METALLIC TRIANGULAR NANOPRISMS | 02-2 | 24 |
| 16:00 | Paulius Imbrasas, Saulius Juršėnas, Tomas Serevičius, Renaldas Rimkus, Alytis Gruodis, Vygtintas Jankauskas.
NEW ANTHRACENE-CARBAZOLE DERIVATIVES FOR OPTOELECTRONIC APPLICATIONS | 02-3 | 25 |
| 16:15 | Regimantas Komskis, Tomas Serevičius, Povilas Adomėnas, Ona Adomėnienė, Vygtintas Jankauskas, Karolis Kazlauskas, Saulius Juršėnas
NONSYMMETRIC 9,10-DIPHENYLANTHRACENE-BASED DEEP-BLUE EMITTERS WITH ENHANCED CHARGE TRANSPORT PROPERTIES | 02-4 | 26 |
| 16:30 | Rokas Skaigiris, Saulius Juršėnas
FLUORESCENCE SENSING OF METAL IONS BASED ON 1,8-NAPHTHALIMIDE DERIVATIVE | 02-5 | 27 |
| 16:45 | Martyna Stańczuk, Sylwia Zięba, Tomasz Buchwald
APPLICATION OF RAMAN SPECTROSCOPY IN ANALYSIS OF CHANGES IN COMPOSITION AND STRUCTURE OF HUMAN ENAMEL | 02-6 | 28 |

17:00 OPENING OF STUDENTS' LABORATORY

19:00 WELCOME EVENING

20 March, THURSDAY

INVITED LECTURE

9:00 **A. Vizbaras K. Vizbarai** , *Brolis Semiconductors, Ltd., Lithuania*
SCIENTIFIC PATH TO SUCCESSFUL CAREER

ORAL SESSION O3

- | | | | |
|-------|---|------|----|
| 10:00 | Justinas Aleknavičius | 03-1 | 30 |
| | PHOTOLUMINESCENCE ENHANCEMENT BY COUPLING WITH LOCALIZED SURFACE PLASMONS IN SILVER NANOPARTICLES DEPOSITED ON InGaN QUANTUM WELLS | | |
| 10:15 | Karolis Stašys, Vaidas Pačebutas, Renata Butkutė | 03-2 | 31 |
| | GROWTH AND CHARACTERISATION OF THICK GaAsBi LAYERS | | |
| 10:30 | Šarūnas Vaškelis, Virginijus Bukauskas, Audružis Mironas, Arūnas Šetkus | 03-3 | 32 |
| | INVESTIGATION OF CHARGE CARRIER TRANSFER MECHANISM IN ULTRA-THIN MULTI-LAYERED METAL OXIDE STRUCTURE FOR GAS DETECTION | | |
| 10:45 | Damian Łukawski, Zygmunt Miłosz, Natalia Michalak, Łukasz Kościński, Małgorzata Błaszyk, Mikołaj Lewandowski, Tadeusz Luciński | 03-4 | 33 |
| | PREPARATION OF IRON OXIDE THIN FILMS ON Ru(0001) | | |
| 11:00 | Maciej Bieniek | 03-5 | 34 |
| | ELECTRONIC AND TRANSPORT PROPERTIES OF TOPOLOGICAL ANDERSON INSULATOR | | |
| 11:15 | Justas Trimailovas, Pranciškus Vitta | 03-6 | 35 |
| | INVESTIGATION AND OPTIMISATION OF THE SPATIAL LUMINOUS FLUX DISTRIBUTION OF SOLID-STATE STREET LUMINAIRE | | |

11:30-14:00 POSTER SESSION P2

BREAK

INVITED LECTURE

14:30 **Prof. J. V. Vaitkus**, *Vilnius University, Lithuania*

ORAL SESSION O4

- | | | | |
|-------|--|------|----|
| 15:30 | Aivaras Žukauskas, Vít Vorobel | 04-1 | 37 |
| | SCINTILLATION DETECTOR TESTING SETUP FOR SUPERNEMO EXPERIMENT | | |
| 15:45 | Jelena Kosmaca, Jana Andzane, Gunta Kunakova, Gvido Petersons, Justin D. Holmes, Donats Erts | 04-2 | 38 |
| | APPLICATION OF DIELECTROPHORESIS FOR MAKING GERMANIUM NANOWIRE ARRAYS | | |
| 16:00 | Adomas Lukenskas | 04-3 | 39 |
| | INVESTIGATION OF ANODIC ALUMINA OXIDE TEMPLATES DOPED WITH IRON USING MOESSBAUER SPECTROMETER | | |
| 16:15 | Sergejus Balčiūnas, Maksim Ivanov | 04-4 | 40 |
| | GRAIN SIZE EFFECT ON DIELECTRIC PERMITTIVITY OF FBSP T PEROVSKITE CERAMICS | | |
| 16:30 | Laurynas Šatas, Tomas Šalkus, Maud Barre, Veyis Gunes | 04-5 | 41 |
| | INVESTIGATION OF AURIVILLUS PHASE Bi₂MO₆ (M = W, MO) ELECTRICAL PROPERTIES | | |
| 16:45 | Rūta Stankevičiūtė, Artūras Žalga | 04-6 | 42 |
| | INFLUENCE OF THE STARTING MATERIALS TO THE FORMATION AND OPTICAL PROPERTIES OF THE FINAL CERAMIC PREPARED BY THE AQUEOUS SOL-GEL SYNTHESIS METHOD | | |
| 19:00 | EXCURSION | | |

21 March, FRIDAY

INVITED LECTURE

9:00 **Prof. David L. Andrews**, *University of East Anglia Norwich, United Kingdom*
ENERGY HARVESTING MATERIALS

ORAL SESSION O5

10:00	Miglė Kišonaitė, Asta Zubrienė, Edita Čapkauskaitė, Daumantas Matulis	05-1	44
	THERMODYNAMICS - STRUCTURE CORRELATIONS OF LEAD COMPOUNDS BINDING TO TARGET PROTEINS		
10:15	Nikita Belko, Sophy Kavalenka, Dmitry Tarasov	05-2	45
	THE BIOTISSUES FLUORESCENCE PHANTOM FOR NIR REGION		
10:30	Agnė Kalnaitytė, Saulius Bagdonas, Ričardas Rotomskis	05-3	46
	EFFECTS OF BLUE LIGHT ON STABILITY AND TOXICITY OF CdSe QUANTUM DOTS IN MEDIA WITH MICROALGAE: SPECTROSCOPIC AND MICROSCOPIC STUDY		
10:45	Dominyka Dapkute, Simona Steponkiene, Ricardas Rotomskis	05-4	47
	SELECTIVE ACCUMULATION OF QUANTUM DOTS IN BREAST CANCER STEM CELLS		
11:00	Sophy Kavalenka, Alena Kavalenka, Vladislav Popov, Valeriy Loban	05-5	48
	APPLICATION OF LASER DIFFRACTOMERTY IN ANALYSIS OF CELLULAR SYSTEMS		
11:15	Vytautas Navikas, Martynas Gavutis, Šarūnas Vaitekoniš, Ramūnas Valiokas	05-6	49
	HIGH-SPEED AND ACCURACY BIOPATTERNING BY DIP-PEN NANOLITHOGRAPHY WITH LIPID INKS		

11:30-14:00 POSTER SESSION P3

BREAK

INVITED LECTURE

14:30 **Dr. Thomas Gajdosik**, *Vilnius University, Lithuania*
HIGGS BOSON

ORAL SESSION O6

15:30	Elena Tamaševičiūtė	06-1	51
	HOW TO KEEP ON A SLIPPERY PEAK		
15:45	Aleksejus Kononovicius, Julius Ruseckas	06-2	52
	NON-EXTENSIVE AND EXTENSIVE STATISTICS IN THE AGENT-BASED HERDING MODEL		
16:00	Wojciech Radosz, Antoni Mituś, Grzegorz Pawlik	06-3	53
	PHOTOMECHANICAL EFFECT IN POLYMERIC FIBERS: ANALYSIS OF LOCAL VOIDS		
16:15	Ilya I. Beterov, Tomas Andrijauskas, Denis B. Tretyakov, Vasilii M. Entin, Elena A. Yakshina, Igor I. Ryabtsev, Silvia Bergamini	06-4	54
	SIMULATING JAYNES-CUMMINGS DYNAMICS IN MESOSCOPIC ENSEMBLES OF INTERACTING ATOMS		
16:30	Kostas Sabulis, Kastytis Zubovas	06-5	55
	PHOTOIONISING RADIATION FEEDBACK IN MOLECULAR CLOUD MODELS		
16:45	Renata Ženovienė, Gražina Tautvaišienė, Edita Stonkutė, Birgitta Nordström, Valentas Bertašius	06-6	56
	CHEMICAL COMPOSITION OF A KINEMATIC STELLAR GROUP IN THE SOLAR NEIGHBOURHOOD		
19:00	CONFERENCE PARTY		
	AWARDS		

List of poster presentations

19 March, WEDNESDAY

11:30 – 14:00 **POSTER SESSION P1**

Julius Vengelis, Karolina Stankevičiūtė, Rosvaldas Šuminas, Agnė Marcinkevičiūtė CONSTRUCTION AND INVESTIGATION OF SYNCHRONOUSLY PUMPED FOLDED CAVITY FEMTOSECOND OPTICAL PARAMETRIC OSCILLATOR	P1-01	58
Eglė Gabrytė, Mikas Vengris, Romualdas Danielius THERMAL EFFECTS IN THE FOURTH HARMONIC GENERATOR OF FEMTOSECOND Yb:KGW LASER	P1-02	59
Ernestas Žeimys, Benas Makauskas, Kęstutis Steponkevičius FOUR-WAVE MIXING OF TUNABLE ULTRASHORT LASER PULSES IN AIR	P1-03	60
Paulius Stanislovaitis, Andrius Narmontas IMPROVEMENT OF THE COHERENCE IN THE SECOND HARMONIC GENERATION BY CONICAL BEAMS	P1-04	61
Ignas Balčiūnas, Rimantas Budriūnas, Tomas Stanislaukas, Arūnas Varanavičius HIGH INTENSITY BROADBAND PULSE COMPRESSION IN BULK MATERIAL	P1-05	62
Rimantė Jarockytė, Ignas Balčiūnas, Šarūnas Straigis, Rimantas Budriūnas, Arūnas Varanavičius GROUP-DELAY MEASUREMENT OF CHIRPED MIRRORS USING WHITE-LIGHT INTERFEROMETRY	P1-06	63
Dainius Kučinskas, Rimantas Budriūnas, Arūnas Varanavičius BREWSTER'S ANGLE GRISM-PAIR STRETCHER MODEL FOR FEMTOSECOND PULSE OPCPA SYSTEM	P1-07	64
Šarūnas Straigis, Linas Karpavičius, Arūnas Varanavičius, Tomas Stanislaukas DEVELOPMENT OF BEAM-POINTING REGISTRATION AND STABILIZATION SYSTEM	P1-08	65
Vladislav Popov COMPARATIVE CHARACTERIZATION OF THE PROPERTIES OF ELECTROMAGNETIC WAVES IN UNIAXIAL CRYSTALS AND HYPERBOLIC METAMATERIALS	P1-09	66
Darius Gailevičius, Lina Maigytė, Vytautas Purlys, Jose Trull, Martynas Peckus, Crina Cojocar, Mangirdas Malinauskas, Kestutis Staliunas WOODPILE PHOTONIC CRYSTALS FOR FLAT LENSING IN VISIBLE RANGE	P1-10	67
Dovilė Mackevičiūtė, Sima Rekšytė, Mangirdas Malinauskas LASER POLYMERIZATION OF MULTI-COMPONENT SCAFFOLDS	P1-11	68
Laurynas Lukoševičius, Mangirdas Malinauskas FABRICATION OF POLYLACTIC ACID MICROSTRUCTURED SCAFFOLDS VIA 3D PRINTING	P1-12	69
Aušra Čerkauskaitė, Domas Paipulas STABILITY OF PHOTOREFRACTIVE MODIFICATIONS IN LITHIUM NIOBATE CRYSTALS INDUCED BY FEMTOSECOND LASER PULSES	P1-13	70
Audrius Puišys, Domas Paipulas INTEGRATION OF FRESNEL ZONE PLATES IN THE BULK OF SAPPHIRE CRYSTAL BY FEMTOSECOND LASER PULSES	P1-14	71
Jonas Berzinš, Mindaugas Gedvilas, Gediminas Račiukaitis ANALYSIS OF SCRIBING SAPPHIRE SUBSTRATES	P1-15	72
Jonas Berzinš LASER DICING OF CERAMICS SUBSTRATES	P1-16	73
Juozas Dudutis, Paulius Gečys NANOSECOND LASER DRILLING OF SODA-LIME GLASS	P1-17	74
Antanas Vinčiūnas, Paulius Gečys RIPPLE FORMATION ON STAINLESS STEEL BY PICOSECOND LASER IRRADIATION	P1-18	75
Antanas Vinčiūnas, Jan Düsing SPATIAL LIGHT MODULATOR AS A BEAM SHAPER IN THIN GOLD FILM REMOVAL	P1-19	76
Tomas Puodžiūnas, Lina Mažulė, Ignas Reklaitis, Domas Paipulas, Valdas Sirutkaitis, Rolandas Tomašiūnas MICRO-FIGURES CUTTING IN MOLYBDENUM FOIL USING A FEMTOSECOND PULSE LASER	P1-20	77

Andrius Subačius, Kęstutis Juškevičius SILICON DIOXIDE THIN FILMS PREPARED BY REACTIVE MAGNETRON SPUTTERING FROM BORON DOPED SILICON TARGET	P1-21	78
Alena Mikitchuk, Konstantin Kozadaev SYNTHESIS OF NANOCOMPOSITE FILMS BASED ON METALLIC NANOPARTICLES	P1-22	79
Laurynas Dagys QUADRUPLAR INTERACTION IN SOLID-STATE NMR SPECTROSCOPY	P1-23	80
Dovilė Lengvinaitė, Kęstutis Aidas NMR PARAMETERS OF ALANINE DIPEPTIDE STUDIED BY MEANS OF QUANTUM CHEMISTRY METHODS	P1-24	81
WITHDRAWED	P1-25	82
Mantas Garliauskas, Konstantinas Zakalskis, Andrius Garbaras, Arūnas Gudelis, Grigorijus Duškesas. CARBON ISOTOPE RATIO MEASUREMENTS IN THE REACTOR GRAPHITE USING ISOTOPE RATIO MASS SPECTROMETRY	P1-26	83
Nikita Yavkin INVESTIGATING ELASTIC STRESSES IN SOLID SOLUTIONS GeSi BASED RAMAN SPECTROSCOPY	P1-27	84
Domantas Ozerenskis, Valdemaras Aleksa INFLUENCE OF SILICON AND GERMANIUM SUBSTITUTES ON STRUCTURAL PARAMETERS OF CYCLOPENTANE	P1-28	85
Domantas Ozerenskis, Valdemaras Aleksa RING FLATTERING IN SIX-MEMBERED ORGANIC COMPOUNDS: RAMAN SPECTROSCOPY AND AB INITIO INVESTIGATIONS	P1-29	86
Giedrius Babrauskas, Ilja Ignatjev, Valdemaras Aleksa INVESTIGATION OF THE PIGMENT LAYER OF 17th CENTURY PAINTING USING RAMAN SPECTROSCOPY METHOD	P1-30	87
Martynas Velička, Cordelia Zimmerer ANALYSIS OF POLYMER INTERFACES BY MEANS OF SURFACEENHANCED INFRARED AND RAMAN SPECTROSCOPIES	P1-31	88
Dominyka Blaževič, Milda Pučetaitė, Valdas Šablinskas APPLICATION OF INFRARED SPECTROSCOPIC MICROSCOPY AND ATR TECHNIQUES FOR STRUCTURAL STUDIES OF URINARY SEDIMENTS	P1-32	89
Grzegorz Zajac, Agnieszka Kaczor, Katarzyna Chruszcz-Lipska, Malgorzata Baranska RESONANCE RAMAN OPTICAL ACTIVITY OF ASTAXANTHIN ENANTIOMERS	P1-33	90
Eglė Bašinskaitė, Jan Alster, Vytautas Butkus, Darius Abramavičius, Leonas Valkūnas, Donatas Zigmantas 2D ELECTRONIC SPECTROSCOPY OF PORPHYRIN NANORINGS	P1-34	91
Edvinas Radiunas, Steponas Raišys PHOTOPHYSICAL PROPERTIES OF THIOPHENE-DIPHENYLAMINE FUNCTIONAL BLOCK	P1-35	92
Simona Streckaitė, Renata Karpicz, Saulius Grigalevičius ELECTRIC FIELD IMPACT TO FLUORESCENCE IN ORGANIC INDOLO[3,2-b]CARBAZOLE COMPOUNDS	P1-36	93
Alina Muravitskaya, Andrey Ramanenka PLASMON-ENHANCED FLUORESCENCE OF LABELED ANTI-ALPHA-FETOPROTEIN MOLECULES	P1-37	94
Ausra Gustainyte, Isabel Pastoriza Santos, Elisa Gonzalez Romero APPLICATION OF GRAPHENE AND RU NANOPARTICLES FOR ELECTROCHEMICAL BIOSENSORS	P1-38	95
Laura Kačenauskaitė, Akvilė Šlėkaitė, Ričardas Rotomskis. SYNTHESIS AND OPTIMISATION OF FLUORESCENT GOLD NANOPARTICLES FOR BIOIMAGING	P1-39	96
WITHDRAWED	P1-40	97
Justina Jovaišaitė, Lina Skardžiūtė, Sigitas Tumkevičius, Saulius Juršėnas FLUORESCENCE PROPERTIES OF PYRIMIDE BASED DERIVATIVES	P1-41	98
Raimundas Burokas, Steponas Raišys, Arūnas Miasojedovas EXCITON DIFFUSION MEASUREMENTS IN THE FILMS OF TRIPHENYLAMINE WITH NAPHTHALIMIDE SIDE-MOETIES	P1-42	99

Žygimantas Žulonas, Artūras Žalga THERMOANALYTICAL STUDY OF INDIUM-MOLYBDATE-TARTRATE GEL PRECURSORS PREPARED BY AQUEOUS SOL-GEL SYNTHESIS ROUTE	P1-43	100
Žygimantas Gričius, Artūras Žalga AQUEOUS SOL-GEL SYNTHESIS, CRYSTAL STRUCTURE, SURFACE MORPHOLOGY AND PHOTOLUMINESCENCE OF EUROPIUM MOLYBDATE	P1-44	101
Gediminas Braziulis, Artūras Žalga AQUEOUS SOL-GEL SYNTHESIS AND FT-IR SPECTROSCOPICAL INVESTIGATION OF Eu³⁺ DOPED MAGNESIUM AND STRONTIUM MOLYBDATES	P1-45	102
Gytautas Janulevičius, Artūras Žalga SYNTHESIS AND LUMINESCENT PROPERTIES OF DOUBLE MIXED SCHEELITE-LIKE CALCIUM MOLYBDATE-TUNGSTATE COMPOUND	P1-46	103
Evelina Štikūnaitė, Jurgis Barkauskas INTERACTION OF GRAPHENE-BASED NANOSTRUCTURES WITH PROTEINS	P1-47	104
Edita Vernickaitė, Henrikas Cesiulis STRUCTURAL AND CORROSION CHARACTERIZATION OF ELECTRODEPOSITED COBALT-TUNGSTEN ALLOYS	P1-48	105
Reda Sabirovaitė, Ingrida Baltiškytė, Valdemaras Aleksa INVESTIGATION OF H/D EXCHANGE IN THE MIXTURES OF IONIC LIQUIDS [BMIM][X] AND D₂O USING RAMAN SPECTROSCOPY	P1-49	106
Darya Dovgal', Anatolij Min'ko, George Pitsevich 3D PES STUDY OF THE O-H GROUP VIBRATIONS IN THE METHANOL DIMER	P1-50	107
Ekaterina Kozlovskaya, Alex Malevich, George Pitsevich SPECTRAL CHARACTERISTICS OF THE DOUBLE HYDROGEN BOND IN FORMIC ACID DIMER	P1-51	108
Yauheni Sliaptsov, Alex Malevich, George Pitsevich INVESTIGATION OF THE SOLVENT POLARITY INFLUENCE ON THE LARGE AMPLITUDE VIBRATIONS FREQUENCY IN THE HYDROGEN-BONDED COMPLEXES	P1-52	109
Iga Smolarkiewicz, Adam Rachocki, Katarzyna Pogorzelec-Glaser, Radosław Pankiewicz, Paweł Ławniczak, Jadwiga Tritt-Goc NEW POLYMERIC PROTON CONDUCTOR BASED ON CELLULOSE FUNCTIONALIZED BY IMIDAZOLE MOLECULES	P1-53	110

20 March, THURSDAY

11:30 – 14:00 **POSTER SESSION P2**

Karolis Madeikis, Linas Minkevičius, Gintaras Valušis	P2-01	112
SUB-TERAHERTZ IMAGING SYSTEM IN TRANSMITTANCE GEOMETRY		
Adomas Eikevičius, Saulius Tumėnas	P2-02	113
SPECTROSCOPIC ELLIPSOMETRY STUDY OF THEOPTICAL DIELECTRIC FUNCTION OF ZINC		
Ieva Kranauskaitė, Jan Macutkevič, Jūras Banys, Alain Celzard, Stefano Bellucci	P2-03	114
DIELECTRIC PROPERTIES OF GRAPHITE LOADED EPOXY RESIN COMPOSITES		
Aurimas Sakanas, Robertas Grigalaitis, Jūras Banys, Liliana Mitoseriu, Vincenzo Buscaglia, Paolo Nanni	P2-04	115
APPLICATION OF LICHTENECKER'S MIXING FORMULA FOR BARIUM TITANATE AND NICKEL-ZINC FERRITE COMPOSITE CERAMICS		
Artem Musiienko, Roman Grill.	P2-05	116
STUDY OF DEEP LEVEL PROPERTIES IN CdTe BY PHOTO-HALL EFFECT MEASUREMENTS		
Agnė Kalpakovaitė, Tomas Grinys, Rytis Dargis	P2-06	117
INVESTIGATION OF SILICON SUBSTRATES WITH RARE-EARTH-OXIDE BUFFER LAYERS FOR GaN GROWTH		
Arnoldas Jasiūnas, Dovilė Meškauskaitė, Eugenijus Gaubas, Tomas Čeponis	P2-07	118
CORRELATIVE ANALYSIS OF THE IN SITU CHANGES OF CARRIER DECAY AND PROTON INDUCED PHOTOLUMINESCENCE IN GaN		
Arnoldas Jasiūnas, Eugenijus Gaubas, Tomas Čeponis, Jevgenij Pavlov	P2-08	119
CORRELATED ANALYSIS OF GROWN-IN IMPURITIES AND RECOMBINATION PARAMETERS IN DIAMOND CRYSTALS		
Donatas Dargis, Gediminas Liaugaudas	P2-09	120
EXPERIMENTAL TECHNIQUES FOR STUDY OF NONEQUILIBRIUM CARRIER DYNAMICS IN HIGHLY EXCITED SiC CRYSTALS		
Vytautas Janonis	P2-10	121
INVESTIGATION OF TlBr PHOTOELECTRIC PROPERTIES OVER WIDE TEMPERATURE RANGE		
Simona Paurazaitė, Saulius Tumėnas	P2-11	122
OPTICAL PROPERTIES OF NATURAL OXIDE LAYER ON ZnMgRE QUASICRYSTALS		
Justas Laužadis, Rimvydas Venckevičius, Irmantas Kašalynas	P2-12	123
INVESTIGATION OF THERMAL EMISSION SPECTRUM OF THE AlGaIn/GaN AND GaAs SAMPLES		
Žydrūnas Podlipskas, Ramūnas Aleksiejūnas, Jūras Mickevičius	P2-13	124
OPTICAL STUDY OF CARRIER RECOMBINATION AND LOCALIZATION IN Al-RICH AlGaIn LAYERS		
Mažena Mackoit	P2-14	125
NONEQUILIBRIUM CARRIER DYNAMICS IN GaN epilayers WITH DIFFERENT EQUILIBRIUM CARRIER DENSITIES		
Kazimieras Nomeika	P2-15	126
OPTICAL STUDY OF RECOMBINATION AND TRANSPORT OF NON-EQUILIBRIUM CARRIERS IN (In,Ga)N QUANTUM STRUCTURES		
Oleg Kravcov, Edmundas Kuokštis	P2-16	127
INFLUENCE OF CARRIER LOCALIZATION ON LUMINESCENCE DYNAMICS IN AlGaIn QUANTUM WELLS		
Augustas Vaitkevičius	P2-17	128
INFLUENCE OF TRENCH DEFECTS ON PHOTOLUMINESCENCE IN InGaIn/GaN QUANTUM WELLS		
Mantas Dmukauskas, Arūnas Kadys	P2-18	129
GROWTH AND CHARACTERISATION OF InGaIn/GaN MULTIPLE QUANTUM WELLS		
Sandra Stanionytė, Tadas Malinauskas	P2-19	130
InGaIn/GaN MQWs ANALYSIS USING HR-XRD ROCKING CURVES		
Algirdas Norkūnas, Artūras Žalga	P2-20	131
PLASMA SYNTHESIS OF TERNARY METAL OXIDE SYSTEMS		
Antanas Kleopas Oginskis, Andrius Maneikis, Bonifacas Vengalis, Gražina Grigaliūnaitė-Vonsevičienė	P2-21	132
ELECTRICAL AND MAGNETIC PROPERTIES OF THE La2/3Sr1/3MnO3 THIN FILMS GROWN ON MgO(100) SUBSTRATES		
Aleksandr Yasunas, Olga Komar	P2-22	133
STRUCTURE AND PROPERTIES OF SILICON DIOXIDE FILMS DEPOSITED BY HDPCVD		
Olga Komar	P2-23	134
EFFICIENCY OF DECOMPOSITION OF WATER ON NANOSTRUCTURED OBJECTS BASED ON POWDERS OF TITANIUM AND SILICON		

WITHDRAWED	P2-24	135
Olga Kozlova	P2-25	136
ELECTRONICS PROPERTIES OF QUASI-TWO-DIMENSIONAL NANOSTRUCTURES BASED ON GROUP-V TRANSITION METAL DICHALCOGENIDES		
Adam Mielnik-Pyszcorski, Krzysztof Gawarecki, Paweł Machnikowski	P2-26	137
PHONON-ASSISTED TUNNELING OF CARRIERS IN A QUANTUM WELL-QUANTUM DOT INJECTION STRUCTURE		
Andrius Sakavičius	P2-27	138
CRYSTALLINE SILICON SOLAR CELLS PASSIVATION		
Artūras Baguckis, Algirdas Novičkovas, Algirdas Mekys, Vincas Tamošiūnas	P2-28	139
APPLICATIONS OF HIGH-POWER LIGHT-EMITTING DIODES FOR SOLAR SIMULATORS		
Elena Levchuk, Leonid Makarenko, Stanislav Lastovski	P2-29	140
MODELING OF DLTS RESPONSE FOR SILICON DIODES WITH DEFECT CLUSTERS		
WITHDRAWED	P2-30	141
Laurynas Dabašinskas, Donatas Meškauskas, Artūras Žukauskas	P2-31	142
ELECTRICAL AND OPTICAL CHARACTERISTICS OF LIGHT-EMITTING DIODES WITH DOUBLE HETEROJUNCTION AS FUNCTION OF AGING DURATION		
Dovilė Meškauskaitė	P2-32	143
ANNEALING STUDIES ON DOFZ AND STFZ Si DIODES AFTER 3.5 MeV ELECTRON IRRADIATION		
Ugis Gertners, Janis Teteris, Zanda Gertnere, Elina Potanina	P2-33	144
DIRECT LIGHT-INDUCED SURFACE PATTERNING IN A-AS2S3 THIN FILMS		
Anton Yermalovich	P2-34	145
MODELLING NANOSTRUCTURED TiO2 CELLS FOR PLASMON-ENHANCED PHOTOCATALYSIS		
WITHDRAWED	P2-35	146
Anna Borisova, Andrey Aniskevich, Mauro Zarrelli	P2-36	147
EPOXY RESIN FILLED WITH CNT AND GNP: RHEOLOGY, DENSITY, AND ELASTIC MODULUS		
Alicja Szczepańska, Dorota Szczepańska, Dorota Kowalczyk	P2-37	148
GREEN SYNTHESIS OF SILVER NANOPARTICLES USING PLANT EXTRACTS		
Małgorzata Kaźmierczak, Katarzyna Pogorzaelec-Glaser, Stefan Jurga, Bartłomiej Andrzejewski	P2-38	149
THERMAL BEHAVIOR AND MAGNETIC PROPERTIES OF ALGINIC ACID – Fe3O4 NANOCOMPOSITES		
Justina Kalvelytė, Andrius Didžbalis, Romualdas Rimeika	P2-39	150
SURFACE ACOUSTIC WAVE PROPAGATION ON 36° ROTATED Y-X LiTaO3		
Mindaugas Kamarauskas, Virginijus Bukauskas, Arūnas Šetkus, Marius Treideris	P2-40	151
INVESTIGATION OF COMPLEX GEOMETRIC SHAPE p-n JUNCTIONS WITH SCANNING PROBE MICROSCOPY		
Edmudas Bružas, Andrius Garbaras, Konstantinas Zakalskis, Vidmantas Remeikis	P2-41	152
GRAPHITE SAMPLE PREPARATION FOR δ13C MEASUREMENT		
Ludmiła Szulakowska.	P2-42	153
The energy spectrum of graphene quantum dots in magnetic field and with staggered potential		
Filip Lisiecki	P2-43	154
MAGNONIC CRYSTALS		
Michał Naskret	P2-44	155
DIY Supercomputer		
Oksana Rudaya, George Pitsevich	P2-45	156
DFT CALCULATIONS OF THE FREQUENCIES AND INTENSITIES OF THE INVERSION VIBRATIONS IN THE AMMONIA MOLECULE		
Joanna Symonowicz	P2-46	157
THE APPLICATION OF THE LIGHT REFRACTION AND POLARIZATION IN MODERN ARCHITECTURE		
Saulė Abbas, Vytautas Aukštikalnis, Darius Bagdonas, Simona Barkauskaitė, Jonas Berzinš, Milda Budreckaitė, Miglius Budriūnas, Vytautas Butkus, Justinas Girsks, Martynas Grybauskas, Nerijus Jurkūnas, Gintarė Kuksėnaitė, Mantas Kulnickas, Birutė Leiputė, Ugnė Nevedomskaitė, Evaldas Paulauskas, Vytenis Pranculis, Maria Razgute, Deividas Sabonis, Edvinas Skliutas, Simona Streckaitė, Greta Striokaitė, Laura Šerkšnytė, Rūta Urbonavičiūtė, Rasa Valentinavičienė	P2-47	158
STUDENTS' SCIENTIFIC ASSOCIATION'S LABORATORY		
WITHDRAWED	P2-48	159

21 March, FRIDAY

11:30 – 14:00 **POSTER SESSION P3**

Karolis Jurkus, Deividas Sabonis, Ignas Astrauskas, Gediminas Dauderis	P3-01	161
TWO-PHOTON ABSORPTION CROSS SECTIONS MEASUREMENTS OF TOLUENE SOLUBLE CDSE/ZNS QUANTUM DOTS		
Greta Jarockytė, Eleonora Žurauskienė, Ričardas Rotomskis	P3-02	162
SPECTROSCOPIC STUDY OF CHLORIN E6 AND BOVINE SERUM ALBUMIN COMPLEXES		
Tomas Biekša, Saulius Bagdonas	P3-03	163
SPECTROSCOPIC STUDY OF HEMATOPORPHYRIN PHOTOTRANSFORMATION IN AQUEOUS MODEL MEDIUM: THE INFLUENCE OF ANTIOXIDANT		
Agnieška Mackoit, Sonata Jarmalaite	P3-04	164
INVESTIGATION OF METHYLATION STATUS OF LONG NON-CODING RNR H19 IN PROSTATE CANCER		
Barbara Urban, Michalina Skupin, Weronika Andrzejewska, Joanna Wolak, Paulina Egierska, Maciej Kozak	P3-05	165
NANOSYSTEMS BASED ON PHOSPHOLIPIDS AND SURFACTANTS AS INNOVATIVE DELIVERY SYSTEMS FOR GENE THERAPY – CIRCULAR DICHROISM STUDIES		
Svetlana Šliachtich, R. Šiekštelė, B. Pudžiuvytė, I. Matijošytė	P3-06	166
SEARCHING OF POTENTIAL BIOCATALYSTS IN METAGENOMIC DNA LIBRARIES		
Nadya Pleshko, Vladimir Krot	P3-07	167
ATOMIC FORCE MICROSCOPY OF COMPLEXES DNA WITH CARBON NANOTUBE		
Piotr Szyperski	P3-08	168
NEW ALGORITHMS FOR IMAGE ANALYSIS IN NON-INVASIVE EXAMINATION METHODS OF CORNEAL AND CONTACT LENS TEAR FILM SURFACE		
Daiga Cerane, Anete Pausus, Peteris Cikmaccs, Gunta Krumina	P3-09	169
VISUAL ACUITY IN PERIPHERY IN TERMS WITH PERCEPTION AND ITS POSSIBLE CORRELATION WITH CENTRAL VISUAL ACUITY		
WITHDRAWED	P3-10	170
Yaroslav Dichenko, Aleksei Yantsevich, Sergei Usanov	P3-11	171
ALTERATION IN CONFORMATIONAL STABILITY OF CYP7B1 ARG486CYS MUTANT IS A REASON OF NEURODEGENERATIVE DISORDER		
Sandra Bakšytė, Aurelija Mickevičiūtė, Vilma Michailovienė, Lina Baranauskienė, Daumantas Matulis	P3-12	172
CHARACTERIZATION OF MEMBRANE-BOUND CARBONIC ANHYDRASE ISOFORMS IV AND XIV		
Justina Kazokaitė, Goda Milinavičiūtė, Joana Gilytė, Virginija Dudutienė, Jurgita Matulienė, Daumantas Matulis	P3-13	173
DIFFERENCES IN THERMODYNAMICS OF INHIBITOR BINDING TO CARBONIC ANHYDRASE VI PURIFIED FROM E. COLI, MAMMALIAN CELLS AND HUMAN SALIVA		
Piotr Stępiński, Emil Paluch, Izabela Konieczna, Konrad Zabłocki	P3-14	174
EFFECTS OF STATIC MAGNETIC FIELD EXPOSURE ON PROKARYOTIC AND EUKARYOTIC CELL GROWTH		
Hanna S. Matsukovich, Elena V. Shabunya-Klyachkovskaya	P3-15	175
THE SURFACE-ENHANCED RAMAN SCATTERING FOR MERCURY SULPHIDE MICROCRYSTALS		
Sylwia Zięba, Martyna Stańczuk, Tomasz Buchwald	P3-16	176
THE APPLICATION RAMAN SPECTROSCOPY IN MEDICINE		
WITHDRAWED	P3-17	177
Aliaksandr Kruhlik, Maksim Fomich, Svetlana Akalovich, Vadim Shmanai	P3-18	178
SYNTHESIS OF TETRACYCLINE-PROTEIN CONJUGATES TO GENERATE MONOCLONAL ANTIBODIES AGAINST TETRACYCLINE		
Joana Gilyte, Asta Zubrine, Virginija Dudutiene, Alexey Smirnov, David D. Timm, Elena Manakova, Saulius Grazulis, Daumantas Matulis	P3-19	179
INTRINSIC STRUCTURE – THERMODYNAMICS CORRELATIONS OF FLUORINATED BENZENSULFONAMIDES AS INHIBITORS OF HUMAN CARBONIC ANHYDRASES		
Dmitri Dormeshkin, Vashkevich Irina, Sviridov Oleg, Andrei Gilep, Sergey Usanov	P3-20	180
CLONING AND EXPRESSION OF THE RECOMBINANT FAB FRAGMENT OF A MONOCLONAL ANTIBODY TO THE HORMONE CORTISOL		
Yekelchyk Michail Dzmityrevich	P3-21	181
THE MAGNETORHEOLOGICAL IMMERSION MEDIUM FOR ULTRASONIC THROMBOLYSIS		

WITHDRAWED

Sabina Brazevič, Magdalena Grajek, Tomasz Kopyciuk	P3-23	183
CHANGES IN THE ECG CURVE IN PATIENTS WITH MYOCARDIAL INFARCTION QUALIFIED FOR CABG SURGERY		
Akvilė Botyriūtė, Vytautas Smirnovas	P3-24	184
FLAVONE-MEDIATED INSULIN FIBRILLATION		
Katažyna Milto, Ksenija Michailova, Vytautas Smirnovas	P3-25	185
ELONGATION OF MOUSE PRION PROTEIN AMYLOID-LIKE FIBRILS: EFFECT OF TEMPERATURE AND DENATURANT CONCENTRATION		
Dovilė Čibiraitė, Sandra Pralgauskaitė, Jonas Matukas	P3-26	186
SPECTRAL AND CORRELATION ANALYSIS OF FLUCTUATIONS OF CARDIOVASCULAR SYSTEM SIGNALS		
Jurgita Stankevičiūtė, Vilmantas Gėgžna, Aurelija Vaitkuvienė	P3-27	187
THE FLUORESCENCE SPECTROSCOPY OF MEDICAL SAMPLES AND THE ANALYSIS OF SPECTRA USING MULTI-CURVE RESOLUTION METHODS		
Vadimas Dudoitis, Vidmantas Ulevičius, Genrik Mordas	P3-28	188
CHITOSAN AEROSOL NANOPARTICLE PRODUCTION BY ELECTROSPRAYING		
Julija Fedorovič, Donatas Pupienis, Ilya Buynevich, Darius Jarmalavičius, Gintautas Žilinskas	P3-29	189
CROSS-SHORE AND LONGSHORE HEAVY-MINERAL CONCENTRATIONS DISTRIBUTION ON THE BALTIC SEA MAINLAND COAST, LITHUANIA		
Steigvilė Byčenkienė, Julija Pauraitė, Vadimas Dudoitis, Vidmantas Ulevičius	P3-30	190
SOURCES OF WINTERTIME BLACK CARBON AEROSOLS IN AN ATMOSPHERE IN VILNIUS		
Inga Rumskaitė and Vytautas Abromaitis	P3-31	191
ADSORPTION OF TARGET ORGANIC COMPOUNDS ON ACTIVATED CARBON		
Inga Rumskaitė, Edvinas Krugly, Jolanta Sedlina, Dainius Martuzevičius, Martynas Tichonovas, Dalia Jankūnaitė, Viktoras Račys and Jonas Baltrušaitis	P3-32	192
DECOMPOSITION OF 2-NAPHTHOL IN SIMULATED WASTEWATER SOLUTION USING DBD PLASMA		
Benjaminas Marcinkevicius, Daniela Ene, Artūras Plukis	P3-33	193
SHIELDING AND ACTIVATION STUDIES TO ESTIMATE THE RADIOACTIVE WASTES ARISING FROM THE OPERATION OF THE ESS BEAM DUMP		
Bartosz Dziedzic	P3-34	194
LOW COST COMPUTER CONTROLLED SAMPLE POSITIONING SYSTEM		
Piotr Rożek	P3-35	195
ENTANGLEMENT DETECTION WITH ENTANGLEMENT WITNESS OPERATOR IN TWO QUBIT SYSTEMS		
Rytis Kazakevičius, Julius Ruseckas	P3-36	196
LEVY FLIGHTS IN NON-HOMOGENEOUS MEDIA AND 1/F NOISE		
WITHDRAWED	P3-37	197
Michal Bogdan	P3-38	198
A REVIEW OF CONTEMPORARY MODELS OF INFLATION THEORY		
Rokas Naujalis, Kastytis Zubovas	P3-39	199
MODELING OF ACTIVE GALACTIC NUCLEI WINDS		
Maryna Hliatsevich, Pavel Bulai, Taras Pitlik	P3-40	200
MATHEMATICAL MODEL OF SIGNAL TRANSDUCTION IN EXCITATORY GLUTAMATERGIC SYNAPSES: WAYS OF TRANSMISSION EFFICACY REGULATION		
Aleksejus Kononovicius, Vygintas Gontis	P3-41	201
LEADERSHIP PHENOMENON IN THE AGENT-BASED HERDING MODEL		
Petras Paulauskas	P3-42	202
INVESTIGATION ON HASH-ROUTING SCHEMES IN INFORMATION-CENTRIC NETWORKS		
Giedrius Tušinskis	P3-43	203
INVESTIGATION OF ABSORPTION IN A FINITE SET OF CYLINDERS		
Jonas Narkeliūnas, Jevgenij Chmeliov, Stepas Toliautas	P3-44	204
MODELLING ELECTRONIC DENSITY OF STATES IN CARBON NANOTUBES		
Kristina Jakubavičiūtė, Kęstutis Aidas	P3-45	205
MOLECULAR DYNAMICS SIMULATION OF ATOMIC IONS IN AQUEOUS SOLUTION		
Giedrius Žlabys, Egidijus Anisimovas	P3-46	206
TUNABLE LIEB AND KAGOME LATTICES FOR ULTRA-COLD YTTERBIUM ATOMS		
Gintaras Kerevičius	P3-47	207
SIMULATION OF THE INTENSITY SPECTRUM OF AUTOIONIZING STATES OF RUBIDIUM ATOM EXCITED		

BY ELECTRON IMPACT

Olga Novichenok, Alena Melnikova, George Pitsevich

P3-48 **208****STUDY OF THE SPECTRAL MANIFESTATIONS OF INTRAMOLECULAR HYDROGEN BOND FORMATION IN THE MALONALDEHYDE MOLECULE**

WITHDRAWED

P3-49 **209**

Veranika Burko, Yana Douhaya, Anastasiya Berezhnaya

P3-50 **210****THE QUANTUM MECHANICAL MODELING OF INTERACTION BETWEEN FRAGMENT OF BACTERIAL CELL WALL AND SILICON SURFACE**

Oral session 1

Laser physics and optical technologies

THERMAL DISTORTIONS IN Nd:YAG CRYSTAL FIBER AMPLIFIER SEEDED BY PICOSECOND PULSES

Dominykas Bričkus, Kasparas Sasnauskas, Aleksej Rodin, Alexander Dement'ev

Department of Laser Technology, Center for Physical Sciences and Technology, Vilnius, Lithuania

dominykus@gmail.com

Fiber lasers mode-locked by semiconductor saturable absorber mirror (SESAM) are unsurpassed in terms of the beam quality, compactness and easy integration. Different techniques are known for subsequent power and energy scaling. In particular, crystal fiber amplifiers benefit from the good overlap between pump and seed beams due to the pump guiding and improved thermal management ensured by the high surface-to-volume ratio [1].

We present results of numerical and experimental investigation of thermally induced beam distortions for Nd:YAG crystal fiber amplifier injected by 5 ps pulses with beam quality factor of $M^2 \sim 1.1$. These seed pulses were emitted from passively mode locked fiber laser running at repetition rate of 29 MHz with average output power of 1.6 mW at wavelength of 1064.14 nm. Single-pass amplifier is end-pumped at 808 nm wavelength by fiber coupled laser diode with Bragg grating (Fig.1 – upper-left). Collimated seed of ~ 0.5 mm diameter counter-propagates through Nd:YAG rod of 1 mm diameter and 50 mm length doped by 0.2% Nd.

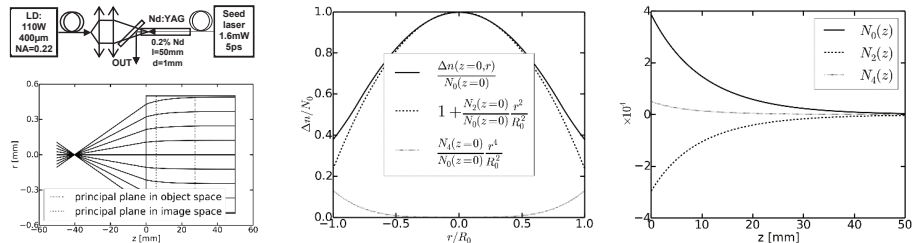


Fig. 1. Experimental lay-out (upper-left), ray tracing of probe beam (bottom-left), cross-section of refractive index distribution with its polynomial fit terms (center), the $N_j(z)$ coefficients along the crystal (right).

Continuous pumping and high repetition rate of seed pulses permits to investigate the steady state case [2]. It is recently shown [3] that the commonly used plane stress or plane strain approximations significantly overestimate the values of face bulging of laser rods under the condition of longitudinal pumping. It is particularly true for long rods when only radial heat flow can be treated. The dependence on the longitudinal coordinate arises due to the heat source. The analytical solutions can be found for different distributions of pump beam taking into account the temperature dependence of thermal conductivity [2]. In this case the temperature change is not parabolic in the region of pump beam even for the top-hat pump beam distribution. It should be noted that one more cause for the occurrence of thermal aberrations is the nonlinear dependence of thermal refractive index change [2]. Thus, in the cylindrically symmetric case it can be presented as $\Delta n_T(r, z) = N_0(z) + N_2(z)(r/R)^2 + N_4(z)(r/R)^4$ where coefficients $N_j(z)$ are found numerically by fitting procedure and $R_0 = 0.5$ mm is the radius of the rod (Fig. 1 - right). Two r -dependent terms are sufficient for the precise fitting of refractive index change (Fig.1 – center). Then, using the methods of matrix optics, the $ABCD$ -matrix of thick lens with inhomogeneous refractive index distribution was found and ray tracing procedure was performed (Fig. 1 – bottom-left). The focal length of thermal lens ($f_T = 46.9$ mm) found during this procedure is slightly longer ($\tilde{f}_T = 43$ mm) than the one found from the optical path difference $OPD(r) = r^2/2\tilde{f}_T - \tilde{N}_4(r/R)^4$. The latter procedure corresponds to averaging of $\Delta n_T(r, z)$ along the rod: $\tilde{N}_j = (1/l) \int_0^l N_j(z) dz$. The difference between these approaches is more significant in defining the positions of principal planes defined with respect to the entrance and exit planes of pump beam: the matrix method gives $d_{en} = 5.7$ mm and $d_{ex} = 22.5$ mm (Fig. 1 – bottom-left) instead of $\tilde{d}_{en} = \tilde{d}_{ex} = 13.9$ mm. The change of near Gaussian seed beam quality to $M^2 = 1.14$ was found using formulae from [4]. For all other pump beam intensity distributions and amplification saturation the M^2 of the seed beam should increase.

Therefore, amplified beam quality degradation is conditioned mainly by thermally induced spherical aberrations. Nevertheless, high quality amplified output beams with $M^2 \sim 1.24$ -1.3 have been achieved from the Nd:YAG crystal fiber amplifier module pumped by 100-110 W with gain in excess of 50 and output power over 80 mW.

[1] X. Dēlen, Y. Zaouter, I. Martial, N. Aubry, J. Didierjean, C. Hönninger, E. Molty, F. Balembois and P. Georges, Yb:YAG single crystal fiber power amplifier for femtosecond sources, Opt. Lett **38**, 109-111 (2011).

[2] A.S.Dement'ev, A.Jovaiša, K.Rackaitis, F.Ivanauskas, J.Dabulytė-Bagdonavičienė, Numerical treatment of the temperature distribution in end-pumped composite laser rods, Lithuanian J. Phys. **47**, 279-288 (2007).

[3] A.S. Dement'ev, A. Jovaiša, E. Stupak and R. Kačianauskas, Thermal stresses and end-bulging in cylindrical laser rods under longitudinal diode laser pumping, Journal of Thermal Stresses, **37**, 73-92 (2014).

[4] A.S.Dement'ev, A.Jovaiša, G.Šilko, R.Čiegis, On alternative methods for measuring the radius and propagation ratio of axially symmetric laser beams, Quantum Electronics, **35**, 1045-1052 (2005).

SPECTRUM EFFECTS OF POLARIZATION SWITCHING IN VERTICAL CAVITY SURFACE-EMITTING LASERS

Eugene Sokolov¹, Leonid Burov¹, Alexander Gorbatshevich¹

¹ Department of Physics, Belarusian State University, Belarus

eugene_sokolov@tut.by

During the last 15 years vertical cavity surface-emitting lasers (VCSELs) were firmly established in the laser diode market and found numerous application areas from multimode fiber optical networks and computer mice to diverse sensing and illumination purposes. Whereas significant progress in VCSEL performance and description has been achieved over the last ten years, there are still relevant problems in their modelling and application. Particularly, controlling the state of polarization, which is highly important for a large number of polarization-sensitive systems, achieving higher (more than 25 Gbit/s) digital data rates and etc.

The present work illustrates usability of the proposed phenomenological model of the polarized radiation formation in the semiconductor injection lasers. The dynamic and spectrum effects of the polarization switching (PS) on the basis of this model are considered.

The theoretical model is based on the polarization components method (PCM). Within this method the field of a plane wave is represented as a superposition of a large number of polarized components. The quasi steady state approximation allows regarding different frequencies independently and introducing frequency components as well. Each polarization and frequency component is described by the rate equation, written in the slowly varying envelope approximation, and the rate equation of carrier concentration is introduced. Gain shape is assumed to have Lorentzian shape with the peak frequency depending on the injection current. Longitudinal mode structure is taken into account by spectral dependence of the reflection coefficient. Further, the numerical methods were used for the solution of the obtained system of equation. Calculations were held for a wide set of parameters values, parameters of the active medium were correlated with ones of the GaAs heterostructures.

Numerical modeling, based on the approach mentioned above, allows to describe polarization effects in the single-mode semi-conductor injection lasers, which are observed experimentally: effect of PS (both with the switching from the mode with higher frequency to the mode with lower frequency and vice versa, see Fig. 1), polarization hysteresis, injection-current and frequency shift of the PS in lasers under the external injection of the polarized signal, dependence of the speed of PS on the duration and polarization angle of the injected impulse, etc.

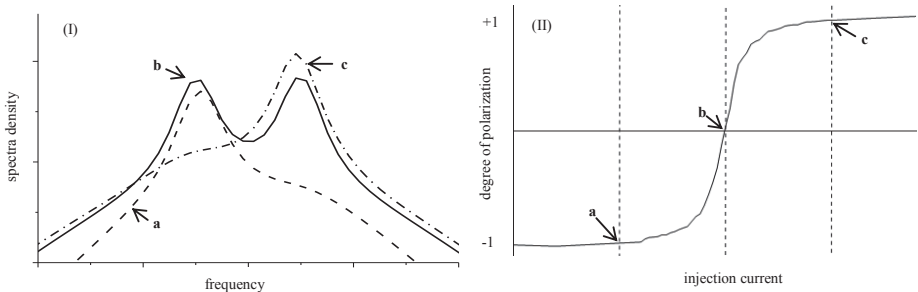


Fig. 1. Optical power spectra (I) and polarization of the output radiation against the injection current (II). Different spectra correspond to the different values of injection current denoted by **a**, **b**, **c**. The corresponding states of polarization are marked on the graphic (II).

The obtained results give simple and consistent physical interpretation of the experimental data, described in the literature on the dynamics of PS in VCSELs (e.g. see [1]), predicts the correlation between characteristics of the output radiation and the parameters of the injected signal. The basic difference of the proposed approach from the widespread spin-flip model [2] of the polarization properties of semiconductor lasers consists in the absence of the rigid conditions on the phase and polarization structure of the radiation, which is formed during the formation of radiation in the laser cavity. It is important to note, that there is a possibility of broadening of the worked-out approach on the description of the higher (not fundamental) modes of the laser output radiation and studying of the specific laser systems, either semiconductor or solid-state.

[1] M. Sondermann, M. Weinkath, and T. Ackemann, Two-frequency emission and polarization dynamics at lasing threshold in vertical-cavity surface-emitting lasers, *Physical review A* **68**, 033822 (2003).

[2] M. San Miguel, Q. Feng, and J. V. Moloney, Light polarization dynamics in surface emitting semiconductor lasers, *Physical review A* **52**, 1728–1739 (1995).

ULTRAFAST PULSED LASER INDUCED LIFT-OFF PATTERNING OF CZTSe THIN-FILM SOLAR CELLS

Edgaras Markauskas

Center for Physical Sciences and Technology, Savanoriu ave. 231, LT-02300, Vilnius, Lithuania
edgaras.markauskas@ftmc.lt

Rapidly growing thin-film photovoltaic market is driven by two polycrystalline technologies: CdTe and $\text{CuIn}_{1-x}\text{Ga}_x\text{Se}_2$ (CIGS) due to relatively high performance for converting sunlight into electricity and low module costs. On the other hand, converging to terawatt-scale deployment, these absorbers have some limitations due to scarcity of indium, gallium and tellurium [1, 2]. In $\text{Cu}_2\text{ZnSnSe}_4$ (CZTSe) absorber these rear elements can be replaced by cheaper and more earth abundant elements such as Zn and Sn, therefore this type of thin-film solar cells have drawn a lot of attention as a perspective material for CIGS technology replacement.

Kesterite (CZTSe) technology shows efficiencies up to 12.6 % for small scale devices [3]. However, after the transition from small scale to full-sized solar modules, high photocurrent and resistance losses are introduced. In order to preserve efficiency of small solar cells, large solar panel is divided into smaller adjacent cells which afterwards are interconnected in series by three patterning processes. These processes are integrated in roll-to-roll production of thin-film solar cells. Recent investigations revealed formation of melted area and degradation of the devices electrical properties even after irradiation of ultrashort laser pulses [4].

For this reason we proposed laser induced material lift-off process for the front side scribing of the CZTSe solar cells. Using proper laser wavelength, it is possible to control laser energy coupling in the complex film layer structure. High absorption at inner interface of the layers triggers localized rapid temperature rise which facilitates localized spallation of the films rather than evaporation. This material lift-off process enables to process thermally sensitive films as all the laser affected material is mechanically removed from the laser ablation area [5].

Ablation and scribing experiments were carried out with fundamental harmonics of the picosecond laser (Atlantic, 1064 nm, 10 ps, from EKSPLA) and tunable pulse duration femtosecond Yb:KGW laser (Pharos, 1030 nm, 300 fs, from Light Conversion).

In our recent investigations, we have studied influence of the laser pulse length to a laser-induced material lift-off process for the front-side scribing of the CZTSe solar cells. Laser pulse duration was changed between 300 fs, 1 ps and 10 ps durations. Two types of multilayer structure of the CZTSe solar cells were investigated: (i) complete structure consisting of TCO top-contact, $\text{Cu}_2\text{ZnSnSe}_4$ absorber layer, molybdenum back-contact and soda-lime-glass as a substrate and (ii) incomplete CZTS/Mo/SLG structure without top-contact.

Single pulse ablation and scribing experiments were performed on thin-film CZTSe structure in order to find optimal conditions for the Mo back-contact exposure in both P2 and P3 processes. It was determined that at specific experimental conditions, constant and high repeatability lift-off craters could be formed in CZTSe thin-film solar cell structures. SEM images, EDX and Raman spectrums were investigated in order to compare laser pulse length influence to lift-off effect.

[1] N. Vora, J. Blackburn, I. Repins, et al., Phase identification and control of thin films deposited by co-evaporation of elemental Cu, Zn, Sn, and Se, *Journal of Vacuum Science & Technology A: Vacuum, Surfaces, and Films*, vol. 30, (2012).

[2] H. Katagiri, K. Jimbo, et al., Development of CZTS-based thin film solar cells, *Thin Solid Films* **517**, 2455-2460, (2009).

[3] W. Wang, M. T. Winkler, O. Gunawan, et al., Device Characteristics of CZTSe Thin-Film Solar Cells with 12.6% Efficiency, *Advanced Energy Materials*, (2013).

[4] P. Gečys, G. Račiukaitis, A. Wehrmann, et al., Scribing of Thin-Film Solar Cells with Picosecond and Femtosecond Lasers, *Journal of Laser Micro / Nanoengineering*, vol. 7, p. 33, (2012).

[5] G. Račiukaitis, S. Grubinskas, et al., Selectiveness of laser processing due to energy coupling localization: case of thin film solar cell scribing, *Applied Physics A: Materials Science & Processing*, 1-6, (2012).

PHOTOREFRACTIVE SELF-INDUCED WAVEGUIDES IN LITHIUM NIOBATE FOR INTEGRATED PHOTONICS APPLICATIONS

Silviu T. Popescu*, Adrian Petris, Valentin I. Vlad

National Institute for Laser, Plasma and Radiation Physics, 409 Atomistilor Street 077125, Magurele, Romania
 silviu.popescu@infllpr.ro

The study of spatial solitons in photorefractive crystals [1] has showed the possibility to guide light by light-induced refractive index changes at very low power levels [2-4]. The light creates a waveguide that guides itself or can guide other beams. In lithium niobate (LN), the self-induced waveguides have a lifetime of the order of ~ 1 year, when guiding beams at wavelengths outside the photorefractive sensitivity range of the crystal. We demonstrated the robustness of these waveguides in guiding of IR ultrashort pulses (femtosecond) at very high peak powers [4, 6, 7]. Depending on the experimental conditions the waveguide's transversal and longitudinal refractive index distribution can take different shapes. This way we can generate different waveguiding elements of particular importance in integrated photonics applications like tapered waveguides, Y junctions or array of waveguides, as shown in Fig.1.

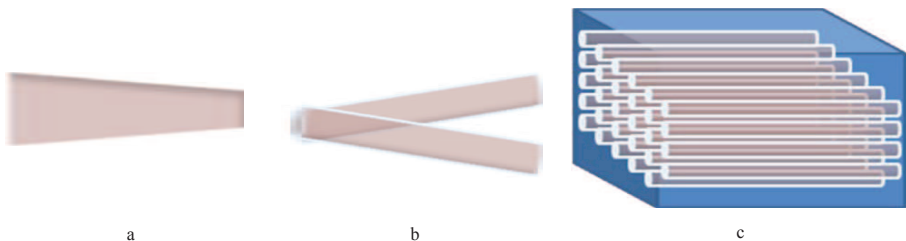


Fig. 1. Different shapes of the photorefractive self-induced waveguides: a) tapered; b) Y junction; c) array.

In the past years we have made significant improvements to the process of waveguides recording. We review our recent results regarding the recording of volume and surface self-induced waveguides in LN

-
- [1] G.C Duree, J.L Shultz, G. J Salamo, M. Segev., A. Yariv, B. Crosignani, P. Di Porto, E.J. Sharp, R.R Neurgaonkar, *Phys. Rev. Lett.* **71**, 533 (1993)
 - [2] M. Morin, G. Duree, G. Salamo, M. Segev, *Opt. Lett.* **20**, 2066-2068 (1995).
 - [3] E. Fazio, F. Renzi, R. Rinaldi, M. Bertolotti, M. Chauvet, W. Ramadan, A. Petris, V.I. Vlad, *Appl. Phys. Lett.* **85**, 2193 (2004).
 - [4] S.T. Popescu, A. Petris, V.I. Vlad, *Appl. Phys. B* **108**, 799 (2012).
 - [5] S.T. Popescu, A. Petris, V.I. Vlad, *J. Appl. Phys.* **113**, 213110 (2013).
 - [6] A. Petris, V.I. Vlad, A. Bosco, E. Fazio, M. Bertolotti, *J. Optoelectron. Adv. M.* **7**, 2133 (2005).
 - [7] A. Petris, S.T. Popescu, V.I. Vlad, E. Fazio, *Rom. Rep Phys* **64**, 492 (2012).

LASER POLYMERIZATION OF NON-PHOTOSENSITIZED MATERIALS USING VARIOUS FOCUSING CONDITIONS

Linus Jonušauskas and Mangirdas Malinauskas

Department of Quantum Electronics, Vilnius University, Saulėtekio Ave., 9,
Vilnius LT-10222, Lithuania
linas.jon@gmail.com

Many works during recent decade were dedicated to prove that polymers as suitable materials for three-dimensional (3D) micro- and nano-structure fabrication. Easy synthesis of polymers allows to chose material best suited for particular structure fabrication and its optimal performance. Cross-linking reaction can be induced by selectively introducing heat or light which allows relatively easy fabrication process. In case of light induced polymerization, most of the materials are photosensitized before exposing them to the irradiation. This is done to enhance their sensitivity to specific light wavelength and thus making fabrication process easier. Photosensitizing is done by doping polymers with 0.1-5 % w.t. photoinitiators [1]. Although these materials increase the photopolymerization reaction efficiency, there is some additional effects associated with photosensitizing, such as increased light absorption [1] and cytotoxicity [2]. This makes polymers doped with photoinitiators not perfectly suited for some researcher areas such as microoptics or biomedicine.

Recent works [3, 4, 5] showed that one way to avoid this problem is to induce polymerization reaction by tightly focused femtosecond laser beam, or, in other words, using Direct Laser Writing (DLW) technique [6]. In this case, because of very high intensity in focal point ($\sim \text{TW}/\text{cm}^2$), nonlinear effects start to occur. It was experimentally demonstrated to be nonlinear absorption and subsequent avalanche ionization which induces bond braking [5]. This way radical polymerization reaction occurs even in non-photosensitized materials which in turn allows true 3D fabrication in micro- and nano-scale with spatial resolution up of hundreds of nanometers [6].

However, although possibility to cross-link polymers using DLW without photoinitiators was already demonstrated, further works have to be done to compare spatial resolution and structures formed out of pure and photosensitized polymers. Also, possibility to fabricate structures with different focusing conditions used to fabricate various kinds of structures have to be investigated. This work addresses these issues. As an additional result, method of using different focusing conditions to form one structure to improve fabrication throughput is proposed and tested. All structures in this work are formed from organic-inorganic polymer SZ2080.

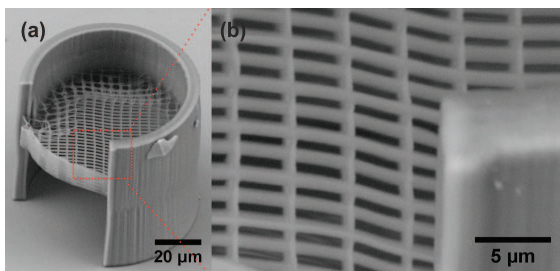


Fig. 1. Prototype of functional microdevice - microfluidic tube with filter fabricated using two different focusing conditions and made of non-photosensitized SZ2080. (a) - overall view; (b) - filter view. Such structure could be applied as biofluidic filter selectively sorting cells.

- [1] M. Malinauskas, A. Gaidukevičiūtė, V. Purlys et al., Direct laser writing of microoptical structures using a Ge-containing hybrid material, *Metamaterials* **5**, 135-140 (2011).
- [2] A. Ovsianikov, M. Malinauskas, S. Schlie et al., Three-dimensional laser micro- and nano-structuring of acrylated poly(ethylene glycol) materials and evaluation of their cytotoxicity for tissue engineering applications, *Acta Biomater.* **7**, 967-974 (2011).
- [3] J. Fischer, J. B. Mueller, J. Kaschke et al., Three-dimensional multi-photon direct laser writing with variable repetition rate, *Opt. Express* **21**(22), 26244-26260 (2013).
- [4] S. Rekšytė, M. Malinauskas, and S. Juodkazis, Three-dimensional laser micro-sculpturing of silicone: towards bio-compatible scaffolds, *Opt. Express* **21**(14), 17028-17041 (2013).
- [5] M. Malinauskas, A. Žukauskas, G. Bičkauskaitė et al., Mechanisms of three-dimensional structuring of photopolymers by tightly focussed femtosecond laser pulses, *Opt. Express*, **18**(10), 10209 (2010).
- [6] M. Malinauskas, M. Farsari, A. Piskarskas, and S. Juodkazis, Ultrafast laser nanostructuring of photopolymers: A decade of advances, *Phys. Rep.* **553**, 1-31 (2013).

HOLOGRAPHIC ELEMENTS FOR 3D MICROSCOPYSergey Nazarov¹, Elen Tolstik^{2,3}, Vladimir Mahilny¹, Rainer Heintzmann^{2,3}, Alexei Tolstik¹¹ Department of Physics, Belarusian State University, Minsk, Belarus² Leibniz Institute of Photonic Technology, Jena, Germany³ Friedrich-Schiller-University, Institute of Physical Chemistry, Jena, Germany
sanazarov@tut.by

Scanning highly-resolved 3D microscopy is widely used in engineering, biological and medical sciences [1]. One of the trends in its development is associated with the ways to obviate the mechanical movement of the optical elements during in-volume scanning of the object. The use of multiplex volume phase holograms characterized by high diffraction efficiency looks very promising for 3D microscopy with a stationary optics. In this way numerous cross-section measurements of one 3D image can be obtained by a single measurement resulting in faster data acquisition. The main idea of the use of volume multiplexing holography is that each of the superimposed holograms provides an image of one of the cross-sections of an object which has been obtained at a specific distance from the objective. Images of the cross-sections at different depths can be multiplexed to different adjacent detectors. They can simultaneously be recorded by a single measurement. For each such detector channel, a multiplexed hologram in the photopolymer is required.

The possibility to use multiplex phase holograms recorded in photopolymer layers is provided by their stability, robustness and long lifetime. The holographic material consists of the polymer (Polymethyl methacrylate), (PMMA) and a photosensitive dye phenanthrenequinone (PQ). This novel material allows to record holographic gratings with high diffraction efficiency (DE is up to 90 %) due to the diffusion-based thermal amplification process [2-3].

During presented study the record of the multiplex holograms of two point sources that are situated on the different distances from the objective lens on the optical axis was performed. Maximum DE during the record of a single grating achieved the values of about 7 %. After post-exposure annealing the DE increased up to 82 % (Figure 1 (a) and (b)).

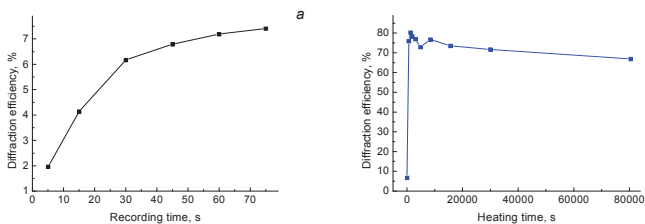


Fig.1. Dependence of the diffraction efficiency on the duration of recording (a) and on the post-exposure annealing time (b) for a single grating record.

The kinetics of the diffraction efficiency of the first and second gratings during the multiplex record is presented in the Figure 2. The post-exposure annealing allows to increase the DE values up to 34 % and 26 % for first and second gratings, respectively.

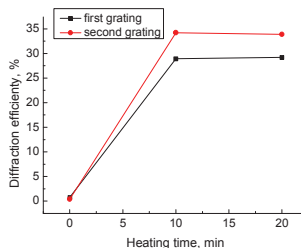


Fig.2. Dependence of the diffraction efficiency from the duration post-exposure annealing of multiplex hologram.

- [1] Luo, Y. et al. Laser-induced fluorescence imaging of subsurface tissue structures with a volume holographic spatial-spectral imaging system. Opt. Lett. 33 (2008).
 [2] U.V. Mahilny, D.N. Marmysh, A.L. Tolstik, V. Matusevich, R. Kowarschik, "Phase hologram formation in highly concentrated phenanthrenequinone-PMMA media," J. Opt. A: Pure Appl. Opt. 10, 085302 (2008).
 [3] Mahilny, U. V. et al. Holographic volume gratings in a glass-like polymer material. Appl. Phys. B 82 (2005).

Oral session 2

Spectroscopy, functional materials and chemistry

LASER ASSISTED TECHNIQUES FOR SYNTHESIS OF COMPOUND NANOPARTICLES IN SOLUTIONS

Natalie Tarasenko, Andrei Butsen

B.I. Stepanov Institute of Physics, 68 Nezalezhnasti Ave., 220072 Minsk, Belarus
n.tarasenko@ifanbel.bas-net.by

Last decades laser assisted methods based on laser ablation and post-ablation irradiation in liquids has become a topic of great interest for targeted synthesis and modification of nanomaterials [1]. In the frame of the laser ablation technique one can combine particle synthesis with functionalization, encapsulation and stabilization of products. Post-ablation irradiation of nanoparticles with laser light can provide an effective way to alter their size and shape as well as to change a composition and inner structure of the particles. However, a practical application of laser methods for fabrication of nanoparticles with desired parameters requires a detailed study of physical processes (heating, melting, evaporation, laser-induced photofragmentation and aggregation) and chemical reactions accompanying laser-target and laser-particle interactions. The changes in nanoparticles induced by laser irradiation are determined by the temperature that is reached during the irradiation. Generally, on the first stage the incident radiation is absorbed by the particle that results in the temperature rise up to melting or even boiling point of the particle material. Exact knowledge of the particle temperature during pulsed laser irradiation is important for correct interpretation of the observed phenomena.

In the present work the capabilities of laser ablation technique with post-ablation irradiation in liquid for synthesis of doped zinc oxide nanoparticles and compound gadolinium-germano-silicides nanostructures has been studied. For controlling the temperature of the laser heated particles the emitted blackbody-like radiation from the hot nanoparticles have been measured and analyzed. Nanoscale compounds and alloys of gadolinium are promising materials for applications as magnetic agents for the hyperthermia treatment. ZnO nanostructures have received a great interest due potential applications in blue/UV light emitting diodes, piezoelectric transducers, gas sensors, etc., that require ZnO homojunctions formed at the interface between p- and n-type ZnO. Because of the intrinsic n-type conductivity, reliable p-type doping of ZnO is still a major problem although examples of p-type ZnO realization using acceptor dopants such as N, As or P, co-doping with nitrogen and a group-III element (Al, In) and dual-acceptor doping method with simultaneous introduction of two acceptors such as Li-N, N-As and N-Ag have been proposed.

The initial colloids were produced by laser ablation in ethanol or water solutions. The experiments were carried out by focusing of radiation of a Nd:YAG laser (LOTIS TII, LS2134D), operating in a double-pulse mode at 1064 nm, on the surface of the target placed in the cell with the solvent (repetition rate 10 Hz, pulse duration 8 ns, pulse energy 50 – 80 mJ). After the preparation the colloids were subjected to laser irradiation by the second harmonic of the Nd:YAG laser (wavelength 532 nm, pulse duration 10 ns) with fluences of 230 and 400 mJ/cm². To prepare p-type ZnO NPs two different synthetic schemes were used. First, the ZnO doped NPs were synthesized by two step process which involved a sequential ablation of Zn and Ag targets in the 0.01M NH₄NO₃ solution followed by the additional laser irradiation of the formed colloid with the second harmonic of the Nd:YAG laser (532 nm, 400 mJ/cm²) (ZnO N2). Second, the colloidal solution was obtained by laser ablation of Zn target in the mixture of Ag colloid in ethanol and NH₄NO₃ (ZnO N3). The compound Gd (Si, Ge) nanoparticles nanostructures were synthesized by four step process which involved a sequential ablation of germanium, silicon and gadolinium targets followed by the additional laser irradiation of the mixture of the formed colloids.

The resulting NPs were characterized by TEM, XRD, SAED and optical absorption spectroscopy. To determine the temperature of the nanoparticles their thermal radiation spectra were fitted by a Planck curve, taking into account the emissivity function of nanoparticles and that the CCD detector counts the number of photons.

It has been shown that laser ablation of Zn target in 0.01 M NH₄NO₃ solution (N1) results in the formation of two types of particles: rod-like and spherical with a size of 30-50 nm. However, the phase composition of both types of particles is analogous. The major phase is polycrystalline ZnO with the hexagonal zincite structure. The impurity hexagonal zinc phase is also present in the diffraction patterns of both types of NPs. The ablation of Ag target in the solution N1 results in the transformation of rod-like particles into spherical ones (N2). The analysis of SAED patterns of the N3 sample showed that the particles are composed of the ZnO NPs in zincite structure and of cubic Ag. Laser irradiation of NPs in the third sample results in the disappearing of ZnO and Ag reflections that can be the consequence of the alloying of Ag and Zn NPs.

Laser assisted technique in liquid has been also demonstrated to be an effective tool to prepare magnetic Gd silicides and germano-silicides particles with sizes in the nanometric range. Magnetic measurements showed that the resulting nanoparticles didn't exhibit hysteresis at low temperature (6 K), which is typical to nanosized magnetic materials demonstrating superparamagnetic behavior.

It has been shown that the detection of black body radiation is a versatile tool for fast non-contact measurements of particle temperature. Based on the thermal radiation of the hot nanoparticles the temperature of the laser heated particles was determined. The resulting temperature (about 3000 K) was shown to be described on the basis of a balance between the absorbed laser energy and heat losses during the laser pulse using the bulk physical constants.

NEAR AND FAR-FIELD OPTICAL PROPERTIES OF METALLIC TRIANGULAR NANOPRISMS

Krzysztof Ptaszyński¹, Bartłomiej Grześkiewicz², Michał Kotkowiak¹

¹ Institute of Physics, Faculty of Technical Physics, Poznan University of Technology, Poland

² Chair of Optical Spectroscopy, of Technical Physics, Poznan University of Technology, Poland
krzysztof.ptaszynski10@gmail.com

Interaction of light with metallic nanostructures with geometrical dimensions smaller than wavelength of incident light may lead to significant enhancement of electric field in the near-field of nanostructure. This effect finds applications in Surface Enhanced Fluorescence Spectroscopy, Surface Enhanced Raman Spectroscopy [1] and photovoltaics [2]. Optical properties of plasmonic structures depend on their geometric parameters and are sensitive to them [3]. Recently, many advanced methods for the preparation of nanostructures have been proposed, however still the geometric parameters are inaccurate [4]. Numerical simulations provide a powerful tool for analysis of plasmonic nanostructures.

In this work far-field and near-field optical properties of gold and silver triangular nanoprisms and their dimers with different geometrical parameters were studied using numerical simulations. For this purpose Finite Integration Technique implemented to the CST Microwave Studio was used. Results of numerical simulations indicate that the radius of the curvature edges strongly affects the plasmon resonant mode frequency and this effect cannot be neglected in plasmonic devices design. Increase in the radius of edge curvature causes main extinction cross section peak blue shift in all cases analyzed. Moreover, calculations imply that the nanoparticle in the gap between prisms strongly influence the dependence of spectral properties on the radius curvature. It was also found that increase of nanoprism thickness cause extinction cross section blue shift when base edge length is kept constant. For some thicknesses distinct extinction band splitting was observed in case of nanoprism with sharp edges, however for nanoprism with rounded edges this effect was not observed.

[1] V. Giannini et al., Plasmonic Nanoantennas: Fundamentals and Their Use in Controlling the Radiative Properties of Nanoemitters, *Chem. Rev.* **111**, 3888-3912 (2011).

[2] H.A. Atwater et al., Plasmonics for improved photovoltaic devices, *Nature Mater.* **9**, 205-213 (2009).

[3] K.L. Kelly et al., The Optical Properties of Metal Nanoparticles: The Influence of Size, Shape, and Dielectric Environment, *J. Phys. Chem. B* **107**, 668-677 (2003).

[4] G. Yamaguchi et al., Characteristics of light intensity enhancement of a silver nanoprism with rounded corners, *J. Microsc.* **229**, 545-550 (2008).

NEW ANTHRACENE-CARBAZOLE DERIVATIVES FOR OPTOELECTRONIC APPLICATIONS

Paulius Imbrasas¹, Saulius Juršėnas²

¹ Faculty of Physics, Vilnius University, Lithuania

² Institute of Applied Research, Vilnius University, Lithuania

paulius.imbrasas@ff.stud.vu.lt

Organic compounds are becoming increasingly popular in the optoelectronics market. OLEDs, organic solar cells, organic semiconductor based sensors are already being made and used in practice. The usage of more complex molecules in these devices show the best results. Because of their efficiency anthracene and carbazole derivatives are a popular choice, therefore improving them is important. However, implementing any kind of new molecular systems first requires a detailed analysis of their photophysical properties.

Here a summary of optical, photoelectrical and quantum chemical properties of 10 new anthracene-carbazole derivatives (see Figure 1) with non-conjugated and conjugated substituents is presented.

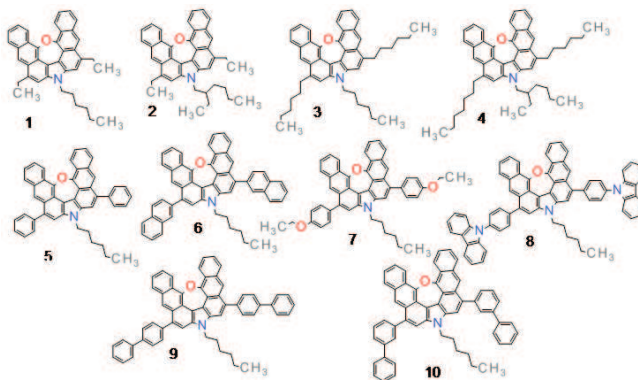


Figure 1. The structural formulas of the NOP 1-10 compounds.

Quantum chemical calculations of charge density distribution of the highest-occupied (HOMO) and lowest-unoccupied (LUMO) molecular orbitals of two characteristic NOP derivatives with conjugated and non-conjugated substituents showed that charge density is distributed over the whole molecular backbone with a slight charge transfer character. The conjugation extends to the aryl substituents (compounds 5-10) resulting in the increase of the molecular dipolar momentum. The measured absorbance spectra resemble those that are typical to anthracene and carbazole derivatives, the first two peaks in the lower energy part corresponding to anthracene and the intense absorption band in the higher energy part is typically seen in carbazole derivatives. The emission spectra have a peak at ~540 nm and a vibronic structure when measured in toluene and are more wide-spread, formless and shifted to the lower energy part by ~20nm in DMF (dimethylformamide). This is a typical result for charge transfer fluorescence. A shift of 10 nm to the lower energy part and an almost doubled extinction coefficient is observed in the compounds with conjugated substituents. The results show a poor quantum yield of the NOP compounds (~4%-12%), however it increases by 2-3 times when the conjugated substituents are added. The fluorescence lifetimes are rather long (~9ns-12ns), increasing with added conjugated substituents. The increase of the quantum yield is due to a higher rate of radiative recombination, which was induced by the increased oscillator strength after the conjugated substituents were introduced. Due to the reduced molecular interactions fluorescence concentration quenching effect was reduced up to 3 times when the bulky aryl moieties were added. NOP derivatives with alkyl groups showed very efficient crystallization and made the estimation of mobility impossible, whereas derivatives with bulky aryl substituents demonstrated high hole drift mobility up to $8 \cdot 10^{-4} \text{ cm}^2/\text{Vs}$. NOP derivatives 1-4 showed an ionization potential of about 4.72 eV which increased up to about 5.17-5.48 eV for derivatives 5-10. High hole mobility and tunable energy of HOMO and LUMO levels make NOP derivatives promising for the applications in OLEDs and organic solar cells.

NONSYMMETRIC 9,10-DIPHENYLANTHRACENE-BASED DEEP-BLUE EMITTERS WITH ENHANCED CHARGE TRANSPORT PROPERTIES

Regimantas Komskis¹, Tomas Serevičius¹, Povilas Adomėnas², Ona Adomėnienė², Vy gintas Jankauskas³, Karolis Kazlauskas¹ and Saulius Juršėnas¹

¹Institute of Applied Research, Vilnius University, Saulėtekio al. 9-III, LT-10222 Vilnius, Lithuania

²UAB „Tikslioji Sintezė“ (Ltd), Kalvarijų g. 201E, LT-03225 Vilnius, Lithuania

³Department of Solid State Electronics, Vilnius University, Saulėtekio al. 9-III, LT-10222 Vilnius, Lithuania

regimantas.komskis@gmail.com

Various modified anthracenes are in a great interest of today's science as a promising emissive material for blue organic light – emitting devices (OLED). It demonstrates good emission efficiency, colour purity and stability. However, like other planar organic compounds, anthracene derivatives tend to crystallize in thin films what strongly deteriorates colour purity and efficiency of OLED device. Additionally, for inexpensive and efficient production of anthracene – based OLED devices it is necessary to improve solubility of these compounds in common solvents. Structural modifications plays a critical role on the optical and electrical properties and the device performance, thus the detail analysis of structure-property relation is mandatory.

In this work a series of structurally modified nonsymmetric 9,10-diphenylanthracene (DPA) derivatives (**Fig. 1**) were investigated. To enhance film forming properties of anthracene compounds they were nonsymmetrically substituted at the 2nd position by using either phenyl or penthyl moiety. In addition to this, different length alkyl groups were attached at the para position of 9,10-phenyl substitutes to determine the impact on the fluorescence efficiency, concentration quenching and carrier drift mobility. Detailed spectroscopic analysis of these compounds in dilute solution, polystyrene matrix and neat films were carried out. Experimental data was compared with theoretical DFT calculations and electrical measurements of the compounds accomplished by partners.

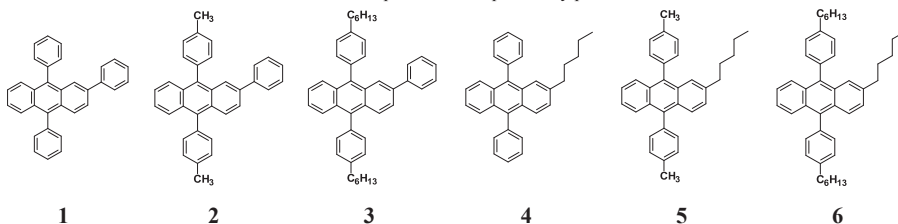


Fig. 1. Chemical structures of the DPA derivatives studied in this work.

Absorption spectra of the DPA compounds **1-6** contain clearly resolved vibronic structure with the dominant 1st vibronic replica similarly to that observed in the spectra of other various DPA derivatives due to the presence of rigid anthracene core. The lowest energy vibronic bands in the absorption spectrum of the 2-phenyl substituted DPA compounds **1-3** peaks at 405 nm, whereas the bands of the 2-pentyl substituted counterparts **4-6** are shifted more in the UV (at about 391 nm) due to the worse π -conjugation of the substituent.

Emission spectra of the DPA compounds **1-6** in the dilute solution also express vibronic bands, however a lack of the mirror images between absorption and emission implies flexibility of the molecules and geometrical transformations occurring in the excited state. In accordance with the absorption spectra, fluorescence bands of more conjugated 2-phenyl-substituted DPA derivatives **1-3** are located at 422-426 nm, and thus are slightly redshifted as compared to those of the less conjugated 2-pentyl-substituted DPA counterparts **4-6** peaking at 416-421 nm. Absorption and fluorescence measurements supported by DFT calculations revealed relatively small shifts in singlet and triplet transition energies (<100 meV), which however, caused drastic changes in the intersystem crossing rate.

The films of the compounds **1-3** and **4-6** emit in the deep blue with maxima positioned at 453-456 nm and 441-450 nm, respectively. Noticeable vibronic structure in the fluorescence lineshapes of the DPA derivatives **1-4** points out dense molecular packing in the films, whereas nearly structureless shapes observed for the compounds **5-6** implies more random molecular arrangement, which is typical for amorphous films.

DPA compounds showed high fluorescence quantum yields, up to 0.7 in a solution and up to 0.9 in a polymer host. The DPA derivatives exhibited almost no concentration quenching of fluorescence up to 8 wt % in PS matrix. Substitution at the 2nd position by penthyl moiety resulted in less pronounced concentration quenching as compared to the substitution by 2-phenyl group. The influence of the alkyl groups attached at the para position of 9,10-phenyls on the emission spectral properties was found to be insignificant, whereas they strongly affected film forming and charge transport properties. It is worth noting that the nonsymmetric DPA derivatives expressed very high hole drift mobilities of up to $4.6 \cdot 10^{-3} \text{ cm}^2/\text{Vs}$ for 2-phenyl-substituted compounds and up to almost $1 \cdot 10^{-2} \text{ cm}^2/\text{Vs}$ for 2-pentyl-substituted analogues at an electric field of 1 MV/cm.

1,8-NAPHTHALIMIDE DERIVATIVE

Rokas Skaisgiris, Saulius Juršėnas

Institute of Applied Research, Vilnius University, Saulėtekio 9-III, LT-10222 Vilnius, Lithuania
rokas.skaisgiris@ff.stud.vu.lt

Transitional metals are widely distributed in nature and they play an important role in many biochemical processes. One of the most abundant metal ion found in mammals is iron (Fe^{3+}). The lack of iron can result in anemia, hemochromatosis, liver damage, diabetes and cancer, while the excess of iron can induce several serious diseases, such as Alzheimer's, Huntington's, and Parkinson's diseases. Therefore it is important to sense Fe^{3+} in living organisms [1]. High sensitivity, rapid response, low cost and easy operation makes fluorescence sensors exceptional in this field. Naphthalimide derivatives have gained increasing interest as fluorescent probes for metal ions because of their unusual photophysical properties [2, 3].

In this paper we investigated photophysical properties of new naphthalimide derivatives containing functional groups of different polarity in 4th position in the absence and in the presence of the salts of several transition metal ions. All naphthalimide derivatives were synthesized by prof. J. V. Gražulevičius group at Kaunas University of Technology (KTU). Absorption and fluorescence spectra of naphthalimide solutions in tetrahydrofuran (THF) were analyzed.

The obtained data revealed a formation of charge transfer states in fluorescence spectra of all derivatives. The fluorescence color varies in whole visible range of spectrum from 387 nm with phenyl substitution to 387 nm with 4-(di-(4-methoxyphenyl)amino)phenyl substitution. The investigation of transitional metal ions effect on fluorescence showed that the fluorescence quenching is higher for a more polar substitution. Naphthalimide derivative with acceptor 4-benzaldehyde showed fluorescence enhancement (up to 1.6 times) in the presence of transitional metals in solution. Meanwhile the derivatives with donor substitutions quenches the intensity of fluorescence and quenching becomes stronger with more polar substitutions.

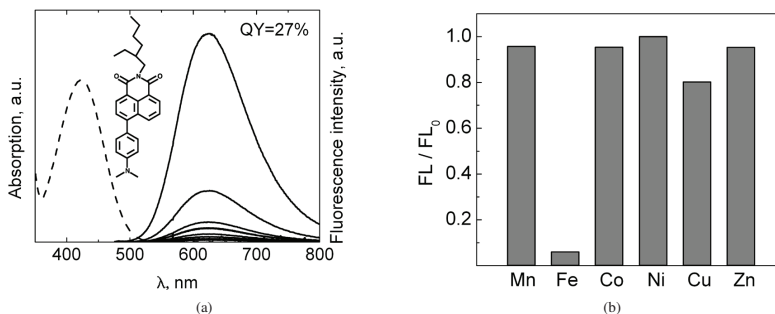


Fig. 1. (a) Fluorescence spectra of 4-(4-dimethylaminophenyl)-N-(2-ethylhexyl)-1,8-naphthalimide in THF in the presence Fe^{3+} . Fe^{3+} concentrations, in decreasing order of the fluorescence intensity, are 0, 10^{-4} , 5×10^{-4} , 10^{-3} , 2.5×10^{-3} , 5×10^{-3} , 10^{-2} and 2×10^{-2} M. (b) Selectivity between other transitional metals of same molecule when the concentration of metal ions is 10^{-3} M.

4-(4-dimethylaminophenyl)-N-(2-ethylhexyl)-1,8-naphthalimide demonstrated a highly selective sensing of Fe^{3+} . Fluorescence is quenched drastically (100 times) when the concentration of iron ions in solution is 100-1000 times higher than the concentration of naphthalimide derivative (Fig. 1). Meanwhile fluorescence quenching with other metal ions is barely visible. This 1,8-naphthalimide derivative can be applied as metal selective Fe^{3+} sensors.

- [1] J.-H. Xu, Y.-M. Hou, Q.-J. Mab, X.-F. Wub, X.-J. Wei, A highly selective fluorescent sensor for Fe^{3+} based on covalently immobilized derivative of naphthalimide, *Spectrochim. Acta A: Mol. Biomol. Spectrosc.* **112**, 116-124 (2013).
- [2] C.-Y. Li, F. Xua, Y.-F. Li, K. Zhou, Y. Zhoua, A fluorescent chemosensor for Hg^{2+} based on naphthalimide derivative by fluorescence enhancement in aqueous solution, *Anal. Chim. Acta* **717**, 122-126 (2012).
- [3] X. Poteau, A. Brown, R. G. Brown, C. Holmes, D. Matthew, Fluorescence switching in 4-amino-1,8-naphthalimides: "on-off-on" operation controlled by solvent and cations, *Dyes Pigm.* **47**, 91-105 (2000).

APPLICATION OF RAMAN SPECTROSCOPY IN ANALYSIS OF CHANGES IN COMPOSITION AND STRUCTURE OF HUMAN ENAMEL

Martyna Stańczuk¹, Sylwia Zięba¹, Tomasz Buchwald²

¹ Poznań University of Technology, Faculty of Technical Physics, ul. Nieszawska 13a, 60-965, Poznań, Poland

² Poznań University of Technology, Faculty of Technical Physics, Chair of Optical Spectroscopy, ul. Nieszawska 13a, 60-965 Poznań, Poland

m.stanczuk93@gmail.com

Dental caries is the most common tooth disease that leads to its lost and concerns almost every person. Early stages of caries are difficult to detect. It is necessary to search for a diagnostic method that will be precise even when sickness just have started developing and won't provide numerous drawback such as fluorescence spectroscopy.

The main goal of research is to study the impact of decay on human enamel in its early stages by using Raman spectroscopy. Next purpose is to compare diagnostic efficiency of Raman spectroscopy and fluorescence spectroscopy in detection of dental caries in initial development of disease.

The areas of advanced and intermediate progression of tooth illness were analyzed as well as healthy enamel. Changes in structure and composition were determined depending on stage of caries progression. Our research indicate that it is possible to detect early stages of dental caries by using polarized laser and scattered beam. By use of Raman spectroscopy, it is also possible to determine changes in intensity of fluorescence emission and Rayleigh scattering, which are associated with the occurrence of caries in the measuring site.

Results of our studies gives basic overview about effectiveness of Raman spectroscopy in analysis of structure changes of the enamel caused by decay, as well as the impact of disease on its structure.

Acknowledgements:

The authors are much grateful to lek. med. M. Peterseil from the Medical University in Poznan for preparation of the material to be studied. All experimental procedures were approved by the local bioethical commission at the Wielkopolska Medical Chamber in Poznan (No 956/11). This work was supported by the Polish National Science Center under the Grant No. 2013/09/N/NZ5/00010.

Oral session 3

Semiconductor and condensed matter physics

PHOTOLUMINESCENCE ENHANCEMENT BY COUPLING WITH LOCALIZED SURFACE PLASMONS IN SILVER NANOPARTICLES DEPOSITED ON InGaN QUANTUM WELLS

Justinas Aleknavičius

Semiconductor Physics Department, Vilnius University, Saulėtekio Ave. 9-III, LT-10222 Vilnius, Lithuania
ju.aleknavicius@gmail.com

Nitride semiconductors have been widely investigated during the last two decades due to their exceptional material properties. The band gap of ternary InGa_N compound can be varied from 0.7 eV (InN) to 3.4 eV (Ga_N). Thus, InGa_N enables fabrication of red, green and blue light emitting diodes (LEDs) using single ternary alloy. InGa_N-based blue LEDs are already commercially available. However, realization of efficient InGa_N-based LEDs emitting at longer wavelengths is still a major challenge, mainly due to high defect density of the active layer.

The emission efficiency in InGa_N active layer can be enhanced by coupling the optical transitions in InGa_N multiple quantum wells (MQWs) with localized surface plasmons (LSPs) in silver nanoparticles (NPs). Since the density of states of LSP mode is large, the QW-LSP coupling rate is fast and it creates a new path for radiative carrier recombination. On the other hand, QW-LSP coupling might also improve the light extraction efficiency.

In this work, the enhancement of InGa_N MQW photoluminescence (PL) by LSPs in silver NPs is investigated. InGa_N/Ga_N MQW structures were grown by metal-organic chemical vapor deposition (MOCVD) on sapphire substrates at the Institute of Applied Research. Silver NPs were fabricated by thermal annealing of thin silver layers deposited on the MQW structures. Silver layers of 5 nm, 8 nm and 12 nm were annealed at two different temperatures (500°C and 300°C).

The samples were investigated using *WITec Alpha300* microscope system working in confocal spectroscopy and atomic force microscopy (AFM) modes. The surface configuration and dimensions of fabricated nanoparticles were characterized using AFM, while the spatial distributions of photoluminescence parameters were measured using confocal microscopy technique. PL was excited using a CW laser diode *ALPHALAS* emitting at 405 nm. Absorption spectra of each sample were measured using *Perkin-Elmer Lambda 950* spectrometer and enabled to determine the wavelength of LSP resonance.

The study of surface morphology showed that annealing at a higher temperature is more favorable for the formation of larger and better separated NPs. It was found that annealing of the thickest silver layers (12 nm) at both temperatures resulted in formation of large NPs (>100 nm in diameter), while smaller NPs (<75 nm in diameter) were formed from 5 nm and 8 nm thick layers.

The measured optical absorption spectra showed that the resonance in larger NPs is better pronounced and occurs at longer wavelength. Moreover, stacked nanostructures exhibit broadening of the absorption bands.

Confocal PL imaging measurements were performed on the surface of the sample with and without silver NPs. The measurements revealed that the amplification of PL intensity is observed only in samples with the largest NPs. The increase of PL intensity (by ~53%) is larger in the sample with the thickest silver layer (12 nm) annealed at lower temperature (300°C) (see Fig. 1), due the better match between the surface plasmon resonance wavelength and the PL emission.

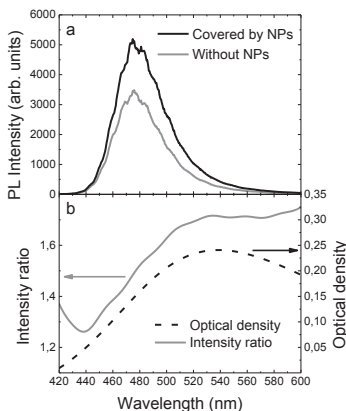


Fig 1. Spatially averaged PL spectra of InGa_N MQWs covered by silver NPs and without NPs (a), ratio of the spectra and optical density of the sample (b)

GROWTH AND CHARACTERISATION OF THICK GaAsBi LAYERS

Karolis Stašys¹, Vaidas Pačebutas¹, Renata Butkutė^{1,2}¹Center for Physical Sciences and Technology, Lithuania²Department of Physics, Vilnius University, LithuaniaKarolis.stashys@gmail.com

Diluted gallium arsenide bismide is a promising material for future telecommunications. By adding even small amounts of bismuth to GaAs, greatly reduces its band gap and GaAsBi has very weak band gap temperature dependence [1]. Today, bismides are used to develop efficient terahertz emitters and detectors. However, growth of high quality GaAsBi structures is still a great challenge. Thick GaAsBi is grown using low temperatures (250-350° C) which increases the amount of crystalline defects. Also, maintaining a very precise As/Ga flux ratio is necessary.

Our main goal was to grow high quality thick (1.5µm) GaAsBi layers with band gap $E_g = 1\text{ eV}$ and characterize crystalline structure, surface morphology as well as carriers dynamics.

Optical transmittance measurements showed that all samples exhibited $E_g = 1\text{ eV}$. From X-ray diffraction measurements Bi concentration was determined to be between 6 and 8%. Using atomic force microscopy surface roughness was determined to be between 0.4 nm and 2.0 nm. Carrier life time measurements performed using optical pump - terahertz probe system showed that most of samples had very short lifetimes in range of 1 – 2.7 ps except one sample B349 – its carries life time was longer than 2.7 ns, which was never observed before in thick GaAsBi layers. The results of carrier dynamics and photoluminescence (PL) measurements of B349 with comparison to B348 are presented in fig. 1.

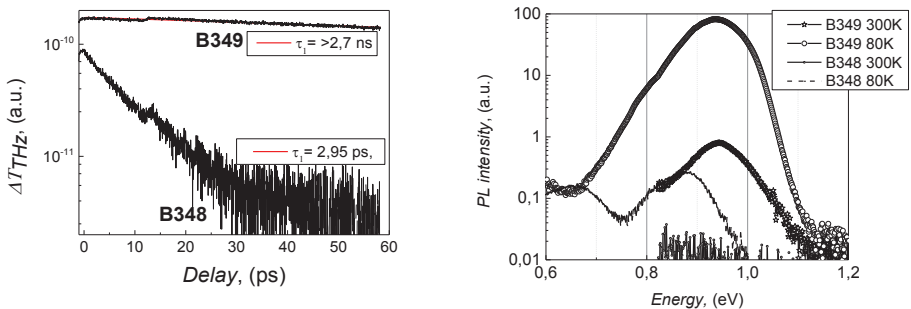


Fig. 1. GaAsBi samples B348, B349 carrier dynamics and photoluminescence spectra measured at 80° K and room temperature.

GaAsBi sample B349 has a considerably longer carrier life time than B348. B349 also has much stronger PL signal than B348 both at 80° K and room temperature. Very long carrier life times and strong PL suggests that sample B349 has very high crystalline quality and at nonradiative recombination centers density is low. Atomic force microscopy showed that this sample has a much smoother surface than others – roughness lower than 0.4 nm. Reciprocal space map measured by X-ray diffraction demonstrates that GaAsBi sample B349 crystal lattice relaxation was 100% at Bi concentrations of 8.3%. Also, a small Bi XRD peak is visible which corresponds to the concentration of 3.8%Bi. A slight inhomogeneity in crystalline structure is suggested. In order to clarify the different Bi content through the layer, 1.5µm-thick GaAsBi layer was etched and 3 steps with various thicknesses were formed for PL measurements. The observed a slight blue shift in spectra and an increase in PL intensity with the decrease of layer thickness could be related to Bi content increase in surface layer. It can point out that even the highest quality GaAsBi crystal has fluctuations in elemental composition.

[1] K. Bertulis et al. Appl. Phys. Lett. 88, (2006) 201112.

[2] X. Lu et al. Appl. Phys. Lett. 95, (2009) 041903.

INVESTIGATION OF CHARGE CARRIER TRANSFER MECHANISM IN ULTRA-THIN MULTI-LAYERED METAL OXIDE STRUCTURE FOR GAS DETECTION

Šarūnas Vaškeļis, Virginijus Bukauskas, Audružis Mironas, Arūnas Šetkus

Department of Physical Technologies, Center for Physical Sciences and Technology, Lithuania
sarunas.vaskelis@ftmc.lt

Thin film metal oxide sensors are frequently used for gas detection but the success of practical applications is typically limited by comparatively high operating temperatures. It seems reasonable to expect that this problem can be solved by creating a new type of sensors. It was demonstrated by our experiments that very thin multi-layered metal oxide structures convert surface chemical interaction into a detectable electrical signal. However detailed studies are required for better understanding of the charge carrier transfer mechanism.

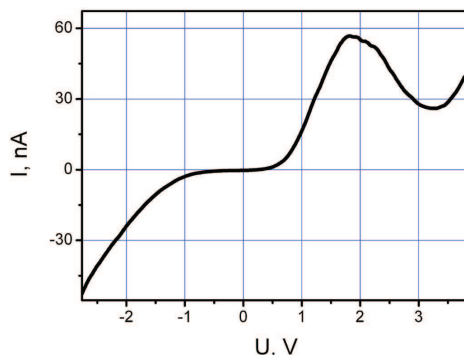


Fig. 1. The I-V characteristic of $\text{Au/In}_{2-x}\text{O}_{3-y}/\text{TiO}_{2-x}$ structure, measured with the scanning probe microscope in a tunneling current mode.

In the ultra-thin layers ($\sim 10\text{nm}$) based on non-stoichiometric metal oxides $\text{In}_{2-x}\text{O}_{3-y}$ and TiO_{2-x} a negative differential resistance (NDR) is typically detected as it can be seen in the I-V dependence in figure 1. Our experiments proved that the NDR is detected if a negative potential is applied to the substrate for at least a few seconds. The external voltage must be not less than several volts, e.g. 4.5 V. If a polarity of the probing voltage is opposite to the activating one the NDR is typically detected in the I-V curve. Considering the results of our studies in [1], we think that the NDR can be explained by redistribution of the oxygen vacancies in the TiO_2 lattice similar to that proposed in [2]. It must be noted here, that the redistribution does not produce noticeable changes in the topography of the studied structures as it was reported in our previous work [1]. The NDR monotonically decreases and disappears finally as the system returns to the initial state. Spontaneous drift produced by the voltage is obtained in the tested structures.

We can conclude that in spite of general understanding of the NDR in local I-V in the multilayered ultra-thin metal oxide structures there are still essential uncertainties about the mechanism of the electrical charge transfer across the structure. Thorough investigations are being done to explain transport mechanism in detail.

- [1] V. Bukauskas, A. Mironas, A. Šetkus, V. Strazdienė, Nanostructures produced by SPM voltage ramping in metal oxide films, *Surf. Interface Anal.* **42**, 991 (2010).
- [2] Yuseok Kim, Jae Hyuck Jang, Sang-Joon Park, Stephen Jesse, Leonard Donovan, Albina Y Borisevich, Woo Lee and Sergei V Kalinin, Local probing of electrochemically induced negative differential resistance in TiO_2 memristive materials, *Nanotechnology* **24**, 085702 (2013).

Preparation of iron oxide thin films on Ru(0001)

Damian Łukawski^{1,2}, Zygmunt Miłosz¹, Natalia Michalak¹, Łukasz Kościński¹, Małgorzata Błaszyk¹, Mikołaj Lewandowski^{1,*}, Tadeusz Luciński¹

¹*Institute of Molecular Physics, Polish Academy of Sciences, M. Smoluchowskiego 17, 60-179 Poznań*

²*Department of Technical Physics, Poznań University of Technology, Nieszawska 13A, 60-965 Poznań*

**lewandowski@ifmpan.poznan.pl*

Surface science is an intensively developing interdisciplinary research field. Properties of the surface differ significantly from the properties of the bulk part of the material, mainly due to different interatomic bond configuration. Recently, thanks to novel fabrication methods and research techniques, it is possible to prepare highly-organized nano-sized materials and to study the structure and properties of their surfaces on the atomic level under idealistic ultra-high vacuum (UHV) conditions.

One of the interesting groups of nanomaterials are thin films of metal oxides grown on metal single crystal surfaces. For example, thin films of FeO(111), Fe₃O₄(111) and α -Fe₂O₃(0001) grown on Pt(111) single crystal exhibit unique electronic [1,2], magnetic [2,3] and catalytic [4] properties, not observed for the corresponding bulk materials. Ultrathin FeO(111) film on Pt(111) is particularly interesting [5]. Due to the difference in surface lattice constants of FeO(111) and Pt(111), a formation of Moiré superstructure, which alters the material's properties, is observed.

It was shown that iron oxide thin films can also be grown on Ru(0001) single crystal surface [6]. Due to a slightly larger than in the case of FeO(111)/Pt(111) difference in lattice constants, the Moiré structure of FeO(111)/Ru(0001) has smaller periodicity. The use of different metal substrate can also influence the properties of oxide films, however, these have not been studied in detail so far. The work includes optimization of the Ru(0001) surface cleaning procedure, growth of iron oxide thin films on Ru(0001) and studies of their structure using low energy electron diffraction (LEED).

[1] E.D.L. Rienks et al., *Phys. Rev. B*, **71** (2005) 241404.

[2] L. Giordano et al., *Phys. Rev. B*, **76** (2007) 075416.

[3] N. Spiridis et al., *Phys. Rev. B*, **85** (2012) 075436.

[4] Y.-N. Sun et al., *Angew. Chem. Int. Ed.*, **49** (2010) 4418.

[5] M. Ritter et al., *Phys. Rev. B*, **57** (1998) 7240.

[6] G. Ketteler et al., *J. Phys. Chem. B*, **107** (2003) 4320.

The work is financed by the Polish Ministry of Science and Higher Education via „Iuventus Plus” programme (2012-2015; project number: IP2011 030071).

ELECTRONIC AND TRANSPORT PROPERTIES OF TOPOLOGICAL ANDERSON INSULATOR

Maciej Bieniek

Institute of Physics, Wrocław University of Technology, Poland
mbieniu@gmail.com

Topological insulators are new state of matter characterized by topological invariants. First predicted in 2005 by Kane and Mele [1] for graphene and then for CdTe/HgTe/CdTe quantum wells [2], were experimentally observed by König et al. [3] in 2007. In 2009 Li et al. [4] discovered that the topological state with quantized conductance can be induced by a sufficiently strong disorder in a system within a trivial insulator regime. This new phase was named topological Anderson insulator (TAI).

In the following work results of CdTe/HgTe/CdTe electronic structure studies are presented within tight-binding approximation framework. Special attention is given to on-site edge potential effect on band structures and edge states. Results show, that it is possible to move bands from valence to conduction band for positive on-site edge potential U . For negative U effect is similar, nevertheless asymmetry of the model is pointed out.

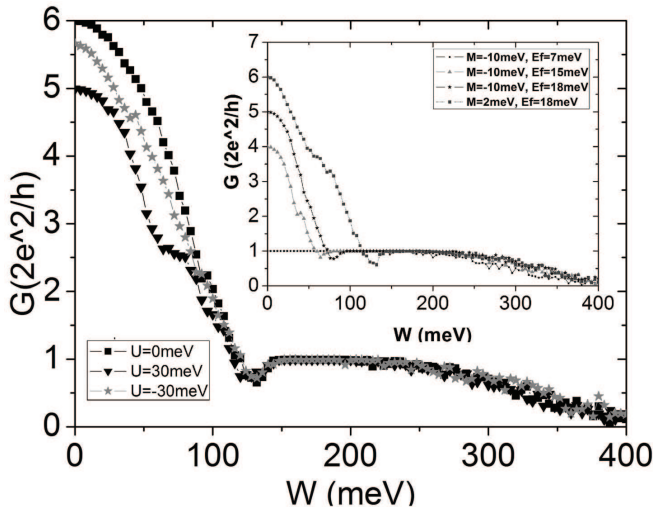


Fig. 1. Conductance (G) in function of Anderson disorder strength (W) for different on-site edge potential strengths (U). Inset presents analogous transport studies for different topological regimes and Fermi energies.

Transport properties were calculated within Landauer-Büttiker formalism and are shown on Figure.1. At first TAI phase is presented for Fermi energy $E_F = 20$ meV along with effect of positive and negative U . Analogous results for topological insulator in non-trivial regime are given in inset of Fig.1 for different Fermi energies. Results show negligible effect on TAI phase, contrary to electronic structure studies, which leads to conclusion, that states entering band gap in CdTe/HgTe/CdTe do not contribute to conductance.

-
- [1] Kane, C. L., and E. J. Mele, Quantum Spin Hall Effect in Graphene, *Phys. Rev. Lett.* 95, 226801 (2005).
 - [2] B. A. Bernevig, T. L. Hughes and S.-C. Zhang, Quantum Spin Hall Effect and Topological Phase Transition in HgTe Quantum Wells *Science* 314, 1757 (2006).
 - [3] M. König, S. Wiedmann, C. Brüne, A. Roth, H. Buhmann, L.W. Molenkamp, X.-L. Qi, and S.-C. Zhang, Quantum Spin Hall Insulator State in HgTe Quantum Wells, *Science* 318,766 (2007).
 - [4] J. Li, R.-L. Chu, J.K.Jain and Sh.-Q. Shen, Topological Anderson Insulator, *Phys. Rev. Lett.* 102, 136806 (2009).

INVESTIGATION AND OPTIMISATION OF THE SPATIAL LUMINOUS FLUX DISTRIBUTION OF SOLID-STATE STREET LUMINAIRE

Justas Trimailovas, Pranciškus Vitta

Institute of Applied Research, Vilnius University, LT-10222 Vilnius, Lithuania

justas.trimailovas@ff.stud.vu.lt

Today mass-produced Light Emitting Diodes (LEDs) have very high luminous efficacy ($\eta_{\text{eff}} > 100 \text{ lm/W}$) [1]. Using these LEDs we can assemble street luminaires with efficiency comparable to the high-pressure sodium lamps. To make an efficient street luminaire we must optimise its electronics as well as optics. Due to strict street illumination standards [2] spatial distribution is very important property of a luminaire and determines the uniformity of street surface and surrounding areas illumination, and disability glare value.

The optimisation process is structured into 3 main parts: digital simulation and optimisation of our street luminaire, prototype production of the luminaire and investigation of spatial distribution of developed luminaire using goniophotometer.

Digital modeling starts from importing of the luminous flux distribution of LEDs and the geometry of street lamp body into the software. The workflow of optimization is a process of choosing main variables of the luminaire (position of LEDs in respect of the lamp body, position of lamp in respect of the street, etc.) and varying one of them at the time. Variable is said to be optimal, when it produces the best light distribution on the street, according to the EN-13201 street illumination standard.

Spatial luminous flux distribution of simulated luminaire prototype is measured using custom made type B goniophotometer (Fig. 1). In the process, Illumination Engineering Society (IES) file is produced. This file is used with optical simulation software to compare the street illumination distribution produced in cases of digital simulation and the real luminaire prototype.

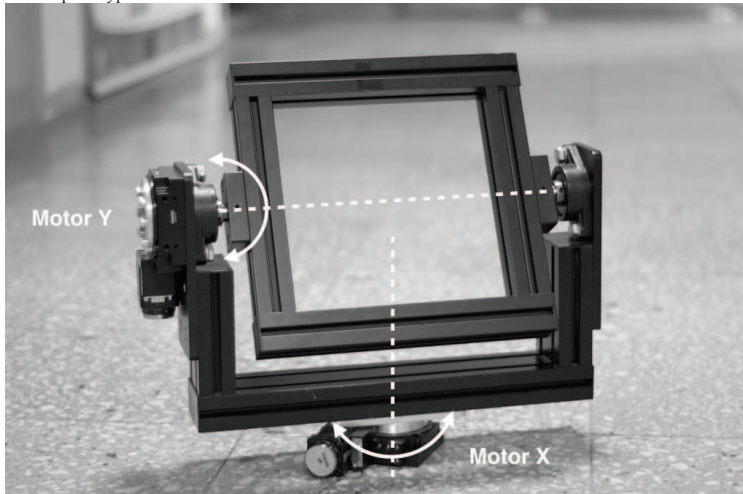


Fig. 1. Custom made type B goniophotometer.

During presentation, results of such investigation and optimisation process will be announced.

[1] E. F. Schubert, *Light-Emitting Diodes* (Cambridge university press, Cambridge, 2006).

[2] European Standard, *EN 13201* (2003).

Oral session 4

Material sciences and modern technologies

SCINTILLATION DETECTOR TESTING SETUP FOR SUPERNEMO EXPERIMENT

Aivaras Žukauskas¹, Vít Vorobel¹

¹Institute of Particle and Nuclear Physics, Charles University in Prague, Czech Republic

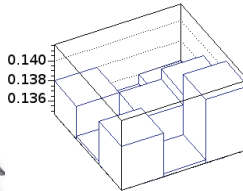
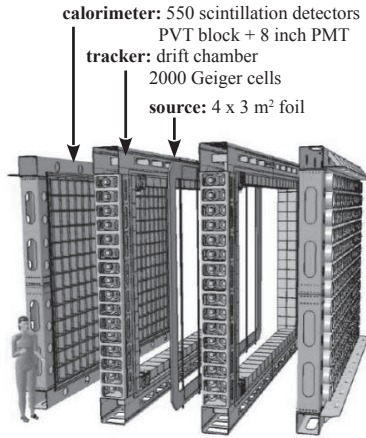
zukauskas@ipnp.troja.mff.cuni.cz

Acknowledgements: On behalf of the NEMO collaboration.

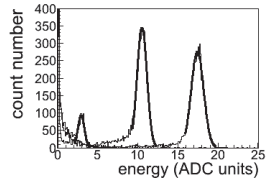
The study was supported by the Charles University in Prague, project GA UK No. 355011.

SuperNEMO (NEMO stands for Neutrino Ettore Majorana Observatory) experiment is devoted to search for the neutrinoless double beta decay - a rare, lepton-number violating, nuclear decay process that would indicate the Majorana nature of neutrinos, as well as provide an estimate for the neutrino mass scale.

The experiment is currently being built; it will consist of identical 20 modules, each housing 7 kg of source (⁸²Se is the baseline choice). The module will consist of thin source foils, placed inside a tracking system, all surrounded by a calorimeter (Fig. 1). This gives the ability to measure individual electron tracks, vertices, energies and time of flight,



(a)



(b)

Fig. 2. (a): Scintillator energy resolution measured in 9 positions, (b): Spectra for 0.3, 1.0 and 1.6 MeV energy electrons

Fig. 1. Exploded view of a SuperNEMO module

and to reconstruct fully the kinematics and topology of an event. Particle identification of gamma and alpha particles, as well as distinguishing electrons from positrons with the help of a magnetic field, form the basis of background rejection.

SuperNEMO aims to achieve the calorimeter energy resolution to 7%/√E (MeV) at full width of half maximum (FWHM). To reach this goal, a large quantity of scintillators will have to be tested before installing. The setup for such tests was developed and built in Prague based on the experience of the collaborators in Bordeaux and Dubna. The setup consists of (i) the steel lightproof black box, with dimensions 100 × 130 × 130 cm³, (ii) movable table in X and Y directions, (iii) so-called deltaE trigger, (iv) source of monochromatic energy electrons, where the electrons from ⁹⁰Sr spectrum with the particular energy (Fig. 2b) may be chosen by applying a magnetic field with variable strength, produced by a coil. All electronic devices are connected with the computer and various settings can be performed by using the custom-built software in Linux operating system.

The setup itself is shown in the Fig. 3. The photomultiplier tube (PMT) is glued with the optical contact to the scintillator. Below the scintillator there is a deltaE trigger, consisting of two 14 mm diameter PMTs coupled to the 100 micron scintillator foil, and the electron source placed on the XY table. The table moves the electron source and the deltaE trigger to the desired position under the scintillator. Electrons with chosen energy cross the trigger and enter the tested scintillator, depositing their energy which is converted to electric signals and measured. The observable is the energy resolution, depending on the homogeneity of the scintillating material as well as on the electron entrance place.

The routine tests of the scintillator detectors started May 2012 and is still ongoing with some breaks for hardware upgrade. The talk discusses various aspects of the setup functionality, data acquisition and technical challenges and solutions.

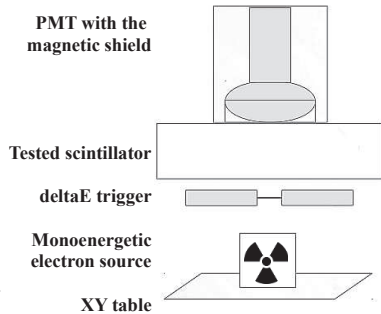


Fig. 3. The setup for scintillator testing

APPLICATION OF DIELECTROPHORESIS FOR MAKING GERMANIUM NANOWIRE ARRAYS

Jelena Kosmaca¹, Jana Andzane¹, Gunta Kunakova¹, Gvido Petersons¹, Justin D. Holmes²,
Donats Erts¹

¹University of Latvia, Institute of Chemical Physics

²Department of Chemistry, National University Ireland, Cork, Ireland

jelena.kosmaca@lu.lv

Dielectrophoresis is polarization of particles suspended in dielectric media placed in the non-uniform electric field. Polarization of the particles causes their motion. This effect can be used for controlled particle transport. In recent years dielectrophoresis has been used for arranging various nanostructures.

Here we present application of dielectrophoresis for aligning germanium nanowires in arrays on an electrode side. Germanium nanowires have been produced with chemical vapor deposition method. We choose hexane as media for germanium nanowires dielectrophoresis. For performing dielectrophoresis we apply AC voltage to gold electrodes on Si/SiO₂ chip then drop a hexane-nanowire solution onto the electrodes. The nanowires from the media tend to attract to electrodes. After removing the media nanowires stay on the electrode. The surface of the electrodes is observed in a scanning electron microscope (Fig.1a). From the SEM images we investigate characteristics of more than 400 individual germanium nanowire positioning (Fig.1b-d).

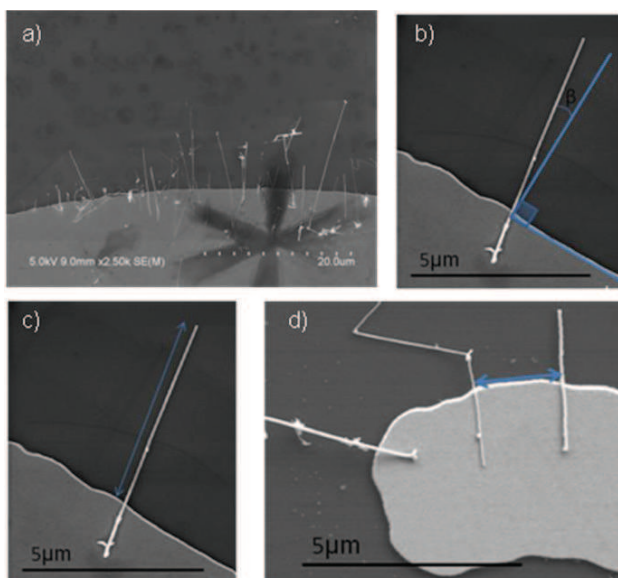


Fig.1. a) Germanium nanowires attracted to the electrode; b)Measuring angle β that shows the angular position of the nanowire in relation to electrode edge; c)Measuring length of the nanowire that lies apart the electrode; d) Measuring distance between two individual nanowires.

We have done number of experiments to investigate germanium nanowire behavior in dielectrophoresis process by changing electric field frequency in range of 200Hz to 2MHz. Accordingly to the results of our experiments we discuss optimal dielectrophoresis parameters for making germanium nanowire arrays.

INVESTIGATION OF ANODIC ALUMINA OXIDE TEMPLATES DOPED WITH IRON USING MOESSBAUER SPECTROMETER

Adomas Lukenskas

¹Institute of Physics, Center for Physical Sciences and Technology, Lithuania
adomas.lukenskas@stud.ff.vu.lt

As quantity of information being stored worldwide nearly doubles every three years, new and more efficient storing methods needs to be developed. To deal with ever growing demand for storage space, perpendicular recording devices has been proposed. One of the most promising materials for perpendicular magnetic devices could be — implemented iron nano-wires into highly ordered porous anodic alumina oxide template. Such nano-wires could be magnetized either up or down representing logical 0 or 1.

Producing highly ordered magnetic nano-wires, however, proves to be somewhat but easy task. The main problem encountered — that iron nano-wires do not behave as bulk iron material, as a consequence of that do not form ferromagnetic compounds. Determining conditions under which anodic aluminum oxide (AAO) templates implemented with iron nano-wires can be produced with good ferromagnetic properties is important task.

Annealing alumina templates in air atmosphere at temperatures up to 600 degrees result in formation of paramagnetic Fe(II) and Fe(III), most probably in a spinel FeAl_2O_4 [1]. Also, researches proved that under influence of atmospheric air iron nano-wires begin to oxidize and degrade [2] forming non-ferromagnetic compounds. Given these facts, this work was made to determine whether annealing AAO templates in vacuum and heating the samples in range of activation temperature 300-400 °C could increase the ferromagnetic properties of these templates.

Using Mossbauer spectrometer, I investigated effects on AAO templates of different heating speed, maximum temperature and cooling speed of for the. All investigated samples displayed highly anisotropic magnetic properties. Typical Moesbauer spectrum is shown in Fig. 1

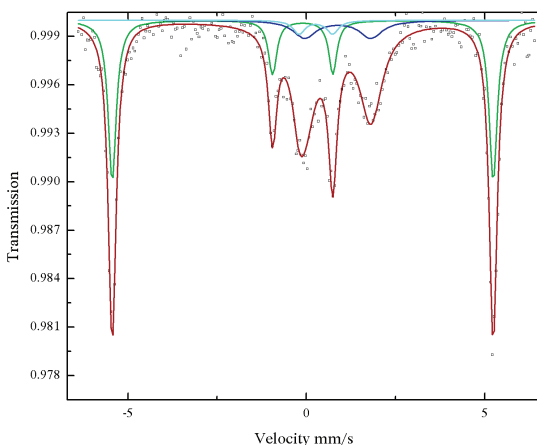


Fig. 1. Typical AAO Moesbauer spectrum, displaying high magnetic anisotropy.

After investigation of spectra, ratios between different iron compounds has been calculated

$$W_i = \frac{\sum_n A_i}{A_j} \quad (1)$$

After this research conclusions has been drawn that at higher annealing temperatures larger α -ferrum dissipates into the alumina template producing larger ratios of Fe(II) and Fe(III) compounds. Also, I managed to disprove that the oxygen responsible for formation of α -Fe ($\text{Fe}_{1-x}\text{Al}_x$)₂O₃; $x = 0,99$; and FeAl_2O_4 compounds has an atmospheric origin.

-
- [1] A. Jagminas, K. Maeika, J. Reklaitis, M. Kurtinaitien, and D. Baltmas. Template synthesis, characterization and transformations of 85 iron nanowires while aging. *Materials Chemistry and Physics*, 109:82-86, (2008).
 [2] A. Jagminas, K. Maeika, J. Reklaitis *Studies of oxidation of iron nanowires encased in porous aluminium oxide template* Institute of Physics, Savanoriu 231, LT-02300 Vilnius, Lithuania

GRAIN SIZE EFFECT ON DIELECTRIC PERMITTIVITY OF xBiScO₃ – (1-x)PbTiO₃ PEROVSKITE CERAMICS

Sergejus Balčiūnas, Maksim Ivanov

Department of Physics, Vilnius University, Lithuania
sergejus.balciunas@gmail.com

Ferroelectric materials are of high interest for both researchers and engineers due to their remarkable properties. Their high dielectric permittivity allows us to make smaller capacitors and their switchable electric polarization can be used for memory storage. We should note that all ferroelectrics have piezoelectric properties [1] and can be used, for example, in piezoelectric motors [2]. In recent decades electronic devices tend to nanoscale, this brings the necessity to research ceramics grain size effects. Although ferroelectric PZT has taken almost all piezoelectric market due to its high piezoelectric coefficient [3], BSPT has ~ 100 K higher Curie temperatures than PZT, this allows making piezoelectric devices for higher temperatures.

In this presentation grain size effect on dielectric permittivity of xBiScO₃-(1-x)PbTiO₃ (BSPT) where x=0.375 ceramics will be presented. Usually dielectric permittivity in ceramics should decrease as its grains get smaller, since the effective volume of grain boundaries grow (grain boundaries has lower permittivity). Effective permittivity of ceramics can be approximated with coated shell model [4]:

$$\varepsilon = \varepsilon_2 \left(\frac{x-n}{1-x} \right) + \left(\frac{1-x}{1-n} \right) \frac{\varepsilon_1 \varepsilon_2}{(1-n)\varepsilon_2 + n\varepsilon_1}, \quad (1)$$

where ε , ε_1 , ε_2 are complex dielectric permittivities of ceramics, grain core and grain shell respectively, x – grain shell volume and n – free parameter, characterizing the particle shape and topology. As we see in figure 1 (a) this model is accurate in low grain size region. The decrease of dielectric permittivity in high grain size region can be explained by Kittel's law which states that reducing crystallites size will decrease domain thickness, thus increasing wall count and in result dielectric permittivity (2). In figure 1 (b) coated shell model with Kittel's law correction fit curves correspond all experimental data.

$$\varepsilon_1 = \varepsilon_{c0} + \frac{C}{\sqrt{D}}, \quad (2)$$

where C – constant, D – grain diameter ε_{c0} – dielectric permittivity without domains.

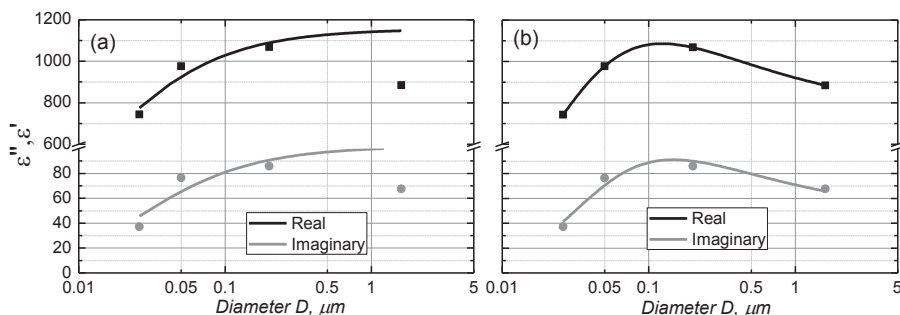


Fig. 1. Dielectric permittivity dependence from crystallites size at 333kHz frequency and 300K temperature. Coated shell model fit curves: (a) without Kittel law correction (b) with Kittel law correction.

[1] G. H. Haertling, "Ferroelectric ceramics: history and technology," Journal of the American Ceramic Society, vol. 82, pp. 797-818, (1999).

[2] T. Morita, "Miniature piezoelectric motors," Sensors and Actuators A: Physical, vol. 103, pp. 291-300, 2/15/ (2003).

[3] R. Guo, L. Cross, S. Park, B. Noheda, D. Cox, ir G. Shirane, "Origin of the high piezoelectric response in PbZr 1-x Ti x O 3," Physical Review Letters, vol. 84, p. 5423, (2000).

[4] J. Petzelt, I. Rychetsky, ir D. Nuzhnyy, "Dynamic Ferroelectric–Like Softening Due to the Conduction in Disordered and Inhomogeneous Systems: Giant Permittivity Phenomena," Ferroelectrics, vol. 426, pp. 171-193, 2012/01/01 (2012).

Investigation of Aurivillius phase Bi_2MO_6 ($M = \text{W}, \text{Mo}$) electrical properties

Laurynas Šatas¹, Tomas Šalkus¹, Maud Barre², Veyis Gunes²

¹ Faculty of Physics, Vilnius University, Lithuania

² Faculte des Sciences, departement Chime-Physique, Universite du Maine, France

sataslaurynas@gmail.com

Oxide ion conductors have been widely studied for use as components of fuel cells, oxygen sensors, oxygen pumps and oxygen-permeable membrane catalysts. The Aurivillius family of structurally related oxides with general formula $\text{Bi}_2\text{A}_{n-1}\text{B}_n\text{O}_{3n+3}$ were originally of interest because of their ferroelectric properties, but they have been recently studied for possible use as oxide ionic conductors.

Previously Bi_2MO_6 were synthesized by many different methods, such as coprecipitation, solid-state reaction, sol-gel, combustion synthesis, ultrasonic and hydro/solvothermal. In this study we investigate material synthesized by relatively new Micro-Wave synthesis method.

Prepared polycrystalline were characterized using X-ray diffraction (XRD), IR spectroscopy followed by differential thermal analyses (DTA) coupled with thermogravimetry (TG). Finally ceramics for impedance and electronic conductivity measurements were prepared. To determinate sintering temperature thermal XRD analysis as well as dilatometry measurements were used. Fine quality ceramics (more than 85% of calculated density) were covered with 9nm platinum electrodes using magnetron for impedance spectroscopy.

Total conductivity for all the samples were measured using impedance spectroscopy method in range of temperatures from 600K to 850K in dry air atmosphere. Electronic conductivity were measured using modified Hebb-Wagner polarization method in temperature range from 600K to 940K.

Both samples showed similar mixed conductivity with activation energies of 1.44eV for Bi_2WO_6 sample and 1.29eV for Bi_2MoO_6 . Partial electronic conductivity in normal oxygen activity is only minor. In both cases electronic conductivity showed strong dependence of partial oxygen activity.

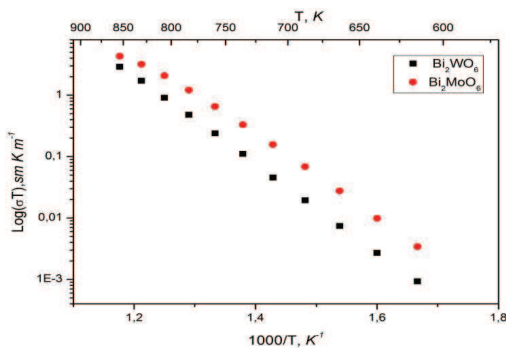


Fig. 1. Arrhenius plots of measured bulk conductivity of Bi_2WO_6 and Bi_2MoO_6 at various temperatures.

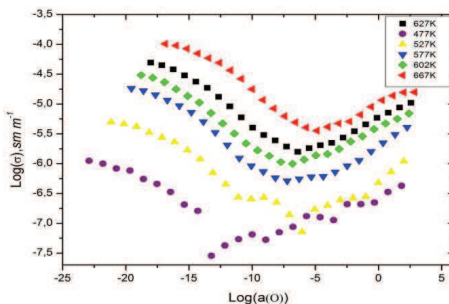


Fig. 2. Bi_2WO_6 electronic conductivity from oxygen activity at various temperatures.

INFLUENCE OF THE STARTING MATERIALS TO THE FORMATION AND OPTICAL PROPERTIES OF THE FINAL CERAMIC PREPARED BY THE AQUEOUS SOL-GEL SYNTHESIS METHOD

Rūta Stankevičiūtė¹, Artūras Žalga¹

¹ Department of Applied Chemistry, Faculty of Chemistry, Vilnius University, Lithuania

ruta.stankeviciute@chf.stud.vu.lt

The measuring of the changes of physical and chemical properties as a function of increased temperature or as a function of time is called thermogravimetric analysis, or TGA.

In TGA, the changes of weight are registered during a procedure with a constant heating rate. TGA can be used for many different purposes, like the characterization of materials through the analysis of decomposition patterns with specific characteristics, the studying of degradation mechanism, and determining the organic and inorganic compounds in a sample. These purposes can be useful for the chemical analysis of, for example, thermally stable polymers and some ceramics, or confirming suspected structures in materials [1].

Nowadays, considerable research attention has been devoted to trivalent lanthanide ions as luminescence centres due to the rapid development of diode lasers [2]. Moreover, it is known that rare-earth elements can form series of isomorphous molybdates with general formula $\text{Ln}_2(\text{MoO}_4)_3$, and some of these compounds show interesting fluorescence properties as well [3]. Recently $\text{La}_2\text{Mo}_2\text{O}_9$ -based oxide-ion conductors have attracted more attention, because of their potential applications in the fields of solid oxide fuel cells (SOFC), oxygen sensors, oxygen pumps and catalysts for selective oxidation [4]. Consequently, different new synthesis methods that could easily produce such kind of materials with well-determined crystallinity and controlled morphology are desirable. From this point of view, compared to other techniques, the wet synthesis route called an aqueous sol-gel method is attractive [5].

The sol can be produced starting both from organic or inorganic precursors, which consist of a metal or metalloid element surrounded by various organic ligands and the whole process is conducted at room temperature. The peculiar thing is that the solid state can be reached at low temperature starting from a solution, and this fact expands greatly the possibility of creating new materials or improving their properties [6].

In this oral presentation, we report the synthesis of the La-Mo-O nitrate-tartrate and nitrate-citrate gel precursors with the initial composition of the $\text{La}_2\text{Mo}_3\text{O}_{12}$ ceramic prepared from different starting materials by an aqueous sol-gel synthesis route using tartaric acid or citric acid as a complexing agent. Moreover, the La-Mo-O carbonate-tartrate and carbonate-citrate gel precursors by aqueous sol-gel synthesis method were also prepared. The thermal decomposition of every La-Mo-O gels were analysed and investigated in detail. X-ray diffraction (XRD) and scanning electron microscopy (SEM) were used for the determination of crystal structure, surface morphology of the La-Mo-O samples annealed at 400, 500, 600, 700, 800, 900 and 1000 °C temperatures, respectively.

[1] A. W. Coats, J. P. Redfern, Thermogravimetric Analysis: A Review, Analyst 88, 906–924 (1963)

[2] P. L. Forster, A. B. Lugao, H. F. Brito, D. F. Parra, Calorimetric investigations of luminescent films polycarbonate (PC) doped with europium complex $[\text{Eu}(\text{TTA})_3(\text{H}_2\text{O})_2]$, J Therm Anal Calorim. 97, 497-502 (2009).

[3] A. Žalga, Z. Moravec, J. Pinkas and A. Kareiva. On the sol-gel preparation of different tungstates and molybdates. J. Therm. Anal. Calorim. 105, 3-11 (2011)

[4] G. G. Zhang, Q. F. Fang, X. P. Wang, and Z. G. Yi, AC impedance and dielectric relaxation study on the effectsof the excess Pb introduced in $\text{La}_2\text{Mo}_2\text{O}_9$ oxide-ion conductors, Phys. Stat. Sol. 199, 329-334 (2003).

[5] K. Tõnsuadu, A. Žalga, A. Beganskiene and A. Kareiva. Thermoanalytical study of the YSZ precursors prepared by aqueous sol-gel synthesis route. J. Therm. Anal. Calorim., 110, 77-83 (2012).

[6] Encyclopedia of Inorganic Chemistry, DOI: 10.1002/0470862106

Oral session 5

Biophysics, medical and environmental physics

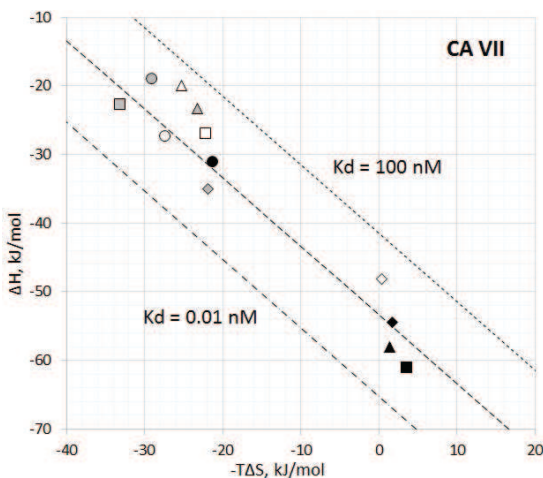
THERMODYNAMICS – STRUCTURE CORRELATIONS OF LEAD COMPOUNDS BINDING TO TARGET PROTEINS

Miglė Kišonaitė, Asta Zubrienė, Edita Čapkauskaitė, Daumantas Matulis

Department of Biothermodynamics and Drug Design, Vilnius University Institute of Biotechnology, Vilnius, Lithuania
kisonaite@ibt.lt

The lead design in drug discovery is based on selecting the highest affinity compounds that bind to the target protein. However, compounds with similar affinities often have very different enthalpic and entropic contributions due to the enthalpy-entropy compensation phenomenon. The binding enthalpy primarily reflects the strength of the interactions of the ligand with the target protein (e.g. van der Waals, hydrogen bonds, etc.). The entropy change, on the other hand, mainly reflects two contributions: changes in conformational entropy and changes in solvation entropy [1].

Many binding reactions are coupled to the absorption or release of protons by the protein or the ligand. This phenomenon can be studied by detecting the heat effect produced by the protons exchanged between the protein and the buffer as a consequence of the inhibitor binding [2]. An investigation of the binding energetics requires the dissection of the buffer-related contributions, because only intrinsic parameters can be correlated with molecular structure and used for rational drug design.



1 Figure. Compensation behavior between enthalpic (ΔH) and entropic ($T\Delta S$) components of free energy of inhibitors binding to carbonic anhydrase VII.

In this work [(2-pyrimidinylthio)acetyl]benzenesulfonamides were investigated as inhibitors of recombinant human carbonic anhydrase isozymes. Many of the carbonic anhydrase isozymes are important therapeutic targets to treat a range of disorders including glaucoma, obesity, epilepsy and cancer [3]. The binding affinity was determined using isothermal titration calorimetry and thermal shift assay. Isothermal titration calorimetry was also used to evaluate protonation/deprotonation coupling and contributions of ΔH and ΔS to the binding affinity. Compounds were mapped in the direction of increasing functional groups to correlate with the increments in the intrinsic thermodynamic parameters.

- [1] S. Leavitt and E. Freire, Direct measurement of protein energetics by isothermal titration calorimetry, *Current Opinion in Structural Biology* **11**, 560-566 (2001).
- [2] R. Ghai, R.J. Falconer and B.M. Collins, Applications of isothermal titration calorimetry in pure and applied research—survey of the literature from 2010, *Journal of Molecular Recognition* **25**, 32-52 (2012).
- [3] E. Čapkauskaitė, A. Zubrienė, A. Smirnov, J. Torresan, M. Kisonaitė, J. Kazokaite, J. Gilyte, V. Michailoviene, V. Jogaite, E. Manakova, S. Grazulis, S. Tumkevicius, D. Matulis, Benzenesulfonamides with pyrimidine moiety as inhibitors of human carbonic anhydrases I, II, VI, VII, XII, and XIII, *Bioorganic and Medicinal Chemistry* **21**, 6937-6947 (2013).

THE BIOTISSUES FLUORESCENCE PHANTOM FOR NIR REGION

¹Nikita Belko, ¹Sophy Kavalenka, ²Dmitry Tarasov

¹ Scientific Research Institute of Applied Physical Problems, Belarusian State University, Belarus

² Scientific Research Institute of Applied Physical Problems, Belarus

nikita.belko@gmail.com

The method of photodynamic therapy is a perspective method to diagnose and treatment of tumor diseases. This method requires special spectrometric equipment, giving stable and easily reproducible results, as well as special material for researching of the effects on biological tissues. As well as studies with living biological objects are costly and methodologically complex, it is necessary to use phantoms, i.e. an objects simulating certain optical properties of the biological tissue (for example: absorption and scattering coefficients, anisotropy, etc.). Currently using optical phantoms, which have equal optical properties with real tissues, have unique multilayer structure as usual, that makes its reproduction very difficult. If the phantom developed for the control and testing of some equipment, quality of its specifications can be substantially reduced. In that case it is enough for the fluorescent specters of the phantoms and biologic tissue preserved during sufficiently large time interval. This phantom can be called imitation measure.

The imaging spectrometric complex for the studying of fluorescence of various objects (biological tissues, securities etc.) was designed in Scientific Research Institute of Applied Physical Problems. The aim of our study was to develop imitation measures for the calibration of the complex. As imitation measures was decided to use cellulose base, which was applied a drop of polymethine dye (PD), which is room-temperature dried room temperature. The dye was selected with the fluorescence spectrum in the near-infrared region. To eliminate the influence of humidity in the laboratory was selected water-insoluble colorant. As the solvent, ethanol was selected. In that work was considered different spectral characteristics of the imitation measures at various concentrations of PD. The range of dye concentrations in which the intensity at the maximum of the fluorescence depends linearly on the concentration was detected. As shown in Figure1, it was elucidated the linear dependence of the intensity maximum in the fluorescence spectrum of the exposure time in the photometer.

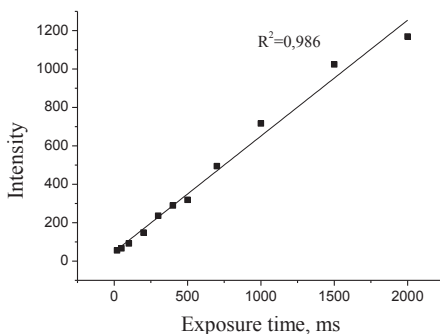


Fig.1. Linear dependence of intensity on exposure time.

The possibility of doubling the concentration of the dye recoating on dry surface of the previous drop was analyzed. The uniformity of the dye spot on the imitation measure was investigated. Time period in which the properties of the phantom can be considered as constant (with the exclusion of light exposure) was determined. It is concluded that the developed phantom can be used for registration photosensitizer's concentration in tissues *in vivo* and control of parameters stability of the spectrometer.

[1] Brian C Wilson and Michael S Patterson. The physics, biophysics and technology of photodynamic therapy. IOP Publishing. Physics in medicine and biology.

[2] Mohammad R. N. Avanakil, Ali Hojjat, and Adrian G. Podeleanu. Multilayer Tissue-Like Optical Phantom; a Model for Skin in Optical Coherence Tomography Imaging. Microscopy Focus.

EFFECTS OF BLUE LIGHT ON STABILITY AND TOXICITY OF CdSe QUANTUM DOTS IN MEDIA WITH MICROALGAE: SPECTROSCOPIC AND MICROSCOPIC STUDY

Agnė Kalnaitytė^{1*}, Saulius Bagdonas¹ and Ričardas Rotomskis²

¹ Quantum Electronics Department, Faculty of Physics, Vilnius University, Saulėtekio ave. 9, c. 3, LT-10222, Vilnius, Lithuania

² Vilnius University Institute of Oncology, Baublio 3b, LT-08406, Vilnius, Lithuania

agne.kalnaityte@ff.stud.vu.lt

Quantum dots (QDs) - semiconductor particles of nanometer-size - are promising fluorescent markers. In comparison with organic dyes and fluorescent proteins, QDs have a narrow and tunable emission band, broad absorption and sharp emission spectra, high brightness, enhanced photostability, resistance to chemical degradation and photobleaching [1]. The research on QDs is important in order to provide safe and effective biosensing materials for medicine [2].

In this study, absorption, steady state spectroscopy and microscopy measurements were performed on CdSe (518nm) quantum dots in biological model environment. Stability, photostability, toxicity and spectral properties of quantum dots were investigated in the presence of *Scenedesmus* microalgae to reveal the effects of QDs interaction with biological system.

Aqueous media induced a time related blue shift of the photoluminescence band of quantum dots from 518 nm to 380 nm, but this shift was not observed in media with microalgae (Fig. 1a). Photoluminescence intensity of QDs was more stable in media with microalgae than in aqueous media. The same effect was reported in studies on QDs interaction with proteins [3]. That could be explained by formation of a new coating layer having a protective effect against degradation of quantum dots.

Samples of QDs in aqueous media and in media with algae were exposed to the blue diode light for an hour (405 nm, 90 mW/cm²) to measure photostability. Photoluminescence intensity of QDs decreased, and spectra shifted towards shorter wavelengths after lighting. However, the exposure only accelerated the changes in CdSe QDs structure induced by aqueous media.

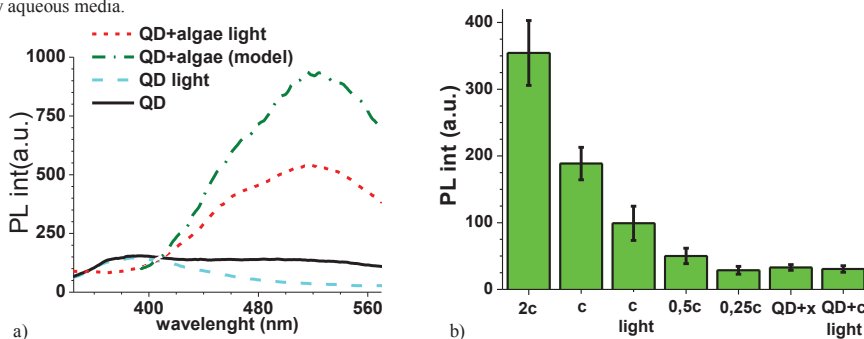


Fig. 1. a) Photoluminescence spectra of quantum dots ($\lambda_{ex}=300\text{nm}$) in aqueous media (solid) and in media with microalgae (dash dot), and after 1 hour exposition of blue light (after one day after exposure) in aqueous media (dash) and in media with microalgae (short dash). b) The autofluorescence intensity of algae (at 682nm maximum) after month, c – relative concentration of microalgae (used in samples with QDs).

Light of a blue diode caused decrease of algae autofluorescence. Photobleaching of chlorophyll fluorescence was reversible. However, the blue light also caused irreversible negative effects on growth of microalgae population. The final algae concentration in samples with QDs was about 25% of the control after a month (Fig. 1b). The damaged cells were seen in the pictures of samples with CdSe QDs taken by means of fluorescence microscope, but not in the samples without QDs, implying that the fragmentation of QDs induced death of algae cells.

[1] Robert E.Bailey, Andrew M.Smith, Shuming Nie, Quantum dots in biology and medicine, *Physica E* **25** (2004) 1–12

[2] J. Drbholavova, V. Adam, R. Kizek and J. Hubalek., Quantum Dots – Characterization, Preparation and Usage in Biological Systems, *Int J. Mol. Sci* **10** (2009) 656-673.

[3] Mopelola Idowu, Emmanuel Lamprecht, Tebello Nyokong, Interaction of water-soluble thiol capped CdTe quantum dots and bovine serum albumin, *Journal of Photochemistry and Photobiology A: Chemistry* **198** (2008) 7–12

CANCER STEM CELLS

Dominyka Dapkute¹, Simona Steponkiene^{2,3}, Ricardas Rotomskis^{2,3}

¹Faculty of Natural Sciences, Vilnius University, Lithuania;

²Faculty of Physics, Vilnius University, Lithuania;

³Biomedical Physics Laboratory, Institute of Oncology Vilnius University, Lithuania

dap.dominyka@gmail.com

A few decades ago it was noticed that cancerous tissue is not homogeneous but has cellular hierarchy and different levels of differentiation [1]. A small subpopulation of cancer cells is associated with tumor regeneration, metastasis, multi-drug resistance. These cells are called cancer stem cells (CSCs) as their properties are similar to normal stem cells [2]. CSCs can initiate tumor growth and give rise to other less aggressive cancer cells. It is very important to define the characteristics of CSCs and to find a new method of treatment targeting exclusively cancer stem cells.

Quantum dots (QDs) are nano-sized crystals made of semiconductor materials. They are advantageous for improved cellular imaging and delivery of active molecules directly to tumors. QDs have broad excitation and narrow fluorescence emission spectra and are more photostable than organic dyes. They can also serve as a platform for biologically active compounds such as antibodies and/or drugs [3].

In our study we used two different breast cancer cell lines – MCF-7 and MDA-MB-231. To determine which cell line has more cells potentially to be cancer stem-like ones we performed three different tests. As CSCs are distinguished by better colony formation, resistance to chemotherapy and expression of specific surface molecules, we used plating efficiency, sensitivity to doxorubicin and immunophenotyping with antibodies against CD44, CD24 and EpCAM antigens (Fig.1.). For accumulation studies we used eFluor® 605NC QDs and the conjugate of anti-CD44 and eFluor® 605NC QDs. The photoluminescence of QDs inside cells was registered by Nikon C1si laser scanning confocal microscope.

The results show that the cell line with the subpopulation of CSCs accumulates much more QDs even without the anti-CD44. Although such a connection between accumulation of QDs and CSCs yet remains to be investigated, it might open the way to the elimination of this critical population of cancer cells.

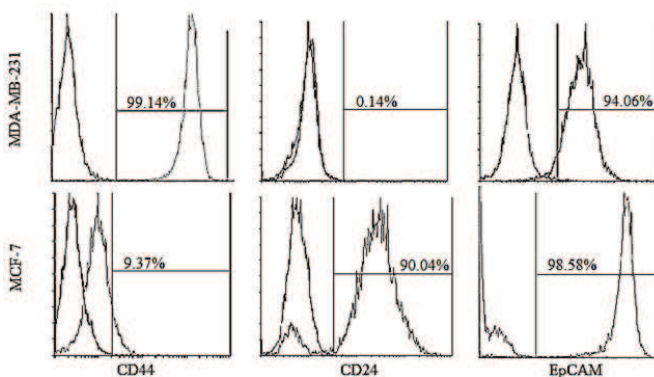


Fig.1. MDA-MB-231 cells express CD44⁺/CD24⁻/EpCAM⁺ immunophenotype which is associated with CSCs [4].

[1] D. Bonnet, J.-E. Dick, Human acute myeloid leukemia is organized as a hierarchy that originates from a primitive hematopoietic cell, *Nature Medicine* **3**(7), 730–737 (1997).

[2] T. Reya, S.-J. Morrison, M.-F. Clarke et al., Stem cells, cancer, and cancer stem cells, *Nature* **414**, 105–111 (2001).

[3] M. A. Walling, J. A. Novak, J. R. E. Shepard, Quantum Dots for Live Cell and In Vivo Imaging, *Int. J. Mol. Sci.* **10**, 441–491 (2009).

[4] M. Al-Hajj, M.S. Wicha, A. Benito-Hernandez et al., Prospective identification of tumorigenic breast cancer cells, *Proc. Natl. Acad. Sci. USA* **100**, 3983–3988 (2003).

APPLICATION OF LASER DIFFRACTOMETRY IN ANALYSIS OF CELLULAR SYSTEMS

Sophy Kavalenka, Alena Kavalenka, Vladislav Popov, Valera Loban

Department of Physics, Belarusian State University, Belarus
skaska24361@gmail.com

Laser diffractometry is an optical coherent method that allow to obtain important information about properties of the different particles including dispersed cellular systems such as blood or bone marrow cells and other [1-4]. The main advantages of laser diffraction method are the lack of contact, the ease to use, high accuracy, ability to automate the measurement. The basis of the method is the analysis of the light scattering patterns that are results of diffraction, refraction, reflection and absorption of laser light during the laser beam interaction with investigated particle/particles [5-7]. The angular dependence of light scattering intensity called the indicatrix is characteristic for the particle size. Therefore, laser diffractometry is the most widely applied for determination of cell sizes.

The ability to aggregate and the deformability during stimulated swelling of cells are studied to determine the key functional properties of blood cells and other, in particularly, erythrocytes, platelets, neutrophils and cancer cells. These researches can be performed by laser diffraction method, too. Holographic digital microscope with semiconductor laser diode and CCD matrix was developed to obtain the 3D images of cells that restore by mathematical analysis of diffraction pictures.

The most often the Fraunhofer approximation or the Mie theory is used for transforming the measured data to a particle size distribution [5-7]. The use of Fraunhofer theory is suitable for large particles but the Mie theory provides the greatest accuracy for the small particle. It has been postulated that scattering events are independent and that total scattering is the sum of individual events. The use of Mie theory presupposes knowledge of the light refractive index of the particles and the dispersion media and the imaginary part of the refractive index of the particles [5-7]. It is important that if the refractive index of the sample and the dispersion media are the same, the laser beam can not be diffracted and this media should be changed. It is necessary to note the disadvantage that the accuracy of measurements for non-spherical particles is unacceptable [5,6]. The exact theory of scattering (Mie theory, T-matrix method, discrete dipole approximation method [5,8-10] and the approximate calculation methods [11] is used to calculate the indicatrix of a single particle. Suspensions of cells can be analyzed using the multi-mode Laplace transformation for detection and separation of multi-modal particle size distributions. The mathematical analysis of experimental data in [12] was performed with application neural network method.

The automated multi-channel laser analyzer for researches of cell structural changes during stimulation was developed in our laboratory (Faculty of Physics, Belarusian State University). Semiconductor laser diode LFD635-5-3 and high-sensitive opto-electronic integrated circuits OPT301 were used in this device as the laser light source and the scattered light intensity detectors, respectively. Microcontroller AtMega8535 provides the control of kinetic data registration and processing. Firmware for the microcontroller was written using Atmel AVR-Studio 6.0. As software UniChrom-97 ("New Analytical Systems", Belarus) was used. To support nephelometer driver DLL was developed using driver development kit UniChrom-DDK.

-
- [1] E. Bedner, Laser scanning cytometry distinguishes lymphocytes, monocytes, and granulocytes by differences in their chromatin structure, *Cytometry* **29**, 191–196 (1997)
 - [2] A.N. Shvalov, Light-scattering properties of individual erythrocytes, *Appl. Optics* **38**, 230–235 (1999)
 - [3] M. Kalashnikov et al., Assessing light scattering of intracellular organelles in single intact living cells, *Optics Express* **17**, 19674–19681 (2009)
 - [4] J. Mourant et al., Light scattering from cells: the contribution of the nucleus and the effects of proliferate status, *J Biomed Opt.* **5**, 131–137 (2000)
 - [5] A. Doicu, T. Wriedt Computation of the beam-shape coefficients in the generalized Lorenz–Mie theory by using the translational addition theorem for spherical vector wave functions, *Appl. Opt.* **13**, 2971–2978 (1997)
 - [6] F.M. Etzler, Particle-size analysis: a comparison of methods, *American Pharm Review* **7**(1), 104–108 (2004)
 - [7] S.A. Kubart, K.M. Keck, Laser diffractometry of nanoparticles: frequent pitfalls and overlooked opportunities, *J. Pharm. Technol. Drug Res.*, <http://www.hoajonline.com/journals/pdf/2050-120X-2-17.pdf> (2013)
 - [8] M.I. Mishchenko, et al., T-matrix computations of light scattering by nonspherical particles, *J. Quant. Spectr. Rad. Transfer.* **55**, 535–575 (1996)
 - [9] P. Platau, Fast solvers for one dimensional light scattering in the discrete dipole approximation, *Opt. Express* **12**, 3149–3155 (2004)
 - [10] D.W. Mackowski, M.I. Mishchenko, Direct simulation of multiple scattering by discrete random media illuminated by Gaussian beams, *Phys. Rev. A* **83**(1), 013804–013814 (2011)
 - [11] P. Chiappetta, B. Torresani, Some approximate methods for computing electromagnetic fields scattered by complex object, *Measur. Sci. Technol.*, **9**, 171–182 (1998)
 - [12] Z. Ulanowski, et al., Application of neural networks to the inverse light scattering problem for spheres, *Applied Optics* **37**, 4027–4033 (1998)

HIGH-SPEED AND ACCURACY BIOPATTERNING BY DIP-PEN NANOLITHOGRAPHY WITH LIPID INKS

Vytautas Navikas^{1,2}, Martynas Gavutis², Šarūnas Vaitekoniš², Ramūnas Valiokas²

¹Faculty of Natural Sciences, Vilnius University, Lithuania

²Department of Nanoengineering, Center of Physical Sciences and Technology, Vilnius, Lithuania
vytautas.navikas@fmcc.lt

DPN is a scanning-probe-based lithography, in which tip is used to make nano-scale chemical patterns by directly transferring molecules to the surface. It was first introduced in 1999 [1]. This method offers a number of advantages over other nanofabrication methods, such as no need of expensive photolithographic masks, but it also has some issues such as slow patterning speed and accurate control of the material amount on the tip, which dramatically affects the repeatability of the structures.

The goal of this study was to explore the possibilities of dip-pen nanolithography (DPN) to fabricate lipid patterns on solid supports. An ink-jet based tip inking [2] was used as a novel method for such a control. Investigation of fluorescent lipid 1, 2-dioleoyl-sn-glycero-3-phosphocholine (DOPC) mixed with 1% 1, 2-dioleoyl-sn-glycero-3-phosphoethanolamine-N-carboxyfluorescein (DOPC-FL) traces on different tips using epifluorescence microscopy showed a reliable repeatability of the material deposited on the tip. After that patterning using JPK scanning probe microscope was done on the silicon dioxide surface in order to investigate how this inking strategy affects DPN patterns. Fabricated patterns investigated by using fluorescence and scanning probe microscopy showed a reasonable repeatability and line widths down to 200 nm on a silicon dioxide surface. Lipids allowed reaching high patterning speeds (up to 100 μm/s). Furthermore, DPN was done on different surfaces such as self-assembled monolayers (SAM's) in order to investigate lipids spreading and behavior on different hydrophobicity surfaces.

Results of this research show that ink-jet material deposition on the tip allows reaching significant improvement over conventional ink well inking and provide possibilities to develop new applications of DPN technology.

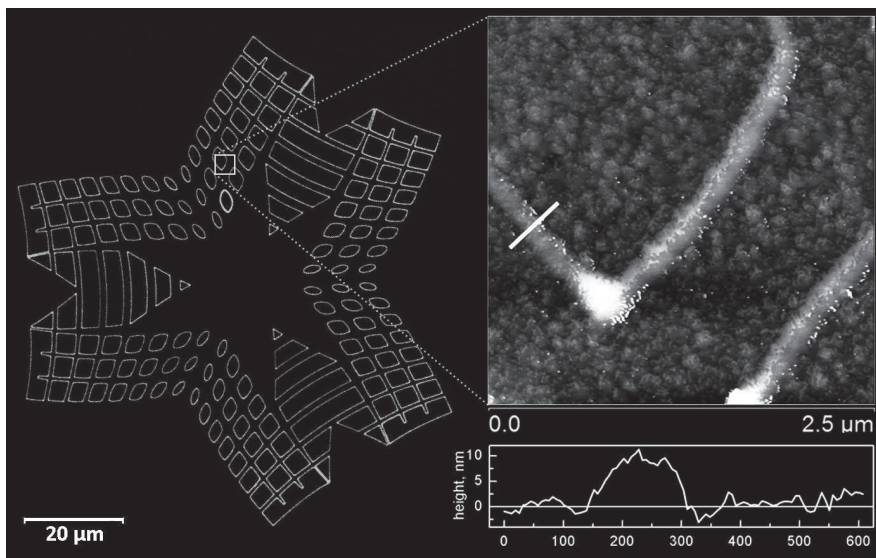


Fig.1 Fluorescence image of DOPC-FL lipid pattern (left) combined with an AFM topography image with 10 nm Ag evaporated on top (right).

[1] Richard D. Piner, Jin Zhu, Feng Xu, Seunghun Hong, Chad A. Mirkin, "Dip-pen" Nanolithography, *Science* **283**, 661 (1999).

[2] Yuhuang Wang, Louise R. Giam, Matt Park, Steven Lenhart, Harald Fuchs, and Chad A. Mirkin, A Self-Correcting Inking Strategy for Cantilever Arrays Addressed by an Inkjet Printer and Used for Dip-Pen Nanolithography, *Small* No. **10**, 1666–1670 (2006).

Oral session 6

Theoretical physics and astrophysics

HOW TO KEEP ON A SLIPPERY PEAK

Elena Tamaševičiūtė

Department of Electronics, Center for Physical Sciences and Technology, Vilnius, Lithuania
elena.tamaseviciute@ftmc.lt

Stabilization of unstable steady states (fixed points) of dynamical systems is of great importance, especially in engineering applications to mechanical, electronic, optical, chemical, biological, etc. systems.



Fig. 1. Peak of Matterhorn.

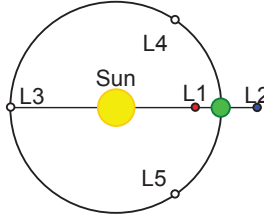


Fig. 2. Sun–Earth Lagrange points.

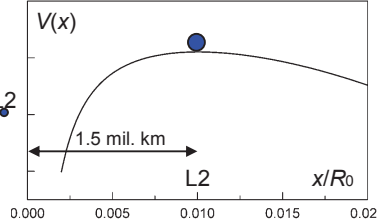


Fig. 3. Potential around Lagrange point L2.

Dynamics of a system, described by a state variable $x(t)$, is given by the second order differential equation:

$$\frac{d^2x}{dt^2} + b \frac{dx}{dt} + \frac{dV(x)}{dx} + \xi = 0, \quad (1)$$

where b is a friction (damping) coefficient, ξ is an unknown (probably slowly varying) force or perturbation. In the vicinity of a fixed point, e.g. a peak of a mountain or the Lagrange point L2, the potential $V(x)$ can be approximated by a downward parabola $V(x) = -x^2/2$. Then Eq. (1) reads

$$\frac{d^2x}{dt^2} + b \frac{dx}{dt} - x + \xi = 0. \quad (2)$$

The steady-state solution $[x_0, dx/dt]$ is simply $[\xi, 0]$. It is an unstable saddle type fixed point, characterized with an odd number of real positive eigenvalues. Moreover, its coordinate x_0 is uncertain because of an unknown ξ . To control unknown saddles Pyragas *et al.* [1] proposed an elegant feedback controller, employing an *unstable* (!) first order filter:

$$\frac{d^2x}{dt^2} + b \frac{dx}{dt} - x + \xi = k(u - x), \quad \frac{du}{dt} = \omega(u - x). \quad (3)$$

The unstable filter method has been successfully applied to several physical, electrochemical and electronic systems [2, 3]. To stabilize a system the cut-off frequency of the filter ω in Eqs. (3) should be less, than the friction coefficient, $\omega < b$. This condition is difficult to meet for systems with low friction ($b \ll 1$), i.e. for “slippery” systems, and quite impossible to fulfill for conservative systems, e.g. the Lagrange points ($b = 0$) [4].

To get around the problem we suggest to supplement the controller with a common stable first order filter:

$$\frac{d^2x}{dt^2} + b \frac{dx}{dt} - x + \xi = k_1(u - x) + k_2(v - x), \quad \frac{du}{dt} = \omega_1(u - x), \quad \frac{dv}{dt} = \omega_2(v - x). \quad (4)$$

Here the cut-off frequencies ω_1 and ω_2 are not limited by b (friction can be very small or even zero). We note, that alone neither the unstable filter (in the case of $b = 0$), nor the stable filter (for any b) can stabilize a saddle steady state. Therefore, the control technique, given by Eqs. (4), can be considered as an extremely efficient synergetic method.

Very recently, two alternative methods [5,6], including a simpler, but more effective technique, using derivatives of both, variable $u(t)$ and variable $x(t)$ [6], instead of the difference term $k_2(v - x)$ in the feedback, have been described.

- [1] K. Pyragas, V. Pyragas, I.Z. Kiss, J.L. Hudson, Stabilizing and tracking unknown steady states of dynamical systems, *Physical Review Letters* **89**, 244103 (2002).
- [2] K. Pyragas, V. Pyragas, I.Z. Kiss, J.L. Hudson, Adaptive control of unknown unstable steady states of dynamical systems, *Physical Review E* **70**, 026215 (2004).
- [3] A. Tamaševičius, E. Tamaševičiūtė, G. Mykolaitis, S. Bumelienė, Switching from stable to unknown unstable steady states of dynamical systems, *Physical Review E* **78**, 026205 (2008).
- [4] A. Tamaševičius, E. Tamaševičiūtė, G. Mykolaitis, S. Bumelienė, R. Kirvaitis, Stabilization of saddle steady states of conservative and weakly damped dissipative dynamical systems, *Physical Review E* **82**, 026205 (2010).
- [5] A. Tamaševičius, E. Tamaševičiūtė, G. Mykolaitis, S. Bumelienė, Enhanced control of saddle steady states of dynamical systems, *Physical Review E* **88**, 032904 (2013).
- [6] E. Tamaševičiūtė, G. Mykolaitis, S. Bumelienė, A. Tamaševičius, Stabilizing saddles, *Physical Review E* **88**, 060901(R) (2013).

Non-extensive and extensive statistics in the agent-based herding model

Aleksejus Kononovicius¹, Julius Ruseckas¹

¹Institute of Theoretical Physics and Astronomy, Vilnius University
aleksejus.kononovicius@gmail.com

Power-law statistical properties are observed in systems with long-range memory and long-range interactions. Systems possessing these anomalous properties can not be understood in a traditional framework of Boltzmann-Gibbs statistical mechanics. Thus they are studied by using a generalized framework, known as non-extensive statistical mechanics [1]. In the core of this framework lies a distribution which is a generalization of the traditional Gaussian distribution, known as a q -Gaussian distribution,

$$p(x) \sim \exp_q \left(-\frac{x^2}{(3-q)\sigma_q^2} \right) = \left[1 + \frac{q-1}{(3-q)\sigma_q^2} x^2 \right]^{-\frac{1}{q-1}} \sim x^{-\frac{2}{q-1}}.$$

In the above $[z]_+ = z$ if $z > 0$, and $[z]_+ = 0$ if $z \leq 0$. It is straightforward to notice that in the limit of large values of x , if $q \neq 1$, the q -Gaussian distribution behaves as a power-law distribution. While if $q \rightarrow 1$ the q -Gaussian distribution reduces to the Gaussian distribution. The q -Gaussian distribution and related concepts from the non-extensive statistical mechanics have found their applications in broad range of fields, such as physics, chemistry, biology, computer science and even social sciences [2].

Contemporary modeling of the complex socio-economic systems frequently uses agent-based modeling framework [3]. In this framework distinct entities acting in the modeled system are replaced by a generalized objects, known as agents. These agents are assumed to act based on a very simple rules. For example, there are agent-based models for the financial markets in which the internal intricacy of the trading mechanics and strategies is successfully replaced by a simple herding interactions. Interestingly enough despite the simplistic behavioral rules in certain cases the ensembles of agents are able to reproduce the complex collective behavior observed in socio-economic systems [4, 5, 6]. In order for agent-based model to be useful it should also be analytically tractable. Analytical tractability introduces certain level of transparency into the model, which may be useful in understanding and further developing the model. Currently there are some approaches starting from the agent-based models, which analytically obtain non-linear stochastic differential equations as a macroscopic model for the agent-based dynamics [3, 4, 5, 7].

In this contribution we consider agent-based herding model proposed by A. Kirman [8]. This agent-based model proves to be very interesting to us as it is able to reproduce both the power-law and Gaussian-like distribution [4, 5]. In [5] Kirman model was tested on random graph, small world and scale-free networks. It was shown that Kirman model produces power-law distribution if average number of contacts of each agent scales linearly with the system size as average degree of nodes in the random graph network, $\langle d \rangle \sim N$. While if the average number of contacts is fixed, as in small world or scale-free network, $\langle d \rangle \sim \text{const}$, the Gaussian-like distribution is observed. In this contribution we discuss how Kirman model works on a densifying network, $\langle d \rangle \sim N^\alpha$ ($0 \leq \alpha \leq 1$), obtaining continuous transition between the non-extensive and extensive statistics.

-
- [1] C. Tsallis, *Introduction to Nonextensive Statistical Mechanics* (Springer, New York, 2009).
 - [2] Cf. M. Gell-Mann, C. Tsallis, *Nonextensive Entropy - Interdisciplinary Applications* (Oxford University Press, New York, 2004).
 - [3] M. Cristelli, L. Pietronero, A. Zaccaria, Critical Overview of Agent-Based Models for Economics, *Proceedings of the School of Physics "E. Fermi" CLXXVI*, 235 - 282 (2012).
 - [4] A. Kononovicius, V. Daniunas, Agent-based and macroscopic modeling of the complex socio-economic systems, *Social Technologies* **3**, 85-103 (2013).
 - [5] S. Alfarano, M. Milakovic, Network structure and N-dependence in agent-based herding models, *Journal of Economic Dynamics and Control* **33**, 78-92 (2009).
 - [6] R. Frederick, Agents of influence, *PNAS* **110**, 3703-3705 (2013).
 - [7] A. Kononovicius, V. Gontis, Agent based reasoning for the non-linear stochastic models of long-range memory, *Physica A* **391**, 1309-1314 (2012).
 - [8] A. P. Kirman. Ants, rationality and recruitment, *Quarterly Journal of Economics* **108**, 137-156 (1993).

Photomechanical effect in polymeric fibers: analysis of local voids

Wojciech Radosz, Antoni C. Mituś, Grzegorz Pawlik

Institute of Physics ,Wroclaw University of Technology, Poland
wojtekradosz@wp.pl

Recently we have formulated a simple Monte Carlo model [1] for the study of the photomechanical effect in polymeric fibers pumped with a linearly polarized laser beam. The model fiber is a host - guest system consisting of the polymeric matrix and azodye chromophores, which undergo multiple trans - cis - trans cycles when illuminated by linearly polarized light. Results that will be presented are focused on the topic closely related to the hypothetical cooperative mechanism of stress relaxation - on the characterization of local voids in computer-generated polymeric matrix (on discrete 3D lattice). We study void-size distributions and void-void correlation functions, all using bond-fluctuating model and Monte Carlo simulations.

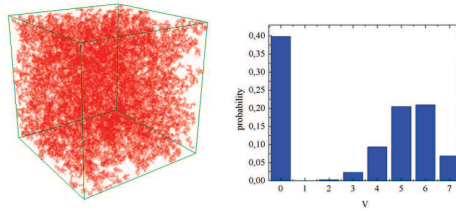


Figure 1. Simulated polymeric system (left) and probability distribution of local void sizes V in the system (right). [2]

After a proper preparation of polymeric matrix (Fig. 1 - left), we introduce local void parameter. It divides cells in view of possibility of movement for foreign objects - so called steric restriction.

Character of local void parameter distribution (Fig. 1 - right) is highly polarized - two groups of strong ($V = 0 - 4$) and weak ($V = 5 - 7$) steric restriction are easily distinguishable. We may suppose that general behaviour and properties of the system will not change together with the change of local void definition.

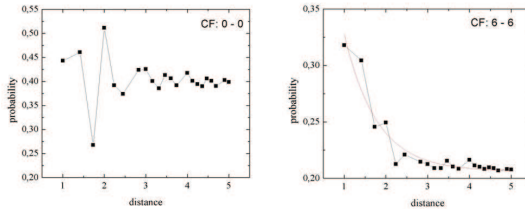


Figure 2. Plot of correlation functions $g_2(r, 0, 0)$ (left) and $g_2(r, 7, 7)$ (right). Solid line: exponential fit. [2]

In Fig. 2 we show plots of correlations functions for cells representing strong (left part) and weak (right part) steric restriction. In the first case we observe typical for liquids oscillations. The second case is very different and displays a decay of correlations with superimposed oscillations which decay with distance. The decay can be fitted by an exponential function. This implies that there is a characteristic length $d_7 = 2.5 - 3$ which characterizes the decay of $7 - 7$ correlations. In other words, a cube with size $5 - 6$ is a typical domain where steric interactions are weak.

[1] G. Pawlik, P. Wrobel, A.C. Mituś, and M.G. Kuzyk, Proc. SPIE 8113 81230Q (2011).

[2] G. Pawlik, R. Orlik, W. Radosz, A.C. Mituś, and M.G. Kuzyk, Proc. SPIE 8474, 84740A (2012).

SIMULATING JAYNES-CUMMINGS DYNAMICS IN MESOSCOPIC ENSEMBLES OF INTERACTING ATOMS

Ilya I. Beterov^{1,2}, Tomas Andrijauskas³, Denis B. Tretyakov¹, Vasilii M. Entin¹,
Elena A. Yakshina^{1,2}, Igor I. Ryabtsev^{1,2,4}, and Silvia Bergamini⁵

¹A. V. Rzhanov Institute of Semiconductor Physics SB RAS, 630090 Novosibirsk, Russia

²Novosibirsk State University, 630090 Novosibirsk, Russia

³Institute of Theoretical Physics and Astronomy, Vilnius University, Vilnius, Lithuania

⁴Russian Quantum Center, Skolkovo, Moscow Reg., 143025, Russia

⁵The Open University, Walton Hall, MK7 6AA, Milton Keynes, UK
tomas.andrijauskas@tfai.vu.lt

The Jaynes-Cummings model [1] is known as a basic model of interaction of a simple two-level atom with a single mode of a quantum electromagnetic field in a cavity. The fluctuation of the number of photons in the mode of the electromagnetic field leads to collapses and revivals of quantum Rabi oscillations in the two-level system. The model has been widely used to describe interaction of quantum system including quantum dots [2] and graphene [3]. The classical simulation of the quantum Jaynes-Cummings model could be of interest due to the simplicity of experimental implementation and ability to observe different dynamic regimes of atom-light interaction.

We describe a semi-classical simulation of the Jaynes-Cummings model based on an interaction of mesoscopic atomic ensembles with a laser radiation, which is considered as a classical electromagnetic field. We show that the Jaynes-Cummings dynamics of Rabi oscillations could be observed in mesoscopic ensembles of Rydberg atoms in the regime of Rydberg blockade due to the \sqrt{N} dependence of the frequency of the collective Rabi oscillations (Fig. 1) on the number N of interacting atoms [4] and random loading of atoms in the optical dipole traps [5]. The Jaynes-Cummings Hamiltonian is written as [1]

$$\hat{H}_{JC} = \frac{1}{2}\hbar\omega_0\hat{\sigma}_z + \hbar\omega\hat{a}^\dagger\hat{a} + \hbar\gamma(\hat{\sigma}^+\hat{a} + \hat{\sigma}^-\hat{a}^\dagger). \quad (1)$$

Here ω_0 is the transition frequency between atomic states, ω is the frequency of laser radiation, γ is the coupling strength, $\hat{\sigma}^-$ and $\hat{\sigma}^+$ are the lowering and raising operators for the atomic levels, \hat{a} and \hat{a}^\dagger are lowering and raising operators for the quantum electromagnetic field. We show that the effective interaction between rydberg atoms in the mesoscopic ensemble is described by a Hamiltonian, that has the same form as the interaction term in the Jaynes-Cummings Hamiltonian (1).

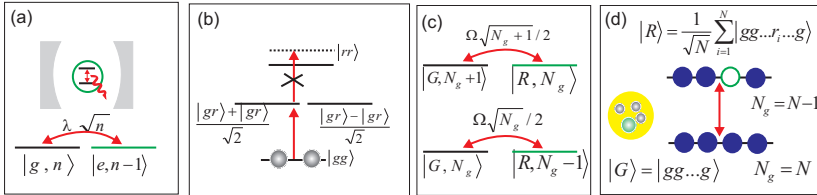


Fig. 1. (a) Jaynes-Cummings model [1]: n is the number of photons. g and e denote the ground and excited states of the atom; (b) Rydberg blockade for two interacting atoms; (c) Scheme of the coupled states of the mesoscopic atomic ensemble. N_g is the number of ground state atoms; (d) Scheme of the collective states of the atomic ensemble with N atoms interacting with the laser radiation in the regime of Rydberg blockade.

We also analyse the cases when the Rydberg blockade breaks down and it is possible to excite more than one atoms to the Rydberg state. Finally, we check whether the dynamics are affected by the spontaneous transition from the Rydberg state to the ground state. The atoms considered in the all the numerical calculations are Rb with 80S Rydberg state. Interaction between such atoms can be described by the Van der Waals potential.

[1] E. Jaynes and F. Cummings, Proceedings of the IEEE **51**, 89 (1963).

[2] F. Meier and D. D. Awschalom, Phys. Rev. B **70**, 205329 (2004).

[3] B. Dora, K. Ziegler, P. Thalmeier, and M. Nakamura, Phys. Rev. Lett **102**, 036803 (2009).

[4] M. Lukin, M. Fleischhauer, R. Cote, L. Duan, D. Jaksch, J. I. Cirac, and P. Zoller, Phys. Rev. Lett. **87**, 037901 (2001).

[5] R. Grimm, M. Weidemuller, and Y. B. Ovchinnikov, Advances in Atomic, Molecular, and Optical Physics **42**, 95 (2000).

PHOTOIONISING RADIATION FEEDBACK IN MOLECULAR CLOUD MODELS

Kostas Sabulis^{1,2}, Kastytis Zubovas²

¹Faculty of Physics, Vilnius University, Lithuania

²Department of Fundamental Research, Centre for Physical Sciences and Technology, Lithuania
kostas.sabulis@ftmc.lt

Molecular hydrogen clouds are known to be the birth places of new stars. These entities collapse and fragment under the influence of many forces among which significant roles are played by gravity, turbulent motion and thermal pressure of the gas, external pressure of surrounding interstellar medium etc. Properties of newly formed stellar systems are determined by interplay of such physical phenomena [1], however, which of these are crucial and which are negligible is not trivial to tell. In order to understand the process of star formation observational data is not enough - interiors of star forming regions are hidden beneath optically thick molecular gas and interstellar dust. Moreover, characteristic timescale of star formation is much longer than human lifetime - observation of star formation dynamics in single molecular cloud is impossible. At this point numerical models can be employed to improve our understanding of star formation as a whole and the importance of each individual physical phenomenon.

This work is mainly concerned with external pressure created by the surrounding hot interstellar medium, which can be generated by multiple supernova explosions [6] or outflows from active galactic nuclei [7]. Such external pressure enhances molecular cloud collapse by reducing the timescale of collapse and compressing gas inwards, so it can not escape dense star forming regions and further fragments into stars. Newly formed stars may influence the surrounding medium and stop further gas fragmentation by heating it with radiation and blowing away some of the gas via stellar winds. Most significant heating is produced by photoionising radiation which is emitted mainly by massive stars ($M > 20M_{\odot}$). In this work we present a parametrised photoionising radiation feedback model which also accounts for radiation pressure. Also, calibration, tests and analysis of the resulting data is presented.

We use the hybrid N -body/SPH code Gadget [2] as the main modelling tool for this work. We have implemented parametrised star formation by introducing sink particles [3], applied a realistic energy balance equation [4], created and implemented parametrised photoionising radiation feedback based on Monte-Carlo radiation transfer method already implemented in Gadget [5]. The resulting data was analysed and visualised within IDL/GDL programming environment.

The work presented here is a part of a long-term project and the primary objective remains the same as in earlier publications [8, 9] - to evaluate the influence of external pressure generated by the hot interstellar matter surrounding the molecular cloud. Data analysis has shown that external pressure generates a shockwave, which is driven inwards, towards centre of the system, which enhances gas fragmentation and reduces the timescale of cloud collapse. Photoionizing radiation feedback was shown to be too weak to stop dense gas from fragmentation and ensuing star formation. Further analysis results are on their way.

[1] Christopher F. McKee and Eve C. Ostriker, *Theory of Star Formation*, ARAA, **45**, 120 (2007).

[2] Volker Springel, *The cosmological simulation code GADGET-2*, MNRAS, **364**, 1-46 (2005).

[3] Matthew R. Bate, Ian A. Bonnell, Volker Bromm, *The formation of a star cluster: predicting the properties of stars and brown dwarfs*, MNRAS, **339**, 27 (2003).

[4] Tsuyoshi Inoue and Shu-ichiro Inutsuka, *Two fluid magnetohydrodynamic simulations of converging HI flows in the interstellar medium. I. Methodology and basic results*, ApJ, **687**, 303-310 (2008).

[5] Sergei Nayakshin, Seung-Hoon Cha, Alexander Hobbs, *Dynamic Monte Carlo radiation transfer in SPH: radiation pressure force implementation*, MNRAS, **397**, 1314-1325 (2009).

[6] H. Zinnecker and T. Preibisch, *The History of Low-Mass Star Formation in the Upper Scorpius OB Association*, ApJ, **117**, 2381 (1999).

[7] K. Zubovas, S. Nayakshin, A. King, and M. Wilkinson, *AGN outflows trigger starbursts in gas-rich galaxies*, MNRAS, **433**, 3079-3090 (2013).

[8] Kostas Sabulis, Kastytis Zubovas, *Turbulent molecular cloud collapse*, 56th scientific conference for young students of physics and natural sciences Open Readings 2013, ISSN 2029-4425, Vilnius University, **59** (2013).

[9] Kostas Sabulis, Kastytis Zubovas, *Numerical models of compressed, moving, cold interstellar clouds*, 40th National Physics Conference of Lithuania, ISBN 978-609-459-210-2, Vilnius University, **40** (2013).

CHEMICAL COMPOSITION OF A KINEMATIC STELLAR GROUPS IN THE SOLAR NEIGHBOURHOOD

R. Ženovienė¹, G. Tautvaišienė¹, E. Stonkutė¹, B. Nordström², V. Bertašius¹

¹Institute of Theoretical Physics and Astronomy, Vilnius University, Lithuania

²Niels Bohr Institute, Copenhagen University, Denmark

renata.zenoviene@tfai.vu.lt

Ancient mergers of dwarf galaxies are believed to play an important role in the formation of the Milky Way galaxy. A number of stellar streams, moving and kinematic groups were identified in the Milky Way galaxy ([1, 2, 3], and references therein). Some of them are suspected to originate from accreted satellites. Evidences of small dwarf galaxy mergers to our Galaxy are Sagittarius [4], the Canis Major [5], and Segue 2 [6] dwarf galaxies.

Signatures of past accretions in the Galaxy may be identified from correlations between stellar orbital parameters, such as apocentre, pericentre, and z-angular momentum, the so-called APL space. Using this technique Helmi et al. [7] identified three coherent groups of stars. They have used an all-sky Geneva-Copenhagen survey catalogue of kinematics, metallicities and ages for about 13.000 nearby F- and G-type stars by Nordström et al. [8]. Those stars were suspected to belong to disrupted satellites.

We determine detailed elemental abundances of 22 chemical elements in stars belonging to the so-called Groups 1 and 2 of the Geneva-Copenhagen survey and compare the chemical composition with Galactic thin- and thick-disc stars. The aim is to investigate the homogeneity of the chemical composition of stars within each group and to search for chemical signatures that might give information about the formation history of those kinematic groups of stars.

Spectra of high-resolving power ($R \approx 68\,000$) in the wavelength range of 3680–7270 Å were obtained with the FIES spectrograph at the Nordic Optical 2.5 m telescope, La Palma, and were analysed with a differential model atmosphere method. Comparison stars were observed and analysed with the same method.

Our study shows that the programme stars are overabundant in oxygen, α -elements and r-process-dominated chemical elements compared with the Galactic thin-disc dwarfs and chemical evolution models. This abundance pattern has similar characteristics as the Galactic thick-disc.

The similarity in chemical composition of stars in Groups 1 and 2 with that in stars of the thick-disc might suggest that their formation histories are linked. The chemical composition together with the kinematic properties and ages of stars in the investigated stars provides evidence of their common origin and possible relation to an ancient merging event. A gas-rich satellite merger scenario is proposed as the most likely origin. Whole three groups of the Geneva-Copenhagen Survey might have originated in the same merging event.

The Group 3 of the Geneva-Copenhagen survey was investigated recently by Stonkutė et al. [9, 10]. The coming papers of this series will focus on a more detailed chemical composition analysis of Group 1 (paper in preparation) and Group 2 [11].

-
- [1] A. Helmi, The stellar halo of the Galaxy, *The Astronomy and Astrophysics Review* **15**, 145-188 (2008).
 - [2] R. Klement, H. W. Rix et al., Halo Streams in the Seventh Sloan Digital Sky Survey Data Release, *The Astrophysical Journal* **698**, 865-894 (2009).
 - [3] B. Sesar, J. G. Kohn et al., Two Distant Halo Velocity Groups Discovered by the Palomar Transient Factory, *The Astrophysical Journal* **755**, 134S (2012).
 - [4] R. A. Ibata, G. Gilmore, M. J. Irwin, A dwarf satellite galaxy in Sagittarius, *Nature* **370**, 194-196 (1994).
 - [5] N. F. Martin, R. A. Ibata et al., Why the Canis Major overdensity is not due to the Warp: analysis of its radial profile and velocities, *Monthly Notices of the Royal Astronomical Society* **355**, L33-L37 (2004).
 - [6] V. Belokurov, M. G. Walker et al., The discovery of Segue 2: a prototype of the population of satellites of satellites, *Monthly Notices of the Royal Astronomical Society* **397**, 1748-1755 (2009).
 - [7] A. Helmi, J. F. Navarro et al., Pieces of the puzzle: ancient substructure in the Galactic disc, *Monthly Notices of the Royal Astronomical Society* **365**, 1309-1323 (2006).
 - [8] B. Nordström, M. Mayor et al., The Geneva-Copenhagen survey of the Solar neighbourhood. Ages, metallicities, and kinematic properties of 14 000 F and G dwarfs, *Astronomy and Astrophysics* **418**, 989-1019 (2004).
 - [9] E. Stonkutė, G. Tautvaišienė et al., Stellar substructures in the solar neighbourhood. I. Kinematic group 3 in the Geneva-Copenhagen survey, *Astronomy and Astrophysics* **541**, A157 (2012).
 - [10] E. Stonkutė, G. Tautvaišienė et al., Stellar substructures in the solar neighbourhood. II. Abundances of neutron-capture elements in the kinematic Group 3 of the Geneva-Copenhagen survey, *Astronomy and Astrophysics* **555**, A6 (2013).
 - [11] R. Ženovienė, G. Tautvaišienė et al., Stellar substructures in the solar neighbourhood. III. Kinematic group 2 in the Geneva-Copenhagen survey, arXiv:1401.5999 (2014).

Poster session 1

Laser physics and optical technologies
Spectroscopy, functional materials and derivatives
Chemistry and chemical physics

Construction and investigation of synchronously pumped folded cavity femtosecond optical parametric oscillator

Julius Vengelis¹, Karolina Stankevičiūtė¹, Rosvaldas Šuminas¹, Agnė Marcinkevičiūtė¹

¹ Laser Research Center, Faculty of Physics, Vilnius University, Lithuania
julius.vengelis@ff.stud.vu.lt

Optical parametric oscillators (OPO) are unique devices providing coherent radiation tunable in a wide spectral region. Femtosecond optical parametric oscillators provide femtosecond laser pulses used for investigation of various ultrafast processes in spectroscopy, material science, biochemistry, etc. In order to generate low energy and high repetition rate tunable femtosecond pulses (which are preferred in the aforementioned applications), synchronously pumped optical parametric oscillator (SPOPO) is constructed. Synchronous pumping means that the generated pulse resonator round-trip time is equal to pump pulse repetition period [1]. This technique is implemented adjusting the SPOPO resonator length according to the aforementioned condition. Nowadays, most femtosecond SPOPOs use Ti:sapphire lasers as pump sources [2]. We seek to create and optimize SPOPOs pumped by mode-locked Yb:KGW “PHAROS” oscillators. Such laser and SPOPO systems should be cheaper, more compact and therefore competitive with Ti:sapphire pumped SPOPOs.

In this study we present experimental data obtained during the investigation of SPOPO pumped by the second harmonic ($\lambda=515$ nm) of Yb:KGW “PHAROS” oscillator providing ~ 105 fs pulses at 76 MHz repetition rate with average output power of 1.71 W. At this stage of our research we constructed a folded cavity SPOPO mounted on a separate optical board. Such scheme is compact, can be moved and will be used as an experimental prototype for future SPOPOs. In this SPOPO the nonlinear medium for parametric generation was a 2 mm β -barium borate (BBO) crystal cut at $\theta=22.2^\circ$ and $\phi=90^\circ$ for type I interaction and AR coated for pump ($\lambda=515$ nm) and signal wave radiation (630 nm – 1030 nm). During parametric generation process two lower frequency waves (called signal and idler) are generated. Their wavelengths are defined by the energy (Eq. 1) and momentum (Eq. 2) conservation laws [3]. We constructed a singly resonant SPOPO, therefore the resonator mirrors were highly reflecting only at one of the generated waves (the signal wave in this case).

$$\frac{1}{\lambda_p} = \frac{1}{\lambda_s} + \frac{1}{\lambda_i} \quad (1)$$

$$n_p \omega_p = n_s \omega_s + n_i \omega_i \quad (2)$$

We measured various SPOPO parameters with and without pump return using intracavity dispersion compensation and without it. We achieved signal wave tuning in 650 nm – 1030 nm range without intracavity dispersion compensation (Fig. 1 left) by rotating the BBO crystal and adjusting the SPOPO resonator length. Maximum output power varied from 202 mW at $\lambda=685$ nm to 3 mW at $\lambda=1030$ nm (Fig. 1 right). Such output power variations were caused mainly by these wavelength dependent factors: signal and idler photon energy ratio, pump and signal wave group velocity mismatch and cavity loss. We also measured output power dependence on pump power at different wavelengths and determined SPOPO generation thresholds for different wavelengths.

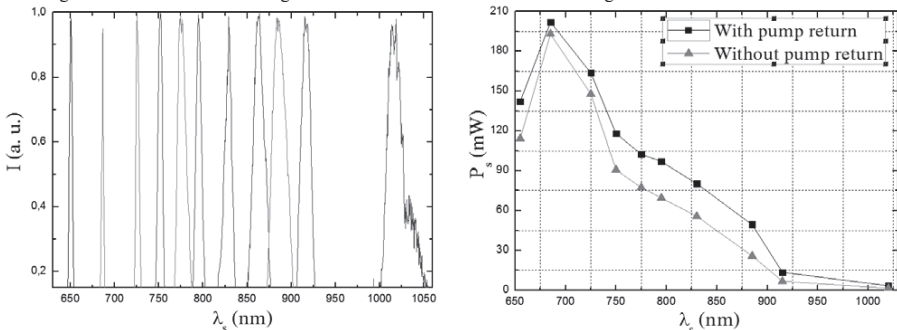


Fig. 1. Left: normalized SPOPO output signal spectra at different wavelengths without pump return and no intracavity dispersion compensation; right: maximum output power dependence on wavelength without intracavity dispersion compensation.

[1] M. Ebrahimzadeh, Parametric light generation, Phil. Trans. R. Soc. Lond. A 361, 2731-2750 (2003).

[2] M. Ebrahim-Zadeh, M. H. Dunn, Optical Parametric Oscillators in Handbook of Optics, Vol. 4. (McGraw-Hill, New York, 2000).

[3] C. L. Tang, L. K. Cheng, Fundamentals of optical parametric processes and oscillators (Harwood academic publishers, 1995).

THERMAL EFFECTS IN THE FOURTH HARMONIC GENERATOR OF FEMTOSECOND Yb:KGW LASER

Eglė Gabrytė^{1,2}, Mikas Vengris^{1,2}, Romualdas Danielius²

¹Department of Quantum Electronics, Vilnius University, Lithuania

²Light Conversion Ltd., Lithuania

egle.gabryte@ff.vu.lt

The availability and range of ultrafast (sub-picosecond) laser applications is spreading rapidly. In addition to scientific research, ultrashort laser pulses are now widely used in many areas, including industrial material processing and medicine [1]. When combined with nonlinear frequency converters, solid-state femtosecond laser systems provide ultrashort pulses in the UV spectral range, which makes them an advantageous tool for precise microfabrication of materials with high heat conductivity (e.g. metals, semiconductors). In such materials, UV pulses are absorbed significantly stronger than near-infrared or visible radiation. The deposited pulse energy is concentrated at the very surface and, consequently, material can be ablated with minimal collateral damage. High beam quality ($M^2 \approx 1$) of the solid-state laser equipped with UV converters ensures small ablating spot size, hence, spatially precise high-quality micromachining. There are also several serious limitations or extensive industrial application of femtosecond UV nonlinear frequency converters operating at high pulse repetition rates. Due to high peak intensities of UV pulses, two-photon absorption becomes significant in glasses and crystalline materials [2, 3] causing thermal-lensing effects in transmitting optical elements (lenses, windows, beamsplitters, etc.). Therefore, both spatial and temporal output characteristics of the converter can deteriorate significantly.

In this work we study the thermal effects in the fourth harmonic generator of 1026 nm Yb:KGW laser operating at multi-kilohertz repetition rates. Start-up dynamics of the frequency converter was investigated and linked to the temperature effects in the fourth harmonic generation crystal. Mathematical model for the simulation of the fourth harmonic power and crystal temperature dynamics at the different crystal tilt angles was developed. The simulated results were compared with the experimentally measured data (Fig. 1).

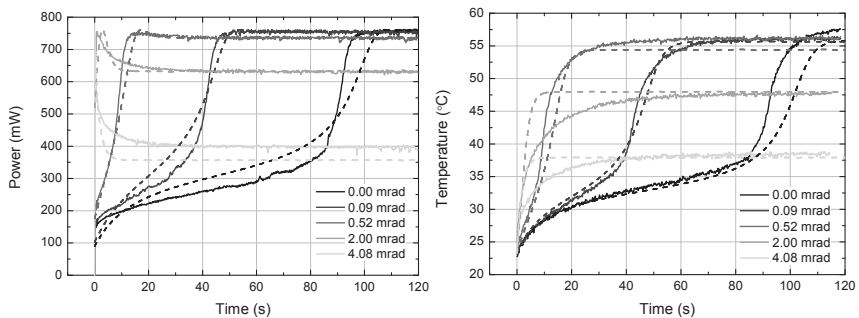


Fig. 1. Dynamics of the fourth harmonic power (left) and the crystal temperature (right) at different crystal tilt angles. Solid-lines denote experimental and dash-lines - simulated data, respectively.

After switching laser radiation on transitional power grow at the output of the femtosecond high pulse repetition rate UV harmonic generator is quite slow (from a few tens of seconds to several minutes). Therefore motorized control of the tilt angles of nonlinear optical crystals can be applied to counterbalance heating induced transitional power change at the output of the UV harmonic generator by changing phase matching conditions over time. We demonstrated, that the steep start-up power grow can be achieved by changing the crystal tilt angle in an exponential manner accordingly to the measured output power dynamics. Also, motorized angular tuning can be applied to improve stability of the UV output power during variation of the duty cycle.

-
- [1] F. Dausinger, F. Lichtner et al., *Femtosecond technology for technical and medical applications* (Springer-Verlag Berlin Heidelberg, Germany, 2004).
 - [2] A. Dubietis, G. Tamošauskas et al., Two-photon absorbing properties of ultraviolet phase-matchable crystals at 264 and 211 nm, *Applied Optics* **39**, 2437-2440 (2000).
 - [3] A. Dragomir, J. G. McInerney et al., Femtosecond measurements of two-photon absorption coefficients at $\lambda = 264$ nm in glasses, crystals, and liquids, *Applied Optics* **41**, 4365-4376 (2002).

FOUR-WAVE MIXING OF TUNABLE ULTRASHORT LASER PULSES IN AIR

Ernestas Žeimys, Benas Makauskas and Kęstutis Steponkevičius

Vilnius University Laser Research Center, Saulėtekio Ave. 10, LT-10223 Vilnius, Lithuania
 ernestas.zeimys@ff.stud.vu.lt

Nowadays, many modern experiments require high-power ultrashort laser pulses. Such pulses are a basic tool in chemistry or biology where most of the processes proceed on an ultrafast time scale. To investigate such processes pump-probe spectroscopy methods are often used, where temporal resolution is limited by the length of the laser pulse. Furthermore, experiments in photochemistry or photobiology additionally require tunability of central wavelength over a broad spectral range [1]. To generate such pulses optical parametric amplifiers (OPA) based on three-wave interactions in $\chi^{(2)}$ nonlinear crystals are widely used. However, in this case effective generation of ultrashort pulses can be achieved across visible (VIS) and infrared (IR) spectral ranges. An alternative way to generate such pulses is based on four-wave mixing (4WM) phenomenon in transparent $\chi^{(3)}$ isotropic media which allows to produce ultrashort pulses in a wide spectral range from vacuum ultraviolet (VUV) to IR. In this paper we report that ultrashort VIS pulses can be generated by 4WM during filamentation of an intense near-infrared (NIR) laser pulse in ambient air.

All the experiments were performed using a Ti:sapphire laser system, which generates ultrashort pulses of 100 fs (FWHM) duration with a central wavelength at 800 nm, a repetition rate of 1 kHz and an energy per pulse of 3.6 mJ. NIR laser beam was splitted into two parts using a beam splitter. One beam was focused into ambient air to produce a filament, while the other one was used to pump OPA. The central wavelengths of the IR beams (signal and idler beams from the OPA) were ranging between 1.2-1.6 μm (*s*-polarization) and 1.6-2.4 μm (*p*-polarization). The NIR and IR pulses were intersected using a dichroic mirror. The delay between these pulses was controlled by an optical delay line. Due to the strong nonlinear interaction between IR and NIR pulses during their copropagation, efficient 4WM was observed within the filament.

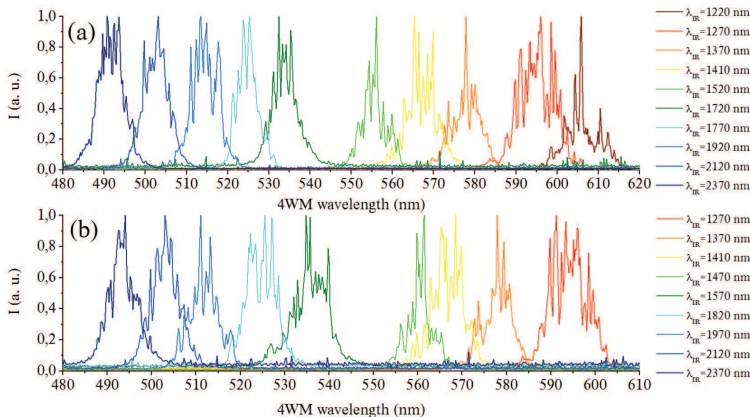


Fig. 1. 4WM spectra with the IR seed (λ_{IR}) superposed in the filament zone when the polarizations of interacting beams are: (a) parallel and (b) perpendicular.

Spectra of the 4WM pulses generated in air were registered for various polarizations and wavelengths of the IR beam. It was found that in both cases (when polarizations of IR and NIR pulses are parallel (Fig. 1a) and perpendicular (Fig. 1b)) the wavelength of generated 4WM pulses is inversely proportional to the IR wavelength and the frequency of the generated pulse is determined by $\omega_{4WM} = 2\omega_{NIR} - \omega_{IR}$.

In conclusion, the efficient generation of tunable ultrashort pulses was demonstrated. Maximal achieved conversion efficiency from IR signal to 4WM signal was about 12 %. Obtained results indicate that the ultrashort VIS pulses can be generated through 4WM in ambient air.

[1] F. Théberge, N. Aközbek, W. Liu, A. Becker, S. L. Chin, Tunable Ultrashort Laser Pulses Generated through Filamentation in Gases, Phys. Rev. Lett. **97**, 023904 (2006).

GENERATION BY CONICAL BEAMS

Paulius Stanislovaitis, Andrius Narmontas

Department of Quantum Electronics, Vilnius University,
 Saulėtekio Avenue 9, Building 3, LT-10222 Vilnius, Lithuania
 paulius.stanislovaitis@ff.stud.vu.lt

In this work, second harmonic (SH) generated from incoherent conical beams, consisting of multiple Gaussian-Schell (GS) [1] model beams is investigated. Theoretical description of the incoherent conical beam is provided. It is demonstrated that in the case of non-collinear phase matching spectrum of the second harmonic beam narrows with the propagation in a nonlinear crystal. An experimental result of a simplified case with 2 intersecting GS model beams is also presented. Numerical simulation results are in good agreement with the theory.

We assumed two fundamental conical beams. Each fundamental beam was constructed from N intersecting beams which spectra lie on the ring. The beams were assumed to be of Gaussian statistics, homogeneous, uncorrelated and their correlation functions were Gaussian. It was found that the spectral intensity in this case is described by the formula

$$G(\beta, \theta) = N b_0^2 \frac{2\sqrt{\pi}}{\Delta\beta\beta_0} \exp\left(\frac{-(\beta^2 - \beta_0^2)}{\Delta\beta^2}\right) \quad (1)$$

where β is the spectral radius, θ is the azimuthal angle, N is the number of beams, b_0 is the amplitude of a single beam, β_0 corresponds to the cone angle and $\Delta\beta = 2/\rho$, where ρ is the radius of the Gaussian autocorrelation function. The spectral intensity of the first beam is described by the Eq. (1) and the spectral intensity of the second beam was obtained from Eq. (1), by letting $\Delta\beta \rightarrow 0$. It means that the second beam was assumed to be radially coherent.

Theoretical analysis of the SH generation was carried out. Analysis, carried out using the nonlinear interaction equations, suggests that when pump is not depleted, the spectral radiance can be expressed as :

$$\frac{G_3(0, 0)}{G_{10}(\beta_0, 0)} = 4N \frac{z^2}{L_n^2} \quad (2)$$

where $L_n = 1/(\sigma b_0)$ is the nonlinear length and is σ the nonlinear interaction coefficient. As can be seen from Eq. (2), the spectral radiance increases quadratically with crystal length z .

The experiment was carried out using only two intersecting beams : one coherent and one incoherent. The incoherent beam was obtained by using a phase distortion filter. The SH was generated from these two beams and recorded with a CCD camera. The results are shown in Fig. 1.

At large z , the SH beam has maximum at line

$$\beta_x = -\beta_y \beta_0 / (k_0 \gamma), \quad (3)$$

as indicated in Fig. 1 (c) by the white diagonal line. In Eq. (3) k_0 is the wave number and γ is the walk-off angle. We note, that the direction of the line can be varied by changing the intersection plane of the pump beams. The results show good agreement with the theoretical calculations. The theoretically calculated spectral radiance in this case is the same as in Eq. (2) with $N = 1$.

In the case of conical beams the interaction plane is undefined and the spectrum of the SH beam has a narrow central spot. This was confirmed by the numerical simulations of nonlinear coupling equations. From Fig. 2 we can see how the spectral width of SH beam narrows during the propagation in a nonlinear crystal.

In conclusion, we have demonstrated the possibility to improve the coherence in the two-dimensional case. The spatial walk-off would provide the improvement only in one direction [2], however, when conical beams are used, the spectrum of the generated SH beam has a central spot, which narrows down with propagation distance.

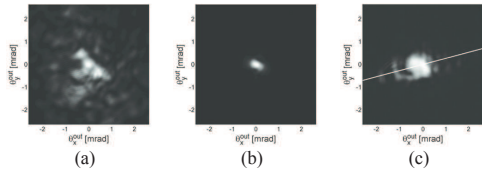


Figure 1. The fundamental incoherent (a) and coherent (b) beams and the SH intensity distribution (c).

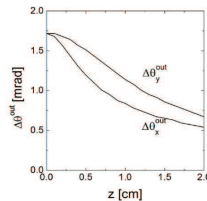


Figure 2. Narrowing of the SH spectrum in case of conical first harmonic beam.

- [1] G. Gbur. "Simulating fields of arbitrary spatial and temporal coherence". Opt. Express 14, 7567 (2006).
 [2] V. Pyragaitė, A. Stabinis, A. Piskarskas, Phys. Rev. A 86, 033812 (2012).

HIGH INTENSITY BROADBAND PULSE COMPRESSION IN BULK MATERIAL

Ignas Balčiūnas, Rimantas Budriūnas, Tomas Stanislauskas, Arūnas Varanavičius

Department of Quantum Electronics, Vilnius University, Sauletekio Ave. 9-III, Vilnius LT-10222, Lithuania
ignas.balciunas@ff.stud.vu.lt

In recent years, optical parametric chirped-pulse amplification (OPCPA) has emerged as a powerful tool for the generation of ultrashort pulses with extreme peak intensity, which are used in different domain of physics, such as nonlinear relativistic optics, heavy particle acceleration and many more [1]. The basic idea beyond this sophisticated method is to amplify and compress an ultrashort laser pulse without the onset of accumulating self-action effects (self-focusing, self-phase modulation, and eventually optical damage) imposed by optical nonlinearities in the amplifier. This is done by stretching the pulse in time by a dispersive element and thereby decreasing its peak power, then amplifying its energy and finally recompressing pulse to its original duration.

In this work we analyse different compressors made from combinations of bulk materials by modeling temporal behaviour of the pulse and possible nonlinear effects during the compression. For the evaluation of the nonlinear phase shift and the effects of self-phase modulation so called B-integral is calculated:

$$B = \frac{2\pi}{\lambda} \int n_2 |E(\mathbf{r}, t)|^2 dz, \quad (1)$$

where n_2 is the nonlinear component of the refractive index. If $B < 1$, the effects are said to be negligible [2]. Propagation of pulse in the material is described by generalized nonlinear Schrödinger equation (2):

$$i \frac{\partial A}{\partial x} = i \frac{\alpha}{2} A(z, t) + \frac{1}{2} \beta_2 \frac{\partial^2 A}{\partial \tau^2} - \frac{1}{6} \beta_3 \frac{\partial^3 A}{\partial \tau^3} - \gamma |A|^2 A(z, t), \quad (2)$$

where $\beta_2 = (\partial^2 k / \partial \omega^2)$ represents dispersion of the group velocity, $\beta_3 = (\partial^3 k / \partial \omega^3)$ represents group delay dispersion, γ is related to the nonlinear refractive index n_2 by the relation $\gamma = n_2 \omega_0 / c$, and $\tau = t - z/v_g$.

Split step Fourier method is used to numerically evaluate (2). The length of material is divided into large number of segments and the propagation of the optical pulse within each segment is calculated in two steps. During the first step only operator which takes into account dispersion is acted on the Fourier transform of the pulse while in the second step only operator describing nonlinear effects is acted on the output pulse. By this procedure, the pulse is propagated from segment to segment, and the degradation effects on the pulse can be studied at the output end of the material.

In this graph we present B-integral accumulation in the compressor consisting of 200 mm SF57 optical glass and 200 mm Fused Silica glass, for 10 mJ pulses and 5 cm beam diameter. Initial pulse of 40 ps was compressed to 200 fs and the B-integral value is estimated to be below 0.82. Various configurations of compressors with the evaluations of B-integrals will be presented in the poster presentation.

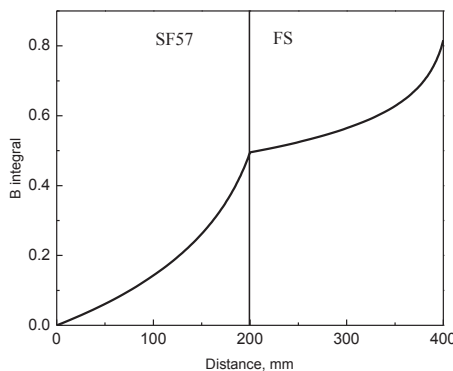


Fig. 1. Accumulated B-integral over the length of the system

[1] G. Mourou, T. Tajima, and S. V. Bulanov, "Optics in the relativistic regime," *Rev. Mod. Phys.*, vol. 78, pp. 309–371, 2006.

[2] M. D. Perry, T. Ditmire, B. C. Stuart, Self-phase modulation in chirped-pulse amplification, *Optics letters* Vol. 19, No.24 (1994).

GROUP-DELAY MEASUREMENT OF CHIRPED MIRRORS USING WHITE-LIGHT INTERFEROMETRY

Rimantė Jarockytė¹, Ignas Balčiūnas¹, Šarūnas Straigis¹, Rimantas Budriūnas¹, Arūnas Varanavičius¹

¹ Department of Quantum Electronics, Faculty of Physics, Vilnius University, Lithuania
rimante.jarockyte@ff.stud.vu.lt

It is necessary to know the dispersion characteristics of optical components in laser systems in order to obtain bandwidth-limited femtosecond pulses. To compensate the normal dispersion in femtosecond laser systems chirped mirrors are usually used. Those chirped mirrors have multilayer dielectric coatings, which modulate the phase of the reflected pulse [1]. Production of such mirrors is a complicated technological process, consequently the produced mirrors have different characteristics from designed ones. The aim of this project is to create an interferometer system to measure the dispersal characteristics of those chirped mirrors.

White light interferometry is one of the simplest ways to measure the dispersion of different materials [2]. In this project we used a Michelson interferometer and a broadband white light continuum source pumped by Q-switched microlaser. The whole optical setup is presented in Fig. 1(a).

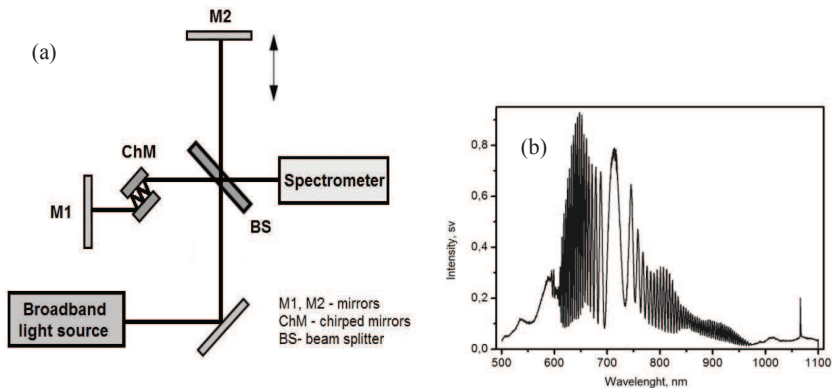


Fig. 1. (a) The Michelson interferometer used for measurements;

(b) Spectrum of interference.

The laser beam is divided by a $3\mu\text{m}$ thickness beam splitter (BS). One of the beams is transmitted through the beam splitter and reflected at the mirror M2, which is placed on a motorized delay line.

The second beam goes through the pair of chirped mirrors and is reflected 4-8 times from each mirror, depending on the angle of incidence. Afterwards, the beam is reflected at mirror M1 and comes back to the beam splitter. Beams from different arms of the interferometer are combined and sent to the spectrometer, where the interference spectrogram is measured (see Fig. 1(b)).

In a spectrogram, the zero order interference fringe is observed. The motion of the delay line changes the position of the zero order interference fringe. Identifying how the central wavelength λ_c of the zero order interference fringe depends on the induced delay leads to finding the group delay dispersion [3].

In this project, the characteristics of two types of chirped mirrors with negative and positive group delay dispersion were measured and compared with the data provided by the manufacturer.

[1] R. Szpöcs, C. Spielmann, F. Krausz, and K. Ferencz, Chirped multilayer coatings for broadband dispersion control in femtosecond lasers, *Optics Letters*, **19**, 201-203 (1994).

[2] Scott Diddams, Jean-Claude Diels, Dispersion measurements with white-light interferometry, *Journal of the Optical Society of America B* 1996, **13**, 1120-1129.

[3] P. Hlubina, White-light spectral interferometry with the uncompensated Michelson interferometer and the group refractive index dispersion in fused silica, *Optics Communications* 2001, **193**, 1-7.

BREWSTER'S ANGLE GRISM-PAIR STRETCHER MODEL FOR FEMTOSECOND PULSE OPCPA SYSTEM

Dainius Kučinskas¹, Rimantas Budriūnas¹, Arūnas Varanavičius¹

¹Department of Quantum Electronics, Faculty of Physics, Vilnius University, Sauletekio Ave. 9, Vilnius LT-10222, Lithuania
dainius.kucinskas@ff.stud.vu.lt

In optical parametric chirped-pulse amplification (OPCPA) systems, high power pulses with bandwidth-limited durations are desired [1]. To compensate the dispersion of the optical system, we use a grism-pair stretcher, composed of two pairs of prisms and reflective diffraction gratings [2]. This kind of stretcher is noted for its flexible control of dispersion and compactness, which is important, as minimising the length of air a pulse must travel through reduces the disturbances in its path, keeping the pulse phase more stable. Because a laser beam's path through a grism stretcher involves many refractions and reflections, efficiency becomes an essential issue.

We used computer ray tracing software, developed in our lab, to model grisms with desired and flexible dispersion characteristics as well as acceptable efficiency. In describing the phase characteristics of the stretcher, the spectral phase Taylor expansion coefficient values are used, primarily group delay dispersion (GDD) and third order dispersion (TOD). To compensate our system's dispersion and work well in tandem with the AOPDF, the target parameters of the grisms are -100000 fs^2 GDD and 0.6 fs TOD/GDD for the central wavelength of the 700-900nm bandwidth. In the model, SF10 glass and 600 grooves/mm gratings were used. The calculated efficiency coefficient of $\eta=0.56$ is quite acceptable, as the laser beam refracts 16 times and reflects off of the gratings 4 times during its traversal of the grisms. To attain the maximum efficiency, the refractions all happen very close to the Brewster's angle, which, to the best of our knowledge, has never been achieved before in a grism stretcher.

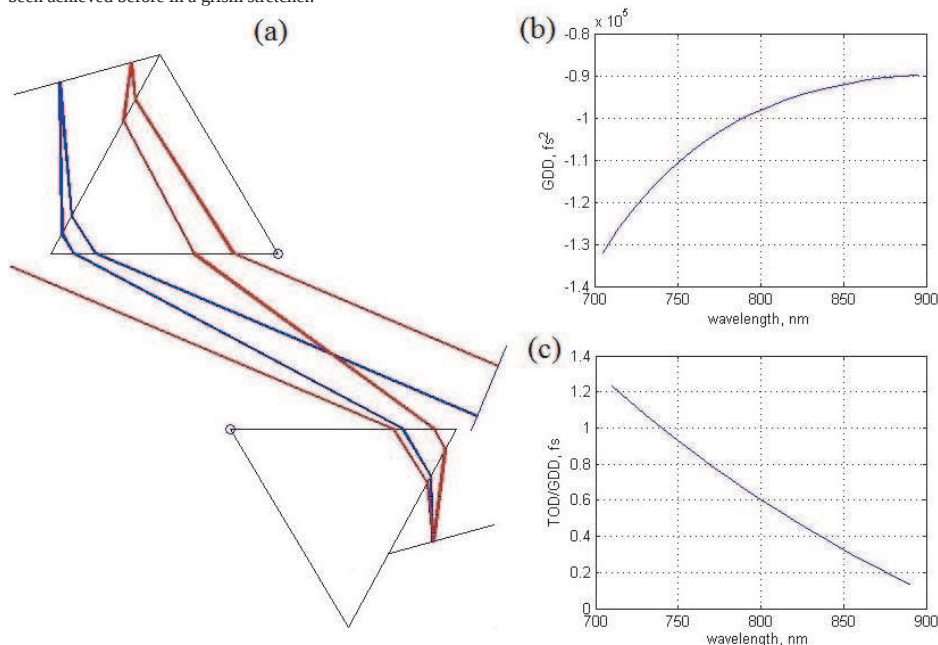


Fig. 1 (a) scheme of the grism configuration and paths of 700-900nm wavelengths. **(b)** GDD dependency of wavelength. **(c)** TOD/GDD dependency on wavelength.

[1] A. Piskarskas, A. Dubietis ir G. Jonušauskas, Optics Communications, 1992, 88, 433-400.

[2] J. Squier ir S. Kane, Journal of the Optical Society of America B, 1997, 14, 661-665.

Open Readings 2014. 57th Scientific Conference for Students of Physics and Natural Sciences

DEVELOPMENT OF BEAM-POINTING REGISTRATION AND STABILIZATION SYSTEM

Šarūnas Straigis, Linas Karpavičius, Arūnas Varanavičius, Tomas Stanislauskas

Faculty of Physics, Vilnius University, Lithuania
sarunas.straigis@gmail.com

One of the most rapidly growing branches of modern physics is ultrashort light pulse generation, amplification, control, detection and application. It granted possibilities for scientists to observe and control microscopic processes in nuclear, plasma, solid state electronics and high energy density physics. Experiments require high stability of the light beam, which is often interfered by vibrations, temperature, moving air, experimentator and etc.

Our scientific group is developing high energy ultrashort pulse generating laser system NAGLIS at VU Laser research center. In order to apply such system in strong electromagnetic field experiments, optical beam will be focused in area smaller than few tens of microns. Thus the accuracy of beam position must also be within this range – round $\pm(5-10)$ microns. For this reason, we are developing beam position tracking and correcting system.

System has few fundamental parts (Fig. 1): position sensitive device (PSD) generating currents (for x and y positions) proportional to intensivity of beam, analog signal to digital converter (ADC), microcontroller unit (MCU) controlling and gathering data from PSD and sending it to personal computer (PC). PC makes data available for experimentator, calculates amount, length and direction of steps which motors have to take and gives orders to driver controlling motors. There are four motors, one pair per mirror for x and y position control.

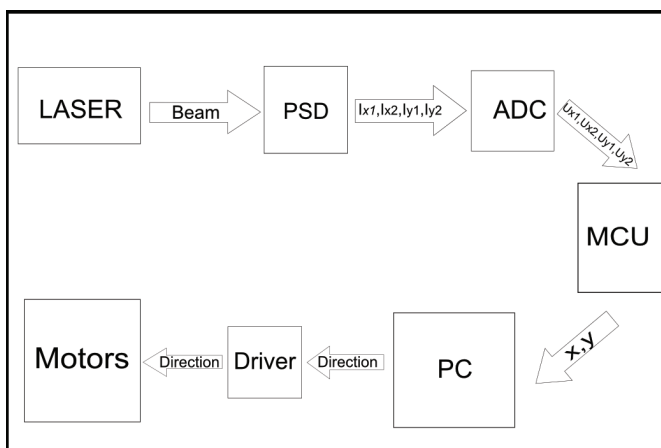


Fig. 1. Positioning and stabilization block scheme

Similar stabilization system was presented in Japan in 2005. It was able to increase stability of beam focus from $\sim 70 \mu\text{rad}$ (without stabilization) to less than $10 \mu\text{rad}$ (with active stabilization). Such results can only be achieved by high resolution mechanical devices, low noise and high speed electronic devices. Piesomotors that will be used in our system will have $<30\text{nm}$ resolution.

The hardest part to implement is electronical (PSD-ADC in Fig. 1.) because of high precision, speed and size requirements. It is difficult to delay photocurrents in order to digitalize them with 16-18 bits resolution when working with ultrashort pulses. This system must also not influence other beam properties and it may be a problem because of high energy of the beam. Programming of MCU and PC software is also needed. We have developed program on MCU to read data from ADC and send it to PC. PC software is programmed with Labview (National Instruments) because of its capability of working with different devices, in our case – MCU and piesomotors driver.

[1] M. Mori, A. Pirozhkov, M. Nishiuchi, K. Ogura, A. Sagisaka, Y. Hayashi, S. Orimo, A. Fukumi, Z. Li, M. Kado, and H. Daido, Development of Beam-Pointing Stabilizer on a 10-TW Ti:Al₂O₃ Laser System JLITE-X for Laser-Excited Ion Accelerator Research (Japan, September 25, 2005).

[2] Robert A. Hardin,* Yun Liu, Cary Long, Alexander Aleksandrov, and Willem Blokland. Active beam position stabilization of pulsed lasers for long-distance ion profile diagnostics at the Spallation Neutron Source (SNS)(Oak Ridge National Laboratory, Oak Ridge, Tennessee 37831 USA).

COMPARATIVE CHARACTERIZATION OF THE PROPERTIES OF ELECTROMAGNETIC WAVES IN UNIAXIAL CRYSTALS AND HYPERBOLIC METAMATERIALS

Vladislav Popov¹

¹Department of Theoretical Physics and Astrophysics, Belarusian State University, Belarus

physics.vlad@gmail.com

In many articles the problem of the reflection and transmission of a plane electromagnetic wave from a uniaxial crystal is solved using a specific system of coordinates. This system of coordinates (the system of the principal axes) is chosen to present the permittivity tensor ϵ in the diagonal form as

$$\epsilon = \begin{pmatrix} \epsilon_o & 0 & 0 \\ 0 & \epsilon_o & 0 \\ 0 & 0 & \epsilon_e \end{pmatrix}.$$

In spite of the system of the principal axes ensures the simplest form of all relations in a transparent uniaxial crystal ($\epsilon_o > 0, \epsilon_e > 0$)., it is completely uncomfortable when one solves the general problem of the reflection of plane electromagnetic waves from a uniaxial crystal with arbitrarily oriented optical axis. Since the expressions in any coordinate system are cumbersome, it was developed the invariant (covariant) approach by F.I. Fedorov [1].

The main aim of the work is the application of invariant methods to hyperbolic metamaterials (HMM) for describing propagation of plane electromagnetic waves. We calculate such characteristics as transmission and reflection coefficients and etc. then we compare the results obtained for uniaxial crystals and HMM.

We consider a plane electromagnetic wave incident onto the interface between vacuum and HMM. For the case of the interface between the vacuum and uniaxial crystal we can use the well-known invariant solution [1]. The quantities ϵ_o and ϵ_e for HMMs are complex numbers which real parts have opposite signs ($\text{Re}(\epsilon_o)\text{Re}(\epsilon_e) < 0$). Then the solution for uniaxial crystals [1] is applicable for HMM as well.

In general, there are four solutions of the wave equation for plane waves (forward and backward ordinary and extraordinary waves). Physically justified solutions correspond to the waves leaving the interface, i.e. meeting condition $(\mathbf{S}\mathbf{q}) > 0$, where \mathbf{S} is the Poynting vector, \mathbf{q} is the vector orthogonal to the interface and directed from vacuum to HMM. It should be noted that wave vector \mathbf{k} can be directed towards the interface ($(\mathbf{k}\mathbf{q}) < 0$). The similar effect is well-known as negative refraction.

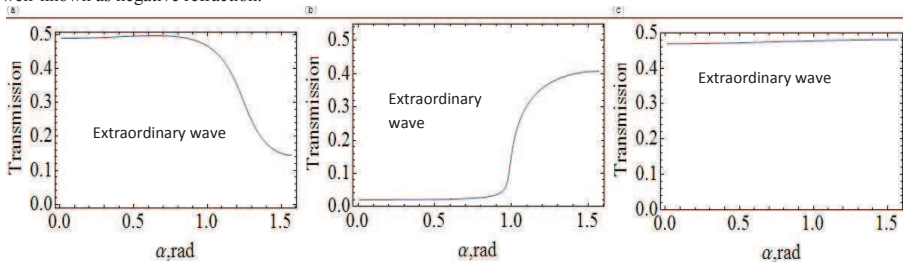


Fig. 1. Transmission coefficients vs. angle α between optical axis and vector \mathbf{q} for (a) HMM ($\epsilon_o = 0.57 + i 0.13, \epsilon_e = -4.22 + i2.03$), HMM ($\epsilon_o = -2.78 + i 0.13, \epsilon_e = 6.31 + i0.09$) [2], uniaxial crystal ($\epsilon_o = 2.75, \epsilon_e = 2.21$).

In Fig. 1 the transmission coefficients for extraordinary waves in HMMs and uniaxial crystals are shown. The abrupt change of the transmission for HMMs can be explained by the great difference of the diagonal permittivities $\epsilon_o - \epsilon_e$. For the normal uniaxial crystal difference and the transmission change are small (Fig. 1(c)).

In conclusion, HMM supply new avenues for manipulation of light, opening the door for such unusual applications as high-resolution imaging and etc. [2]. The advantages of the invariant method are as follows: its results can be applied for arbitrary case of the orientation of the optical axis and arbitrary angle of incidence of a plane wave on a surface of a crystal or HMM.

[1] F.I. Fedorov, *Optics of anisotropic media* (Publication Academy of Sciences of BSSR, Minsk, 1958).

[2] Vladimir P. Drachev, Viktor A. Podolskiy, Alexander V Kildishev, Hyperbolic metamaterials: new physics behind a classical problem. *Opt. Express* **21**, 15048-15064 (2013).

WOODPILE PHOTONIC CRYSTALS FOR FLAT LENSING IN VISIBLE RANGE

Darius Gailevičius¹, Lina Maigyte², Vytautas Purlys¹, Jose Trull², Martynas Peckus¹, Crina Cojocaru², Mangirdas Malinauskas¹, Kestutis Staliunas^{2,3}

¹Laser Research Center, Department of Quantum Electronics, Vilnius University, Lithuania

²Departament de Física i Enginyeria Nuclear, Universitat Politècnica de Catalunya, Spain

³Institució Catalana de Recerca i Estudis Avançats (ICREA), Spain

darius.gailevicius@ff.stud.vu.lt

Spatial periodic modulation of the refractive index on a wavelength scale in photonic crystals (PhCs), provides control of both temporal and spatial dispersion properties of light waves, in the latter case offering the possibility to manipulate the spatial propagation of the light beams. PhCs of particular geometries may provide anomalous spatial dispersion for a beam propagating inside the structure that can lead to the so called flat PhC lensing [1] effect.

The concept of flat PhC lensing is based on the transforming the phases of the different spatial spectrum field components. The convex-curved phase-shifts of field components accumulated during the propagation inside the PhC can be compensated by usual concave-curved phase-shifts during propagation in the homogeneous material, both in front and behind the PhC, resulting in focusing behind the PhCs.

Such focusing has been experimentally shown only for microwaves [2] and for sound waves [3]. Moreover even the 1D focusing/imaging by PhC slabs was demonstrated only in the near infrared frequency range [4]. Here full two-dimensional (2D) focusing by a polymer based three-dimensional (3D) woodpile PhC is demonstrated.

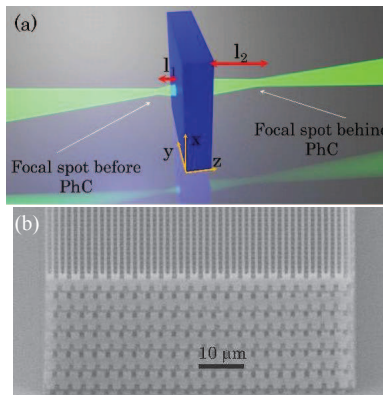


Fig. 1. (a) flat PhC lensing scheme [1], (b) a SEM image of the PhC – 45 deg oblique view [1].

PhC samples were fabricated in hybrid organic inorganic sol-gel photopolymer by direct laser writing technique. The PhC parameters used in FDTD calculations and experiments were the same: transverse period $d_x = 0.9 \mu\text{m}$, longitudinal period $d_z = 6 \mu\text{m}$, (filling factor 70%), transverse dimension $80 \mu\text{m}$, and length of the crystal $L \sim 30 \mu\text{m}$ (5 longitudinal periods).

[1] L. Maigyte, V. Purlys, J. Trull, M. Peckus, C. Cojocaru, D. Gailevičius, M. Malinauskas, and K. Staliunas, Flat lensing in the visible frequency range by woodpile photonic crystals, *Opt. Lett.* **38**, pp. 2376-2378 (2013).

[2] Z. Lu, J. A. Murakowski, C. A. Shuetz, S. Shi, G. J. Schneider, and D. W. Prather, Three-Dimensional Subwavelength Imaging by a Photonic-Crystal Flat Lens Using Negative Refraction at Microwave Frequencies, *Phys. Rev. Lett.* **95**, 153901 (2005).

[3] A. Cebrecos, V. Romero-Garcia, R. Pico, I. Perez-Arjona, V. Espinosa, V. J. Sanchez-Morcillo, and K. Staliunas, Formation of collimated sound beams by three-dimensional sonic crystals, *J. Appl. Phys.* **111**, 104910 (2012).

[4] E. Schonburn, T. Yamashita, W. Park, and C. J. Summers, Negative-index imaging by an index-matched photonic crystal slab, *Phys. Rev. B* **73**, 195117 (2006).

LASER POLYMERIZATION OF MULTI-COMPONENT SCAFFOLDS

Dovilė Mackevičiūtė, Sima Rekšytė, Mangirdas Malinauskas

Department of Quantum Electronics, Vilnius University, Saulėtekio Ave. 9, Vilnius LT-10222, Lithuania
 dovile.mackeviciute@ff.stud.vu.lt

Multi-photon laser polymerization is an attractive direct laser writing (DLW) technique for micro-/ nanostructuring. This method allows fabrication of complex 2D and 3D objects with sub-diffraction resolution. A tightly focused ultrafast pulsed laser beam induces photopolymerization in the volume of the photosensitive material. By translating the sample, the position of the focal spot is changed, thus point-by-point structures can be written inside the material [1]. Promising applications have already been demonstrated in microoptics, microfluidics, photonics and biomedicine.

Laser polymerization can be applied for production of artificial scaffolds on which cells could controllably grow and form tissues required in tissue engineering and regenerative medicine [2]. To achieve this, it is important to mimic the composition and structure of the natural tissues. Chemical and geometrical properties of the scaffolds play an important role in regulating cell migration, proliferation and differentiation. Laser polymerization opens a way to produce structures with desired geometry, pore size or porosity from a variety of different materials [3]. Such composite constructions provide not one but several desired biological spatially located features including biostability, biocompatibility or biodegradation.

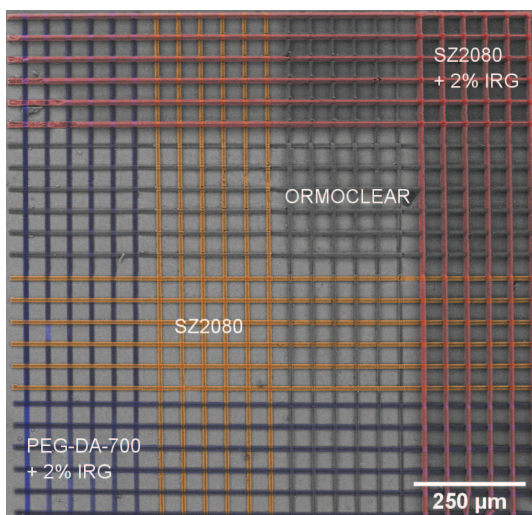


Fig. 1. Multi-component microstructured scaffold fabricated out of SZ2080 + 2% IRG, OrmoClear, SZ2080 without photoinitiator and PEG-DA-700 + 2% IRG. Structure size is 1.2x1.2 mm², pore size is 40 μm.

In this work we demonstrate the capability to fabricate microstructured multi-component scaffolds consisting out of four polymeric materials: organic-inorganic hybrids OrmoClear, SZ2080 non-sensitized and photosensitized with 2% 2-benzyl-2-(dimethylamino)-4'-morpholinobutyrophenone (IRG) and biodegradable PEG-DA-700 + 2% IRG (Fig. 1).

- [1] M. Malinauskas, V. Purlys, A. Žukauskas et al., Laser two-photon polymerization micro- and nanostructuring over a large area on various substrates, Proc. SPIE **7715**, 77157F-1 (2010).
- [2] V. Melissinaki, A.A. Gill, I. Ortega et al., Direct laser writing of 3D scaffolds for neural tissue engineering applications, Biofabrication **3**, 045005 (2011).
- [3] P. Danilevičius, S. Rekšytė, E. Balčiūnas et al., Direct laser fabrication of polymeric implants for cardiovascular surgery, Mater. Sci. **18**(2), 145-149 (2012).

FABRICATION OF POLYLACTIC ACID MICROSTRUCTURED SCAFFOLDS VIA 3D PRINTING

Laurynas Lukoševičius, Mangirdas Malinauskas

Department of Quantum Electronics, Vilnius University, Saulėtekio Ave. 9, Vilnius LT-10222, Lithuania
laurynaslu@yahoo.com

A thermal extrusion „Ultimaker Original“ 3D printer (Fig. 1) – a simple, low-cost tabletop device enabling rapid materialization of CAD models in plastics – was used to produce scaffolds (Fig. 2A) with a microstructures out of polylactic acid (PLA). Features that distinguish PLA: biocompatibility, biodegradability, non-toxicity[1].

The direct laser writing (DLW) with femtosecond laser beam was used to modify the 3D printed (3DP) PLA surfaces (Fig. 2B,C). Different structure geometry on macro- to micro- scales could be finely tuned by combining these fabrication techniques for the reason that cells growth depends on the surface[2].

Such artificial 3D scaffolds could be used for cell growth or as biodegradable implants in tissue engineering. Investigation of cell proliferation and tissue formation on such artificial scaffolds (in vitro) and their implantation (in vivo) experiments are currently in progress[3].

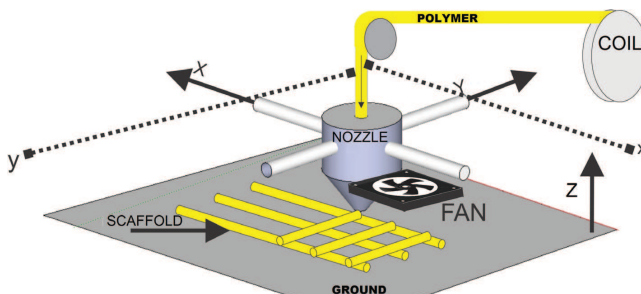


Fig. 1. Three-dimensional printer.

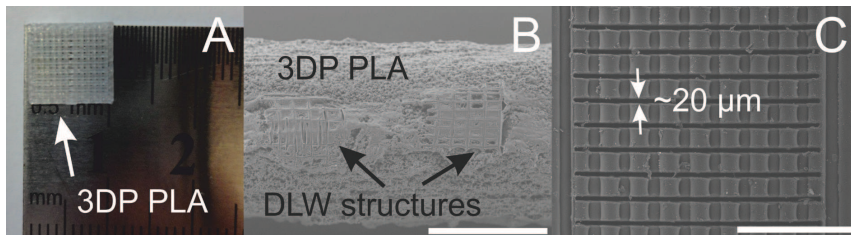


Fig. 2. 3DP microstructured objects: A – a 3DP woodpile scaffold of $1 \times 1 \times 0.1 \text{ cm}^3$; B – DLW μ -grating structures on a log of 3DP woodpile structure as in A; C – 3D printed vertically wavy structures and horizontally ablated lines. Scale bars in B and C - $500 \text{ }\mu\text{m}$.

-
- [1] D.E. Henton, P. Gruber, J. Lunt and J. Randall "Polylactic Acid Technology", 429 (2005).
 - [2] L. Xiao, B. Wang, G. Yang, M. Gauthier, Poly(Lactic Acid)-Based Biomaterials: Synthesis, Modification and Applications, InTech (2012).
 - [3] E. Balčiūnas, L. Lukoševičius, D. Mackevičiūtė, S. Rėkštytė, V. Rutkūnas, D. Paipulas, K. Stankevičiūtė, D. Baltriukienė, V. Bukelskienė, A. P. Piskarskas and M. Malinauskas, "Combination of thermal extrusion printing and ultrafast laser fabrication for the manufacturing of 3D composite scaffolds", Proc. SPIE., in press (2014).

STABILITY OF PHOTOREFRACTIVE MODIFICATIONS IN LITHIUM NIOBATE CRYSTALS INDUCED BY FEMTOSECOND LASER PULSES

Aušra Čerkauskaitė, Domas Paipulas

Laser Research Centre, Vilnius University
ausra.cerkauskaite@ff.stud.vu.lt

Lithium niobate (LiNbO_3) is a very promising material used for various optical applications due to its strong piezoelectric and ferroelectric effect. This nonlinear crystal also has its photorefractive properties which means that it is possible to selectively change material's refractive index using intense radiation. In a way, the photoinduced change of refractive index is reversible and may be optically erased or manipulated without any changes in crystal lattice. [1] Photorefractive effect leads LiNbO_3 to state-of-the-art applications, for example real-time holographic data storage, volume holographic memories, rewritable holographic data storage systems [2].

Although this effect is known for decades [3], the photorefractive modifications recorded in LiNbO_3 crystal by femtosecond pulses have not been understood completely. For this reason, the main goal of this research was to induce such dynamic modifications in the volume of the doped with iron (0.05 %) lithium niobate ($\text{LiNbO}_3:\text{Fe}$) crystal by illumination with near infrared wavelength (1030 nm), 300 fs pulse duration laser radiation and to examine the stability of induced information.

It is shown in this work that using various writing / erasing parameters information can be selectively modified without destroying remaining information. To be more precise, in the volume of the used nonlinear crystal photorefractive modifications are recorded perpendicular to the c axis of the crystal and they are erased moving laser beam along the c axis. Fig. 1. presents the surface view of the crystal. This photorefractive modifications writing method might be used as rewritable data storage.

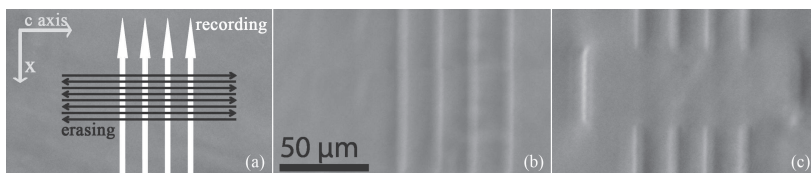


Fig. 1. (a) Principle scheme of selective erasing. (b) Modifications in the volume of $\text{LiNbO}_3:\text{Fe}$ are recorded perpendicular to the c axis and (c) erased along the c axis.

-
- [1] Buse K. , Light-induced charge transport processes in photorefractive crystals I: Models and experimental methods, Appl. Phys. B, **64**, 273-291 (1997).
 - [2] P. Gunter, J.-P. Huignard *Photorefractive Materials and Their Application 2* (Springer, Germany, 2007).
 - [3] A. Ashkin, Optically-induced refractive index inhomogeneities in LiNbO_3 and LiTaO_3 , Appl. Phys. Lett. **9**(1), 72–74 (1965).

INTEGRATION OF FRESNEL ZONE PLATES IN THE BULK OF SAPPHIRE CRYSTAL BY FEMTOSECOND LASER PULSES

Audrius Puišys¹, Domas Paipulas¹

¹ Laser Research Center, Department of Quantum Electronics, Vilnius University, Saulėtekio Ave. 10, LT-10223

Vilnius, Lithuania

audrius.puysys@ff.stud.vu.lt

Sapphire due to its excellent mechanical and optical properties is widely used in optoelectronic and microelectronic applications. Besides its wide use in high power laser optics, sapphire gained interest as a good substrate for gallium nitride (GaN) growing in light emitting diode (LED) technologies. Unfortunately, because of its hardness and chemical stability, it is difficult to apply traditional machining methods and tools to sapphire crystal, especially when precise machining is needed. However, ultrafast lasers become a promising tool for micromachining all sorts of materials, including sapphire. Cutting and micropatterning of sapphire surface is extensively studied nowadays [1]. Moreover, with femtosecond laser machining it is possible to integrate various photonic devices directly into the bulk of transparent materials [2]. This technology was successfully demonstrated in a wide variety of glasses; however, the integration capabilities into sapphire are not well documented. It is known that focused femtosecond laser pulses can modify sapphire properties [3], but this result is still waiting to be exploited.

In this work we attempted to integrate Fresnel zone plates with diameters up to 300 μm in the volume of sapphire crystal by direct laser writing technique. Plate consists of series of concentric rings (zones) with periodically altered light transmission properties. The working principle of a zone plate relies on the diffraction of light, i. e. the incident monochromatic light is diffracted by the periodically alternating zones and, depending on the dimensions of the zones, constructively interferes at a designed focal point (see Figure 1). These zone plates are intended to be integrated directly into GaN LED substrate: due to the fact that sapphire can transmit UV wavelengths, the ability of a zone plate to focus this type of radiation and the fact that the largest volume of sapphire production is expected to be for substrates for high brightness LED devices [4], it would be advantageous to employ sapphire not only as a substrate but also as a medium for integration of zone plates which could potentially increase the efficiency of UV LED devices.

For integration tasks we used femtosecond (300 fs) high repetition rate (100 kHz) Yb:KGW laser pulses together with high precision linear positioning stages. By exposing sapphire to focused femtosecond laser radiation, regions of modified refractive index were induced and required zone plates were patterned. The discussions about optimal fabrication parameters and patterning algorithms as well as focusing properties of fabricated zone plates are presented in this study.

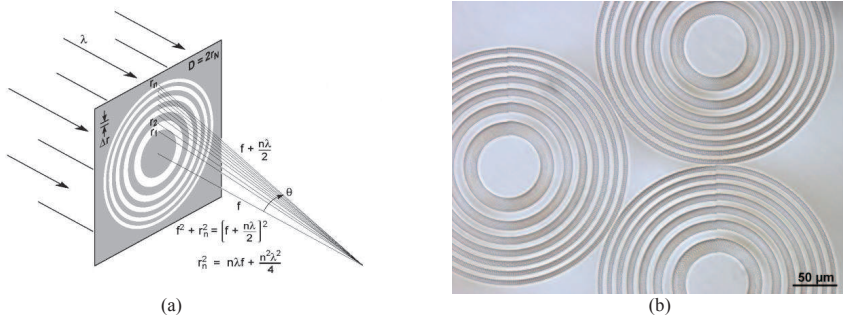


Figure 1. (a) The basics behind the working principle of a zone plate [5]. (b) Zone plates fabricated in the bulk of sapphire crystal by means of direct laser writing.

[1] C.-W. Chang et al., Sapphire surface patterning using femtosecond laser micromachining, *Appl. Phys. A* **109** (2), 441–448 (2012).

[2] K. M. Davis et al., Writing waveguides in glass with a femtosecond laser, *Opt. Lett.* **21** (21), 1729–1731, (1996).

[3] S. Juodkazis et al., Control over the crystalline state of sapphire, *Adv. Mater.* **18** (11), 1361+ (2006).

[4] M. S. Akselrod and F. J. Bruni, Modern trends in crystal growth and new applications of sapphire, *J. Cryst. Growth* **360**, 134–145, (2012).

[5] D. T. Attwood, *Extreme Ultraviolet Radiation: Principles and Applications* (Cambridge Univ. Press, Cambridge, 1999).

ANALYSIS OF SCRIBING SAPPHIRE SUBSTRATES

Jonas Berzinš, Mindaugas Gedvilas, Gediminas Račiukaitis

Center for Physical Sciences and Technology, Savanoriu Ave. 231, LT-10227, Vilnius, Lithuania
jonasberzins@gmail.com

Sapphire Al_2O_3 wafers are usually used as wafers in manufacturing of light emitting diodes (LEDs). Properties such as high thermal conductivity, transparency in a wide range of wavelengths and crystallographic similarity to GaN makes it the best substrate for epitaxial growth of GaN. Scribing these wafers into small LED chips is essential in the manufacture. Several scribing methods, included laser fabrication, are being analyzed.

One step is the growth of semiconductor materials on the surface of the substrate, during this step there is necessity of the similarity between the structures. The hexagonal structure of GaN demands same or similar structure as well. Despite that it would be ideal to use the same material as the substrate, its' high cost and difficulty of production makes it not applicable. That is why we need alternative substrates and many including based on Si were invented, however neither are as good as made of synthesized sapphire. The deviation between the crystallographic structures is approximately 13 %, high transparency gives the possibility to transfer the light through the wafer.

Other step is the scribing of the wafer which leads to thousands of LEDs in the size of few hundred micrometers and importance of this is not lesser. Industrial applications utilize diamond blade or ablation by nanosecond laser [1]. Their low efficiency led researchers to development of new method – stealth dicing (Fig. 1).

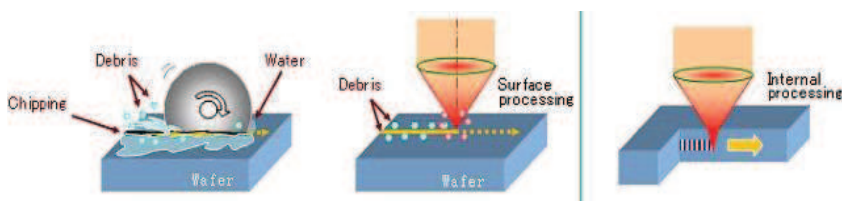


Fig. 1. The comparison of sapphire scribing methods: dicing with a diamond disc, scribing by using laser ablation and stealth dicing.

The experiments were carried out by using picosecond laser and simple diamond blade for the comparison. It was proved that the stealth dicing by using picosecond laser is the most effective method, while diamond disc dicing and ablation was not as accurate as crack width was bigger and additional debris occurred.

[1] M. Kumagai, IEEE Trans. Semicond. Manuf. 20(3), 259-265 (2007).

LASER DICING OF CERAMICS SUBSTRATES

Jonas Berzinš

Center for Physical Sciences and Technology, Savanoriu Ave. 231, LT-10227, Vilnius, Lithuania
jonasberzins@gmail.com

Ceramics such as alumina are widely used as substrates or components for electric applications. Due wide range of applications these ceramics need to be manufactured in different shapes and sizes. Laser technologies may give the precision and be efficient enough.

During this experimental work ceramics were diced by using nanosecond laser Baltic HP (Ekspla) irradiation at 532 nm wavelength. Laser beam positioned by galvanometer scanner (ScanLab). The task was to get the highest possible cutting speed so the highest pulse energy of 360 uJ was selected. The method of dicing ceramics is so called scribe & break method as the samples are not scribed through their whole thickness and even though the mechanical breaking is needed it is the most efficient method.

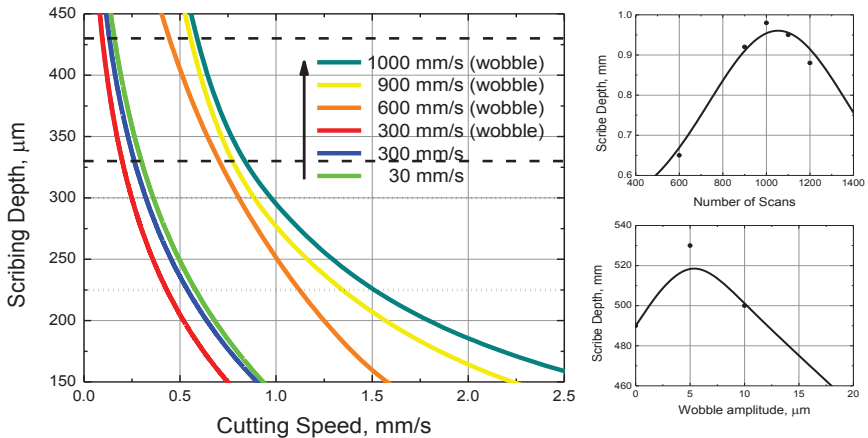


Fig. 1. Scribing depth as a function of cutting speed while varying the scanning speed (left), acceptable regions for breakage are bounded by dash lines for 1 mm and dot lines for 0.635 mm thick samples. Scribing depth as a function of number of scans and as a function of wobble parameter (right).

The achieved dicing results point that the wobble option adds only slight but still an increase in the scribing depth. The best wobble parameters were considered to be 1.5 kHz at repetition rate and 5 μm at amplitude. While it is understandable that by increasing scanning speed we widen the distance between pulses, it was proved that to assure a good break we need a distance lesser than the width of a single pulse. As we see in figure, for a sample of 1 mm thickness we need a scribe of 330-430 μm and that may be achieved by the scanning speed as high as 1000 mm/s, according to this the obtained cutting speed would vary from 0.6 to 0.85 mm/s, the thinner sample of 0.635 mm thick required only 200-300 μm to break, so the cutting speed was progressively bigger.

NANOSECOND LASER DRILLING OF SODA-LIME GLASS

Juozas Dudutis, Paulius Gečys

Center for Physical Sciences and Technology, Savanoriu ave. 231, LT-02300, Vilnius, Lithuania

juozas.dudutis@gmail.com

Various glasses act as important engineering materials for different applications. The quality and efficiency of processing these materials are becoming crucial. Conventional methods of drilling or cutting glass by using diamond tools cannot ensure the increased requirements of manufacturers.

Over the last years many laser processing technologies have been patented and it is an emerging scientific and industrial trend. Short-pulse laser machining of glass offers a non-contact method, high accuracy, localized material removal, reduced thermal effects and cracks formation [1]. The laser and transparent materials interaction strongly depends on laser pulse duration. High intensity laser radiation is absorbed in the bulk of transparent materials by optical breakdown via multiphoton or avalanche ionization [2, 3].

In this work we carried out the series of experiments of helical drilling in silicate glass. In these experiments helical drilling was initiated from the back side of the glass plate. Initially laser beam was focused between the positioning stage and the sample back surface and the focal position was being moved in the volume of glass towards the front surface by constant speed.

Glass drilling experiments were carried out by using the fundamental harmonic of nanosecond Q-switched diode pumped solid state Nd:YVO₄ laser (Baltic HP, 1064 nm, 13.3 W, 10-20 ns, 10-100 kHz, from Ekspla). The laser beam was positioned in the XY plane by the galvanometer scanner (SCANgine 14, ScanLab) and focused by the f-theta lens with the focal length of 80 mm. Samples were positioned in the vertical axis by moving stage with a stepper motor (8MT167-100, Standa). The galvanometer scanner, laser and positioning stage were synchronized to start and finish the drilling process at the same time.

Arrays of holes were drilled in the soda-lime glass plate with the thickness of 4 mm. The quality of drilled holes was evaluated by an optical microscope. The zone of glass chips and surface cracks were measured for a number of holes drilled by different sets of parameters. Scanning speed in the XY plane, spiral scanning amplitude and frequency, laser power, repetition rate and vertical speed were changed while carrying out experiments. The regimes with the maximum processing speed were found for various laser power and pulse energy (Fig. 1).

The quality of drilled holes depended on laser power, the overlap of laser pulses and vertical speed. It was possible to drill a hole of 1 mm diameter in the 4 mm thick soda-lime glass plate per 1.2 s but the high quality holes required longer processing time. The quality was higher at the rear side of the processed glass surface.

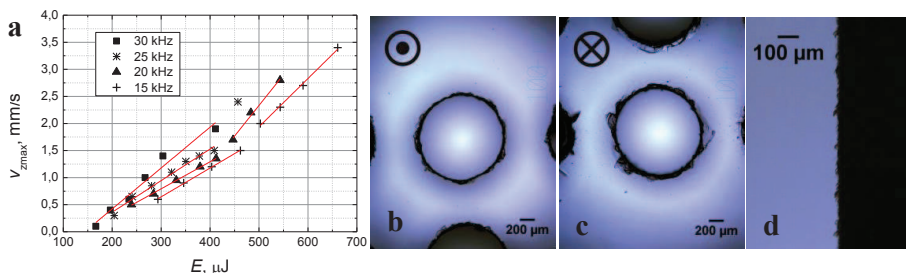


Fig. 1. Maximum possible vertical speed for different laser pulse energy (a). Optical microscope images of a drilled hole in the 4 mm thick glass plate: rear (b) and front (c) surface (13.2 W, 50 kHz, 0.6 mm/s vertical speed), profile (d)

In conclusion, 1064 nm nanosecond laser radiation is suitable for rapid and efficient helical drilling in soda-lime glass, initiating the process from the backside and moving the focal position towards the front surface of the glass plate. Drilling debris is effectively removed through the drilled channel and does not scatter the laser radiation so we keep the constant density of laser power and it is possible to drill high aspect ratio holes with high perpendicularity of walls.

[1] S. Nikumb, Q. Chen, C. Li, H. Reshef, H. Y. Zheng, H. Qiu, and D. Low, Precision glass machining, drilling and profile cutting by short pulse lasers, *Thin Solid Films*, **477**(1-2), 216-221 (2005)

[2] M. R. Kasaai, V. Kacham, F. Theberge, and S. L. Chin, The interaction of femtosecond and nanosecond laser pulses with the surface of glass, *J. Non. Cryst. Solids*, **319**(1-2), 129-135 (2003)

[3] P. Baling and J Schou, Femtosecond-laser ablation dynamics of dielectrics: basics and applications for thin films, *Rep. Prog. Phys.*, **76**(3), p. 036502 (2013)

RIPPLE FORMATION ON STAINLESS STEEL BY PICOSECOND LASER IRRADIATION

Antanas Vinčiūnas, Paulius Gečys

Center for Physical Sciences and Technology, Laser Technology Department, Lithuania
antanas.vinciunas@ftmc.lt

Laser induced periodic surfaces structures (LIPSS), also called ripples, have been observed on metallic surfaces at laser fluencies close to material ablation threshold. Ripple formation is attributed to the interference between the incident laser and the surface scattered light field. The periods of surface ripples are usually close to the laser wavelength λ [1, 2].

Ripples change optical properties of a metal surface and therefore they can be applied to blacken the metals to achieve better light absorption, as well as they show a huge potential in solar energy and sensitive optical elements [3].

The formation of ripples depends on material properties as well as experimental parameters such as laser wavelength, pulse duration, pulse energy, overlap of the pulses, polarization etc.

In this work ripples were formed on a stainless steel surface using fiber laser (pulse duration 15 ps, pulse repetition rate 2 MHz) operating at 532 nm wavelength and samples were analyzed using scanning electron microscope (SEM). Optimal experimental conditions for ripple formation were found and the influence of experimental parameters on ripple morphology was studied.

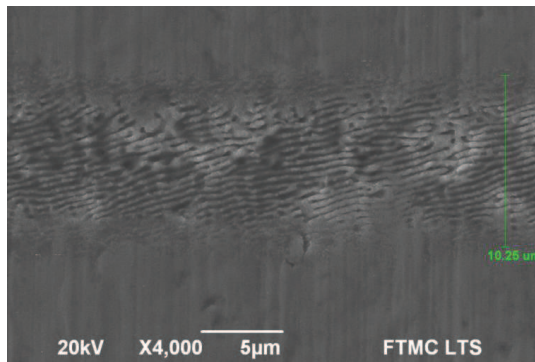


Fig. 1. SEM image of ripple structures on stainless steel plate. Laser power 360 mW, pulse repetition rate 2 MHz, scanning speed 100 mm/s.

-
- [1] S. Hou, Y. Hou, P. Xiong et al., Formation of long- and short-periodic nanoripples on stainless steel irradiated by femtosecond laser, *J. Phys. D: Appl. Phys.* **44**, 505401 (2011).
- [2] J. P. Colombier, F. Garrelie, N. Faure et al., Effects of electron-phonon coupling and electron diffusion on ripples growth on ultrafast-laser-irradiated metals, *J. Appl. Phys.* **111**, 024902 (2012).
- [3] A. Y. Vorobyev and C. L. Guo, Effects of nanostructure-covered femtosecond laser-induced periodic surface structures on optical absorbance of metals, *Appl. Phys. A* **86**, 321–324 (2007).

SPATIAL LIGHT MODULATOR AS A BEAM SHAPER IN THIN GOLD FILM REMOVAL

Antanas Vinčiūnas^{1,2}, Jan Düsing²

¹ Center for Physical Sciences and Technology, Lithuania

² Laser Zentrum Hannover, Germany

antanas.vinciunas@ftmc.lt

Spatial light modulator (SLM) is a general term describing devices that are used to modulate amplitude, phase, or polarization of light waves in space and time. Current SLM systems are based on either optical MEMS (microelectromechanical system) or LCD (liquid crystal displays) technology [1].

High spatial resolution, direct programmability, easy integration and low cost of liquid crystal (LC) SLMs make them invaluable tool in many different optical applications, such as optical tweezers, optical data processing, beam steering and shaping, optical communications, adaptive optics, real-time holography, micromachining etc. [2–4]. In these applications SLM is used as a programmable diffractive optical element (DOE).

During our experiments HoloEye LC2002 SLM was used as a phase modulating spatial beam shaper. The modified Young's interferometer setup was used for the calibration of the SLM and iterative Gerchberg-Saxton algorithm was chosen to calculate computer generated holograms, which were further converted to grayscale images using calibration curve and displayed on the SLM screen to produce desired intensity distributions in the image plane of the lens.

The addition of small-angle prism phase to original computer generated hologram was employed to separate desired intensity distribution from the 0th order beam and time-averaging technique, which employs an array of 10 different alternating holograms of the same desired intensity distribution, was shown to be successful to average speckle-dependent inhomogeneities in the removal of thin gold films giving relatively good reproducibility.

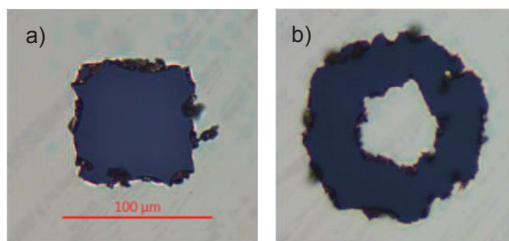


Fig. 1. Removal of gold-on-glass films of 100 nm thickness using a) top-hat (fluence 0.29 J/cm²) and b) ring (fluence 0.16 J/cm²) shaped beams. Laser wavelength 515 nm, pulse duration 600 fs, pulse repetition rate 10 kHz.

[1] V. Bagnoud and J.D. Zuegel, Independent phase and amplitude control of a laser beam by use of a single-phase-only spatial light modulator, *Opt. Lett.* **29**, 295-297 (2004).

[2] A.L. Gaunt and Z. Hadzibabic, Robust Digital Holography For Ultracold Atom Trapping, *Sci. Rep.* **2**, 721 (2012).

[3] R.J. Beck, J.P. Parry et al., Application of cooled spatial light modulator for high power nanosecond laser micromachining, *Opt. Express* **18**(16), 17059-17065 (2010).

[4] E. Buckley, Computer-Generated Phase-Only Holograms for Real-Time Image Display, *Advanced Holography - Metrology and Imaging* (InTech, 2011).

MICRO-FIGURES CUTTING IN MOLYBDENUM FOIL USING A FEMTOSECOND PULSE LASER

Tomas Puodžiūnas¹, Lina Mažulė¹, Ignas Reklaitis², Domas Paipulas¹, Valdas Sirutkaitis¹, Rolandas Tomašiūnas²

¹Laser Research Center, Vilnius University, Sauletekio ave. 10, LT-10223 Vilnius, Lithuania

²Institute of Applied Research, Vilnius University, Sauletekio ave. 10, LT-10223 Vilnius, Lithuania
puodziunas.tomas@gmail.com

Femtosecond lasers provide us the ability to process materials with great precision. Because of the short pulse duration we can get smoother and cleaner side walls compared to picosecond and nanosecond lasers [1]. These advantages can be used for laser processing in semiconductor technology particularly for the fabrication of mask for ohmic contacts.

Molybdenum is used in semiconductor technology for its high melting point and one of the lowest coefficients of thermal expansion among commercially used metals. These qualities lead Mo to be the best choice for this particular technology. [2]

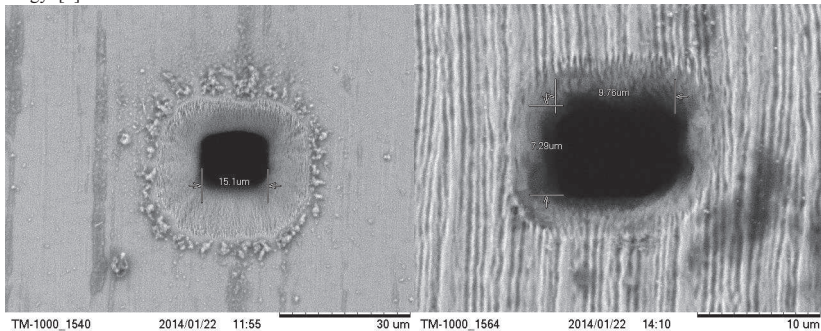


Fig. 1. Figures cut with different techniques and different parameters. Left image was operated using 0.02 W energy, 25kHz repetition rate and cutting speed of 1mm/s. Right one uses same options but different cutting technique – material ablation before cutting the particular figure.

We present experimental results on micro-fabricated figures in a Molybdenum foil using 280 fs pulse high repetition rate Yb:KGW laser (central wavelength 1030 nm). The aspheric lens ($F=4.03$ mm and $NA=0.62$) was used to focus the laser beam on the molybdenum foil surface. The beam diameter on the surface of the foil was $1.7\text{ }\mu\text{m}$. The optimal micro-fabrication parameters (the speed of the cutting, pulse energy and repetition rate) were evaluated for cutting of square and circle figures in $30\text{ }\mu\text{m}$ thickness Molybdenum foil. The squares and circles with sub- $10\times 10\text{ }\mu\text{m}$ size were fabricated.

[1] R. Moser, M. Kunzer, C. Gößler, *Laser processing of GaN-based LEDs with ultraviolet picosecond laser pulses* (Laser Sources and Applications, Proc. of SPIE Vol. 8433, 2012).

[2] X. Zhu, A.Yu. Naumov, D.M. Villeneuve, P.B. Corkum, *Influence of laser parameters and material properties on micro drilling with femtosecond laser pulses* (Appl. Phys. A 69 [Suppl.], S367–S371 (1999)).

SILICON DIOXIDE THIN FILMS PREPARED BY REACTIVE MAGNETRON SPUTTERING FROM BORON DOPED SILICON TARGET

Andrius Subačius, Kęstutis Juškevičius, Ramutis Drazdys

State scientific research institute Center for Physical Sciences and Technology Savanoriu ave. 231, LT-02300 Vilnius, Lithuania

subacius.andrius@gmail.com

In industry of optical coatings silicon dioxide (SiO_2) is commonly used as low refractive index material [1, 2]. Reactive magnetron sputtering technique was used for preparing SiO_2 thin films. Since pure silicon is insulating material it can only be sputtered using radio frequency (RF) power supply. The main goal was to sputter silicon using direct current (DC) power supply, since plasma created by DC power supply is denser and concentrated closer to target [3]. That lets to avoid plasmas interaction with substrates, increases deposition rate [4]. For those reasons conducting boron doped silicon target was used.

SiO_2 coatings were deposited on fused silica substrates by reactive magnetron sputtering. In basic magnetron sputtering process a target is bombarded by energetic ions generated in glow discharge plasma. The bombardment process causes the removal of target atoms, which then condense on a substrate as a thin film.

Single layers of SiO_2 were deposited using different process parameters such as oxygen flow and target voltage. Fig 1. shows target voltage dependence on oxygen flow. Different setpoint values were chosen for depositing SiO_2 layers. Optical properties (refractive index n and extinction coefficient k) were determined from transmittance spectra which was performed in 190-1000 nm wavelength range. Surface roughness of thin films were measured using atomic force microscope (AFM). All optical and physical properties of SiO_2 layers prepared by DC reactive magnetron sputtering were compared to SiO_2 layers prepared by RF reactive magnetron sputtering.

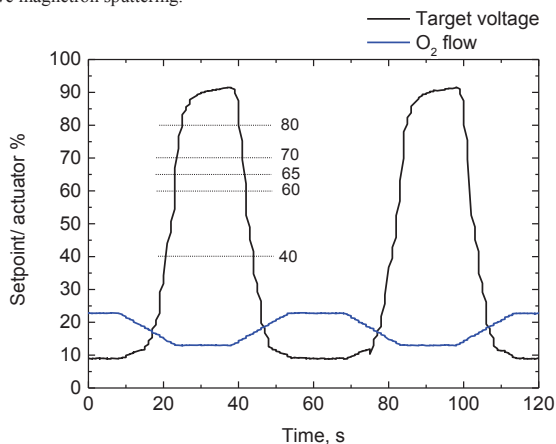


Fig 1. Target voltage as a function of oxygen flow. Dashed lines represent setpoint values at which experiments were performed.

1. Y.-z. Wang, J.-d. Shao, J.-b. Huang, Y.-x. Jin, H.-b. He, K. Yi, and Z.-x. Fan, "Design of different bandwidth dispersive mirrors," *Optik - International Journal for Light and Electron Optics* **122**, 2065-2070 (2011).
2. L. Lan, Y. Fang, X. Lin, J. Chen, D. Li, and G. Feng, "Identifying contributions of individual layers constituting multilayer dielectric mirrors," *Optics & Laser Technology* **37**, 211-216 (2005).
3. M. F. Dony, A. Ricard, J. P. Dauchot, M. Hecq, and M. Wautelet, "Optical diagnostics of d.c. and r.f. argon magnetron discharges," *Surface and Coatings Technology* **74–75, Part 1**, 479-484 (1995).
4. D. Depla, and R. De Gryse, "Target voltage measurements during DC sputtering of silver in a nitrogen/argon plasma," *Vacuum* **69**, 529-536 (2003).

Open Readings 2014. 57th Scientific Conference for Students of Physics and Natural Sciences
SYNTHESIS OF NANOCOMPOSITE FILMS BASED ON METALLIC NANOPARTICLES

Alena Mikitchuk, Konstantin Kozadaev

Department of Radiophysics and Computer Technologies, Belarusian State University, Belarus
helenay@yandex.by

Nanocomposite materials based on dielectrics containing metal nanoparticles formed by a random arrangement of inclusions in a matrix could be employed in the design of frequency-selective materials or EM absorbers with dimensions much smaller than those of conventional ones [1]. Laser ablation in liquids provides the new synthesis technique for the metallic nanoparticles, which can be employed in nanocomposite production by liquid deposition [2]. The nanocomposite synthesis procedure are investigated with the aim of microwave absorbers production.

The aqueous colloidal solution of Co nanoparticles is prepared using Nd:YAG laser ablation setup from chemically homogeneous massive plate of cobalt [3]. The synthesis is performed under the laser wavelength of 1.06 μm , pulse duration of 20 ns, pulse repetition rate was 5 Hz and an average energy of 200 mJ. The optimal power density on the spot is found to be $\sim 1 \text{ GW/cm}^2$. Typical exposure time for the preparation of optically dense samples of metal colloids is chosen to be 10 min for one sample with the water volume of 120 ml. It important to note, that ablation process occurs in the air followed by nanoparticles sedimentation into the water. The samples of nanoparticles are studied by the transmission electron microscopy and characteristic radiation. Fig. 1 *a* shows the characteristic radiation spectrum, which correspond to metallic cobalt. The nanocomposite films are prepared by the deposition of the solution of the nanoparticles in the polymer matrix. At the final stage the nanocomposite contains polyvinyl alcohol matrix and cobalt nanoparticles.

The microwave performance of the obtained nanocomposite samples is investigated with vector network analyzer in the frequency range of 8 – 12 GHz. Fig. 1 *b* shows the insertion loss of the 0.5 mm and 2 mm thickness samples of nanocomposite. One can see the the spectrally flat insertion loss of the nanocomposites on amount of 4–12 dB. This fact allows us to consider synthesized Co nanocomposite as microwave absorbers.

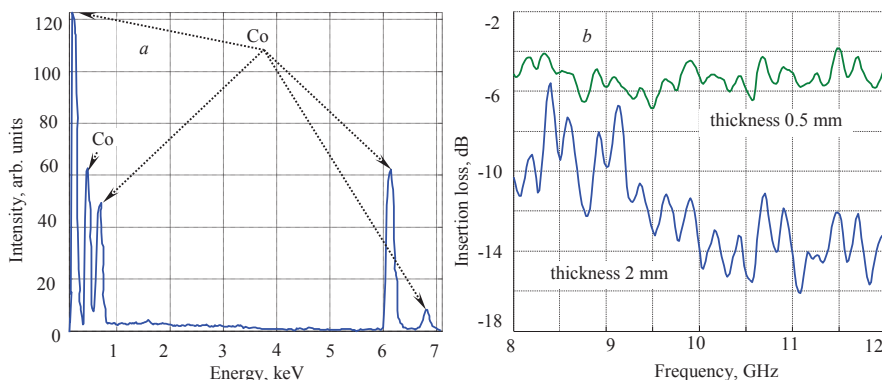


Fig. 1. Characterization of the nanocomposites: *a* – the characteristic radiation spectrum, *b* – the insertion loss of the nanocomposite in the microwave frequency range versus frequency for the different sample thickness.

An advantage of the proposed nanocomposite synthesis procedure is simplicity of the of the production of the microwave absorbers. The developed technique can be used in the microwave shielding production in the specified frequency range.

The further investigations will be performed in the direction obtaining the frequency-selective microwave absorbing nanocomposite material.

[1] S. Celozzi, R. Araneo, G. Lovat, *Electromagnetic shielding* (IEEE Publishing, New York, 2008).

[2] V.K. Goncharov, K.V. Kozadaev, D.V. Shehegrikovich, Investigation of noble metals colloidal systems formed by laser synthesis at air, *Advances in Optical Technologies*, **2012**, 907292, (2012)

[3] V.K. Goncharov, K.V. Kozadaev, M.I. Kunitskii, M.V. Puzyrev, Laser probing of optical media with nanodimensional particles, *Journal of engineering physics and thermophysics*, **78** (6), 1171-1174 (2005).

QUADRUPOLEAR INTERACTION IN SOLID-STATE NMR SPECTROSCOPY

Laurynas Dagys

Department of General Physics and Spectroscopy, Vilnius University, Lithuania
dagys.laurynas@gmail.com

Over 70% of all nuclei in the Periodic Table have a spin quantum number greater than one half ($I \geq 1$). Therefore their quadrupolar moment interacts with electric field gradient. And unlike in liquid-state, in solid-state NMR spectroscopy chemical shift anisotropy, dipole-dipole coupling and quadrupolar interactions are not averaged by rapid molecular tumbling. The last mentioned interaction is denoted by the spin Hamiltonian for the full electric quadrupolar interaction of the spin I :

$$\hat{H}_Q^{full} = \frac{eQ}{2I(2I-1)\hbar} \hat{I} \hat{V} \hat{I}; \quad (1)$$

where tensor V is electric field gradient and Q is quadrupolar moment [1]. If quadrupolar interaction is considerable compared to Zeeman effect, standard perturbation theory is used. Depending on interaction strength first-order ($H_Q^{(1)}$) and if needed second-order ($H_Q^{(2)}$) expansion terms are considered.

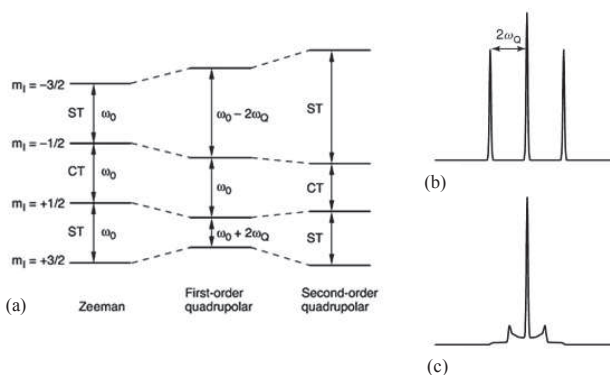


Fig. 1 Perturbation of the spin $I = 3/2$ Zeeman energy levels by the quadrupolar coupling to first- and second-order approximations. (b) Simulations of the resulting (single-crystal) NMR spectra. (c) Corresponding powder NMR spectra. [2]

$H_Q^{(1)}$ term splits the central line into $2I-1$ satellite lines but the central line remains at Larmor frequency ω_0 [2]. Second-order term shifts all of the lines, including the central line, but this effect is observed only with strong quadrupolar interactions [2]. These effects make the interpretation of spectra more difficult. First-order term is proportional to second-order Legendre polynomial which itself can be evaluated to zero by picking angle of 54.7° , where it is angle with polarizing field B_0 allowing to average $H_Q^{(1)}$ term to zero. This method is called Magic Angle Spinning and is commonly used in solid-state NMR spectroscopy, however it does not eliminate second-order $H_Q^{(2)}$ expansion term, because it is equivalent to fourth-order Legendre polynomial. Although there are methods to average this term such as Double Rotation (DOR), it is uncommon since second-order perturbation usually has insignificant effect in NMR spectra.

[1] Malcolm H. Levitt, Spin Dynamics: basics of nuclear magnetic resonance, John Wiley & Sons, pg 206-209, 614-615 (2008).

[2] Roderick E. Wasylishen, Sharon E. Ashbrook, Stephen Wimperis, NMR of quadrupolar nuclei in solid materials, A John Wiley and Sons, pg 1-15, 48-50 (2011)

Open Readings 2014. 57th Scientific Conference for Students of Physics and Natural Sciences

NMR PARAMETERS OF ALANINE DIPEPTIDE STUDIED BY MEANS OF QUANTUM CHEMISTRY METHODS

Dovilė Lengvinaitė, Kęstutis Aidas

Dept. of General Physics and Spectroscopy, Faculty of Physics, Vilnius University, Lithuania
dovile.lengvinaitė@ff.stud.vu.lt

Nuclear magnetic resonance spectroscopy (NMR) is a widely used method which provides detailed information about the chemical bonding, molecular structure and dynamics. NMR spectroscopy is widely applied to study proteins and nucleic acids. Oxygen is a common chemical element in nature, however, ^{17}O NMR spectroscopy is rarely applied because this isotope has very low natural abundance. It was observed that using density functional theory (DFT) and dielectric continuum (DC) methods, the ^{17}O NMR shielding constant is sensitive to both the structure of the peptide [1] and interactions with the aqueous environment [2]. The ^{17}O NMR shielding constant of alanine dipeptide (Fig. 1) is potentially a appropriate probe of its structure and intermolecular interactions.

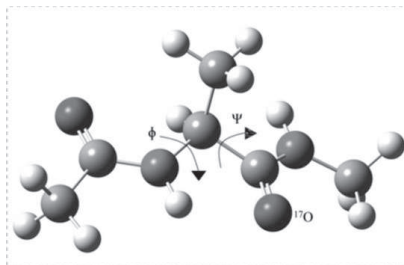


Fig. 1. Alanine dipeptide

In this work, the NMR parameters of alanine dipeptide were investigated by means of quantum chemical methods. The alanine dipeptide has been extensively used to study the structure of proteins. The main reason resides in the fact that alanine dipeptide is able to model almost all known amino acid conformations commonly found in proteins. Conformers of the alanine dipeptide are fully characterized by the Ramachandran angles ϕ and ψ [3]. Nine conformers were modeled in vacuum and aqueous solution.

Another important NMR parameter of the alanine dipeptide is the $^3J(\text{H}(\alpha)\text{-HN})$ spin-spin coupling constant which can provide information about the molecular geometry. Our modeling shows that the spin-spin coupling constant is not sensitive to the solvent, yet this constant is sensitive to conformation of the structure.

We have also applied the combined quantum mechanics/molecular mechanics (QM/MM) methods to calculate the NMR observables. In these calculations, the hydrogen bonding between alanine dipeptide and water molecules has been treated explicitly. The ^{17}O NMR shielding constant varies slightly due to influence of the solvent for the three most stable conformers PPII, $\alpha(\text{R})$ and C5 in aqueous solution. We have concluded that ^{17}O NMR conformational analysis is not suitable for alanine dipeptide, however, it can be expected that ^{17}O NMR can provide important information about the protein structure.

[1] F. Mocci, *Torsion angle relationship of the ^{17}O NMR chemical shift in α, β -unsaturated carbonyl compounds*, Magn. Reson. Chem. **2009**, 47, 862-867.

[2] K. Aidas, A. Mogelhoj, H. Kjær, C. B. Nielsen, K. V. Mikkelsen, K. Ruud, O. Christiansen, J. Kongsted, *Solvent effects on NMR isotropic constants. A comparison between explicit polarizable discrete and continuum approaches*, J. Phys. Chem. A **2007**, 111, 4199-4210.

[3] F.F. Garcia-Prieto, I. F. Galvan, M. A. Aguilar, M. E. Martin, *Study on the conformational equilibrium of the alanine dipeptide in water solution by using the averaged solvent electrostatic potential from molecular dynamics methodology*, J. Phys. Chem. **2011**, 135, 194502.

WITHDRAWED CONTRIBUTION

CARBON ISOTOPE RATIO MEASUREMENTS IN THE REACTOR GRAPHITE USING ISOTOPE RATIO MASS SPECTROMETRY

Mantas Garliauskas^{1,2}, Konstantinas Zakalskis¹, Andrius Garbaras², Arūnas Gudelis², Grigorijus Duškesas²

¹Faculty of Physics, Vilnius University, Lithuania

²Institute of Physics, Center for Physical Sciences and Technology, Lithuania
garliauskas.mantas@gmail.com

Graphite is an important material used to moderate neutrons in nuclear reactors. It is evaluated that about 250,000 tons of spent graphite are already accumulated in still operating or being decommissioned nuclear reactors. In spite that nuclear graphite is a very pure material, it still contains some impurities of various elements. These impurities and carbon are activated by neutrons resulting in long-lived elements (e.g., ^{14}C , ^{36}Cl , transuranium elements). Therefore it is very important to know the radionuclide composition of the material in order to safely manage nuclear waste [1].

The aim of this work is to find optimal preparation of the sample and conditions at which precise carbon isotope ratio could be measured.

All carbon isotope data are reported in the delta notation $\delta^{13}\text{C}$ or differences from the given standards, expressed in parts per thousand (‰) and are calculated according to the formula:

$$\delta^{13}\text{C} = \left(\frac{\left(\frac{^{13}\text{C}}{^{12}\text{C}} \right)_{\text{sample}}}{\left(\frac{^{13}\text{C}}{^{12}\text{C}} \right)_{\text{standard}}} - 1 \right) \times 1000 \text{ ‰} \quad (1)$$

Samples from Poland of virgin graphite (not irradiated) have been shredded into small and flat particles. Measurements of the carbon isotopic composition of graphite have been made with the Elemental Analyzer (FlashEA 1112) connected to a stable isotope ratio mass spectrometer (ThermoFinnigan Delta Plus Advantage). Carbon analysis has been performed after sample combustion in an oxidation furnace at the temperature of 900 K with the oxygen excess.

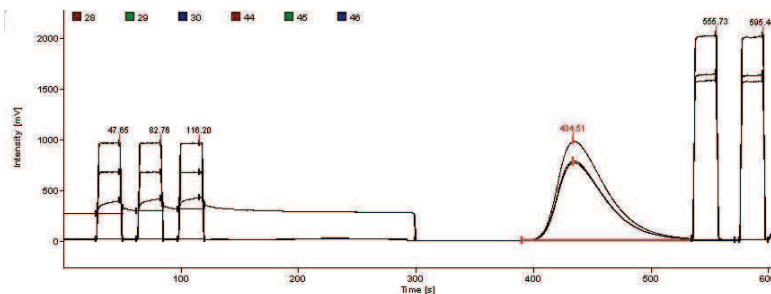


Fig. 1. Spectrum of the graphite sample

As seen in Fig. 1, the curve of measured graphite sample intensity over time (starts at 400th second) is asymmetric. It indicates that some of graphite was left unburned in the combustion oven. That was common for most samples. Therefore, samples must be well shredded for precise results. It was found that all burns that are left in the combustion oven are enriched with ^{13}C isotope and affects $\delta^{13}\text{C}$ value of the next measurement. Quantity of unburned graphite only depends on the properties of the sample (size of shredded particles) [2].

Measured $\delta^{13}\text{C}$ values varied from -18.99 ‰ to -22 ‰ for virgin graphite and from -25.03 ‰ to -28.54 ‰ for irradiated graphite from Ignalina RBMK reactor. $\delta^{13}\text{C}$ values of irradiated graphite give possibility to estimate the neutron flux in the certain points of the graphite stack.

[1] V. Remeikis, A. Plukis, R. Plukienė, A. Garbaras, R. Barisevičiūtė, A. Gudelis, R. Gvozdaite, G. Duškesas, L. Juodis, Method based on isotope ratio mass spectrometry for evaluation of carbon activation in the reactor graphite // Nuclear engineering and design. ISSN 0029-5493. Vol. 240, iss. 10 (2010), p. 2697-2703.

[2] Konstantinas Zakalskis, Reaktorius grafito anglies izotopų santykio matavimai masių spektrometrijos metodu (Bachelor thesis, Vilnius, 2012).

Investigating elastic stresses in solid solutions GeSi based Raman spectroscopy

Nikita Yavkin

Department of physical informatics and atomic and molecular physics, Belarusian State University, Minsk, Belarus
Nikita.yavkin92@yandex.ru

Solid solutions of semiconductors are of interest as a system with smoothly varying properties as materials that can be run with predetermined physical parameters. From this perspective, of particular interest are systems GeSi. However, the lattice constant of Ge and Si materials differ by about 4% , so the solid solutions GeSi appear fitted elastic stresses that significantly affect the band structure of the charge carriers and phonon spectra . In this paper we investigate features of the phonon spectra in solid solutions GeSi and estimates the changes of the lattice parameters.

One of the methods of structural analysis , allowing the study of the phonon spectra and their changes is Raman spectroscopy (RS) . For studies used single-crystal samples of solid solutions Ge_{1-x}Si_x (x = 0-0,06) c resistivity 1 Om.sm.

Figure 1 shows the dependence of the intensity of cattle (α) wave number (λ) solid solutions Ge_{1-x}Si_x, due to local vibrational mode due Ge-Ge and Ge-Si. With increasing silicon content is clearly visible associated with changes in the values of shear deformation peaks local Ge-Ge vibrations in the region of small wave numbers (Fig.2).

Changing the unit cell volume Ge easily estimated by using the ratio Gruneisen (v_0 / v) = (v / v_0) γ , where v_0 - under volume of the unit cell of silicon , v - volume of the unit cell of silicon in solid solution , v_0 - optical-phonon frequency in bulk unstrained material , v - optical-phonon frequency of the same material in the solid solution , γ - Gruneisen parameter .

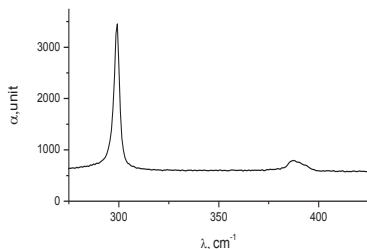


Fig. 2. Raman spectra of the first order for solid solutions Ge_{1-x}Si_x (x = 0.06).

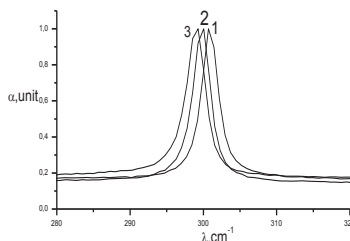


Fig. 2. Raman spectra of the first order for solid solutions Ge_{1-x}Si_x with different silicon content x: 1-0; 2-0,031; 3-0,06.

From the experimental results determined that the lattice constant of the solid solution Ge_{1-0,06}Si_{0,06} 0.17% greater than the lattice constant of pure germanium.

Thus, from the analysis of the results shows that the silicon due to its smaller covalent radius leads to stretching of the germanium lattice in solid solution GeSi.

INFLUENCE OF SILICON AND GERMANIUM SUBSTITUTES ON STRUCTURAL PARAMETERS OF CYCLOPENTANE

Domantas Ozerenskis, Valdemaras Aleksa

Department of Physics, Vilnius University, Lithuania
d.ozerenskis@gmail.com

Five-membered rings have been of interest to structural physicist and chemist because they may have any one of the three different stable conformers, i.e., planar, twisted and envelope forms, or possibly more than one of these forms [1]. Also, when one of the CH_2 groups in cyclopentane is replaced by a SiH_2 , GeH_2 , O, NH, etc., the potential barrier between the cyclopentane conformational forms is so small for some of these molecules that the ring motion can be described as pseudo rotation, which is nearly barrier-free for cyclopentane [2]. So, it is important to investigate structural parameters of substituted cyclic organic compounds.

In this work the Raman spectrum and the polarized Raman spectrum (Fig. 1) of liquid 1,1,3,3-tetrachlor-1,3-disilacyclopentane have been recorded. Additionally, geometry optimization, Raman activities, depolarization ratios and scaled vibrational wavenumbers have been determined from *ab initio* calculations and compared with experimental values when available. It was determined that anharmonic calculations are more accurate than harmonic. Finally, the ring torsional angles in cyclopentane are increasing when Si or Ge substitutes are added. This difference causes the cyclopentane ring to be much “flatter” than the disilacyclopentane ring.

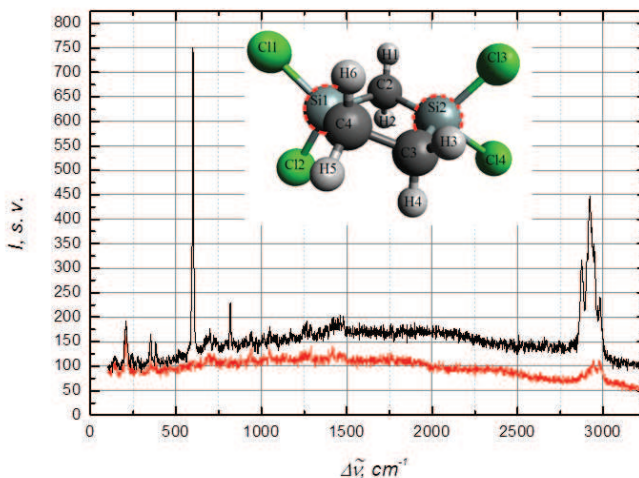


Fig 1. Polarized Raman spectrum of 1,1,3,3-tetrachlor-1,3-disilacyclopentane

Acknowledgements:

This work was supported by the Lithuanian Science Council research Grant MIP-071/2013.

- [1] G. A. Guirgis, A. M. El Defrawy, T. K. Gounev, M. S. Soliman, and J. R. Durig, “Conformational stability, r0 structural parameters, ab initio calculations, and vibrational assignment for germacyclopentane,” *J. Mol. Struct.*, vol. 834–836, pp. 17–29, 2007.
- [2] C. Zheng, M. R. Yazdi, V. F. Kalasinsky, and J. R. Durig, “Vibrational spectra, conformational stability, structural parameters and ab initio calculations of 2,2,5,5-tetramethyl-2,5-disila-1-oxacyclopentane,” *J. Raman Spectrosc.*, vol. 37, no. 1–3, pp. 52–67, 2006.

RING FLATTERING IN SIX-MEMBERED ORGANIC COMPOUNDS: RAMAN SPECTROSCOPY AND *AB INITIO* INVESTIGATIONS

Domantas Ozerenskis, Valdemaras Aleksa

Department of Physics, Vilnius University, Lithuania
d.ozerenskis@gmail.com

The stereochemistry of cyclohexane has been thoroughly studied for a long time, and substituted cyclohexanes were among the first examples of molecules exhibiting conformational equilibria [1]. If a carbon atom in cyclohexane is substituted with a silicon atom, a silacyclohexane is formed and the steric and electronic effects are changed. The silacyclohexanes are more unstable than the corresponding cyclohexanes and less experimental information is available. Therefore, *ab initio* calculations were made using MP2 method.

Raman spectra of liquid germacyclohexane and liquid 2,2-dimethyl-1,2-oxasilinane was recorded and depolarization data obtained. MP2 calculations were made and structural parameters were obtained. Germacyclohexane, germacyclopentane and cyclohexane structural parameters comparison is shown in Table 1. It was determined, that cyclohexane, substituted with Si or Ge, exist in a modified chair form in which the ring is more flattened than cyclohexane in the region of substitute and is more puckered in the opposite part of the ring. In 2,2-dimethyl-1,2-oxasilinane the ring is even more flattened than germacyclohexane because of two methyls groups added to substituted atom.

Structural parameter	Germacyclohexane	Germacyclopentane [2]	Cyclohexane
$r_{\text{Ge-C}_{2,6}}$	1,968	1,969	1,529
$r_{\text{Ge-H}_{1,2}}$	1,541	1,524	1,099
$r_{\text{C}_2\text{-H}_{3,4}}$	1,097	1,095	1,099
$\angle \text{H}_1\text{GeH}_2$	108,9	109,0	106,6
$\angle \text{C}_2\text{GeC}_6$	102,9	93,2	111,2
$\tau_{\text{C}_1\text{C}_2\text{GeC}_6}$	43,9	-	55,6
$\tau_{\text{C}_2\text{C}_3\text{C}_4\text{C}_5}$	68,5	-	55,6
$\tau_{\text{GeC}_2\text{C}_3\text{C}_4}$	56,5	-	55,6

Table 1. Structural parameters (Å and degree) of various substituted cyclohexane. τ – stands for torsional angle.

Acknowledgements:

This work was supported by the Lithuanian Science Council research Grant MIP-071/2013.

-
- [1] G. A. Guirgis, C. J. Nielsen, A. Horn, V. Aleksa, and P. Klæboe, "Infrared and Raman spectra, DFT-calculations and spectral assignments of silacyclohexane," *J. Mol. Struct.*, vol. 1023, pp. 189–196, Sep. 2012.
- [2] G. A. Guirgis, A. M. El Defrawy, T. K. Gounev, M. S. Soliman, and J. R. Durig, "Conformational stability, r_0 structural parameters, *ab initio* calculations, and vibrational assignment for germacyclopentane," *J. Mol. Struct.*, vol. 834–836, pp. 17–29, 2007.

USING RAMAN SPECTROSCOPY METHOD

Giedrius Babrauskas¹, Ilja Ignatjev², Valdemaras Aleksa¹

¹Vilnius University, Faculty of Physics, Department of General Physic and Spectroscopy,
Sauletekio av. 9 – 3, LT – 10222 Vilnius, Lithuania

² Institute of Biochemistry, Mokslininkų 12, LT-08662, Vilnius, Lithuania
giedrius.babrauskas@ff.stud.vu.lt

Vibrational spectroscopy method is a very useful tool to investigate pigments used on artworks [1]. In this study four samples of the painting were investigated by Raman spectroscopy method, because microchemical analysis did not give any answer to the question about the chemical structure of the pigments, which are on different sample layers. Micro-probed Raman spectra of the different layers of the samples were obtained by using Renishaw „InVia“ Raman microscope through 20x objective of a „Leica microscope“. The Raman spectra were excited by a 785.0 nm wavelength solid state laser with backscattering geometry. The laser power was 5 mW and integration time was 200 s. The Raman bands (Fig. 1.) of the pigment spectra were assigned using Raman spectra libraries [2, 3]. The pigments identified in this work are cinnabar, orpiment and red ochre.

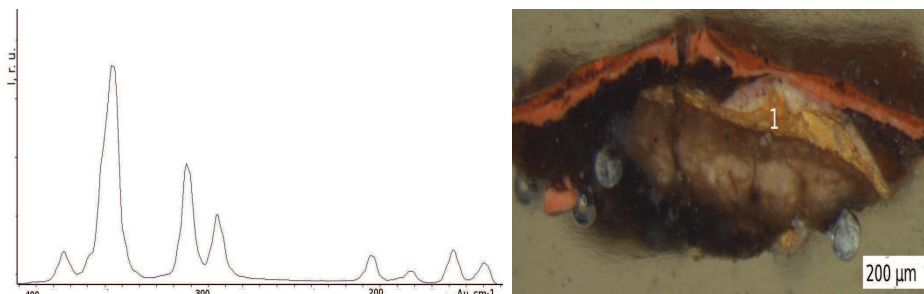


Fig.1. Raman spectrum of the yellow layer of sample 1. Image of layer cross section on the right.

Investigation revealed that the yellow layer of sample 1 is orpiment (Fig. 1.) and the red layer is cinnabar. The red layer from sample 2 is red ochre.

Acknowledgements. We thank prof. G. Niaura (Institute of Chemistry, Vilnius) for the opportunity to use the experimental equipment.

[1] Robin J. H. Clark, *Raman Microscopy in the Identification of Pigments on Manuscripts and Other Artwork*, 2005, 162 – 163.

[2] <http://www.chem.ucl.ac.uk/resources/raman/>

[3] <http://www.fis.unipr.it/phevix/ramandb.html>

APPLICATION OF INFRARED SPECTROSCOPIC MICROSCOPY AND ATR TECHNIQUES FOR STRUCTURAL STUDIES OF URINARY SEDIMENTS

Dominyka Blaževič, Milda Pučetaitė, Valdas Šablinskas

Department of General Physics and Spectroscopy, Faculty of Physics, Vilnius University, Lithuania
dominyka.blazevic@ff.stud.vu.lt

About 2% of Lithuanian citizens are diagnosed with kidney stone disease and this number is increasing every year. Usually kidney stone disease is diagnosed too late, when kidney stone is too big to be removed naturally. This causes severe pain and more complicated medical procedures are needed for treating the disease, for example extracorporeal shock wave lithotripsy or even open surgery. The treatment is much simpler when kidney stone disease is diagnosed early. Just use of medicaments in such cases can be sufficient [1]. The disease can be diagnosed early by examining chemical composition of urine sediments. Optical microscopy seems to be a "gold standard" in present medicine. Identification of chemical origin of the sediment is based on its morphological structure. Unfortunately, direct correlation between shape and chemical origin of the sediment exists only in case of monocrystalline sediment, what leads to frequent misinterpreting chemical composition of urine sediments. Infrared spectroscopic microscopy and attenuated total reflection method (ATR) could be used as more reliable tools for identification of chemical composition of urine sediments.

This spectroscopic study was conducted as part of CHANCE project that is funded under the European Commission's 7th Framework Programme. The aim of the project is to elucidate relation between quality of food and health. One way to reach the aim is to identify chemical composition of urine sediments.

In order to record infrared absorption spectra by means of infrared spectroscopic microscopy in transmission mode, the sample must be 10-30 μm thick, what is difficult to achieve. When sample is too thick, the infrared light is almost totally absorbed, therefore identification of chemical composition of urine sediments from such spectra is unreliable. Infrared absorption spectra of urine sediments were recorded by Hyperion 3000 IR microscope combined with FTIR spectrometer Vertex (both from Bruker). In most cases (80%) thickness of urine sediments was suitable for recording of the spectra and chemical composition was identified. Remaining 20% of urine sediments were too thick and the spectra were not suitable for identification of chemical composition Fig. 1 (A).

In order to avoid the thickness restriction ATR technique was used. In ATR experimental setup electromagnetic wave penetrates approximately 2 μm into the sample [2]. Spectra of urine sediments by ATR method were recorded with Bruker Alpha spectrometer equipped with diamond single pass ATR prism. Using this method the spectra of thick urine sediments were recorded and chemical composition was identified Fig. 1 (B).

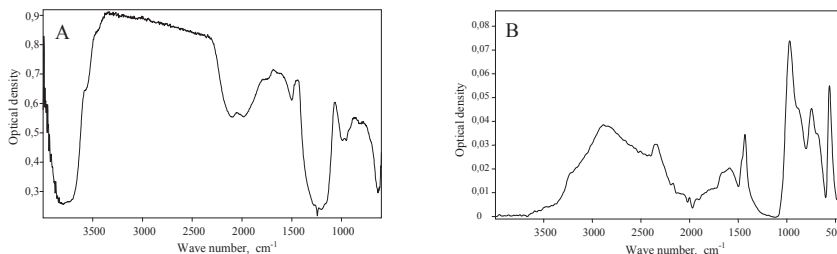


Fig. 1. IR absorption spectra of urine sediment (struvite crystal) recorded by infrared spectroscopic microscopy (A) and ATR (B) methods

Structural studies of urine sediments by means of infrared spectroscopic microscopy and ATR techniques are both more informative and reliable than by means of optical microscopy, which is currently used in medicine. It is notable, that infrared spectroscopic microscopy is rather complicated technique what restricts its use as routine clinical application. ATR method is easy to use, sample preparation for spectra recording is simple and fast, and the method is still more informative than optical microscopy. So, ATR technique can replace optical microscopy for identification of chemical composition of urine sediments. It has big potential to be used as standard method for early diagnosis of kidney stone disease.

[1] Andrew P.Evan, Physiopathology and etiology of stone formation in the kidney and urinary tract, *Pediatr Nephrol* 831-841 (2010).

[2] P. R. Griffiths, J.A. de Haseth, *Fourier Transform infrared spectroscopy*, 2nd ed. (John Wiley & Sons, 2007).

RESONANCE RAMAN OPTICAL ACTIVITY OF ASTAXANTHIN ENANTIOMERS

Grzegorz Zajac¹, Agnieszka Kaczor^{1,2}, Katarzyna Chruszcz-Lipska^{1,2}, Małgorzata Barańska^{1,2,*}

¹Faculty of Chemistry, Jagiellonian University, Ingardena 3, 30-060 Krakow, Poland

²Jagiellonian Centre for Experimental Therapeutics (JCET), Bobrzynskiego 14, 30-348 Krakow, Poland

grzegorz.zajac90@gmail.com

Raman optical activity (ROA) is a vibrational optical activity technique, complementary to the vibrational circular dichroism (VCD), which is based on observation of small difference between intensity of Raman scattering from chiral molecules in right- and left-circularly polarized incident light (ICP ROA – *incident circular polarization*), or small difference between intensity of right- and left-circularly polarized components in scattered light, in use of fixed polarization incident light (SCP-ROA – *scattered circular polarization*). In ROA spectra plus- and minus-sign bands are observed, and spectra of two enantiomers are mirror images of each other, so it provides information about absolute configuration of chiral compounds. Furthermore, ROA is sensitive to the conformational structures, so in use of theoretical computations, it provides information about conformational resolution in solutions or neat liquids, which is a big advantage in drug analysis relative to x-ray crystallography, which gives information of crystals structure. However ROA effect is extremely weak, so it requires long accumulation time and high sample concentrations [1].

When wavelength of incident light is matched to the electronic transition of molecule, resonance Raman optical activity (RROA) can be observed. The theory of RROA in single electronic state limit predicts that the every bands in the spectrum of one enantiomer are plus-sign and minus-sign for another. Furthermore, signs of bands should be opposite to related electronic band in circular dichroism spectrum of each enantiomer [2].

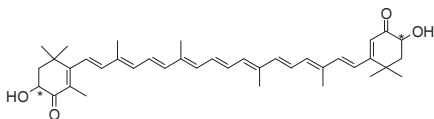


Fig. 1. Astaxanthin structure, “*” denotes chiral centers.

Astaxanthin (3,3'-dihydroxy- β -carotene-4,4'-dione) is a xanthophyll (family of carotenoid), which is one of the most potent antioxidant agent known in nature. It is a red pigment used in diet of salmonids and crustaceans [3].

This work reports RROA spectra of (3*S*,3'*S*) and (3*R*,3'*R*) astaxanthin enantiomers along with DFT calculations for six most populated conformers of this compound [4]. The geometry optimizations and ROA calculations were obtained using Gaussian 09 package with the B3LYP/6-31+G(d,p) and M05/6-31+G(d,p) levels of theory. Experimental ROA spectra were collected using ChiralRAMAN-2X SCP-ROA spectrometer (BioTools Inc.) with 532 nm excitation line. Both enantiomers of astaxanthin were measured, following their separation from a racemate mixture, where corresponding diastereomeric astaxanthin-di-(-)-camphanates esters were synthesized and separated on gravity column chromatography [5].

Obtained results of DFT calculations have shown that RROA bands signs strongly depend not only on configuration, but also on conformational structures. Intensities of bands in the averaged spectrum of six conformers are in the order of magnitude lower than corresponding intensities in the individual spectra of most conformers. Furthermore, different DFT functionals gave different sign of bands in RROA spectrum of (3*S*,3'*S*)-astaxanthin.

Acknowledgement

The project was financially supported by National Center of Science (DEC-2012/07/B/ST5/00889).

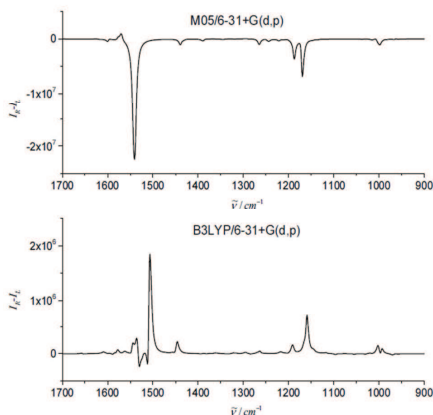


Fig. 2. Averaged theoretical RROA spectra of six (3*S*,3'*S*)-astaxanthin conformers.

- [1] Barron, L. D.; Zhu, F.; Hecht, L.; Tranter, G. E.; Isaacs, N. W. *Journal of Molecular Structure* **2007**, 834-836, 7-16.
- [2] Nafie, L. A. *Chemical Physics* **1996**, 205, 309-322.
- [3] Kaczor, A.; Pilarczyk, M. Chapter 11 in: *Optical Spectroscopy and Computational Methods in Biology and Medicine*, M. Barańska (Ed.), Springer, Series: Challenges and Advances in Computational Chemistry and Physics, Vol. 14, Due: December 31, 2013, ISBN 978-94-007-7831-3
- [4] Kaczor, A.; Barańska M. *Analytical Chemistry* **2011**, 83(20), 7763-7770.
- [5] Müller, R. K.; Bernhard, K.; Mayer, H.; Rüttimann, A.; Vecchi, M. *Helvetica Chimica Acta* **1980**, 63(6), 1654-1664.

¹ Department of Theoretical Physics, Faculty of Physics, Vilnius University, Vilnius, Lithuania

² Department of Chemical Physics, Lund University, Lund, Sweden

³ Molecular Compounds Physics Laboratory, Center for Physical Sciences and Technology, Vilnius, Lithuania
egle.basinskaite@ff.stud.vu.lt

2D Electronic Spectroscopy (2DES) is a state-of-the-art ultrafast optical spectroscopy technique, used to probe the dynamics in the system after excitation [1]. Direct mapping of excitation energy transfer in molecular systems enriched our knowledge about energy structure of many essential systems, for example, Photosynthetic reaction centers [2] and light harvesting complexes [3].

The cyclic porphyrin hexamer–template complex or porphyrin nanoring (PNR) is fully-conjugated belt-shaped system with different properties when compared with single porphyrins or linear porphyrin polymers. Large red-shift is present in absorption spectrum as well as appearance of three peaks structure in absorption bands (Fig. 1). Structural similarity with light harvesting complexes (particularly with LH2 [4]), encouraged scientists to synthesize and examine porphyrin polymers shaped in a cyclic manner [5,6].

In this study, analysis of energy transfer in PNR system using 2DES is presented. 2D spectra, measured in room (300K) and cryogenic (77K) temperature, revealed energy levels in the PNR complex, different compared with single porphyrin. Two different energy transfer rates were found between the levels – fast energy transfer to the lowest excited state with the lifetime of 200 fs, followed by a slower relaxation to the ground state with lifetime of 280 ps. The work is concluded by comparing experimental maps with those obtained from simulation.

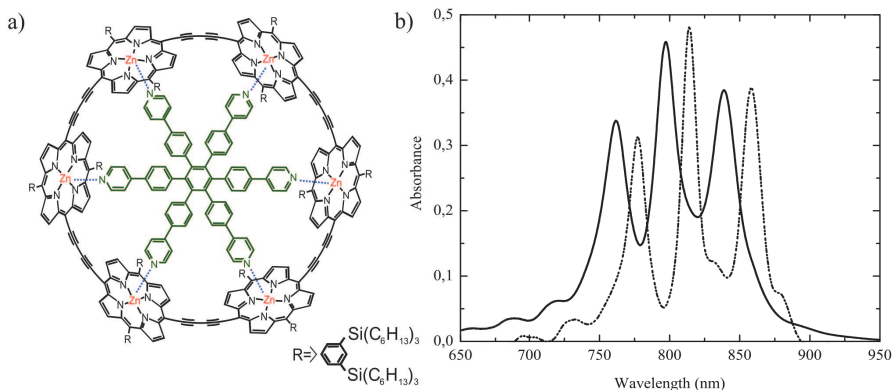


Fig. 1. Structure of Porphyrin Nanoring (a) and corresponding linear absorption spectra at 300 K (solid line) and 77 K (dashed line) temperatures (b).

- [1] S. Mukamel, *Principles of Nonlinear Optical Spectroscopy* (Oxford University Press, New York, 1995).
- [2] S. Westenhoff et al., Coherent picosecond exciton dynamics in a photosynthetic reaction center, *Journal of the American Chemical Society*, **134**(40), 16 484–16 487 (2012).
- [3] T. Pullerits, D. Zigmantas, and V. Sundström, Beatings in electronic 2D spectroscopy suggest another role of vibrations in photosynthetic light harvesting, *Proceedings of the National Academy of Sciences*, **110**(4), 1148–1149 (2013).
- [4] G. McDermott, S. M. Prince et al., Crystal structure of an integral membrane light-harvesting complex from photosynthetic bacteria, *Nature*, **374**(6522), 517–521 (1995).
- [5] M. Hoffmann, C. J. Wilson et al., Template directed synthesis of a p-conjugated porphyrin nanoring, *Angewandte Chemie International Edition*, **46**(17), 3122–3125 (2007).
- [6] J. K. Sprafke, D. V. Kondratuk, et al., Belt-shaped p-systems: Relating geometry to electronic structure in a six-porphyrin nanoring, *Journal of the American Chemical Society*, **133**(43), 17262–17273 (2011).

PHOTOPHYSICAL PROPERTIES OF THIOPHENE-DIPHENYLAMINE FUNCTIONAL BLOCK

Edvinas Radiunas, Steponas Raišys

Institute of Applied Research, Vilnius University, Lithuania
eradiunas@gmail.com

Thiophene is one of the most popular building blocks used in conductive organic polymers due to excellent charge transport properties. Diphenylamine-based compounds (such as classical hole-transporter TPD [1]) are known for their high hole mobility and also efficient fluorescence. The aim of this work is to combine these two functional units to produce a multifunctional material capable of transporting charges as well as delivering intense emission. Multifunctional materials could ease fabrication of organic light-emitting diodes by simplifying complex multi-layer technological procedures.

In this work, photophysical properties of the new thiophene-diphenylamine compound (see Fig. 1) were investigated. Optical measurements of the compound were performed in toluene solution (10^{-5} mol/l), polystyrene matrix (0.5 wt%) and neat film. The techniques such as absorption and fluorescence spectroscopy, fluorescence quantum yield (Φ_F) and fluorescence lifetime were employed to reveal the optical properties of the compound.

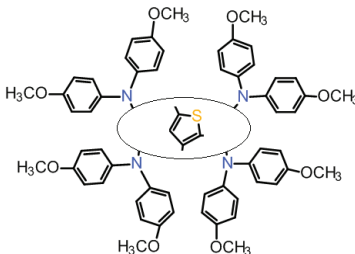


Fig. 1. Chemical structure of thiophene-diphenylamine compound.

Absorption spectra of the compound measured in toluene solution and neat film are very similar with the first peak at 430 nm. Toluene solution and neat film exhibit fluorescence in sky blue-green region with emission maximum ranging from 498 nm to 500 nm. Fluorescence spectrum of the compound dispersed in polystyrene is slightly blue shifted with the maximum at 483 nm. Φ_F in toluene solution and polystyrene matrix is found to be 17% and 19%, respectively. However, Φ_F of the neat film reaches only 0.3%. Since molecules of the compound in the toluene and polystyrene matrix are weakly interacting owing to their low concentration, fluorescence lifetime is longer and Φ_F is higher. Conversely, densely packed molecules in the neat film strongly interact, therefore, it is likely that exciton migration and migration-induced exciton quenching at the defect sites in the neat films cause low Φ_F and short fluorescence lifetime.

[1] P. J. Low, M. A. J. Paterson, D. S. Yufit et al., Towards an understanding of structure–property relationships in hole-transport materials: The influence of molecular conformation on oxidation potential in poly(aryl)amines, *J. Mater. Chem.* **15**, 2304–2315 (2005).

ELECTRIC FIELD IMPACT TO FLUORESCENCE IN ORGANIC INDOLO[3,2-*b*]CARBAZOLE COMPOUNDS

Simona Streckaitė¹, Renata Karpicz¹, Saulius Grigalevičius²

¹Institute of Physics, Center for Physical Sciences and Technology, A. Gostauto Ave. 11, LT-01108 Vilnius, Lithuania

²Department of Organic Technology, Kaunas University of Technology, Radvilėnų pl. 19, LT-50254, Kaunas, Lithuania

simona.streckaitė@gmail.com

Future of low-cost and easy processing optoelectronics is expected to be organic semiconductors which promise flexible devices and large area applications from solutions. The most widely used organic small molecule p-type semiconductors exhibit excellent hole-transporting properties although the morphological stability of amorphous films often is poor because of low glass transition temperatures. For this reason organic semiconductor materials are required to be suitable for forming amorphous films with high thermal and morphological stability possessing good hole-transport, mechanical and electrochemical properties.

To comply with all the requirements, effective hole-transport materials based on indolo[3,2-*b*]carbazole are investigated. These materials have nitrogen atom in the carbazole fragment which provides electron-donating ability. Moreover because of high glass transitions temperatures, indolo[3,2-*b*]carbazole compounds provide great thermal and morphological constancy. These advantages make indolo[3,2-*b*]carbazole compounds promising as excellent hole transport layers in OLEDs [1, 2].

In our work, we present investigation of six newly synthesised indolo[3,2-*b*]carbazole molecules, which differ in connected functional group. The optical and electrical properties of these derivatives as hole-transporting materials for blue light emitting diodes are reported. The aim of this work was to reveal fluorescence changes in mentioned materials caused by electric field and ascertain differences among all studied compounds determined by connected functional group.

Compounds were investigated as solutions using chloroform solvent and as thin films by using steady-state and ultrafast time-resolved spectroscopy. Films were made few hundred nanometres thick by spin coating technique.

Large influence of oxygen and evaporated aluminium electrodes to fluorescence quenching was observed. For SV100, SV101 and SV106 compounds impact of oxygen to fluorescence quenching was stronger than for M47, M60 and M66. Connected functional groups have more influence for shape of absorption spectra compared to almost not influenced fluorescence spectra of materials.

Fluorescence changes due to applied electric field are depicted in Fig. 1. Fluorescence of SV101 showed no dependence of added electric field. In SV106 compound fluorescence changes very weakly, also fast degradation was observed for this material. In SV100 electric field induced fluorescence changes are most noticeable. However, in M materials electric field influence to fluorescence is stronger than in SV materials, due to specific connected functional groups.

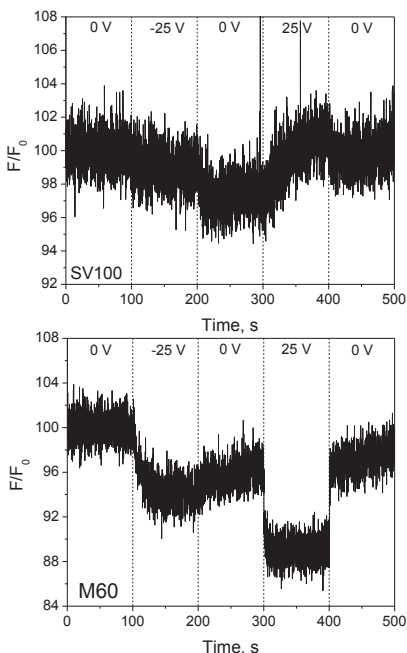


Fig. 1. Fluorescence changes due to applied electric field in SV100 and M60 compounds.

[1] H. P. Zhao et al., Structure and electronic properties of triphenylamine-substituted indolo[3,2-*b*]carbazole derivatives as hole-transporting materials for organic light-emitting diodes, *Chem. Phys. Lett.* **439**, 132–137 (2007).

[2] H. P. Zhao et al., Effect of substituents on the properties of indolo[3,2-*b*]carbazole-based hole-transporting materials, *Org. Electron.* **8**, 673–682 (2007).

PLASMON-ENHANCED FLUORESCENCE OF LABELED ANTI-ALPHA-FETOPROTEIN MOLECULES

Alina Muravitskaya¹, Andrey Ramanenka¹

¹ Department of Physics, Belarusian State University, Belarus

alina.mur@mail.ru

Fluorescence is a highly sensitive technique, where single molecules can readily be detected, but there is still a drive for reduced detection limits. The detection of a fluorophore is usually limited by its quantum yield, autofluorescence of the samples and/or the photostability of the fluorophores [1]. Plasmon-enhanced luminescence of molecular probes in plasmonic nanostructures is a highly developing field providing a number of new methods in chemical and biomedical analysis. The proximity of a metal nanobody gives rise to an increase in local electromagnetic radiation intensity, changes the probability of spontaneous photon emission, and also promotes multiple enhancement of nonradiative relaxation of an excited state [2]. To make use of enhancement factors one has to engineer the optimal topology of a probe–metal nanostructure to get positive balance of competing enhancement/quenching effects. In other words, the luminescent probe is to be displaced at a certain distance on metal nanobodies at a point where quenching is yet negligible but field and density of states enhancement still present [3].

Proteins covalently labeled with fluorophores are widely used as reagents, for example, in immunoassays or for the immunostaining of biological specimens with specific antibodies. In this paper we investigated plasmon-enhanced luminescence of anti-Alpha-Fetoprotein (anti-AFP) molecules conjugated with fluorescein isothiocyanate that widely used in immunoassay. For this purpose multilayer nanostructures “silver nanoparticles – polyelectrolytes – protein molecules” were prepared by successive deposition. Silver sol was synthesized by the AgNO₃ citrate reduction technique. Deposition has been performed by dipping of half of a substrate surface in a silver sol for 24 h. The silver-free remaining portion of the substrate served as a reference sample. Luminescence spectra were registered with a grating spectrograph S3801 (Solar TII, Belarus) combined with a liquid nitrogen cooled silicon CCD camera (Princeton Instruments, USA). Luminescence excitation was performed with a cheap and affordable commercial light-emitting diode with the emission spectrum peaking at 460 nm. All optical measurements were made at room temperature (~300 K). It was found that silver containing samples enhanced luminescence in comparison to the reference samples on glass substrates without silver coatings. Concentration dependence (from 0,5 to 40 µg/ml) of the signal for the anti-AFP appeared to be with saturation in both silver/not silver samples. On the linear part of this dependence the average enhancement factor was 1,4 times, but with rise of the concentration factor increase to 6 times.

[1] K. Aslan et al., «Metal-enhanced fluorescence: an emerging tool in biotechnology.» Current Opinion in Biotechnology. V. 16, P. 55-62 (2005).

[2] D. V. Guzatov et al., “Plasmonic enhancement of molecular fluorescence near silver nanoparticles: theory, modeling, and experiment,” J. Phys. Chem. C 116(19), 10723–10733 (2012)

[3] S. V. Gaponenko, Introduction to Nanophotonics, Cambridge University Press, Cambridge (2010).

APPLICATION OF GRAPHENE AND RU NANOPARTICLES FOR ELECTROCHEMICAL BIOSENSORS

Ausra Gustainyte¹, Isabel Pastoriza Santos², Elisa Gonzalez- Romero³

¹Center for Physical Sciences and Technology, Savanoriu Ave 231, Lithuania

²Colloid Chemistry Group, Department of Physical Chemistry, University of Vigo, Spain

³Electroanalysis and Biosensors Group, Department of Analytical and Food Chemistry, University of Vigo, Spain
gustainyteausra@gmail.com

Biosensors can be applied in various samples including body fluids and environmental samples. We used innovative Screen-Printed Graphene Electrodes (SPGPHEs), because of high surface area of graphene, thermal and electric conductivity. The electrodes were modified with nanoparticles to improve the electrocatalytic properties toward b-Nicotinamide (NADH) oxidation, so that it can be used for electrochemical biosensor device [1]. Our results are shown in Fig. 1. The Fig. 1a is TEM image of the triangular ruthenium nanoparticles obtained using hydrothermal synthesis method [2].

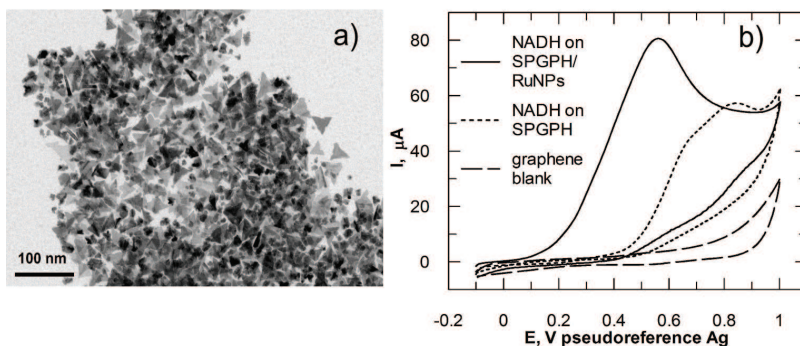


Fig. 1. 1a-TEM image of RuNPs, 1b-Cyclic Voltammograms in presence of 5 mM NADH in 5mM PBS (pH 6.8) at unmodified and at different modied surfaces, and in absence of NADH (PBS on SPGPHE), scan rate 50 mV s^{-1} : graphene blank (dash) , NADH on SPGPH-1 scan (dot), NADH on SPGPH/RuNPs-1 scan (line).

As shown in (Fig. 1), curves are cyclic voltammograms of NADH on bare SPGPHE (dot) and SPGPH/RuNPs modified electrode (line), graphene blank (dash). A remarkable catalytic oxidation current at the modified electrode occurred at ca. 0.2 V, which negatively shifted higher than 350 mV, compared with that at bare SPGPHE (ca. peak potential at 0.870 V). The electrocatalytic current decreased significantly (more than 40%) when the RuNPs were absent from the electrode surface. Our results demonstrated that the SPGPH/ RuNPs maintained a good electrochemical activity toward NADH and could be applied to the field of electrochemical biosensors.

[1] Li Li, et al., Talanta **113**, 1-6 (2013).

[2] An-Xiang Yin, et al., Am. Chem. Soc. **134**, 20479-20489 (2012).

SYNTHESIS AND OPTIMISATION OF FLUORESCENT GOLD NANOPARTICLES FOR BIOIMAGING

Laura Kacenauskaitė^{1,2}, Akvile Slekaitė^{1,2}, Ricardas Rotomskis^{2,3}

¹Faculty of Natural Sciences, Vilnius University, Lithuania

²Laboratory of Biomedical Physics, Institute of Oncology, Vilnius University, Lithuania

³Faculty of Physics, Vilnius University, Lithuania

laura.kacenauskaitė@gmail.com

Current breakthrough in nanotechnology is particularly important for biomedicine, where nanoparticle-based assays have shown a great promise in battle against the most common diseases. During the last few years gold nanoparticles have had an important role in cancer diagnostics and treatment because of their extensive scale of sizes, easy surface functionalization and advantageous properties such as localized surface plasmon resonance and fluorescence.

Extra small fluorescent gold nanoparticles – gold nanoclusters (AuNCs), composed of several gold atoms, demonstrate great potential for *in vivo* tumor imaging and are considered as novel, effective contrast agents because of their biocompatibility and easy modification process for a specific application or selective uptake [1]. Although future perspectives are promising, there are still some obstacles to overcome. Overlapping AuNCs and tissue fluorescence bands as well as insufficient fluorescence intensity are the main problems that prevent further experiments.

This research demonstrates that fluorescence intensity of MES (2-(*N*-morpholino)ethanesulfonic acid) capped AuNCs could be increased a few times depending on synthesis temperature [2]. During this experiment fluorescent gold nanoparticles were synthesized using Bao et al. [3] suggested method in the temperature range from 37°C to 85°C. As it is shown in Fig. 1 room-temperature Au NCs have a fluorescence peak at 480 nm (excitation peak is at 420nm). Synthesis at different temperatures have not shown any effect on these parameters although fluorescence intensity has grown more than five times with increasing synthesis temperature from 37°C to 70°C. However, higher temperatures lead to decrease of fluorescence intensity and formation of more precipitates instead.

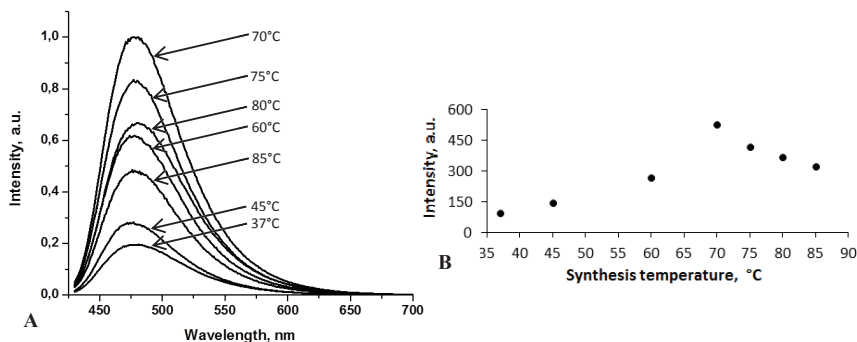


Fig. 1. Normalized fluorescence emission (A), B - dependence of fluorescence intensity on synthesis temperature in range from 37°C to 85°C

The growth of fluorescence intensity with higher temperatures can be result of increased oxidation potential of MES and related kinetics. Higher temperatures influence the efficiency of entire synthesis reaction products including non-fluorescent gold particles present in the colloid. After a temperature reaches a certain critical point, more large non-fluorescent particles are formed in the expense of small fluorescent AuNCs and therefore fluorescence intensity decreases.

In our observations all synthesized fluorescent AuNCs show great stability over time and can be concentrated up to ten times without any unfavourable changes.

Results obtained from this research show a method that allows to increase fluorescence intensity of MES capped AuNCs. In our knowledge this dependance on temperature in range from 60°C to 85°C is described for the first time and have never been published in any other references.

[1] W. Cai, T. Gao, H. Hong, J. Sun, Applications of gold nanoparticles in cancer nanotechnology, *Nanotechnol Sci Appl*. 2008; 1: 17–32.

[2] L. Wintzinger, W. An, C. H. Turner, Y. Bao, Synthesis and Modeling of Fluorescent Gold Nanoclusters, *JOSHUA*, 2010, vol. 7, 24-27.

[3] Y. Bao, H. Yeh, C. Zhong, S. Ivanov, J. Sharma, M. Neidig, D. Vu, A. Shreve, R. Dyer, J. Werner, J. Martinez, Formation and Stabilization of Fluorescent Gold nanoclusters Using Small Molecules, *J. Phys. Chem.*, 114(38), 15879-15882 (2010).

WITHDRAWN CONTRIBUTION

FLUORESCENCE PROPERTIES OF PYRIMIDE BASED DERIVATIVES

Justina Jovaišaitė¹, Lina Skardžiūtė¹, Sigita Tumkevičius², Saulius Juršėnas¹

¹ Institute of Applied Research, Vilnius University, Saulėtekio 9-III, LT-10222 Vilnius, Lithuania

² Department of Organic Chemistry, Vilnius University, Naugarduko 24, LT-03225 Vilnius, Lithuania
jovaisaite.justina@gmail.com

Pyrimidine derivatives are organic compounds that have a benzene ring and two nitrogen atoms at positions 1 and 3. These derivatives are one of the main DNA nucleic acid consisting parts [1]. Pyrimidine and their derivatives are well known due to their biological activity [2]. These compounds show antibacterial, antiviral, antimicrobial, antitumor, antituberculous properties [3]. It was observed that pyrimidine derivatives have an efficient fluorescence and that they are sensitive to the polarity of the environment [4]. Therefore lots of research has been carried out recently seeking to adapt these compounds in the manufacture of sensors and biosensors [5].

In this work a new series of pyrimidine derivatives has been studied. The pyrimidine compounds differ in substituents and their positions (see Fig 1). The aim of this work was to find out the dependence of the photophysical properties of pyrimidine derivatives on different substituents and their positions and also on various solution polarity. For that reason, pyrimidine samples were made using four solutions with increasing polarity: toluene, chloroform, acetone, dimethylformamide. To find out all the optical properties measurements of absorption and fluorescence spectra, fluorescence quantum yields and lifetimes were carried out.

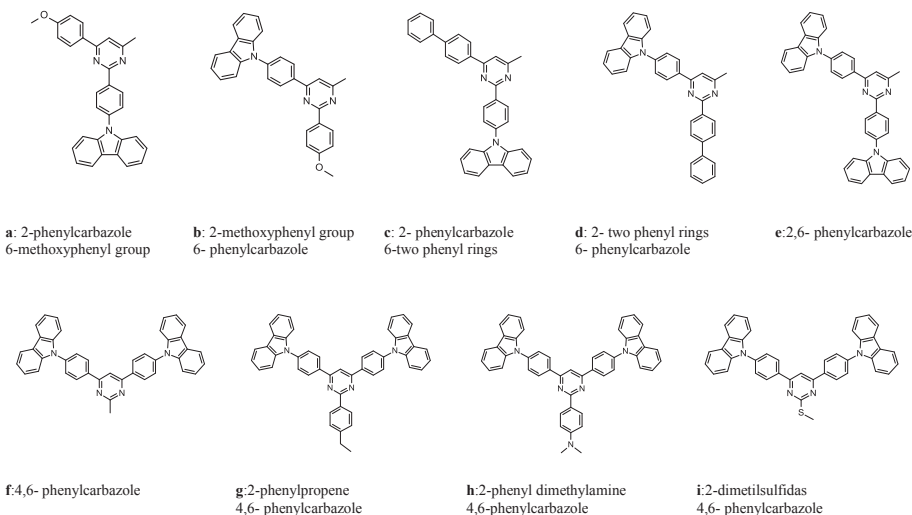


Fig. 1. Structural formulas of a new series of pyrimidine derivatives.

Pyrimidine compounds have demonstrated high fluorescence quantum yields (up to 75%) in a wide spectrum range (from 378 nm to 520 nm). The fluorescence efficiency of the derivatives in a polar environment is influenced by two competing factors. One of them is increased radiative fluorescence lifetimes (from 3-4 ns in a nonpolar solution to 8-51 ns in a polar solution) due to intramolecular charge transfer. The other one is increased nonradiative fluorescence lifetimes (from 1,5-7 ns in a nonpolar solution to 16-27 ns in a polar solution) due to reduced intersystem crossing.

[1] JM. Arivazhagan and D. Anitha Rexalin, "Vibrational spectra, UV-vis spectral analysis and HOMO-LUMO studies of 2,4-dichloro-5-nitropyrimidine and 4-methyl-2-(methylthio)pyrimidine," *Elsevier*, pp. 347-358, 2013.

[2] H. Kılıç, "Electronic absorption study on hydration, solvation behavior for some keto and thioketo pyrimidine derivatives," *Elsevier*, pp. 328-336, 2013.

[3] A. Diğli, S. Mercan, and S. Yavuz, "Synthesis and Antimicrobial Activity of New Pyrimidine Derivatives Incorporating 1H-Tetrazol-5-ylthio Moiety," *Wiley Online Libr.*, vol. 50, 2013.

[4] S. Velázquez-Olvera, H. Salgado-Zamora, M. Velázquez-Ponce, E. Campos-Aldrete, and C. Reyes-Arellano, Alicia Pérez-González, "Fluorescent property of 3-hydroxymethyl imidazo [1,2-a]pyridine and pyrimidine derivatives," *Chem. Cent. J.*, pp. 1-9, 2012.

[5] V. D. Suryawanshi, A. H. Gore, L. S. Walekar, P. V. Anbhule, S. R. Patil, and G. B. Kolekar, "Solatochromic fluorescence behavior of 2-amino-6-hydroxy-4- (3,4-dimethoxyphenyl)-pyrimidine-5-carbonitrile: A sensitive fluorescent probe for detection of pH and water composition in binary aqueous solutions," *J. Mol. Liq.*, pp. 4-9, 2013

EXCITON DIFFUSION MEASUREMENTS IN THE FILMS OF TRIPHENYLAMINE WITH NAPHTHALIMIDE SIDE-MOETIES

Raimundas Burokas, Steponas Raišys, Arūnas Miasojedovas

Institute of Applied Research, Vilnius University, Saulėtekio al.9-III, LT-10222 Vilnius, Lithuania
raimundasbur@gmail.com

Organic semiconductors are very attractive for material research since they can be structurally manipulated by means of chemical engineering to achieve better performances in optoelectronic devices [1]. Triphenylamine (TPA) derivatives are widely investigated because of their excellent thermal and electrochemical stability, electron donating ability and optoelectronic properties. These properties are essential for solar cells fabrication. One of the most important factors in the operation of organic solar cells is exciton diffusion. Excitons are bound electron-hole pairs which are created in organic material by light absorption and need to be separated into free charges to generate photocurrent [1]. Thus, combining TPA with compounds exhibiting good electron accepting ability, such as naphthalimide, potentially could be applied for the fabrication of organic solar cells.

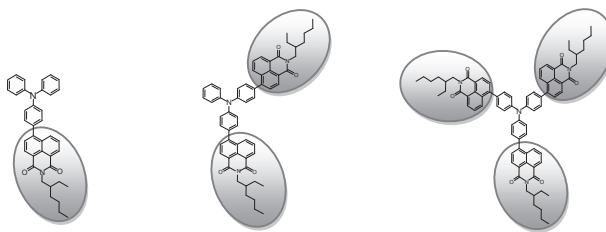


Fig. 1. Triphenylamine compounds with different number of naphthalimide side-moieties.

In this work, exciton diffusion length in the TPA-naphthalimide compounds bearing different number (from 1 to 3) of naphthalimide side-moieties was investigated (Fig. 1). The measurement of the exciton diffusion length was based on estimation of fluorescence lifetime of the TPA-naphthalimide compounds blended with various concentration of phenyl-C61-butyric acid methyl ester (PCBM) fluorescence quencher. Since oxygen acts as effective fluorescence quencher, films were prepared in nitrogen environment and encapsulated between two glass plates. Fluorescence kinetics of the TPA-naphthalimide:PCBM blends were estimated by time correlated single photon counting method and modeled with Monte Carlo simulation of 3D exciton hopping to estimate exciton diffusion coefficient [1].

The obtained results demonstrate that increasing number of naphthalimide side-moieties results in prolonged average fluorescence lifetime from 10 ns to 13 ns and enlarged exciton diffusion coefficient from $2.7 \cdot 10^{-6} \text{ cm}^2/\text{s}$ to $6.4 \cdot 10^{-6} \text{ cm}^2/\text{s}$. The enhancement of fluorescence lifetime and diffusion coefficient results in increase exciton diffusion length from 2.9 nm to 5.1 nm.

Tailoring of exciton diffusion length by introducing larger number of naphthalimide side-moieties might be applied in designing new compounds for the application in organic solar cells.

[1] O.V.Mikhnenko, H.Azimi, M.Scharber et al, Exciton diffusion length in narrow bandgap polymers, Energy Environ. Sci. **5**, 6960-6965 (2012).

THERMOANALYTICAL STUDY OF INDIUM-MOLYBDATE-TARTRATE GEL PRECURSORS PREPARED BY AQUEOUS SOL-GEL SYNTHESIS ROUTE

Žygimantas Žulonas, Artūras Žalga

Department of Applied Chemistry, Faculty of Chemistry, Vilnius University, Naugarduko Str. 24, 03225 Vilnius, Lithuania

zygimantas.zulonas@chf.stud.vu.lt

Binary and ternary metal oxide systems have been subjects of intense interest as their characterization is essential for design of new materials of different types, like semiconductors, magnetic and optical materials or construction materials of specific thermal, mechanical or chemical properties [1]. In accordance to some recent findings, $\text{In}_2\text{Mo}_3\text{O}_{12}$ compound is an outstanding catalyst for active and selective catalysts of different processes of oxidation of organic compounds, e.g. methanol to formaldehyde, propene to acrylaldehyde or acrylic acid, or benzene to maleic anhydride, or paraffin to olefin [paraffin = olefin + hydrogen] through dehydrogenation followed with selective hydrogen combustion in a process which is not thermodynamically restricted [2]. Moreover, the selective oxidation of different organic compounds was successfully used in semiconducting sensors for detection of oxidating gases O_3 and NO_2 . Besides, it has been established that the characteristics of the sensors based on MoO_3 and In_2O_3 significantly depend on the conditions of their synthesis, which affect the structure, phase composition and degree of oxidation of molybdenum and indium.

From this point of view many different preparation techniques, such as traditional solid-state reactions, combustion, Czochralski method, solvothermal processes, microwave irradiation, spray pyrolysis, the facile microemulsion mediated hydrothermal process, electrochemical, sonochemical, and sol–gel synthesis are successfully used for the synthesis of In_2O_3 – MoO_3 and $\text{In}_2\text{Mo}_3\text{O}_{12}$ compounds. Among these synthesis routes, the solution-based synthetic methods play a crucial role in the design and production of fine ceramics and have been successful in overcoming many of the limitation of the traditional solid-state, high-temperature methods [3].

In the past few decades, many researchers have carried out the studies on the formation of metal complexes with organic ligands. Furthermore, the metal complexes with organic ligands have been used for the preparation of ceramics and metal oxide thin films by sol–gel process, using metal nitrates, chlorides, and acetates as starting materials. Besides, metal salts are very useful, inexpensive, and very easy to handle in comparison to metal alkoxides, and hence they are good alternatives for the conversion to oxides by thermal decomposition. They can be dissolved in many kinds of organic solvents in which metal complexes are formed. From this point of view, the wet synthesis route called an aqueous sol–gel method, is really attractive and compared to other techniques, as it has the advantages of a good control of the starting materials and of the processing parameters, a high purity of the raw materials, and the low temperature of the process. A good homogeneity of the product could be achieved by control of the stoichiometry of the starting solution [4, 5].

In this work, In–Mo–O nitrate–tartrate gel precursors under different synthesis conditions have been prepared by the aqueous sol–gel synthesis method. In order to explain and better understand the possible initial composition of as-prepared gels the thermal decomposition behaviour of the synthesized precursors and crystallization process of the final materials by the thermogravimetric and differential scanning calorimetric analysis (TG/DSC), X-ray diffraction (XRD) and scanning electron microscopy (SEM) was performed.

-
- [1] E. Filipek, I. Rychlowska-Himmel, A. Paczesna, Thermal stability of $\text{In}_2(\text{MoO}_4)_3$ and phase equilibria in the MoO_3 – In_2O_3 system, *Journal of Thermal Analysis and Calorimetry* **109**, 711–716 (2012).
- [2] B. A. Marinkovic, M. Ari, P. Mendes Jardim, et al., $\text{In}_2\text{Mo}_3\text{O}_{12}$: A low negative thermal expansion compound, *Thermochimica Acta* **499**, 48–53 (2010).
- [3] G. Brazilius, G. Janulevicius, R. Stankeviciute, A. Zalga, Aqueous sol–gel synthesis and thermoanalytical study of the alkaline earth molybdate precursors, *Journal of Thermal Analysis and Calorimetry*, DOI 10.1007/s10973-013-3579-0.
- [4] A. Zalga, Z. Moravec, J. Pinkas, A. Kareiva, On the sol-gel preparation of different tungstates and molybdates, *Journal of Thermal Analysis and Calorimetry* **105**, 3-11 (2011).
- [5] K. Tonsuadu, A. Zalga, A. Beganskiene, A. Kareiva, Thermoanalytical study of the YSZ precursors prepared by aqueous sol-gel synthesis route, *Journal of Thermal Analysis and Calorimetry* **110**, 77-83 (2012).

Open Readings 2014. 57th Scientific Conference for Students of Physics and Natural Sciences
AQUEOUS SOL-GEL SYNTHESIS, CRYSTAL STRUCTURE, SURFACE
MORPHOLOGY AND PHOTOLUMINESCENCE OF EUROPIUM
MOLYBDATE

Žygimantas Gričius, Artūras Žalga

Department of Applied Chemistry, Faculty of Chemistry, Vilnius University, Naugarduko Str. 24, 03225 Vilnius,
Lithuania

zygimantas.gricius@chf.stud.vu.lt

The synthesis of nano- to micro scale inorganic materials with specific size and morphology is of great interest for the study of materials chemistry because of the potential technology applications of such materials [1]. Due to their wide potential application, including solid-state lasers, optical fibers, stimulated Raman scatters, catalysts and microwave applications, in recent years, molybdates and tungstates have become the main focus of many technological fields and scientific areas.

Consequently, different new synthesis methods which could easily produce such kind of materials with designed crystalline structure and controlled morphology are still very desirable. Many different preparation techniques, such as traditional solid-state reactions, combustion, Czochralski method, solvothermal processes, microwave irradiation, spray pyrolysis, the facile micro emulsion mediated hydrothermal process, electrochemical, sonochemical and sol-gel synthesis are successfully used for the synthesis of different inorganic ceramic materials. However, among these different synthesis routes, the solution-based synthesis has been successful in overcoming many limitations of the traditional solid-state, high-temperature methods. The use of solution chemistry can eliminate major problems, such as long diffusion paths, impurities, and agglomeration providing the products with improved homogeneity [2].

In the past few decades, many researchers have carried out the studies of the formation of metal complexes with organic ligands. Furthermore, the metal complexes with organic ligands have been used for the preparation of ceramics and metal oxide thin films by sol-gel process, using metal nitrates, chlorides, and acetates as starting materials. Besides, metal salts are very useful, inexpensive, and very easy to handle in comparison to metal alkoxides, hence they are good alternatives for the conversion to oxides by thermal decomposition. They can be dissolved in many kinds of organic solvents in which metal complexes are formed [3].

In this study a sample of citric acid has been used to carry out an aqueous sol-gel method based synthesis of $\text{Eu}_2\text{Mo}_3\text{O}_{12}$. In this case, the mechanism of thermal decomposition of as-prepared Eu-Mo-O nitrate-citrate sol precursor has been investigated performing the thermo gravimetric and differential scanning calorimetric analysis (TG/DSC). The crystal structure and surface morphology of Eu-Mo-O sample have been determined at different temperatures by X-ray diffraction (XRD) and scanning electron microscopy (SEM). Moreover, the photo-luminescent properties of as-prepared $\text{Eu}_2\text{Mo}_3\text{O}_{12}$ ceramic powders have also been investigated.

-
- [1] L. Wei, Y. Liu, Y. Lu, T. Wu, Morphology and photoluminescence of $\text{Ba}_{0.5}\text{Sr}_{0.5}\text{MoO}_4$ powders by a molten salt method, *Journal of Nanomaterials* DOI 10.1155/2012/398582.
- [2] A. Zálga, Z. Moravec, J. Pinkas, A. Kareiva, On the sol-gel preparation of different tungstates and molybdates, *Journal of Thermal Analysis and Calorimetry* **105**, 3-11 (2011).
- [3] G. Braziulis, G. Janulevicius, R. Stankeviciute, A. Zálga, Aqueous sol-gel synthesis and thermoanalytical study of the alkaline earth molybdate precursors, *Journal of Thermal Analysis and Calorimetry*, DOI 10.1007/s10973-013-3579-0.

AQUEOUS SOL-GEL SYNTHESIS AND FT-IR SPECTROSCOPICAL INVESTIGATION OF Eu^{3+} DOPED MAGNESIUM AND STRONTIUM MOLYBDATES

Gediminas Braziulis, Artūras Žalga

Department of Applied Chemistry, Faculty of Chemistry, Vilnius University, Naugarduko Str. 24, 03225 Vilnius, Lithuania

gedim@vgtu.lt

The host materials play an important role in exploring novel optical materials, this is the reason why tungstate and molybdate have attracted great attention due to their applications as scintillating materials in electro-opticals-like solid-state lasers and light-conversion phosphors for solid-state lighting [1]. Among them, molybdates (MoO_4^{2-}) contain the central Mo ion coordinated either by six oxygen ions in a relatively stable octahedral symmetry or by four oxygen ions in a relative stable tetrahedral symmetry. From the structural point, the differences between alkaline earth metal molybdates (AMoO_4 , A = Mg, Sr) mainly consist in ionic radius of the A-site. If the ionic radius of the A-site ion is smaller than 1.0 Å as is the case for MgMoO_4 ceramic, the compounds show a wolframite structure with octahedral coordination. Alternatively, if the ionic radius of the A-site is larger than 1.0 Å as is the case for Sr^{2+} in AMoO_4 , the compounds show a scheelite structure with tetrahedral coordination [2]. Moreover, as well as the crystal structure, the surface morphology also significantly affects both the optical and electrical properties of alkaline earth metal molybdates. Thus, according to this the synthesis method that could be chosen for the preparation of these ceramic materials has significant importance.

Many different preparation techniques, such as traditional solid-state reactions, combustion, Czochralski method, solvothermal processes, microwave irradiation, spray pyrolysis, the facile microemulsion mediated hydrothermal process, electrochemical, sonochemical, and sol-gel synthesis are successfully used for the synthesis of different inorganic ceramic materials. Among these different synthesis routes, the solution-based synthetic methods play a crucial role in the design and production of fine ceramics and have been successful in overcoming many of the limitation of the traditional solid-state, high-temperature methods [3].

From this point of view, the wet synthesis route called an aqueous sol-gel method, is really attractive and compared to other techniques, as it has the advantages of a good control of the starting materials and of the processing parameters, a high purity of the raw materials, and the low temperature of the process. A good homogeneity of the product could be achieved by control of the stoichiometry of the starting solution [4].

In this work, $\text{MgMoO}_4:\text{xEu}^{3+}$ and $\text{SrMoO}_4:\text{xEu}^{3+}$ ($\text{x} = 0.5, 1.0, 2.0, 4.0$ and 8.0) compounds has been prepared by the aqueous sol-gel synthesis method using tartaric acid as a complexing agent in the sol-gel processing. In order to explain and better understand the possible thermal decomposition behaviour of the synthesized precursors and crystallization process of the final materials, the thermal analysis (TG/DSC) of the as-prepared Mg-Mo-O nitrate-tartrate gel and Sr-Mo-O nitrate-tartrate gel was performed. Also, the crystal phase structures, surface morphologies and characteristic vibrations of the functional groups of the as-prepared compounds were investigated by X-ray diffraction (XRD), scanning electron microscopy (SEM) and infrared spectroscopy (FT-IR).

-
- [1] Z. Xia, D. Chen, Synthesis and Luminescence Properties of $\text{BaMoO}_4:\text{Sm}^{3+}$ Phosphors, *Journal of American Ceramic Society* **93**, 1397-1401 (2010).
- [2] G. Braziulis, G. Janulevicius, R. Stankeviciute, A. Zalga, Aqueous sol-gel synthesis and thermoanalytical study of the alkaline earth molybdate precursors, *Journal of Thermal Analysis and Calorimetry*, DOI 10.1007/s10973-013-3579-0.
- [3] A. Zalga, Z. Moravec, J. Pinkas, A. Kareiva, On the sol-gel preparation of different tungstates and molybdates, *Journal of Thermal Analysis and Calorimetry* **105**, 3-11 (2011).
- [4] K. Tonsuaadu, A. Zalga, A. Beganskiene, A. Kareiva, Thermoanalytical study of the YSZ precursors prepared by aqueous sol-gel synthesis route, *Journal of Thermal Analysis and Calorimetry* **110**, 77-83 (2012).

SYNTHESIS AND LUMINESCENT PROPERTIES OF DOUBLE MIXED SCHEELITE-LIKE CALCIUM MOLYBDATE-TUNGSTATE COMPOUND

Gytautas Janulevičius, Artūras Žalga

Department of Applied Chemistry, Faculty of Chemistry, Vilnius University, Naugarduko Str. 24, 03225 Vilnius, Lithuania

gytautas.janulevicius@chf.stud.vu.lt

In recent years, the tunable micro- and nano-structures with uniform shape and narrow size distribution have been of great interest in various researches and application fields. The synthesis of inorganic materials with varied morphology and texture, controlled crystallography, and micro- or nano-scale architectures is an important goal because of their novel chemical and physical properties. As one of important materials in the electro-optical industry, CaWO_4 with scheelite-type structure has been of practical interest for a long time because of its attractive application in X-ray phosphors, scintillators, laser crystal, and host lattices in electron spin resonance. Moreover, many RE^{3+} -doped scheelite related phosphors have also been studied extensively and reveal a non-radiative mechanism for energy transfer to the activator ion [1].

Energy transfer plays a crucial role in luminescent materials and the luminescence intensities are also various with the co-doped ions due to the existence of the energy transfer [2]. One of the potential high quantum yield red phosphors is Eu^{3+} incorporated CaMoO_4 which belongs to scheelite related structure. The central Mo^{6+} ion is coordinated to four oxygen atoms in tetrahedral symmetry (T_d). Hence molybdates are chemically stable and they can be a good choice for phosphors matrix.

Previous investigations have shown that the luminescent properties of $\text{CaMoO}_4:\text{Eu}^{3+}$ exhibited a desirable absorption in near-ultraviolet (UV) as well as a strong red emission. Therefore, these red phosphors can be potentially applied in LEDs for generating white light, and they have drawn considerable attention. By now, the improved luminescence is achieved via different methods, i. e. energy transfer from Bi^{3+} , charge compensation by Li^+ , Na^+ , K^+ and surfactants [3].

Synthesis process on the study of the crystal structure, surface morphology and luminescent properties of $\text{CaMo}_{0.5}\text{W}_{0.5}\text{O}_4:\text{Na}^+$, Eu^{3+} has not yet been reported, since most of $\text{CaMoO}_4:\text{RE}^{3+}$ and $\text{CaWO}_4:\text{RE}^{3+}$ phosphors were prepared by traditional solid state reaction. Zhou et al. reported the citric acid based sol-gel method which was used for the synthesis of $\text{CaMoO}_4:\text{Eu}^{3+}$ [4]. However, details on morphology of the particles were insufficient, and the influence of the complexing agent in the aqueous sol-gel synthesis on the crystallinity, morphology and optical properties is not clear. In the present work, the aqueous sol-gel method is applied to synthesize the $\text{Ca}_{0.8}\text{Eu}_{0.1}\text{Na}_{0.1}\text{Mo}_{0.5}\text{W}_{0.5}\text{O}_4$ particles. The crystal structure, surface morphology and luminescence of the as-prepared phosphors were also investigated in detail.

-
- [1] F.Yu, J. Zuo, Z. Zhao et al., Low temperature synthesis and photoluminescent properties of $\text{CaMoO}_4:\text{Eu}^{3+}$ red phosphor with uniform micro-assemblies, *Materials Research Bulletin* **46**, 1327–1332 (2011).
- [2] Y. Jin, J. Zhang, Z. Hao et al., Synthesis and luminescence properties of clew-like $\text{CaMoO}_4:\text{Sm}^{3+}$, Eu^{3+} , *Journal of Alloys and Compounds* **509**, L348–L351 (2011).
- [3] H. Wu, Y. Hu, W. Zhang et al., Sol-gel synthesis of Eu^{3+} incorporated CaMoO_4 : the enhanced luminescence performance, *Journal of Sol-Gel Science Technology* **62**, 227–233 (2012).
- [4] L. Zhou, L. Wang, F. Gong et al., Synthesis and photoluminescence of CaMoO_4 superfine powder, *Nature Science* **32**, 394–397.

INTERACTION OF GRAPHENE-BASED NANOSTRUCTURES WITH PROTEINS

Evelina Štikūnaitė¹, Jurgis Barkauskas¹

¹Department of General and Inorganic Chemistry, Vilnius University,
Naugarduko 24, Vilnius, Lithuania
evelina.stikunaitė@chf.stud.vu.lt

One of the most widely used and investigated graphene-based nanostructures is graphene oxide (GO). GO has a large surface area and a variety of oxygen functional groups (carboxy, hydroxy, epoxy, etc.). It is thought that hydroxyl and epoxy groups are present in high concentrations on the basal planes, and carboxylic groups are situated around the periphery of the residual graphene sheet (Fig. 1). Functional groups are responsible for the hydrophilic properties and dispersibility of GO in water. Due to the abundance of functional groups, GO sheets in aqueous dispersions are negatively charged [1]. Another type of graphene nanostructures is exfoliated graphene oxide (GO_E). GO_E can be produced from GO at high temperatures. GO_E has a significantly increased distance between the graphene layers and reduced amount of the oxygen-containing functional groups. After exfoliation, conjugated π electron system in graphene layer is partially restored, so GO_E is electrically conductive. The nanoscale sheets of GO and GO_E can react with molecules containing different functional groups including proteins. For example, bovine serum albumin protein due to hydrophobic and electrostatic interactions can be adsorbed on the surface of the GO [2]. In this way, graphene-based nanostructures can be adapted to different types of biosensors. Recently, GO has been adapted to DNA detection [3].

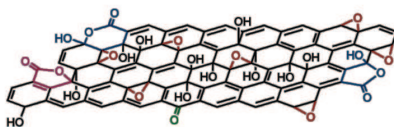


Fig.1. Structure of graphene oxide

In our work GO was synthesized from graphite using a Hummers and Offeman method. GO_E was made from GO at high temperature. For investigation of GO and GO_E interaction with protein molecules egg white proteins were used. Analysis was performed using gel electrophoresis, dynamic light scattering (DLS), scanning electron microscope (SEM), Fourier transform infrared spectroscopy (FT-IR) and Boehm titration methods. The results of the analysis showed that GO and GO_E interact differently with protein molecules. In the case of GO_E, interaction with protein molecules is weaker than GO. It is considered that this is due to the smaller amount of oxygen functional groups on GO_E surface compared with those of GO. We also determined that contact of proteins with GO and GO_E results in GO and GO_E surface morphology changes.

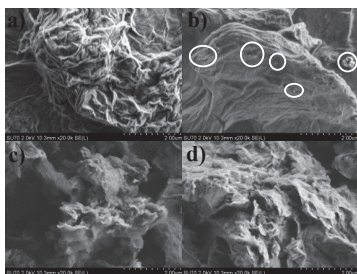


Fig. 2. SEM images of GO and GO_E. a – GO, b – GO and immobilized egg white proteins (marked), c – GO_E, d – GO_E and immobilized egg white proteins

[1] D. R. Dreyer, S. Park, C. W. Bielawski, R. S. Ruoff, The Chemistry of Graphene Oxide, Chem. Soc. Rev., **39**, 228 (2010)

[2] W. Hu, Ch. Peng, M. L. Xiaoming Li, Y. Zhang, N. Chen, Ch. Fan, Q. Huang, Protein Corona-Mediated Mitigation of Cytotoxicity of Graphene Oxide, ACS Nano, 3693-3700 (2011)

[3] J. Balapanuru, J. X. Yang, S. Xiao, Q. Bao, M. Jahan, L. Polavarapu, J. Wei, Q-H. Xu, P. K. Loh, Angew. Chem., **122**, 6699-6703 (2010)

STRUCTURAL AND CORROSION CHARACTERIZATION OF ELECTRODEPOSITED COBALT-TUNGSTEN ALLOYS

Edita. Vernickaite¹, Henrikas Cesiulis¹

¹ Department of Physical Chemistry, Vilnius University, Lithuania
henrikas.cesiulis@chf.vu.lt

Co-W is nominated as a promising environmental friendly alloy to replace hard chromium due to the satisfactory appearance of the coating, and their mechanical and anti-corrosion properties. In this work Co-W alloy coatings were deposited by DC at 60 °C onto stainless steel substrates from citrate electrolytes with different pH (5 ÷ 8). The corrosion resistance of prepared Co-W coatings was studied in 0,01 M H₂SO₄ solution open to air and at 24±1 °C. The corrosion test consisted of electrochemical impedance spectroscopy (EIS) at open circuit potential (OCP). The amplitude of the modulation potential for the EIS measurements was 5 mV, and the frequency range was 10 kHz-0.01 Hz. The structure, morphology and composition of deposited alloy coatings were determined by X-ray diffraction, scanning electron microscopy (SEM), and energy dispersive X-ray spectrometer (EDS) respectively.

The influence of the pH and current density on Co-W deposits is shown in Fig. 1. It is seen that the morphology evolves from coarse-grained lenticular growth to nodular growth. Typical changes in the diffraction patterns of Co-W coatings with different W content is shown in Fig. 2. Increasing W content in the studied alloys results in a broadening of the diffraction peaks, indicating that the crystallographic texture changes to “amorphous-like”.

The Nyquist plots for various alloys are presented in Fig. 3. Generally, the corrosion resistance of Co-W alloys increased with W content up to 25 at.% and then decreased.

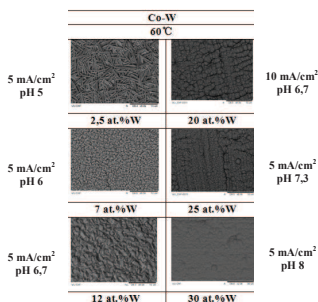


Fig. 1. SEM images of Co-W coatings.

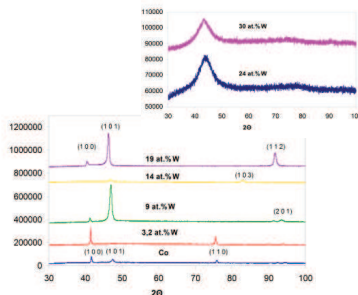


Fig.2. XRD patterns of Co-W coatings.

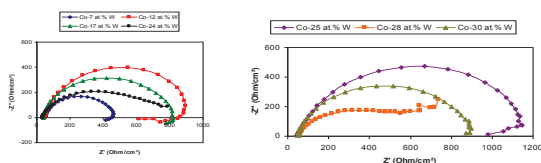


Fig. 3. EIS Nyquist plots for Co-W coatings on stainless steel in 0,01 M H₂SO₄.

Acknowledgment: This work was done under partial financial support by the grant obtained from Lithuanian agency of ESF (No. VPI-3.1-SMM-08-K-01-014).

(1)

INVESTIGATION OF H/D EXCHANGE IN THE MIXTURES OF IONIC LIQUIDS [bmim][X] AND D₂O USING RAMAN SPECTROSCOPY

Reda Sabirovaitė, Ingrida Baltmiškytė, Valdemaras Aleksa

Department of General Physics and Spectroscopy, Faculty of Physics, Vilnius University, Lithuania
reda.sabirovaitė@ff.stud.vu.lt, ingrida.baltmiskyte@ff.stud.vu.lt

There has been a growing interest in the study of room temperature ionic liquid (IL) – water mixtures, because the presence of a small amount of water can affect the ionic liquid dynamics [1, 2]. Raman spectroscopy has been used to observe the duration, until hydrogen/deuterium (H/D) exchanges, and the effect of deuterated water on the conformational equilibrium between the *gauche* and *trans* conformers on 1-butyl-3-methylimidazolium ([bmim]) cation in mixtures of heavy water (concentration $X_M=0.01$ mol). The preparation time of mixtures by the addition of room temperature D₂O to the IL (liquid or solid aggregate state) in the sample cell was from 3 to 6 minutes. Raman spectra were measured at room temperature (295 K) by the Raman spectrometer. The 514.5-nm emission line from Ar⁺ ion laser was used as an excitation source with an average power of 200 mW and the resolution of 1 cm⁻¹. There were several ionic liquids used for studies: [bmim][X], where X= Cl, Br, BF₄, CF₃SO₃.

H/D exchange was determined by observing the intensity changes of vibrational bands in 980-1040 cm⁻¹ wavenumber region. The duration of hydrogen/deuterium exchange, when all ILs were in the liquid aggregate states, in the case of [bmim][Br] – D₂O mixture was $\tau^{\text{Br}} = (39 \pm 2.5)$ hours and for [bmim][Cl] – D₂O mixture – $\tau^{\text{Cl}} = (122 \pm 20)$ min. In the case of [bmim][BF₄] – D₂O and [bmim][CF₃SO₃] – D₂O mixtures H/D exchange does not occur. The duration was much longer in the case of [bmim][Cl] – D₂O mixture was $\tau^{\text{Cl}} = (253 \pm 20)$ min when the IL was in the solid aggregate state. Vibrational band with a lower frequency is denoted as a C2-D vibration and the band with a higher frequency – C2-H. Time evolutions of the bands intensity ratio are shown in Fig.1. We suspect that H/D exchange duration depends on the purification of the sample and aggregation state of IL, it requires further investigations. Intensity changes of vibrational bands at 602 cm⁻¹ and 620 cm⁻¹ attributed to *gauche* and *trans* conformers respectively in the case of [bmim][Br] – D₂O mixture (fig 2). H/D exchange induced the increase in a *gauche* conformer of [bmim] cation in the D₂O mixtures [1].

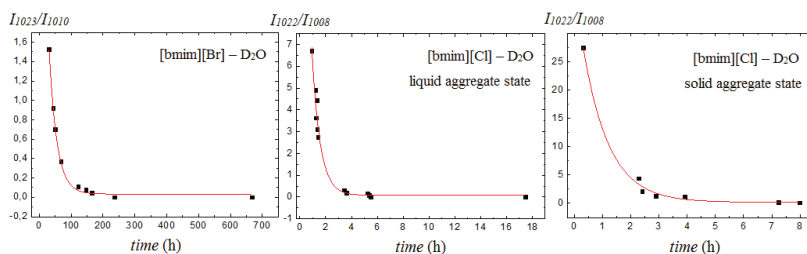


Fig. 1. Time evolution of the ratio (I_{C2-H}/I_{C2-D}) of two peaks for C2-H and C2-D.

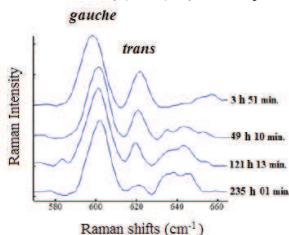


Fig. 2. [bmim][Br] – D₂O mixture Raman spectral changes in time domain.

[1] Naohiro Hatano, Mayuko Watanabe, Takahiro Takekiyo, Hiroshi Abe, Yukihiro Yoshimura, *Anomalous Conformational Change in 1-Butyl-3-methylimidazolium Tetrafluoroborate–D₂O Mixtures*, The Journal of physical chemistry A, 1208–1212 (2012).

[2] Souichi Ohta, Akio Shimizu, Yusuke Imai, Hiroshi Abe, Yukihiro Yoshimura, *Peculiar Concentration Dependence of H/D Exchange Reaction in 1-Butyl-3-methylimidazolium Tetrafluoroborate–D₂O Mixtures*, Open Journal of Physical Chemistry, 1, 70–76 (2011).

3D PES STUDY OF THE O-H GROUP VIBRATIONS IN THE METHANOL DIMER

Darya Dovgal¹, Anatolij Min'ko, George Pitsevich

Department of Physical Optics, Belarusian State University, Belarus.

d.dovgal@tut.by

Methanol (Me) is the simplest representative of nonrigid molecules with internal rotation, that is capable to self-associate. Clusters formation of different sizes and configurations leads to appearance of the second type of vibrations with large amplitude. While the first one is associated with the internal rotation around the C-O bonds, the second one is caused by the stretching vibrations of O-H bonds (ν_{OH}^d) in the donor molecules of clusters. The current study is the calculation of the frequencies of OH group vibrations in Me₂ using anharmonic approximation and by constructing 3D PES followed by comparison with experimental results.

Computations of spectral and structural characteristics of Me and Me₂ were performed in the approximation B3LYP/cc-pVTZ. It was shown earlier, that this approximation is quite acceptable for calculations of the structure, FTIR spectra and potential energy surfaces of organic molecules. Calculations of FTIR spectra in harmonic and anharmonic approximations (first approach) were performed for Me and Me₂. In the process of geometry optimization for these compounds, the fact that minima on the potential surface were reached has been supported by the absence of imaginary frequencies in vibrational spectra. Calculations of the potential surfaces (second approach) were realized in accordance with [1, 2].

According to calculations of the equilibrium configuration of Me₂, there is a formation of H-bond with great length of the hydrogen bridge (2.848 Å) and the value of the angle O-H-O that is far from the flat angle (165.26°) in the dimer. Length of O-H bond (0.9685 Å) slightly increasing in comparison with the length of hydroxyl bonds in the monomer (0.9606 Å). Slight differences in geometric parameters of acceptor and donor methanol molecules however, lead to significant differences in the force fields and in the frequencies of vibrations. Diagonal force constants of O-H group in Me and Me₂ correspondingly equals to 0.527 и 0.501 H/bor². Anharmonicity constants for ν_{OH} and ν_{OH}^d modes in Me and Me₂ correspondingly equals to -84.5 и -108.9 cm⁻¹. It should be noted that in harmonic approximation the frequency of O-H stretching vibrations in acceptor molecule (ν_{OH}^m) is more than the monomer one (ν_{OH}^m) and the frequency of the latter is significantly higher than ν_{OH}^d . In anharmonic approximation frequency ν_{OH}^d is slightly (by 2 cm⁻¹) but higher than ν_{OH}^m , at the same time the frequency ν_{OH}^d turns out to be more then by 150 cm⁻¹ lower. There is a great difference between values of the frequencies for in-plane and especially for out-of-plane bending vibrations of the donor hydroxyl group ($\delta_{OH}^{d(ip)}$ and $\delta_{OH}^{d(oop)}$ respectively). Frequency of the latter one increases to more than two times in the donor molecule of dimer in comparison with the monomer.

The further calculations were carried out in order to specify the PES associated with the hydrogen atom motion. As well as earlier [1, 2] we calculated PES moving H atom in 3D Cartesian space at the fixed positions of the other atoms of the complex. The position of the Cartesian coordinate system is described above. The motion of the hydroxyl H atom along the X axis is associated with the stretching vibrations of the hydroxyl group. In-plane and out-of-plane bending vibrations of O-H group can be associated with the motion along Y and Z axes.

Frequencies of stretching and bending vibrations of the donor hydroxyl group in methanol dimer were calculated using two independent approaches. The weakness of the hydrogen bond in the dimer and, as a consequence, moderate anharmonicity of the vibrations of O-H bond causes good agreement between vibrational frequencies obtained using both approaches. Precise experimental data on the frequency of the stretching vibration of the donor hydroxyl group in vacuum (3575.0 cm⁻¹) that are presented in the literature allow us to consider the results of the calculations in anharmonic approximation (3500.5 cm⁻¹) and results obtained by constructing 3D PES (3511.8 cm⁻¹) satisfactory enough. The previously used method, which combines the advantages of both approaches [1, 2] allows to bring the calculated value of the vibrational frequency (3535.7 cm⁻¹) even closer to the experimental. Calculated values of the frequencies of bending vibrations of the donor hydroxyl group using two approaches also have good agreement with each other and with the experimental data obtained for samples in matrix isolation. In the latter case, however, experimental studies of methanol dimer in the gas phase at low temperatures are required. We should admit that the success of the second approach is largely due to the good choice of coordinates which describe the vibrational motion of a hydroxyl group. That allowed to significantly simplify the form of the Schrödinger equation, which means the simplification of its solutions.

[1] G. A. Pitsevich, A. E. Malevich, Simple method of the formation of the Hamiltonian matrix for some Schrödinger equations describing the molecules with large amplitude motions, OPJ 2, 332-337 (2012).

[2] G. A. Pitsevich, A. E. Malevich et al. 3D calculations of O-H vibrations frequencies in Pyo-TCA complex, Vestnik of the Foundation for Fundamental Research, 63, 80-88 (2013).

SPECTRAL CHARACTERISTICS OF THE DOUBLE HYDROGEN BOND IN FORMIC ACID DIMER

Ekaterina Kozlovskaya, Alex Malevich, George Pitsevich

Department of Physics, Belarusian State University, Belarus
kozlovskayaen@gmail.com

As known molecules of formic acid forms stable even in gas phase dimers. According to microwave data they have plane structure belonging to C_{2v} group symmetry. IR and Raman spectra of formic acid dimer are also available in literature. One can see that this dimer is a good object for testing methods of large amplitude motions of hydrogen atoms involved in hydrogen bonds.

First of all the geometry of formic acid dimer was optimized under condition of preservation C_{2v} symmetry using B3LYP/cc-pVTZ approximation (Fig. 1).

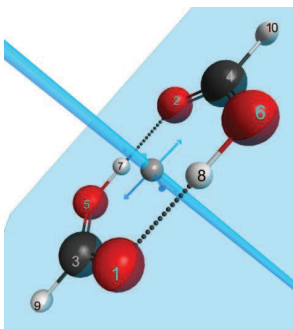


Fig. 1. Equilibrium structure of formic acid dimer.

To analyze stretching vibrations of hydroxyl group we have choose lengths of O-H bonds as vibrational coordinates. According to [1] the exact form of 2D kinetic energy operator in vibrational Hamiltonian for two stretching coordinates can be written as:

$$\left[-\frac{\hbar^2}{2\mu_{ab}} \frac{2}{I_{ab}^0 + q} \right] \frac{\partial}{\partial q} + \left[-\frac{\hbar^2}{2\mu_{bc}} \frac{2}{L_{bc}^0 + Q} \right] \frac{\partial}{\partial Q} + \left[-\frac{\hbar^2}{2\mu_{ab}} \right] \frac{\partial^2}{\partial q^2} + \left[-\frac{\hbar^2}{2\mu_{bc}} \right] \frac{\partial^2}{\partial Q^2} - \frac{\hbar^2 \cos \theta}{M_s} \frac{\partial^2}{\partial q \partial Q} = \quad (1)$$

$$-\frac{\hbar^2}{2\mu_{ab}} \frac{\partial^2}{\partial q^2} - \frac{\hbar^2}{2\mu_{bc}} \frac{\partial^2}{\partial Q^2} - \frac{\hbar^2}{2\mu_{ab}} \frac{2}{I_{ab}^0 + q} \frac{\partial}{\partial q} - \frac{\hbar^2}{2\mu_{bc}} \frac{2}{L_{bc}^0 + Q} \frac{\partial}{\partial Q} - \frac{\hbar^2 \cos \theta}{M_s} \frac{\partial^2}{\partial q \partial Q}$$

If we will consider q and Q as $\Delta l_{O,H_7}$ and $\Delta l_{O,H_8}$, take into account that $A \rightarrow H$; $B \rightarrow O$; $C \rightarrow H$ and the fact that kinematic interaction between this internal coordinates is absent we can rewrite this expression as:

$$\left[-\frac{\hbar^2}{2\mu_{oi}} \frac{2}{I_{oi}^0 + q} \right] \frac{\partial}{\partial q} + \left[-\frac{\hbar^2}{2\mu_{oi}} \frac{2}{L_{oi}^0 + Q} \right] \frac{\partial}{\partial Q} + \left[-\frac{\hbar^2}{2\mu_{oi}} \right] \frac{\partial^2}{\partial q^2} + \left[-\frac{\hbar^2}{2\mu_{oi}} \right] \frac{\partial^2}{\partial Q^2} = \quad (2)$$

$$-\frac{\hbar^2}{2\mu_{oi}} \frac{\partial^2}{\partial q^2} - \frac{\hbar^2}{2\mu_{oi}} \frac{\partial^2}{\partial Q^2} - \frac{\hbar^2}{2\mu_{oi}} \frac{2}{I_{oi}^0 + q} \frac{\partial}{\partial q} - \frac{\hbar^2}{2\mu_{oi}} \frac{2}{L_{oi}^0 + Q} \frac{\partial}{\partial Q}$$

1D and 2D potential energy surfaces (PES) calculations were carried out in the approximation B3LYP/cc-pVTZ. The energy values were calculated with the spacing of 0.1 Å between the nodes on the rectangular grid of the linear dimensions $d \times D = 1.6 \times 1.6$ Å². The variation boundaries of the coordinates were used $\Delta q \in [-0.8; 0.8]$ and $\Delta Q \in [-0.8; 0.8]$. The analytical representation of potential energies $U(q)$; $U(Q)$ and $U(q, Q)$ were made by the third order spline interpolation using Mathematica package [2]. The results of this calculation will be reported.

[1] G.Pitsevich, V.Balevichus, Hydrogen bonded pyridine *N*-oxide/trichloroacetic acid complex in polar media: 2D potential energy surface and O–H...O vibration analysis using exact vibrational Hamiltonian, J. Mol. Struct. (2014) in press.

[2] Mathematica, Wolfram Research, Inc., <http://www.wolfram.com/mathematica/>

INVESTIGATION OF THE SOLVENT POLARITY INFLUENCE ON THE LARGE AMPLITUDE VIBRATIONS FREQUENCY IN THE HYDROGEN-BONDED COMPLEXES.

Yauheni Sliaptsov, Alex Malevich, George Pitsevich.

Department of Physical Optics, Belarusian State University, Belarus.

zhenya.sleptsov@gmail.com

As well-known molecular structure and molecular vibrational spectra are different in gas, liquid and solid phases. Usually theoretical background for assignments of molecular spectra in liquid and solid phase based on calculations for free molecule. But this is incorrect. On other hand the current situation with the accounting of the medium influence on the IR spectra of dissolved molecules remains controversial. From the description of quantum-chemical package is not clear whether the static permittivity of the medium (ϵ_{stat}) used both for geometry optimization and IR frequency calculations or frequency dependence of ϵ is taken into account in the last case. There are also no recommendations for PES calculations for molecules and complexes in solution. Only recently the leading developers of PCM started to focus on the effect of the solvent on the frequency of anharmonic vibrations [1]. Obviously, the user's choice is limited to two options:

1) optimize the geometry and calculate PES dissolved complex for $\epsilon = \epsilon_{stat}$

2) optimize the geometry of the dissolved complex for $\epsilon = \epsilon_{stat}$ and then to calculate the PES for permittivity of the medium at optical frequencies ($\epsilon = \epsilon_{opt}$) or for some intermediate value between ϵ_{opt} and ϵ_{stat} . Both options are not perfectly logical, since in case 1) we presumably relatively overestimate the ϵ value, and in case 2) we building the PES for the nonequilibrium configuration of complex. Since the standard recommendation for users GAUSSIAN and GAMESS package requires working with equilibrium configurations we used first way studying O-H vibrations for *PyO TCA* complex in acetonitrile [2]. The ν_{OH} wave numbers for both conformers obtained in the anharmonic approximation are far from the experimental ones and extremely low. At the same time the corresponding values obtained in 3D PES calculations are close for both conformers (1006 and 1027 cm^{-1}) and are in a good agreement with the experimental value in spite of the simplified form of the kinetic energy operator in Hamiltonian. A good agreement between the frequencies of hydroxyl group bending vibrations obtained in the anharmonic approximation and using the 3D PES calculations for both conformers is worth to be noted. The comparative analysis of the PESs of the free complex and that dissolved in acetonitrile has shown that the anharmonicity of the hydroxyl group vibrations increases for the dissolved complex.

Our current interest is to find the way by changing parameters of PCM to save good agreement between calculated and experimental data using for permittivity of the medium some intermediate value between ϵ_{opt} and ϵ_{stat} . In doing so we calculated number of 1D potential curves focusing on stretching O-H vibrations only. As well as earlier [2] we assumed that hydroxyl H atom moves at the fixed positions of the other atoms of the complex. For convenience the origin of Cartesian coordinate system in the equilibrium configurations of the complex is placed at H atom, X axis is directed to the nearest oxygen atom (along O-H bond). Y axis is located in the plane formed by atoms O-H---O, and Z axis supplements axes X and Y to the right-hand triple. So the motion of the hydroxyl H atom along the X axis is associated with the stretching vibrations of the hydroxyl group. Potential energy values were calculated using B3LYP/cc-pVTZ approximation with different PCM parameters for acetonitrile in some points for the intervals of H shifting from the equilibrium position from -1 Å to +0.5 Å along X axis. In order to determine the vibrational frequencies for the hydroxyl group it was necessary to solve the Schrödinger equations:

$$-R \frac{d^2 \Psi(x)}{dx^2} + U(x) \Psi(x) = E \Psi(x). \quad (1)$$

where $R = \frac{\hbar^2}{2m_{H^*} l_0^2} = 16.735 \text{ cm}^{-1}$; $x = \frac{\Delta X}{l_0}$, - dimensionless variable ($l_0 = 1 \text{ Å}$). The equation (1) was solved

numerically using the program set [3]. The way of the solution is partly described in [2] and in more detail in [4]. The results of this calculation will be reported.

[1] C. Cappelli, F. Lipparini et al., Towards an accurate description of anharmonic infrared spectra in solution within the polarizable continuum model: Reaction field, cavity field and nonequilibrium effects. *J.Chem.Phys.* **135**, 104505-1-15 (2011).

[2] G. Pitsevich, A. Malevich et al., Pyridine *n*-oxide/trichloroacetic acid complex in acetonitrile: FTIR spectra, anharmonic calculations and computations of 1-3D potential surfaces of O-H vibrations. *Spectrochim. Acta A*, **120**, 585-594 (2014).

[3] Mathematica, Wolfram Research, Inc. <http://www.wolfram.com/mathematica/>

[4] G.A. Pitsevich, A.E. Malevich, Simple method of the formation of the Hamiltonian matrix for some Schrödinger equations describing the molecules with large amplitude motions. *OPJ* **2** 332-337 (2012).

NEW POLYMERIC PROTON CONDUCTOR BASED ON CELLULOSE FUNCTIONALIZED BY IMIDAZOLE MOLECULES

Iga Smolarkiewicz^{1,2}, Adam Rachocki¹, Katarzyna Pogorzelec-Glaser¹,
Radosław Pankiewicz³, Paweł Ławniczak¹, Jadwiga Tritt-Goc¹

¹Institute of Molecular Physics, Polish Academy of Sciences, M. Smoluchowskiego 17, 60-179 Poznań, Poland

²NanoBioMedical Centre, Adam Mickiewicz University in Poznań, ul. Umultowska 85, 61-614 Poznań, Poland

³Faculty of Chemistry, Adam Mickiewicz University in Poznań, ul. Umultowska 89b, 61-614 Poznań, Poland
smolarkiewicz@ifmpan.poznan.pl

The content of the work is in the mean stream of the research for new proton conducting materials exhibiting high electrical conductivity (above 0.1 S/m) which can be used in the temperature range above 100 °C. Such materials as solid electrolytes have a big potential to be applied as membranes in fuel cells or batteries.

We expect that the combination of selected polymers natural in origin (e.g., cellulose) with heterocyclic molecules containing nitrogen atoms (e.g., imidazole and its derivatives) will allow for obtaining new, biodegradable proton conducting materials.

The integration of heterocyclic molecules in the polymer matrix should result in a dynamic network of hydrogen bonds linking the polymer macromolecules to heterocyclic molecules whose continuous reorganization will enable the transport of protons in the polymer matrix. Proton transport mechanism at the molecular level is still discussed in the proton conductors known up to now. Generally, the Grotthuss mechanism is postulated - a two-step process involving the proton transfer in the hydrogen bond with simultaneous reorientation of the imidazole ring. The research will be conducted in three main areas: the molecular basis of proton transport, diffusive motion, reorganization of the hydrogen bond network.

The newly synthesized compound was examined for thermal stability and thermal decomposition by differential scanning calorimetry (DSC) and thermogravimetry analysis (TGA). Samples of microcrystalline cellulose functionalized by imidazole molecules were analysed by means of impedance spectroscopy. The obtained spectra have shown the differences in conductivity of microcrystalline cellulose matrix and that of doped by imidazole molecules. Further systematic studies will be focused on the crystal structure, molecular dynamics, and electric conductivity properties to identify the characteristics of proton transport mechanism in new proton-conducting materials.

Poster session 2

Semiconductor and condensed matter physics
Material sciences and modern technologies
Functional materials and derivatives

SUB-TERAHERTZ IMAGING SYSTEM IN TRANSMITTANCE GEOMETRY

Karolis Madeikis^{1,2}, Linas Minkevičius¹, Gintaras Valušis^{1,2}

¹ Semiconductor Physics Institute of Center for Physical Sciences and Technology,
A. Goštauto str. 11, LT-01108, Vilnius, Lithuania

² Vilnius University Faculty of Physics, Saulėtekio al. 9, bldg. III, LT-10222 Vilnius, Lithuania

karolismadeikis@gmail.com

Advantages of non-destructive and non-ionizing terahertz (THz) waves applications for security and imaging [1] remains the main stimulus to develop compact and sensitive THz imaging systems which would operate at room temperature. This work is dedicated for THz source based on frequency multiplying chain analysis and usage in imaging systems.

The “Virginia Diodes” terahertz source was analyzed by measuring emitted power and beam profile at 180-210 GHz, 285-313 GHz and 555-630 GHz frequency ranges and at separate distances from THz source. Power of terahertz source was measured using Thomas Keating power meter, signal generator modulation frequency was 33 Hz. Beam profiles of the source were imaged at 3-12 cm distance from antenna with no additional optical components. Spatial resolution was set of 0.3 mm in y-direction, and 0.1 mm in x-direction. Shape of the emitted beam was measured close to Gaussian with small side lobes at 180-210 GHz, 285-313 GHz and 555-630 GHz frequencies.

Set-up of terahertz imaging system in transmission geometry is shown in Fig. 1. The signal was detected with the “bow-tie” diode [2]. The smart cards and Radio-frequency identification (RFID) cards were imaged. Signal generator modulation frequency was set to 2 kHz, positioning stage spatial resolution is 0.1 mm in x-direction and 0.3 mm in y-direction. Image of the card, where antenna and chip is clearly visible, is presented in Fig. 2. As we can see, integrated objects with different absorption signatures can be screened and identified without destroying the sample.

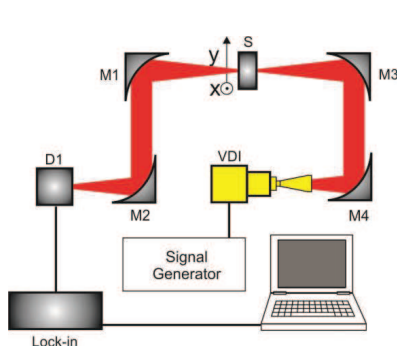


Fig. 1. Set-up of imaging system (D1 is detector, M are parabolic mirrors, S is sample, VDI is THz source).

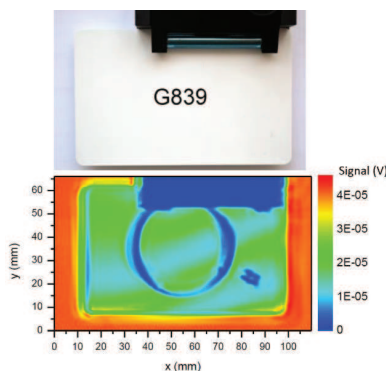


Fig. 2. RFID card image at 200 GHz.

To summarize, the performance of the electronic THz sources emitting at 180-210 GHz, 285-313 GHz and 555-630 GHz frequencies was tested. The imaging setup based on electronic THz source was used to image samples at 200 GHz, 300 GHz and 600 GHz frequencies.

ACKNOWLEDGEMENT

This work was supported by Research Council of Lithuania under the grant “HeTeFo” MIP-093/2012.

- [1] John F Federici, Brian Schulkin, Feng Huang, Dale Gary, Robert Barat, Filipe Oliveira and David Zimdars, THz imaging and sensing for security applications—explosives, weapons and drugs, *Semicond. Sci. Technol.* **20** (7), 266-280 (2005).
- [2] L. Minkevičius, V. Tamošiūnas, I. Kašalynas, D. Selinta, G. Valušis, A. Lisauskas, S. Boppel, H. G. Roskos and K. Köhler “Terahertz heterodyne imaging with InGaAs-based bow-tie sensors”, *Appl. Phys. Lett.* **99** (13), 131101 (2011).

SPECTROSCOPIC ELLIPSOMETRY STUDY OF THE OPTICAL DIELECTRIC FUNCTION OF ZINC

Adomas Eikevičius, Saulius Tumėnas

Semiconductor optics laboratory, Center for Physical Sciences and Technology, Vilnius, Lithuania
a.eikevicius@gmail.com

In this work we present spectroscopic ellipsometry (SE) study of monocrystalline zinc carried out in the 0.73 – 6 eV spectral range. The optical response of Zn, uniaxial material, depends significantly on the polarization of the probing light beam. The Zn optical features due to interband optical transitions across pseudogaps are quite different for light polarized along the optical axis ($\mathbf{E} \parallel C_6$) and for the light polarized perpendicular to the optical axis ($\mathbf{E} \perp C_6$). The main experimental problem for determination of both the ordinary and extraordinary components of the zinc dielectric function is that the determination requires measurements from several crystallographic planes. In Zn, only the (001) surface can be disclosed by a cleavage. The (110) surface of Zn was prepared by careful mechanical polishing, chemical polishing and, finally, by Ar⁺ sputtering in a UHV chamber.

The optical response of Zn was measured using a dual rotating compensator multichannel ellipsometer RC2 (J. A. Woollam Co Inc.) in the 0.73 – 6 eV spectral range, in the steps of 0.01 eV at various incidence ϑ and azimuthal ϕ angles in the intervals of 45–80° and 0–90°, respectively. At each incidence and azimuthal angle, the experimental ellipsometric parameters Ψ and Δ were simultaneously recorded. The values of Ψ and Δ changed by azimuthally rotating the (110) surface indicating in-plane anisotropy.

An analysis of the data was carried out using the software CompleteEASE (J. A. Woollam Co., Inc.), which can perform a batch analysis of data for all wavelengths. The ordinary component of the Zn dielectric function in the first iteration was determined from the cleaved Zn (001) SE data. The extraordinary component was deduced by analyzing the Mueller matrix data recorded from the Zn (110) sample. Figure 1 illustrates the analysis by representing the experimental ellipsometric parameters of Zn (dots) at different azimuths and results of modeling (curves). Optical model was based on a uniaxial substrate covered with ultrathin surface overlayer. Substrate was parameterized using B-splines [1] and surface layer was treated as dielectric and parameterized using Cauchy model.

The successful fit of numerous ellipsometric data allowed for a determination of both ordinary and extraordinary components of zinc dielectric function tensor.

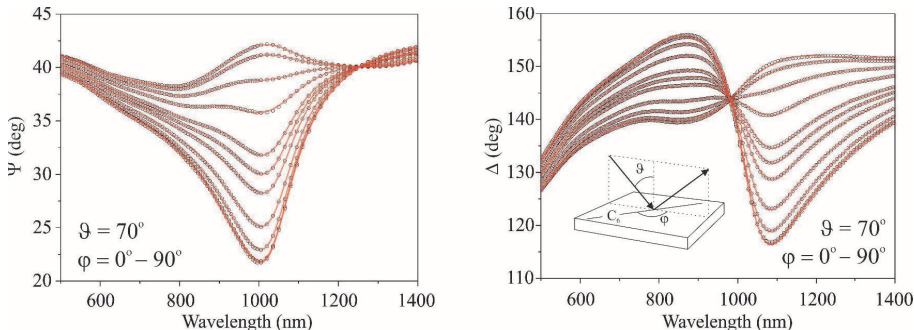


Fig 1. The ellipsometric parameters recorded from the Zn (110) surface at $\vartheta = 70^\circ$ and at different azimuthal angles $\phi = 0^\circ - 90^\circ$ in steps of 10° . Dots present experimental data and curves correspond to results of analysis.

[1] B. Johs and J. S. Hale, Dielectric function representation by B-splines, Phys. Status Solidi A 205, 715 (2008)

DIELECTRIC PROPERTIES OF GRAPHITE LOADED EPOXY RESIN COMPOSITES

Ieva Kranauskaitė¹, Jan Macutkevič¹, Jūras Banys¹, Alain Celzard², Stefano Bellucci³

¹Faculty of Physics, Vilnius University, Vilnius, Lithuania

²IJL – UMR CNRS 7198 AND LERMAB – ENSTIB, Epinal, France

³INFN-Laboratori Nazionali di Frascati, Frascati, Italy

ieva.kranauskaite@ff.stud.vu.lt

Polymer composites with various carbon inclusions, like single- or multi- walled carbon nanotubes, carbon black, graphite or graphene are interesting for fundamental research and very attractive for various applications due to possibility to manipulate composite properties at nanoscale. The value of dielectric permittivity and electrical conductivity of these composites could be very high close to percolation threshold. However, despite of lot of publications is a lack of deep understanding relation between carbon filler microscopic properties and composite dielectric properties [1].

In this contribution were investigated epoxy resin composites filled with various size graphite flake inclusions, namely natural graphite (diameter of the graphite flakes are $d = 500 - 750 \mu\text{m}$), coarse graphite ($d = 150 - 800 \mu\text{m}$), medium graphite ($d = 44 - 75 \mu\text{m}$), fine graphite ($d = 15 - 44 \mu\text{m}$) and exfoliated graphite. The concentration of graphite inclusions was from 0.25 to 2.0 wt. %. Dielectric investigations were performed in frequency range from 20 Hz to 1 MHz, while the temperature interval was from 10 K to 450 K, by measuring loss tangent and capacity with LCR meter (HP – 4284A).

The dielectric properties of all investigated composites, except composites with exfoliated graphite, are very similar to the dielectric properties of pure resin. At temperatures close to room temperature the dielectric dispersion in these composites is mainly caused by alfa relaxation in pure epoxy resin. At higher temperatures, similarly to pure epoxy resin electrical conductivity appears. The concentration dependence of conductivity activation energy and freezing temperature will be discussed in this presentation. In contrast in composites with exfoliated graphite a percolation occurs at concentration 1.5 wt. %.

This research is funded by the European Social Fund under the Global Grant measure.

[1] W. Bauhofer, J. Z. Kovacs, *Composite Science and Technology* 69, 1486 (2009)

Application of Lichtenecker's Mixing Formula for Barium Titanate and Nickel-Zinc Ferrite Composite Ceramics

Aurimas Sakanas¹, Robertas Grigalaitis¹, Jūras Banys¹, Liliana Mitoseriu², Vincenzo Buscaglia³, Paolo Nanni⁴

¹Faculty of Physics, Vilnius University, Vilnius, Lithuania

²Physics Department, University "Alexandru Ioan Cuza", Iasi, Romania

³Institute of Energetics & Interphases, IENI-CNR, Genoa, Italy

⁴Department Chemical & Process Engineering, University Genoa, Genoa, Italy
aurimas.sakanas@ff.vu.lt

There are numbers of various mixing formulae proposed for calculating the effective permittivity of a mixture [1]. For such analysis, the most suitable approach taken is the effective medium approximation (EMA). One of the main models, derived using differential analysis is Lichtenecker's mixing formulae [2]. The effective macroscopic response of the composite mixture is calculated according to its constituents.

Barium titanate and nickel-zinc ferrite composites, having chemical formula $x\text{BaTiO}_3 - (1-x)\text{Ni}_{0.5}\text{Zn}_{0.5}\text{Fe}_2\text{O}_4$ with the volume fractions $x=0.466, 0.567$ and 0.67 , were investigated by the means of the broadband dielectric spectroscopy methods. The measured frequency and temperature ranges are 20 Hz to 50 GHz and 100 K to 500 K. Dielectric spectroscopy results indicate that the properties of pure barium titanate are preserved however, noticeable conductivity is induced due to the ferrite phase of the composite.

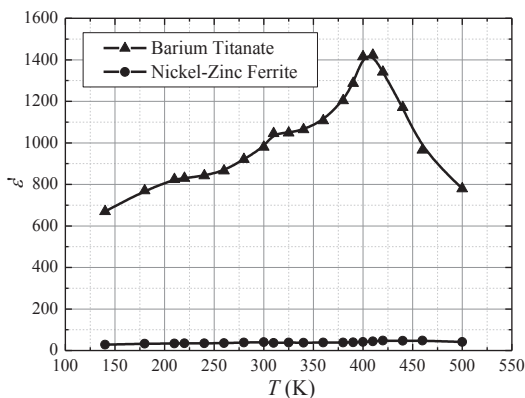


Fig. 1: The real part of dielectric permittivity of barium titanate and nickel-zinc ferrite at 100 MHz frequency, calculated from the experimental results using Lichtenecker's mixing formula

Lichtenecker's mixing formula was adapted in the approximation process of the experimental effective permittivity data of the composite ceramics. The results of the calculated dielectric response in composites, presented in Figure 1, manifest the presence of three peaks corresponding to phase transitions of pure barium titanate. The values are in a good agreement with the typical values which could be expected for barium titanate ceramic materials. On the other hand, nickel-zinc ferrite exhibits almost no dependency on the temperature, and the real part of permittivity is much smaller in comparison to the ferroelectric part.

[1] L. Jylha, and A. Sihvola, "Equation for the effective permittivity of particle-filled composites for material design applications", J. Phys. D: Appl. Phys., vol 40, p. 4966 – 4973, 2007.

[2] T. Zakri, J. P. Laurent, and M. Vaublin, "Theoretical evidence for 'Lichtenecker's mixture formulae' based on the effective medium theory", J. Phys. D: Appl. Phys., vol. 31, p. 1589-1594, 1998.

STUDY OF DEEP LEVEL PROPERTIES IN CDTE BY PHOTO-HALL EFFECT MEASUREMENTS

Musiienko Artem, Roman Grill

Faculty of Mathematics and physics, Charles University in Prague, Czech Republic

musiienko.art@gmail.com

CdTe is a compound semiconductor involving a large concentration of defects produced during growth and material processing. A large number of defects have been detected using a number of techniques: the deep-level transient spectroscopy(DLTS), photo-induced current transient spectroscopy(PICTS)[1]. But, for highly resistive materials DLTS is not useful. Also, PICTS can't give information about the sign of Hall voltage.

CdTe has long been known as an interesting semiconductor with applications such as gamma ray detection and solar cell fabrication. Many of the physical properties of CdTe are controlled to some extent by the relative position of the energy levels within the forbidden gap associated either native defects or impurities. Only by understanding the nature and origin of the defects, can their concentration be controlled[2].

In this presentation we extend our previous studies of deep levels in CdTe done by photo-conductivity and Pockels effect measurements [3]. In view of the fact that these methods bestow only indirect information on the character of principal deep levels, we study the transport of photoexcited charge in the magnetic field where the sign of Hall voltage gives us an explicit evidence on the level [4].

The principle of the research is apparent in attached figure(fig.1). In case of trap level localized in the upper part of the forbidden gap the dominant optical transitions will excite electrons at the energy $E_{T1} - E_V$ from the valence band creating positive holes there and inducing positive sign of the Hall voltage. Oppositely, the level at the bottom part of the gap will induce the negative Hall voltage after the excitation at the energy $E_C - E_{T2}$.

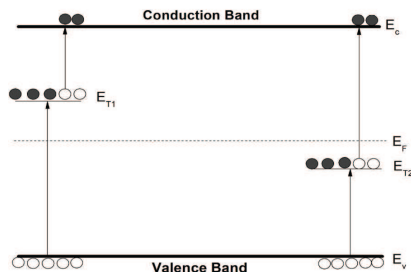


Fig. 1. Distribution of energy levels in the gap.

Spectral measurements of the photo-Hall effect were used to determine energy levels responsible for polarization and to find the optimal wavelength for optical depolarization of the detectors[3].

- [1] Xavier Mathew, Photo-induced current transient spectroscopic study of the traps in CdTe, Solar Energy materials 76, 225-242(2003)
- [2] R.E. Kremer, W.B. Leigh, Deep levels in CdTe, Journal of Crystal Growth 86, 490-496 (1988).
- [3] J. Franc, V. Dedič, R. Grill, Flux-dependent electric field changes in semi-insulating CdZnTe, J. Phys. D: Appl. Phys. 46 (2013).
- [4] P. Höschel, P. Moravec, A. Martinaitis, Study of the Photo-Hall Effect on Single Crystals of CdTe, Phys. Stat. sol. 48, 1978.

INVESTIGATION OF SILICON SUBSTRATES WITH RARE-EARTH-OXIDE BUFFER LAYERS FOR GaN GROWTH

Agnė Kalpakovaitė¹, Tomas Grinys², Rytis Dargis³

¹ Faculty of Physics, Vilnius University, Saulėtekio av. 9, 10222 Vilnius, Lithuania

^{1,2} Institute of Applied Research, Vilnius University, Saulėtekio av. 10, 10223 Vilnius, Lithuania

³ Translucent Inc., 952 Commercial St, Palo Alto CA 94303, USA

Agne.Kalpakovaitė@ff.stud.vu.lt

Gallium nitride is typically grown on sapphire substrates, but this technology is expensive at large diameters. This problem could be solved by growing GaN on silicon wafers. Growth on silicon is complicated because of large difference in thermal expansion coefficient and lattice mismatch between gallium nitride and silicon, which can lead to bowing and furthermore cracking of wafers.

In this work we studied a new method of improving GaN growth on silicon by inserting rare-earth-oxide buffer layers (Er_2O_3 and Gd_2O_3) into the structure. We investigated thermal stability of these oxide-coated substrates and crystalline quality of GaN grown on them.

Two types of substrates, provided by Translucent Inc., were investigated – silicon wafer with rare-earth-oxide layers, and distributed Bragg reflectors (DBR) (Fig. 1). Research showed, that silicon wafers with erbium and gadolinium oxide layers (Fig. 1a) were thermally stable at temperatures up to 1050 °C although originally had slightly cracked surface. On these substrates GaN was grown by metalorganic chemical vapor deposition (MOCVD) method. Full width at half maximum (FWHM) of samples GaN (0002) X-ray diffraction (XRD) omega scan was measured to be 822 arcsec. DBR substrate surfaces had no cracks, but were thermally unstable at temperatures higher than 900 °C. Optical microscopy images of those substrates showed damaged regions after annealing (Fig. 3), which might have emerged due to chemical reactions between Si layers and oxides at high temperatures. In both cases the grown GaN layers had a smooth mirror like surface with dense network of cracks.

Because of their thermal stability silicon wafers with rare-earth-oxide layers are suited for GaN growth by MOCVD, but further research is needed in order to produce crack free GaN.

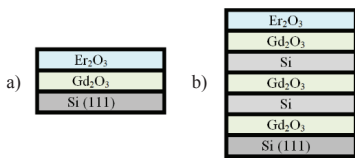


Fig. 1. Structures of substrates: a) silicon wafer with rare-earth-oxide layers, b) DBR.

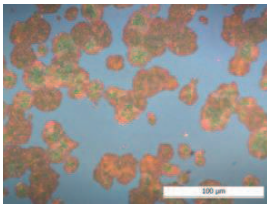


Fig.3 Optical microscopy image of DBR substrate after annealing at 1000 °C.

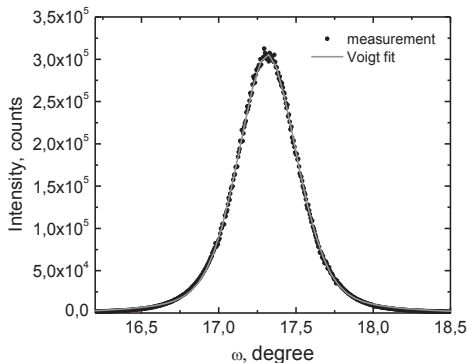


Fig 2. XRD omega scan over GaN (0002) peak for GaN samples grown on silicon with rare-earth-oxide layer.

CORRELATIVE ANALYSIS OF THE IN SITU CHANGES OF CARRIER DECAY AND PROTON INDUCED PHOTOLUMINESCENCE IN GaN

Arnoldas Jasiūnas, Dovilė Meškauskaitė, Eugenijus Gaubas, Tomas Čeponis

Vilnius University, Institute of Applied Research, Vilnius LT-10222, Lithuania
arnoldas.jasiunas@ff.stud.vu.lt

Crystalline GaN is a promising material for manufacturing of the radiation hard particle detectors capable to operate in harsh areas of particle accelerators [1]–[4]. Moreover, GaN crystals show rather efficient luminescence properties under excitation by high energy radiation [5]–[7]. Thereby, GaN material can be utilized for fabrication of the combined device which is able to operate both as scintillating and charge collecting detector. However, efficiency of such detectors and their functionality is investigated insufficiently.

This work is addressed to study of the efficiency of proton induced steady-state photoluminescence. To evaluate the density of the high energy proton induced excess carriers, the correlation between the microwave probed photoconductivity (MW-PC) transients and the proton induced luminescence (PI-L) intensity has been examined. The proton energy range (1.6 MeV) has been chosen to implement the nearly homogeneous and rather strong excitation of the 2.5 μm thick GaN epi-layers. To estimate radiation hardness of such material, evolution of MW-PC and PI-L characteristics has been studied by the in situ measurements of the changes of PI-L intensity and MW-PC decay rate during exposure to a proton beam reaching fluences up to 10^{15} cm^{-2} .

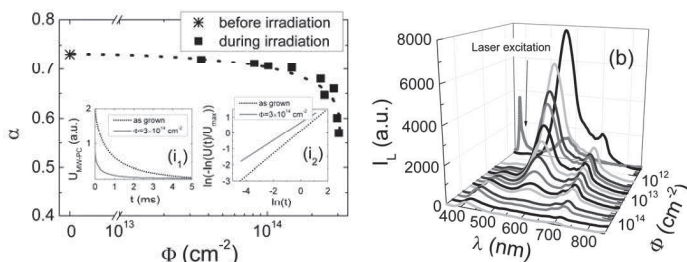


Fig. 1. Variation of the stretched-exponent (SE) index dependent on irradiation fluence measured in situ (left panel). Inset i2 in this panel represents a traditional plot employed for analysis of MW-PC transients illustrated within inset i1 for evaluation of SE index of carrier decay in the non-irradiated and proton irradiated GaN. In the right panel, evolution of PI-L spectra with irradiation fluence is demonstrated. Here, the LS-L spectrum is also shown.

The 2.5 μm thick GaN epi-layers [3]–[5], [8] grown by metal-organic chemical vapour deposition (MOCVD) technique on sapphire substrate have been examined. Dislocation density in these epi-layers was evaluated to be of about 10^{10} cm^{-2} .

Comparison of luminescence spectra induced by proton beam and by a laser pulse enabled us to evaluate the efficiency of carrier pair generation, - being of $1 \times 10^7 \text{ cm}^{-3}$ per 1.6 MeV proton, and 40 carrier pairs per micrometer of layer depth. This result indicates that GaN layers can be an efficient material for detection of particle flows. It has been demonstrated that GaN material can also be a rather efficient scintillating material within several wavelength ranges.

-
- [1] P. J. Sellin and J. Vaitkus, Nucl. Instrum. Methods Phys. Res. A 557, 479 (2006).
 [2] E. Gaubas, S. Jursenas, R. Tomasiunas, J. Vaitkus, A. Zukauskas, A. Blue, M. Rahman, and K. M. Smith, Nucl. Instrum. Methods Phys. Res. A 546, 247 (2005).
 [3] E. Gaubas, V. Kovalevskij, A. Kadys, M. Gaspariunas, J. Mickevicius, A. Jasiunas, V. Remeikis, A. Uleckas, A. Tekorius, J. Vaitkus, and A. Velicka, Nucl. Instrum. Methods Phys. Res. B 307, 370 (2013).
 [4] E. Gaubas, K. Kazlauskas, R. Tomasiunas, J. Vaitkus, and A. Zukauskas, Appl. Phys. Lett. 84, 5258 (2004).
 [5] E. Gaubas, S. Jursenas, S. Miasojedovas, J. Vaitkus, and A. Zukauskas, J. Appl. Phys. 96, 4326 (2004).
 [6] A. Y. Palyakov, A. S. Usikov, B. Theys, N. B. Smirnov, A. V. Govorkov, F. Jomard, N. M. Shmidt, and W. V. Lundin, Solid-State Electron. 44, 1971 (2000).
 [7] P. Pittet, G.-N. Lu, J.-M. Galvan, J.-M. Bluet, I. Anas, J.-Y. Giraud, and J. Balosso, Opt. Mater. 31, 1421 (2009).
 [8] E. Gaubas, T. Čeponis, A. Jasiūnas, E. Jelமாகas, S. Jursenas, A. Kadys, T. Malinauskas, A. Tekorius, and P. Vitta, AIP Adv. 3, 112128 (2013).

CORRELATED ANALYSIS OF GROWN-IN IMPURITIES AND RECOMBINATION PARAMETERS IN DIAMOND CRYSTALS

Arnoldas Jasiūnas, Eugenijus Gaubas, Tomas Čeponis, Jevgenij Pavlov

Vilnius University, Institute of Applied Research, Vilnius LT-10222, Lithuania
arnoldas.jasiunas@ff.stud.vu.lt

Diamond is one of the most promising wide-gap materials for applications in high power/high frequency sensors/transducers and radiation tolerant particle detectors [1]. However, the impact of the technological defects is clarified insufficiently, when the prevailing metal and nitrogen impurities are distributed non-homogeneously. The excess carrier lifetime is one of the most sensitive parameters to electrically active defects in material. Also, carrier lifetime is the main limiting factor for charge collection efficiency in diamond based sensors and detectors. Thereby, control of the recombination parameters enables ones to correlate the distribution of the technological impurities with the grown-in defects and to separate the prevailing channels of radiative and non-radiative recombination.

The wafer samples were sliced from the diamond single crystals (Fig. 1), synthesized by the high pressure (4.5-5.0 GPa) and high (1350-1450C) temperature (HPHT) technology using the Ni-Fe liquid solvent/catalyst system.

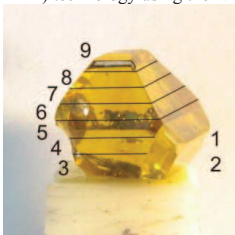


Fig. 1. HPHT grown synthetic diamond (numbers represent different samples cut from the crystal bulk).

In this work, the profiling of the microwave probed photoconductivity transients and time resolved photoluminescence spectra have synchronously been performed on the synthetic diamond wafer samples in order to clarify correlation of the distribution of the grown-in defects and carrier radiative and non-radiative recombination channels. To estimate the microscopic characteristics of the grown-in defects, the microscopy imaging and the angular and temperature dependent EPR spectroscopy have been performed (Fig. 2a). FTIR spectrometry (Fig. 2b) has been performed on diamond samples in order to measure the variations of the grown-in impurity density by analyzing intensities of defect specific IR peaks [2].

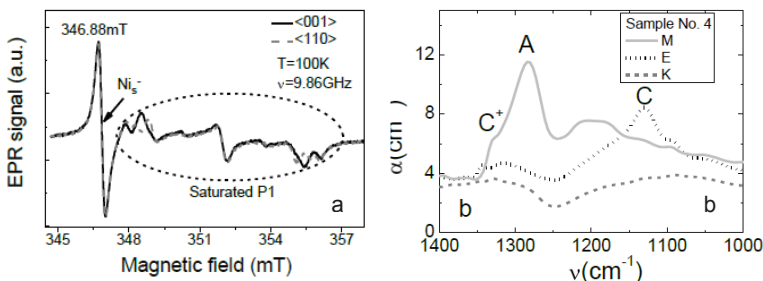


Fig. 2. EPR spectra of diamond sample (a), FTIR spectra in three various places of diamond sample (b).

The correlation between the parameters extracted from the absorption spectra and recombination characteristics has also been obtained. The changes of carrier lifetime ascribed to the radiative and non-radiative recombination have been resolved. The prevailing grown-in point defects, associated with neutral and charged nitrogen impurity complexes as well as the pairs of nitrogen atoms on neighbouring sites, and the precipitates have been unveiled.

[1] D. R. Kania, M. I. Landstrass, M. A. Plano, L. S. Plan, and S. Han, Diamond radiation detectors, *Diamond and Related Materials* **2**, 1012-1019 (1993).

[2] S.C.Lawson, D.Fisher, D.C.Hunt, and M.E.Newt, On the existence of positively charged single-substitutional nitrogen in diamond. *J.Phys.: Condens. Matter.* **10**, 6171-6180 (1998).

Experimental techniques for study of nonequilibrium carrier dynamics in highly excited SiC crystals

D. Dargis, G.Liaugaudas

Department of Semiconductor, Vilnius University, Lithuania

Donatas.Dargis@ff.stud.vu.lt

Progress in the epitaxial growth technologies of SiC has expanded its application for power devices, such as high frequency power controllers and bipolar switching devices, which operate under high injection conditions. Therefore, in addition to the structural quality of the grown materials, appropriate attention must be paid to the peculiarities of recombination and transport processes at high nonequilibrium carrier densities.

In this work, we present a study of non-equilibrium carrier recombination and diffusion in various p-type SiC polytypes using differential transmittivity (DT) and light-induced transient gratings (LITG) techniques. Band to band generation was performed using third/fourth harmonics ($\lambda_{3,4}=351, 263$ nm) of the picosecond Nd:YLF laser. In the LITG method, the decay of the transient grating was monitored by an optically delayed probe beam with the wavelength $\lambda=1053$ nm (with ~ 13 ps resolution). In addition, slower nonequilibrium carrier dynamics was also monitored by electronically delayed probe beam ($\lambda=1064$ nm) with about 2 ns pulse duration.

DT measurements by employing the electrical delay line showed that free carrier recombination time in 6H-SiC was $\tau_R \approx 100$ ns, which was the longest among the studied samples; free carrier lifetimes of about 50 ns were measured in the other samples.

DT kinetics in low-doped 4H-SiC epilayer showed dependence of decay of the fast component on the injected carriers, which can be described by a function $\tau_R \propto \Delta N^{0.51}$, implying the effects of carrier recombination at the surface. The data are compared with results of work which reported the similar while stronger dependence [1]. The measured injection dependence of the diffusion coefficient in 3C-SiC and 6H-SiC samples revealed a significant reduction of the diffusion coefficient with increasing excess carrier concentration, which is due to the band-gap narrowing (BGN) [2].

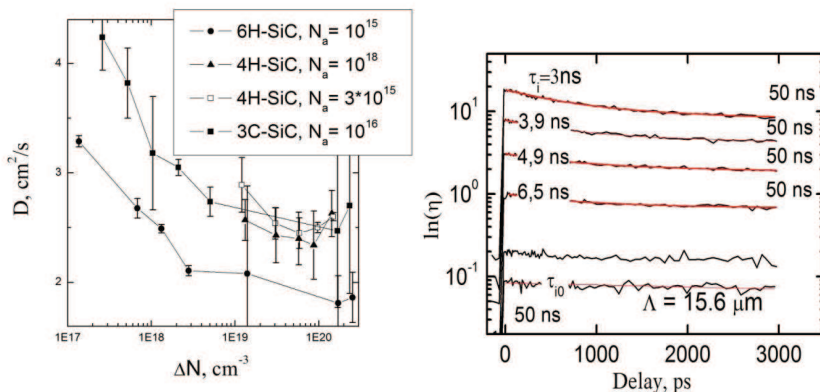


Fig. 1. a) Room temperature diffusion coefficient dependence on the excess carrier concentration; b) Room temperature DT kinetics for the low-doped p-type 4H-SiC epilayer measured at different excitations.

[1] P. Ščajevo, V. Gudelis, K. Jarašiūnas, P. B. Klein, Fast and slow carrier recombination transients in highly excited 4H- and 3C-SiC crystals at room temperature, J Appl. Phys. 108 023705 (2010)

[2] Paulius Grivickas, Optical studies of carrier transport and fundamental absorption in 4H-SiC and Si, Doctoral dissertation, Royal Institution of Technology (KTH), 2004.

Investigation of TlBr photoelectric properties over wide temperature range

Vytautas Janonis

Institute of Applied Research, Vilnius University, Saulėtekio Ave. 9-III, LT-10222, Vilnius, Lithuania

Vytautas.Janonis@ff.stud.vu.lt

Thallium bromide is a very promising material for the fabrication of low noise, high resolution X-ray and γ -ray detectors, which could be used at room temperature. Main properties of thallium bromide, important for production of good quality detectors are its wide band gap (2.68 eV), high density (7.56 g/cm³) and high atomic numbers (Tl: 81 and Br: 35). These properties ensure high photon stopping efficiency, which is required for a sensitive detector. Main problems in using TlBr detectors are caused by the high quality of required material, also by the degradation resulting from ionic conductivity within the crystal. Moreover, thallium bromide is hygroscopic and toxic, therefore cannot be left in a room environment. [1, 2]

The aim of this research was to investigate photoelectrical properties and surface topography of two thallium bromide samples. Dark and photocurrent current - voltage dependencies also thermally stimulated currents were investigated at different temperatures from 20 to 300 K. Photoconductivity spectra were measured at 20K temperature.

Surface topography was measured, using optical and atomic force microscopes. Sample with best surface processing was identified. Also the effect of surface processing on electrical properties of the samples was identified in the research.

After investigating dark current - voltage characteristics at different temperatures ohmic behavior was confirmed, therefore it was stated that processes associated with contacts were negligible. While investigating photo-current - voltage characteristics space charge limited currents were observed due to large charge photo-excitation.

Temperature dependencies of the dark current and thermally stimulated current (TSC) were measured. Several peaks were identified in each samples TSC measurements. Charge-trapping level energies were calculated and effect of surface processing identified.

After measuring photoconductivity spectra, at 20 K temperature, several defect levels with different ionization energies were identified in each sample which led to conclusion that samples had different types of impurities which were caused by the methods which manufacturers used for growing and purifying the samples. After investigating relative defect peak height values and specific electric sample resistance values, sample with better crystalline quality was identified.

[1] Kažukauskas, V., Jurgilaitis, A., Vaitkus, J., Gostilo, V. & Shorohov, M. Photoelectrical Phenomena and Current Kinetics in TlBr. *Mat. Sci.* **14**, 5–8 (2008).

[2] Kozlov, V. *TlBr raw material purification , crystal growth , annealing , detector fabrication and characterisation for gamma-ray detector applications* PhD Doctoral Thesis, University of Helsinki (2010).

OPTICAL PROPERTIES OF NATURAL OXIDE LAYER ON ZnMgRE QUASICRYSTALS

Simona Paurazaitė, Saulius Tumėnas

Center for Physical Sciences and Technology, Gostauto 11, LT-01108 Vilnius, Lithuania
simona.paurazaitė@ff.stud.vu.lt

We present results of spectroscopic ellipsometry (SE), a nondestructive optical technique, study of the natural oxide surface layers of icosahedral ZnMgRE (RE = Y, Ho, Er) single-grain quasicrystals. Samples were grown by the liquid-encapsulated top-seeded solution-growth method [1]. After an optical surface preparation by mechanical polishing, the samples were naturally oxidized under normal atmospheric ambient. The spectroscopic ellipsometry measurements in the spectral range 0.73 – 6 eV were carried out by the dual rotating compensator ellipsometer RC2 (J. A. Woollam Co, Inc.) in steps of 1 nm at 45, 55, 65 and 75 degrees of the incident angle. The measured SE spectra were analyzed by several fitting models, which construction was based on the X-ray photoemission spectroscopy (XPS) depth profile measurements. The XPS measurements were carried out by VG Scientific ESCALAB MK II spectrometer equipped with Al K α (1.487 keV) X-ray source.

The experimental spectra of ellipsometric parameters [Fig. 1(a)] show that the optical response of naturally oxidized ZnMgRE quasicrystals manifests distinct features due to an optical interference in semitransparent film. In the analysis of the SE data, a native oxide layer was described using the Bruggeman effective medium approximation (EMA) [2] by modeling the layer as a physical mixture of three distinct phases: zinc oxide, magnesium oxide and ZnMgRE quasicrystal. The refractive indices of ZnO and MgO were taken from literature [3]. Optical constants of ZnMgRE quasicrystals were determined from the same samples after careful removal of native oxide films by combined mechanical polishing and plasma etching technique.

The ZnMgRE surface layer is inhomogeneous, its refractive index profile varies with depth according to XPS data. The XPS depth profile [Fig. 1(b) inset] clearly shows the inhomogeneous profile of atomic composition (measured at different sputter times). In modeling of SE data, we used the grading model in which the relative fractions of ZnO, MgO and ZnMgRE optical parameters were varied along the surface normal. The graded layer was divided into numerous sublayers of equal thicknesses. Each sublayer was assumed to have a uniform composition, its variation from one sublayer to another was assumed to have a linear staircase profile. The graded model suggested a remarkably good fit over an entire spectral range and for all incident angles [Fig. 1(a)]. This allowed to reliably determinate the thickness of the layer thicknesses and the refractive index profile [Figure 1(b)]. The index profile determined by SE analysis was found to be consistent with the XPS atomic composition profile.

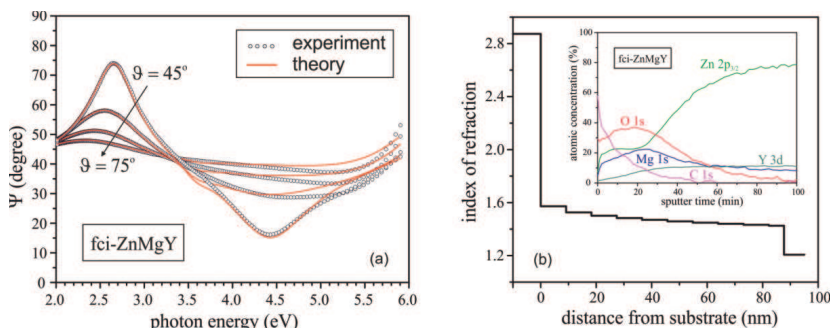


Fig. 1. (a) Measured (dots) and calculated (solid lines) Ψ spectra at various angles of incidence. (b) The refractive index ($\lambda = 745$ nm) profile of the fci-ZnMgY surface layer determined from an analysis of SE data. Inset shows the XPS depth profile of atomic composition.

[1] A. Langsdorf and W. Assmus, J. Cryst. Growth **192**, 152 (1998)

[2] D. A. Bruggeman, Ann. Phys. Leipzig **24**, 636 (1935)

[3] E. D. Palik, Handbook of Optical Constants Solids (Academic, New York, 1985).

INVESTIGATION OF THERMAL EMISSION SPECTRUM OF THE AlGaN/GaN AND GaAs SAMPLES

Justas Laužadis, Rimvydas Venckevičius, Irmantas Kašalynas

Center for Physical Sciences and Technology, Vilnius, Lithuania

justas.lauzadis@ff.stud.vu.lt

The application of terahertz (THz) radiation in security and medical diagnostics besides sensitive THz detectors also requires developing of compact high-power THz emitters performing at room environment. In this work, emission of the AlGaN/GaN based hetero-structures and GaAs semiconductors were investigated in THz spectral region.

An AlGaN/GaN hetero-structure based transistor as voltage controlled THz source was proposed recently [1]. On the other hand, the radiation of plasmon-phonon polaritons of thermally stimulated GaAs was demonstrated in mid infrared (IR) spectrum [2]. In this work, thermally stimulated emission of the AlGaN/GaN hetero-structures and two differently doped GaAs crystal were investigated by Fourier transform spectroscopy.

Spectrometer was based on Michelson interferometer. The radiation emitted by the sample was collimated with the off-axis parabolic mirrors and guided to the Michelson interferometer. The HDPE beam splitter and two – moveable and fixed – optical mirrors modulate intensity of the beam. After interferometer, the modulated beam was focused into the opto-acoustic detector (Golay cell). Additional optical filters were used to optimize spectrum measurement.

The bias current was determined by power supply, which operated on constant current mode. The temperature of the sample was measured by the thermoresistor. The process was monitored on computer with the help of software created in “LabView” programming environment.

In this work, we investigated thermal emission dependence on bias current of the GaAs and AlGaN/GaN samples. The temperature of the sample was modified due to ohm Joule heating. Measured results are shown in Fig. 1. Note that emission intensity is plotted in log scale. All samples demonstrated a broad band radiation spectrum similar to the black body. In addition, spectra of the GaAs are modulated at around 260 cm^{-1} , in area of the Reststrahlen band in the semiconductor. The optical phonon energies of GaAs are $h\nu_{TO} = 33.19\text{ meV}$ (268 cm^{-1}), $h\nu_{LO} = 36.08\text{ meV}$ (291 cm^{-1}) (at 60°C). The optical phonon energy of GaN is 87.3 meV (704 cm^{-1}) [3]. Different spectrum modulation is due to higher free carrier density in GaAs 1 sample in respect to GaAs 2 leading to different excitation efficiency of the plasmon-phonon polaritons. Note that dips in the spectrum at around 370 cm^{-1} and 430 cm^{-1} are caused by dispersion of optical components used in spectrometer.

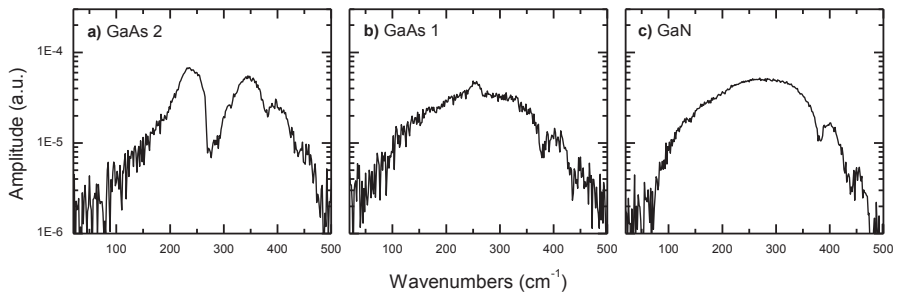


Fig. 1. Emission spectra of two different GaAs samples (a, b) and AlGaN/GaN hetero layer (c) at 60°C

In conclusion, thermal emission of the GaAs and AlGaN/GaN samples has been measured in mid-IR and THz spectrum. Emission intensity of the GaAs was found modulated at frequency of 260 cm^{-1} .

-
- [1] A. El Fatimy, N. Dyakonova, Y. Meziani, T. Otsuji, W. Knap, S. Vandenbrouk, K. Madjour, D. Theron, C. Gaquiere, M. a. Poisson, S. Delage, P. Prystawko, C. Skierbiszewski, „AlGaN/GaN high electron mobility transistors as a voltage-tunable room temperature terahertz sources,” *Journal of Applied Physics*, vol. 107, no. 2, p. 024504, 2010.
- [2] J. Požėla, E. Širmulis, K. Požėla, A. Šilėnas, V. Jucienė, “SiC and GaAs emitters as selective terahertz radiation sources,” *Lithuanian Journal of Physics*, Vol. 53, No. 3, p. 163-167, 2013.
- [3] <http://www.ioffe.ru/SVA/NSM/Semicond/index.html>

OPTICAL STUDY OF CARRIER RECOMBINATION AND LOCALIZATION IN Al-RICH AlGa_N LAYERS

Žydrūnas Podlipskas, Ramūnas Aleksiejūnas, Jūras Mickevičius

Department of Semiconductor Optoelectronics, Institute of Applied Research, Vilnius University,
Saulėtekio Avenue 9-3, Vilnius 10222, Lithuania
Zydrunas.Podlipskas@ff.stud.vu.lt

In majority of studies, carrier recombination processes are investigated in complex LED structures, where the basic processes are considerably obscured due to the structure-specific features like built-in electric field, carrier localization because of well thickness variation, or impact of electrical contacts. To avoid these additional factors, we performed optical study of thick AlGa_N layers seeking to clarify the radiative and non-radiative recombination pathways, and carrier localization influence to them in AlGa_N.

We studied 10 μm thick Al_{0.68}Ga_{0.32}N layers with different molar concentrations of Al (48 – 71 %), grown using MEMOCVD™ on the AlN/sapphire templates. To assess the parameters of carrier localization, photoluminescence (PL) measurements under quasi-steady-state conditions were performed in a wide range of excitation power densities from 10 kW/cm² to 10 MW/cm² at the temperatures ranging from 8 to 300 K. Carrier lifetime τ_R and diffusivity D was measured using light-induced transient grating (LITG) technique. Transient gratings of different period (1.9 – 7.8 μm) were recorded using 25 ps pulses at 213 nm with energy fluence ranging from 0.016 to 0.48 mJ/cm² and temperature varying from 80 to 420 K.

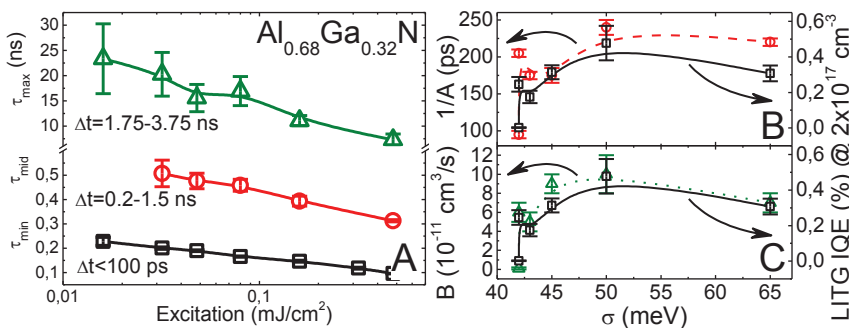


Fig. A LITG decay time constant as function of excitation at various delay ranges in Al_{0.68}Ga_{0.32}N layer;
B and C Carrier nonradiative recombination time constant $1/A$ (dash line), radiative recombination coefficient B (dot line) and internal quantum efficiency IQE (solid line) as functions of localization depth σ .

LITG decay revealed non-exponential kinetics with at least three distinct components. Assuming these components reflect independent decay processes, we fitted them with a single-exponential function within three distinct decay ranges. The corresponding decay time constants τ_{\min} , τ_{mid} and τ_{\max} of those components at moderate injection (0.16 mJ/cm²) varied from sample-to-sample within ranges of $\tau_{\min}=75\text{--}150$ ps, $\tau_{\text{mid}}=95\text{--}475$ ps and $\tau_{\max}=7\text{--}23$ ns. Decay rate of all components increased with injection (Fig. A) due to emerging radiative recombination (for fast decay component), and localized states filling (for slow decay component). Carrier nonradiative recombination rate A decreased with increasing localization depth σ (Fig. B) due to diminishing probability of carrier capture to nonradiative recombination centers, reaching the minimum value at $\sigma \sim 50$ meV. However, further increase of structural disorder initiates deterioration of crystal quality and rise of recombination states. Nonradiative recombination rate increased with temperature possibly due to multiphonon emission.

The determined radiative recombination coefficient B of the best quality AlGa_N layers was $(5\text{--}10) \times 10^{-11}$ cm³/s, and increased with localization depth (Fig. C.), reaching the maximum value at $\sigma \sim 50$ meV. Temperature dependence of radiative recombination coefficient matched theoretical function $B \sim T^{-3/2}$ within the experimental uncertainties.

Two sets of internal quantum efficiency (IQE) values were estimated using independent LITG and PL techniques. Both sets of IQE values positively correlated with each other, nonradiative recombination decay time $1/A$ and radiative recombination coefficient. IQE increased with localization depth, reaching the maximum value at $\sigma \sim 50$ meV (Fig. B and C).

The diffusion coefficient D of all AlGa_N layers was immeasurably small (<0.1 cm²/s), and not increased neither with temperature nor with nonequilibrium carrier density. Therefore nonradiative recombination was not diffusion-governed process within temperature range of $T=80\text{--}420$ K.

NONEQUILIBRIUM CARRIER DYNAMICS IN GaN EPILAYERS WITH DIFFERENT EQUILIBRIUM CARRIER DENSITIES

Mažena Mackoit

Semiconductor Physics Department, Vilnius University, Saulėtekio Ave. 9-III, LT-10222 Vilnius, Lithuania

mazena.mackoit@ff.stud.vu.lt

GaN and its derivatives are very important for their wide range of applications in modern optoelectronics. Although there has been a rapid progress in the development of these devices during the last decades, the details of the radiative and nonradiative recombination processes are not well understood. Instead, as a popular tool, simple nonequilibrium electron density rate equation is widely used to separate different recombination channels by their respective carrier density dependence.

The aim of this research was to model the carrier recombination mechanisms in GaN and to investigate the influence of equilibrium carrier densities on carrier dynamics. All the samples studied were grown on c-plane sapphire substrate using Metal-Organic Chemical Vapor Deposition. A number of GaN epitaxial layers with different equilibrium carrier densities ranging from $2.8 \cdot 10^{16} \text{ cm}^{-3}$ to $1 \cdot 10^{18} \text{ cm}^{-3}$ were selected for the study and grouped according to their equilibrium carrier density and carrier lifetimes into six series.

The PL study in this work has been performed under quasi-steady-state excitation. PL spectra at different excitation power densities were measured, and the PL spectral parameters were compared between and within the series. All the measurements were performed at room temperature.

Experimental results were approximated using luminescence intensity dependence on the equilibrium and nonequilibrium electron densities

$$I_{LUM} \propto B \cdot \Delta n (n_0 + \Delta n),$$

where B is coefficient of bimolecular recombination, n_0 – equilibrium electron density, Δn – nonequilibrium electron density.

The carrier dynamics is studied using solution of the rate equations with equilibrium carrier densities taken into account. The results show that in samples with similar carrier lifetime, the deviation from the quadratic dependence of the PL intensity on excitation power density appears at lower excitation intensities in samples containing larger equilibrium carrier density. The influence of carrier lifetime on the quadratic dependence was found to be negligible.

The droop effect was observed in all the samples. It was found that, the samples with higher carrier lifetimes reached the onset of the droop effect at lower excitation intensities, as expected due to a higher carrier density at a fixed photogeneration rate.

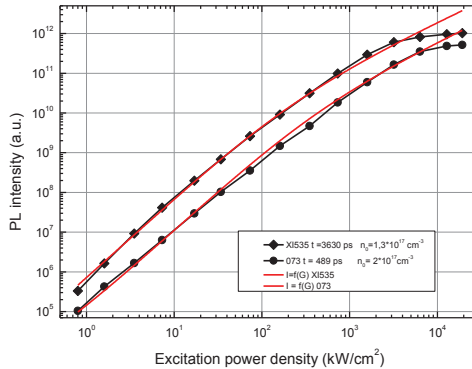


Fig. 1. Spectrally integrated PL intensity dependence on excitation power density of epitaxial GaN samples with similar carrier concentration and different lifetime: experimental (points) and calculated (lines).

Optical study of recombination and transport of non-equilibrium carriers in (In,Ga)N quantum structures

Kazimieras Nomeika

Institute of Applied Research and Faculty of Physics, Vilnius University

Kazimieras.Nomeika@ff.stud.vu.lt

Search and study of materials for lighting and display technologies attracts a lot of attention during the recent decades. (In,Ga)N is one among those that allow achieving a high efficiency of visible and UV range optoelectronic devices that currently are in huge demand. Understanding of recombination and transport of non-equilibrium carriers in such materials is crucial in order to obtain a clear view of non-radiative losses, occurring in light emitting diodes (LEDs) at high carrier densities. Such a monitoring of excess carriers can be achieved by optical pump-probe methods, which are non-destructive, do not require any special preparations of the samples, and most important- they allow measurements at high carrier densities, i.e. at conditions close to the operation point of a high power device.

In this work, five (In,Ga)N samples with same multilayered LED structures, but with differing In concentrations in quantum wells are investigated. The methods used are photoluminescence (PL) and light-induced transient gratings (LITG). In the latter experiment samples are excited selectively by using the optical parametric amplifier (OPA). The compared samples consist of 4 periods of GaN barriers and $\text{In}_x\text{Ga}_{1-x}\text{N}$ QWs, where x varies from 0,15 to 0,32. All measurements are carried out at room temperature ($T=300\text{ K}$).

The results show, that photoluminescence intensity decreases with In content in QWs, as shown in figure 1 (a). LITG kinetics show shorter effective carrier lifetimes in samples with higher x , which may be attributed to more rapid non-radiative and/or radiative recombination, while diffusion coefficient at low pump intensities (up to $0,018\text{ mJ/cm}^2$) also drops (figure 1 (b)). These facts suggest that by introducing higher indium concentrations, the electric properties of the samples deteriorate, as the densities of recombination, localization and scattering centers grow. However, at higher pump intensities, diffusivity acts in the opposite way (figure 1 (b)).

All specimens show rise in diffusion coefficient with increasing excitation, which is most likely due to the filling of the localization centers, whereas shortening of the excess carrier lifetimes is attributed to density activated non-radiative recombination [1].

Simple modeling with non-equilibrium carrier lifetimes demonstrates, that increase in both non-radiative and radiative recombination rates is feasible with higher In content.

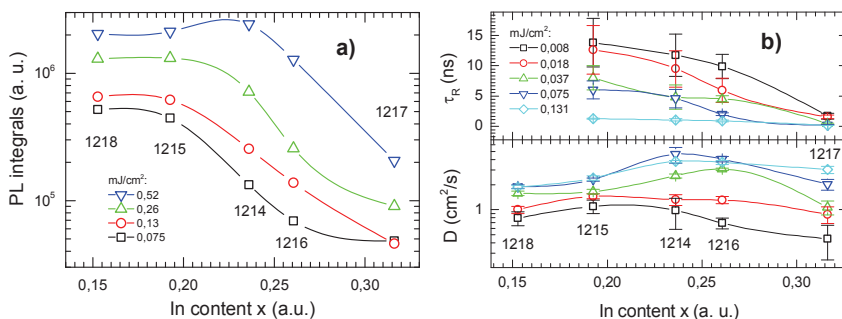


Fig. 1. Dependancies of PL spectra integrals (a), carrier lifetimes and diffusion coefficient (b) on In content in quantum wells at different pump intensities.

[1] J. Hader, J. V. Moloney, and S. W. Koch, Density-activated defect recombination as a possible explanation for the efficiency droop in GaN-based diodes, Appl. Phys. Lett. 96, 221106 (2010); doi: 10.1063/1.3446889

INFLUENCE OF CARRIER LOCALIZATION ON LUMINESCENCE DYNAMICS IN ALGaN QUANTUM WELLS

Oleg Kravcov, Edmundas Kuokštis

Department of Physics, Vilnius University, Lithuania

Oleg.Kravcov@ff.stud.vu.lt

High efficiency light-emitting diodes based on the wide-band-gap nitrides such as InGaN or AlGaN recently gained a lot of interest. Although AlGaN has a great potential in UV optoelectronics, there are a lot of experimental results demonstrating the undesirable decrease of quantum efficiency at high excitation density [1]. This effect called “efficiency droop” and yet is not fully understood. In this paper, we investigate the behavior of the dynamics of the photoluminescence (PL) by the theoretical calculation of the PL spectrum and comparison with the experimental data in AlGaN quantum wells.

The theoretical model of the PL is based on the band-to-band recombination with intensity:

$$I_L(E) = K \frac{g(E)f(E)\tau_{PL}(E)}{\tau_r} \quad (1)$$

where E is a photon energy, $g(E)$ is a density of states, $f(E)$ is a Fermi-Dirac distribution function, $\tau_{PL}(E)$ is an energy-dependant PL life time, and τ_r is a radiative recombination time of nonequilibrium carriers.

Nitride-based quantum structures, especially with higher Al concentration have a nonhomogeneous distribution of the AlGaN content which leads to considerable gap energy fluctuations and as a result formation of the localized states [2]. We use the Gaussian distribution model of the localized states. Thus, the density-of-states function becomes:

$$g(E) = \int_0^\infty \frac{m_e^*}{\pi \hbar^2} \sum_{i=1} \Theta \left(\tilde{E} - E_g - \frac{\hbar^2 n^2}{2m_e^* d^2} \right) \cdot \frac{1}{\sqrt{2\pi}\sigma_b} \exp \left(-\frac{(E - \tilde{E})^2}{2\sigma_b^2} \right) d\tilde{E} \quad (2)$$

The localization of the carriers in potential wells due to potential fluctuations leads to longer PL life time in the corresponding photon energy region, while carriers with higher energy above the mobility edge have higher probability to find and recombine nonradiatively via corresponding centers. The latter process leads to the decrease of the PL life time for higher photon energy. In this model, we apply the empirical formula extracted from experiment for describing τ_{PL} dependence on energy as follows:

$$\tau_{PL}(E) = \frac{\tau_r}{1 + \exp \left(\frac{E - E_{me}}{E_0} \right)} \quad (3)$$

The calculated PL spectra and their comparison with experiment are illustrated in Fig. 1.

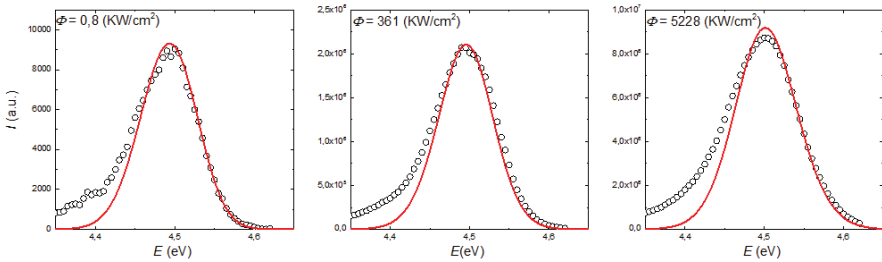


Fig 1. Experimental (circles) and theoretical PL spectra (lines) of AlGaN quantum wells at different excitation density.

In conclusion, by taking into account the localized states distribution and the energy-dependant PL life time it is possible to achieve rather good coincidence of the experimental and theoretical PL spectra at various excitations. The “efficiency droop” is discussed in the frame of the proposed model.

[1] J. Mickevicius, G. Tamulaitis, M. Shur *Internal quantum efficiency in AlGaN with strong carrier localization* Appl. Phys. Lett. **101**, 211902 (2012);

[2] E. Kuokštis, W. H. Sun, M. Shatalov *Role of alloy fluctuations in photoluminescence dynamics of AlGaN epilayers* Appl. Phys. Lett. **88**, 261905 (2006);

INFLUENCE OF TRENCH DEFECTS ON PHOTOLUMINESCENCE IN InGaN/GaN QUANTUM WELLS

Augustas Vaitkevičius¹

¹ Institute of Applied Research and Semiconductor Physics Department, Vilnius University, Saulėtekio av. 9, Building III, 10222 Vilnius, Lithuania
Augustas.vaitkevicius@ff.stud.vu.lt

The band gap of indium gallium nitride spans the entire visible spectrum and can be adjusted by changing the indium-to-gallium ratio. Consequently, InGaN structures are attractive for applications in optoelectronics. InGaN is already widely used in commercial blue and white light-emitting diodes as well as laser diodes. These devices are typically manufactured from InGaN/GaN heterostructures. Lattice mismatch between sapphire and GaN buffer layer and between GaN and InGaN layers generates a high density of threading dislocations. Threading dislocations can manifest on the sample surface as V-pits or as three-dimensional loop structures called trench defects, the latter being much less studied.

In this work, the trench defects and their influence on photoluminescence (PL) were studied in InGaN multiple quantum wells (MQWs) with different indium content ranging from 15 % to 35 %. The quantum well structures were grown by metal-organic chemical vapor deposition (MOCVD). The active layer of each sample consists of 5 InGaN quantum wells, 2.8 nm in width, separated by 20 nm thick GaN barriers.

The samples have been studied using confocal and atomic force microscopy. The mapping and study of spatial variation in PL spectra parameters was performed using a confocal microscope installed on the WITec Alpha 300 S microscope system. An objective with numerical aperture $NA = 0.9$ was ensured in-plane spatial resolution of ~ 250 nm. The microscope was coupled by optical fiber with a spectrometer followed by a thermoelectrically cooled CCD camera. A CW laser diode, emitting at 405 nm and He-Cd CW laser, emitting at 442 nm, were exploited for excitation. Surface topography was investigated using an atomic force microscope (AFM) installed in the aforementioned microscope system. The spatial resolution of the AFM measurements was ~ 10 nm. Use of the multi-microscope system enabled spatial matching of the surface topography images with the spatial distributions of PL parameters. All the measurements were performed at room temperature.

The confocal photoluminescence microscopy results show that the spatial distribution of spectrally integrated PL intensity (Fig. 1 A) consists of bright areas on a dark homogenous background. The bright areas are approximately 250 nm in diameter. The analysis of spectral data shows that the photoluminescence spectrum in the dark homogeneous areas is composed of two bands. Meanwhile, the spectra from the bright areas consist of a single band that is blueshifted in comparison to both bands observed in the dark areas (Fig. 1 C).

Atomic force microscopy revealed the presence of both pits and trench defects (Fig. 1 B). Further analysis showed that the areas enclosed by a trench loop are at the same level or elevated above the surrounding surface. Not all the observed trench structures feature a complete loop. The densities of both types of defects as well as the surface roughness increase with increasing indium content. In samples with indium content above 30 %, the surface becomes too rough to distinguish separate surface features.

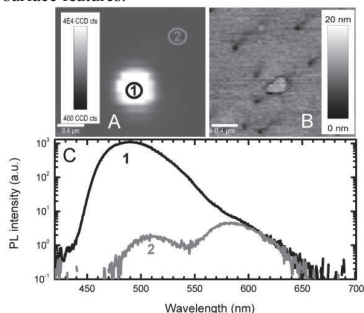


Fig. 1. Spatial distribution of spectrally integrated photoluminescence intensity in InGaN MQWs (A), surface topography image (B) from the same surface area, and spatially integrated spectra (C) from two areas indicated in (A).

Scanning of same area in both confocal photoluminescence microscopy and atomic force microscopy modes revealed that strong, blueshifted photoluminescence is observed from the areas surrounded by trench defects. The observed structural and photoluminescence features are interpreted by defect diffusion towards trench loops during crystal growth. As a result, a column like volume of structural quality superior to that outside the trench is formed. Stress relaxation, variations in indium content and quantum well thickness in the nanocolumns are also discussed.

GROWTH AND CHARACTERISATION OF InGaN/GaN MULTIPLE QUANTUM WELLS

Mantas Dmukauskas, Arūnas Kadys

Institute of Applied Research, Vilnius University, Saulėtekio Ave. 9-III, LT-10222 Vilnius, Lithuania
mantasdmuk@gmail.com

Indium gallium nitride (InGaN) has been the subject of extensive research, because of their wide application in optoelectronics. InGaN can cover light spectrum from near-infrared to ultraviolet range, depending on In and Ga concentration ratio in alloy. The growth of high quality InGaN multiple quantum wells (MQW) is a great challenge, because of lattice mismatch between InN and GaN and the different growth temperatures.

The main goal of this work was to optimize MOCVD growth conditions in order to get InGaN MQWs structures with high luminescence efficiency at around 400 nm.

$\text{In}_x\text{Ga}_{1-x}\text{N}/\text{GaN}$ MQW structures were grown on sapphire C-plane substrates with GaN buffer layer in a vertical flow close-coupled showerhead reactor. We used standard precursors for GaN MOCVD growth – trimethyl gallium, trimethyl indium, ammonia and hydrogen for GaN or nitrogen for InGaN as the carrier gases. The growth was monitored using in situ laser interferometer, determining process steps. The set of samples were grown by using different growth temperatures of the MQWs (720 ÷ 800 °C).

Indium concentration was determined using photo-luminescence and X-Ray diffraction measurements.

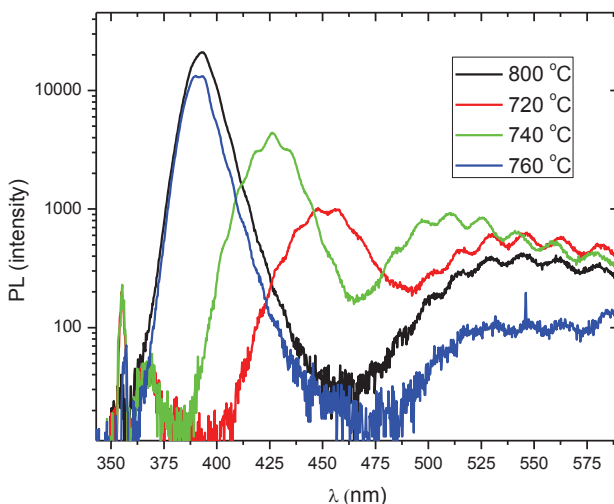


Fig.1. PL spectra measured in InGaN/GaN MQWs with different In content.

InGaN/GaN MQWs ANALYSIS USING HR-XRD ROCKING CURVES

Sandra Stanionytė^{1,2}, Tadas Malinauskas²¹ Department of Chemistry, Vilnius University, Lithuania² Institute of Applied Research, Vilnius University, Lithuaniasandra.stanionyte@chf.vu.lt

Wide band-gap materials such as GaN and InGaN are very attractive because of their suitability for the fabrication of high efficiency light-emitting devices (LEDs) used for various applications including general lighting. The main part of led structure is multiple quantum wells (MQWs) which emits light. The radiation wavelength emitted from InGaN multiple quantum wells can be varied in wide visible and UV region by changing indium content [1].

One of the most convenient ways to analyze MQW structure is High Resolution X-Ray Diffraction (HR XRD). Information about the number of quantum wells, indium content, the well and barrier thicknesses interface and crystal quality can be extracted from XRD rocking curve measurements. Some of parameters could be obtained by measuring simple measurement of angular distance between XRD peaks, but usually sophisticated modeling is applied for simulation of whole XRD curve for simultaneous extraction of the set of parameters.

In the part of paper we will present modeling of XRD (002) rocking curves in order to show how different parameters of MQW structure influence the shape of rocking curves. Scattering from MQWs can be understood by analogy to scattering from an optical grating, where the number of thickness fringes is related to the number of repeats. The number of smaller fringes depends from the number of wells, the distance between bigger fringes depends from one well and one barrier structure thickness, between smaller fringes – from all wells and barriers overall thickness. The position of zeroth order peak (on the left from GaN peak) depends from well and barrier thickness, but mostly from indium content [2].

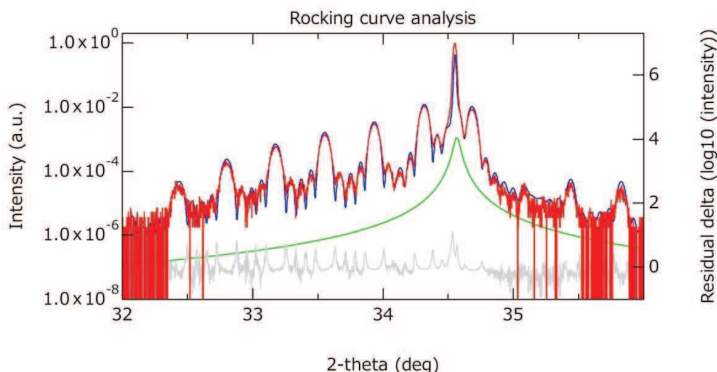


Fig. 1. InGaN/GaN MQW containing 5 MQWs with 13% indium content, 5.8 nm well and 18.6 nm barrier thicknesses model.

The (002) rocking curves were measured and modeled for the series of MOCVD grown InGaN/GaN MQWs with different In composition (Fig 1). The indium content in quantum wells was compared with data obtained by photoluminescence (PL). The clear correlation was obtained between two methods, although exact indium content values showed significant discrepancy, what was explained by nonrectangular In concentration profile in QWs.

[1] H. H. Lee, M. S. Yi, H. W. Jang et al., Determination of absolute indium content in InGaN/GaN multiple quantum wells using anomalous x-ray scattering, *Applied Physics Letters* **81**, 5120-5122 (2002).

[2] M. A. Moram, M. E. Vickers, X-ray diffraction of III-nitrides, *Rep. Prog. Phys.* **72**, 1-40 (2009).

Algirdas Norkūnas, Artūras Žalga

Department of Applied Chemistry, Faculty of Chemistry, Vilnius University, Naugarduko Str. 24, 03225 Vilnius,
Lithuania

algirdas.norkunas@chf.stud.vu.lt

Aluminium molybdate and tungstate are the representative of the class of the $\text{Me}_2(\text{MoO}_4)_3$ compounds, where $\text{Me}=\text{Y}, \text{Sc}, \text{In}, \text{Al}$, as well as the rare earth elements from Ho to Lu and $\text{M}=\text{Mo}^{6+}$ or W^{6+} with orthorhombic structure of the $\text{Sc}_2(\text{WO}_4)_3$ type (space group Pnca). Because of their high charge, trivalent ions should, however, have strong interactions with surrounding anions and thus they are generally considered to be immobile species in solid ion conductors. The study of $\text{Sc}_2\text{W}_3\text{O}_{12}$ -type negative thermal expansion (NTE) material has gained considerable impetus recently due to its potential application in a large range of fields and $\text{Al}_2\text{W}_2\text{MoO}_{12}$ is one of the most intensely studied members. It can not only be used as a NTE material, acting as a filler in making composite to control the bulk thermal expansion coefficient, but also can be used as zero thermal expansion material which is desirable in optics, electronics and other fields, where exact positioning of parts is crucial. Moreover, the $\text{Sc}_2\text{W}_3\text{O}_{12}$ -type NTE material attracts an extensive interest because of its thermodynamic stability and great chemical flexibility. [1].

Production of high quality ceramic powders for high technology ceramics is becoming one of the most urgent issues in the ceramic industries. In particular, the development of fine ceramic powders with unusual and superior properties is important and has a great interest between many scientists [2]. The technology of optical ceramics includes three main stages: fabrication of nanopowders; preparing of highly dense compacts and sintering of the compact to the non-porous ceramics. Many investigations show, that to fabricate transparent ceramics ultrafine, monosized low-agglomerated nanopowders with high sintering activity have to be preliminary obtained [3].

In this communication we report a thermal plasma preparation technique supported by the tartaric acid assisted aqueous solution of aluminum (III) nitrate, ammonium molybdate (VI) and/or ammonium tungstate (VI) for the synthesis of $\text{Al}_2(\text{Mo}_{1-x}\text{W}_x\text{O}_4)_3$ ($x=0, 0.5$ and 1) ternary system. The thermal decomposition, crystal structure and surface morphology of the as-prepared oxides obtained after both plasma treatment and additional sintering at 400, 500, 600, 700, 800 and 900 °C temperatures were investigated by thermal analysis (TG/DSC), X-ray diffraction (XRD), and scanning electron microscopy (SEM). According to the thermogravimetric analysis the stability of $\text{Al}_2\text{Mo}_3\text{O}_{12}$ and $\text{Al}_2\text{W}_3\text{O}_{12}$ crystal phases over 800 °C has decreased by the partial decomposition of the as-formed ternary oxides and thereafter by the sublimation of MoO_3 and WO_3 , respectively. Besides, it is important to note that the thermal decomposition of the as-prepared $\text{AlMo}_{1.5}\text{W}_{1.5}\text{O}_{12}$ compound after plasma treatment completely differs comparing with the above described thermogravimetric behavior of the ternary systems. In this case, by increasing of temperature from 700 to 1,000 °C, no mass losses in the TG curve have observed. The structure and the size of the resulted products have shown clear defined dependence from the temperature. These obtained results were consistent with the conclusions made from TG–DSC analysis of Al–Mo–W–O precursors, which showed well-expressed ending temperature of mass loss and suggested possible crystallization point of final material with initial composition of $\text{Al}_2\text{Mo}_3\text{O}_4$ and $\text{Al}_2\text{W}_3\text{O}_{12}$ phases.

-
- [1] G. F. Xu, Q. Q. Liu, J. Yang, X. J. Sun, X. N. Cheng, Study on the synthesis of $\text{Al}_2\text{W}_2\text{MoO}_{12}$ by a simple stearic acid route and its negative thermal expansion property, *Ceramics International* **35**, 3131–3134 (2009).
[2] P.C. Kong, Y.C. Lau, Plasma synthesis of ceramic powders, *Pure Applied Chemistry* **62**, 1809–1816 (1990).
[3] V. Nikolov, I. Koseva, R. Stoyanova, E. Zhecheva, Conditions for preparation of nanosized $\text{Al}_2(\text{WO}_4)_3$, *Journal of Alloys and Compounds* **505**, 443–449 (2010).

ELECTRICAL AND MAGNETIC PROPERTIES OF THE $\text{La}_{2/3}\text{Sr}_{1/3}\text{MnO}_3$ THIN FILMS GROWN ON $\text{MgO}(100)$ SUBSTRATES

Irina Černiukė¹, Antanas Kleopas Oginskis¹, Andrius Maneikis¹, Bonifacas Vengalis^{1,2}, Gražina Grigaliūnaitė-Vonsevičienė²

¹ Center for Physical Sciences and Technology, A. Goštauto 11, LT-01108 Vilnius, Lithuania

² Vilnius Gediminas Technical University, Saulėtekio al. 11, LT-10223 Vilnius, Lithuania
lapkina@gmail.com

Hole-doped perovskite manganites referred to by the general formula $\text{Ln}_{2/3}\text{A}_{1/3}\text{MnO}_3$ ($\text{Ln}=\text{La, Nd, ...}$; $\text{A}=\text{Ca, Sr, Ba}$) have attracted considerable attention due to unusual electronic structure, paramagnetic-to-ferromagnetic phase transition and strong interplay between magnetic ordering and electrical transport properties. Most of the compounds provide great potential for applications in various spin-electronics devices due mainly to the so-called colossal magnetoresistance effect and presence of spin-polarized carriers occurring below the characteristic Curie temperature T_c ($\approx 100\div 350\text{K}$) [1]. $\text{La}_{2/3}\text{Sr}_{1/3}\text{MnO}_3$ (LSMO) demonstrating the highest T_c values ($\approx 350\text{K}$) and particularly thin films of the compound are of great importance for room temperature applications.

It is well known that lattice-matched single crystalline substrates such as SrTiO_3 , LaAlO_3 , NdGaO_3 are needed to grow the highest crystalline quality LSMO films. Meanwhile polycrystalline quality is usually indicated for the films grown on Si, GaAs, Al_2O_3 [2,3] and other lattice-mismatched crystalline substrates. However, it was reported recently, that LSMO films of epitaxial quality may be grown also on (100)-plane oriented MgO crystals in spite of rather high lattice mismatch (of about 8%) [2]. Following such a possibility, the goal of this work was to grow series of LSMO films on $\text{MgO}(100)$ substrates held at various temperatures to investigate their crystallinity as well as possible variation of their electrical and magnetoresistive properties.

The LSMO films were grown *in-situ* on cleaved (100) faces of MgO single crystal by magnetron sputtering of disk-shaped ceramic LSMO target ($\varnothing = 25\text{ mm}$). The Ar-O_2 (1:1) gas mixture with partial oxygen pressure of about 15 Pa was used for sputtering. During the deposition, the MgO substrates were kept at 6 fixed temperatures ranging from 550°C to 800°C. After the deposition, the films were cooled down slowly to a room temperature under an oxygen pressure of about $5\times 10^{-4}\text{ Pa}$ to ensure oxygen stoichiometry. Thickness of the prepared films measured by a DEKTA profilometer ranged typically from 150 to 200 nm. X-ray diffraction spectra measured in $\varnothing\text{-}2\theta$ geometry using $\text{CuK}\alpha$ radiation revealed highly [100]-axis oriented film material when grown at 700°C, 750°C and 800°C while increasing number of randomly oriented grains and reduced surface roughness were indicated for the films grown at lower temperatures ($T_s=650, 600$ and 550°C).

Resistivity (ρ) of the LSMO films grown at different substrate temperatures is shown in Fig. 1. The characteristic $\rho(T)$ curves with resistance peaks at $T=T_p>310\text{ K}$ measured for the LSMO films (prepared at 700°C, 750°C and 800°C) are typical for the highest crystalline quality oxide material when grown on lattice-matched substrates. The highest values of negative magnetoresistance ($MR=[R(B=0)-R(B=0.7\text{ T})]/R(B=0)$) up to about 15% have been measured for the films at $T=295\text{K}$. At the same time, negligible MR values measured for the films at $T=78\text{K}$ indicated absence of grain boundaries. In contrast, polycrystalline films with grain boundaries (when grown at 550°C and 600°C) demonstrated the highest MR values (up to 20%) at $T=78\text{K}$. It is important to note also that the film prepared at 650°C demonstrated significant MR values in a wide temperature range ($T=78\div 295\text{ K}$). We conclude therefore that LSMO films of various crystalline quality and certain controllable electrical and magnetoresistive properties may be grown on MgO substrates by applying dc magnetron sputtering and varying substrate temperature in the range 550°C -800°C.

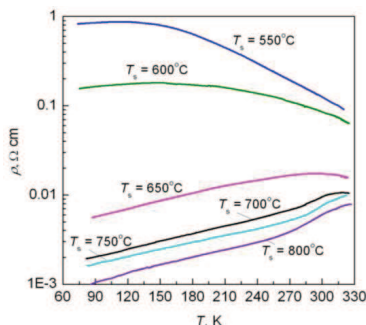


Fig. 1. Resistivity vs temperature for the LSMO films grown on $\text{MgO}(100)$ substrates at different temperatures.

[1] F.H. Li, T.-H. Lee and J.C.A. Huang, Modified surface electronic and magnetic properties of $\text{La}_{0.6}\text{Sr}_{0.4}\text{MnO}_3$ thin films, NSRRC Activity Report 2011.

[2] M. Spankova, S. Chromik, I. Vavra, K. Sedlackova, P. Lobotka, S. Lucas, S. Stancek, Epitaxial LSMO films grown on MgO single crystalline substrates, *Applied Surface Science* **253**, 7599–7603 (2007).

[3] S.Y. Yang, W.L. Kuang, Y. Liou, W.S. Tse Lee, Y.D. Yao, Growth and characterization of $\text{La}_{0.7}\text{Sr}_{0.3}\text{MnO}_3$ films on various substrates, *Journal of Magnetism and Magnetic Materials* **268**, 326–331 (2004).

STRUCTURE AND PROPERTIES OF SILICON DIOXIDE FILMS DEPOSITED BY HDPCVD

Aleksandr Yasunas, Olga Komar

Department of micro- and nanoelectronics, Belarusian State University of Informatics and Radioelectronics,
Republic of Belarus
olga_komar@tut.by

The plasma enhanced chemical vapor deposition of SiO_2 was carried out in a vacuum chamber installation YPM 3 3.279.050 with the use of an inductively coupled high-density plasma source operating at 13.56 MHz frequency 240 mm diameter. The initial pressure in the chamber is not worse than $3 \cdot 10^{-3}$ Pa. The operating pressure in the experiments was within the range from 1 to 10 Pa. [1]. The TEOS tank temperature is 21°C . Also the silicon oxide films deposition with different flow ratio of argon and oxygen into the chamber were carried out (Fig. 1).

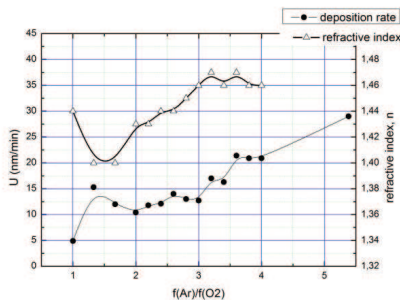


Fig. 1. The dependence of the refractive index and the SiO_x film growth rate on the ratio of Ar and O_2 in the working mixture.

The flow ratio of argon to oxygen flow varied from 1 to 10; besides the argon flow rate was constant and equal to 110 sccm. The pressure in the chamber varied from 2.5 to 5 Pa. We see that the reduction of oxygen in the steam-gas mixture linearly increases the growth rate of the film, with the ratio $f(\text{Ar}) / f(\text{O}_2)$ more than 4. The refractive index n exceeded 1.52 in the same conditions, simultaneously the transparency of the film was deteriorating. With the flow ratio $3 \leq f(\text{Ar}) / f(\text{O}_2) \leq 4$ the deposition rate increased, and the refraction index was within $1.46 \leq n \leq 1.47$, what shows the good quality of the formed film. With the ratio $f(\text{Ar}) / f(\text{O}_2) \geq 3$, the deposition rate is more complex: it decreases to the ratio of two, then it increases within the ratio of 1.25-1.75 and then decreases again. In this case, the refractive index is constantly decreasing, what indicates the porosity of the formed film (Fig. 2)[2].

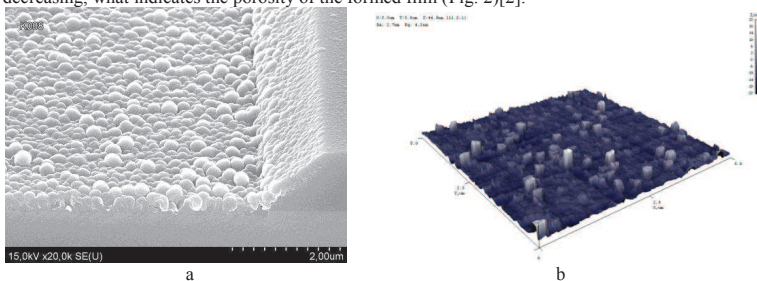


Fig. 2. a) – SEM picture of SiO_2 film on the $\langle 111 \rangle$ crystal-oriented silicon; b) AFM picture $f(\text{Ar})/f(\text{O}_2)=2.5$.

The analysis of the experimental results shows that the method of dielectrics deposition in a high-density plasma allows to deposit stoichiometric silicon dioxide films at a substrate temperature of 200°C , and at the same time stoichiometry can be controlled by varying the reaction components ratio.

[1] D.G. Gromov, *Metallization systems with nanoscale elements*. (Training Manual – Moscow: MIET, 2011).

[2] A.Yasunas, *Optical properties and structure of HDPCVD silicon dioxide* (EuroDisplay 2013 (33rd International Display Research Conference)16-19 September 2013. – London, 2013).

EFFICIENCY OF DECOMPOSITION OF WATER ON NANOSTRUCTURED OBJECTS BASED ON POWDERS OF TITANIUM AND SILICON

Olga Komar

Department of micro-and nanoelectronics, Belarusian State University of Informatics and Radioelectronics,
Republic of Belarus
olga_komar@tut.by

Constant searches for new ways of synthesis of hydrogen and its use as an alternative fuel in different spheres of production define a trend in the development of new approaches in the development of technologies for synthesis of materials which are capable of decomposing water into hydrogen and oxygen.

Solid solution based on titanium disilicide (TiSi_2) with an electrical resistance $\geq 1000 \text{ Ohm} \cdot \text{cm}$ is an attractive material for use in solar energy during the decomposition of water as a photocatalyst due to the higher bandgap ($E_g \approx 3,4 \text{ eV}$) [1]. It is capable to decompose water by visible light ($\lambda = 420 - 760$).

Hours of photocatalysts based on the TiSi_2 in a sunny day is up to $1,0\text{-}90 \text{ cm}^3$ per hour. The highest efficiency of decomposition of water was observed during the time interval of 12-16 hours a day (Figure 1). Ceteris paribus solar radiation efficiency of the decomposition of water depends on the technological parameters such as: the presence of a magnetic field, the rate of mixing water, the size of the photocatalyst, pH and temperature of the water, the weight ratio of water and the catalyst and the wavelength of the solar radiation [2].

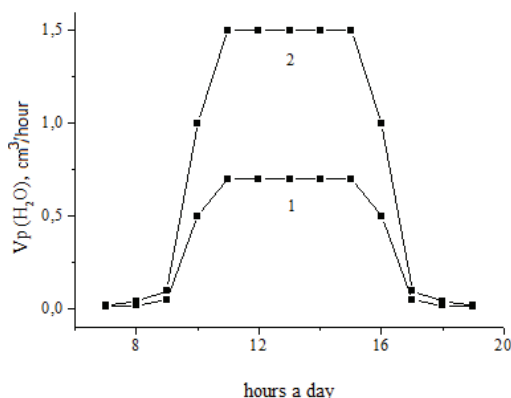


Fig. 1. Change in the efficiency of the decomposition of water on nanostructured solid solution of titanium disilicide during the day: 1 - the ratio of mass of titanium disilicide to the mass of water 1:150, 2 - 1:75.

Experimentally found that the most significant of technological parameters, which determine the effectiveness of the decomposition of water, are the concentration of solar radiation, time of day during of which solar radiation is the most effective, particle size of the photocatalyst, the temperature and pH of the water. An important advantage of nanostructured photocatalysts based on TiSi_2 , is that they are effectively converted into chemical energy concentrated solar radiation with any degree of $K = 50\text{-}1000$ concentration of suns that can not be done by the other photocatalysts. Thus, the photocurrent increases linearly with increasing of the luminous flux concentration generated by the solar cell. The yield of hydrogen with the decomposition of water increases linearly. The optimal material for the manufacture of such photocatalysts, as was shown from obtained results is titanium disilicide (TiSi_2) with particle size $\leq 70\text{nm}$, based on the photocatalysts which can reach 98% of efficiency.

- [1] Kovalevskii, A. A. *Oxidation Behavior of Micro- and Nanostructured Silicon Powders* (Published in Neorganicheskie Materialy. – 2008. – V. 44, N. 5. – P. 519–523.)
- [2] Kovalevskii, A.A. *Nano- and Microstructural Silicon Powders in the Synthesis and Storage of Hydroge* (Advances in Nanotechnology, (Nova Science Publishers / Editor E.J. Chen and N. Peng. – 2010. – V. 1. – P. 173–189.)

WITHDRAWN CONTRIBUTION

ELECTRONICS PROPERTIES OF QUASI-TWO-DIMENSIONAL NANOSTRUCTURES BASED ON GROUP-V TRANSITION METAL DICHALCOGENIDES

Olga Kozlova

Department of Micro- and Nanoelectronics, Belarusian State University of Informatics and Radioelectronics, Belarus
olga.bsuir@gmail.com

Ultrathin two-dimensional structure of layered transition metal dichalcogenides (TMDs) technologically simple to manufacture and effective in use. Structures consisting of one or several TMD layers are direct-gap semiconductors, its' value gap and charge carrier type varies depending on the crystallographic configuration, chemical composition and dimensions of the compounds. Thus, the possibility of modifying the electronic structure of TMD makes them attractive in a wide range of applications in micro- and nanoelectronics.

A dimensionality plays a crucial role in determining the basic electronic properties of TMD compounds in addition to its composition and crystallographic configuration of the atoms. The most outstanding example is graphene, the unique properties which are absent in bulk graphite [1 - 3]. The rapid pace of graphene study and developed of methodologies of thin layers obtaining led to the development of the other two-dimensional materials. In particular, the two-dimensional structures of TMD monolayers similar to that of graphene, have received considerable attention because of its large band gap value and naturally abundant [4].

Group-V TMD compounds are narrow-gap semiconductors or semimetals, characterized by low value of electrical resistivity ($\sim 10^{-6} \text{ Ohm} \cdot \text{cm}$) and periodic redistribution of electronic, ionic and total charges (charge density wave) [5]. M - M bond length in MX_2 structures (where M- group V transition metal, X – chalcogen) ranges from 3,15 Å to 4,03 Å, depending on the size of the metal, crystallographic configuration, and chalcogen ion. These values are 15-25% greater than the length of the bonds in the transition metals solids, indicating the limited energy and spatial overlap of d-orbitals in TMD compounds [6]. Crystallographic configuration of M metal in TMD structure can be trigonal prismatic (D_{3h}) or trigonal antiprismatic (D_{3d}) (Fig. 1).

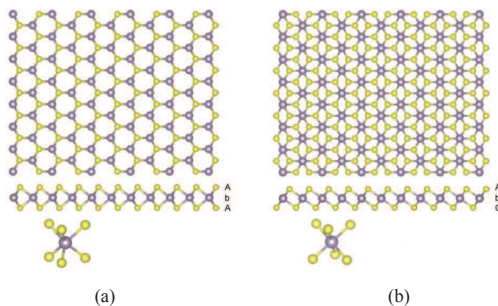


Fig. 1. Crystallographic configuration of quasi-two-dimensionao TMD:
 (a) trigonal prismatic; (b) trigonal antiprismatic

The diversity of physical and chemical composition quasi-two-dimensional TMD structures provides many opportunities for the use of its' electronic and magnetic properties in a wide range of applications for micro- and nanoelectronics, particularly for energy storage devices, the catalytically active elements in optoelectronics, and structural components for microelectronic devices. However, key challenges remain associated with an increase of electrical conductivity and increase of two-dimensional structure stability, the solution of which requires integration of experimental and theoretical studies.

- [1] K. S. Novoselov et al. Electric Field Effect in Atomically Thin Carbon Films // Science. Vol. 306. P. 666–669 (2011).
- [2] A. H. Castro Neto, F. Guinea, N. M. R. Peres, K. S. Novoselov, A. K. Geim. The electronic properties of graphene // Rev. Mod. Phys. Vol. 81. P.109–162 (2009).
- [3] A. K. Geim. Graphene: status and prospects // Science Vol. 324. P. 1530–1534 (2009).
- [4] H. Li et al. Fabrication of Single- and Multilayer MoS₂ Film-Based Field-Effect Transistors for Sensing NO at Room Temperature// Small. 2012. Vol. 8. P. 63–67 (2009).
- [5] Castro Neto A. H. Charge Density Wave, Superconductivity, and Anomalous Metallic Behavior in 2D Transition Metal Dichalcogenides // Phys. Rev. Lett. Vol. 86. P. 4382–4385 (2001).
- [6] M. Chhowalla, H.S. Shin, G. Eda, L.-J. Li, K. P. Loh, H. Zhang. The chemistry of two-dimensional layered transition metal dichalcogenide nanosheets // Nature chemistry. Vol. 5. P. 263–275 (2013).

PHONON-ASSISTED TUNNELING OF CARRIERS IN A QUANTUM WELL-QUANTUM DOT INJECTION STRUCTURE

Adam Mielnik-Pyszcorski¹, Krzysztof Gawarecki¹, Paweł Machnikowski¹

¹ Institute of Physics, Wrocław University of Technology, 50-370 Wrocław, Poland
adam.pyszcorski@gmail.com

The development of technology of stacking thin layers enabled production of quantum dots with desired parameters, such as size and composition. Additionally carrier confinement in three dimensions allows the emission of quantum dots to be highly tunable. We can create accurate lasers using quantum dots. One of the advantages is small spectral widening.

Lasers based on quantum dots have many virtues, but unfortunately also low efficiency. The reason is small volume of dots, which leads to low density of states and insufficient supply of carriers. One of proposed solutions is quantum well-quantum dot tunnel injection structure. It was shown experimentally, that quantum well, used as a reservoir with high density of states, located near a quantum dot increases efficiency of carriers injection due to phonon-assisted relaxation processes. We provide theoretical model and investigate the problem numerically. We study the dependence of the relaxation time on the system parameters.

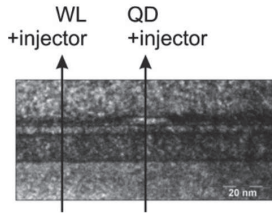


Fig. 1. Quantum well-quantum dot injection structure [1].

We have simplified numerical calculations using cylindrical symmetry of the system. Taking into account cylindrical coordinates we substitute Laplacian by its new form:

$$\nabla^2 = \frac{1}{r} \frac{\partial}{\partial r} r \frac{\partial}{\partial r} + \frac{1}{r^2} \frac{\partial^2}{\partial \theta^2} + \frac{\partial^2}{\partial z^2}, \quad (1)$$

and the wave function

$$\psi(r, \theta, z) = e^{iM\theta} \varphi(r, z), \quad (2)$$

where M is angular momentum eigenvalue.

This allowed us to reduce problem from three to two dimensions and add third dimension dependence after all calculations.

[1] G. Sęk, J. Andrzejewski, K. Ryczko, P. Poloczek, J. Misiewicz, E. Semenova, A. Lemaitre, G. Patriarche, A. Ramdane, *Semicond. Sci. Technol.* **24**, 085011 (2009).

CRYSTALLINE SILICON SOLAR CELLS PASSIVATION

Andrius Sakavicius^{1,2}¹Department of Semiconductor Physics, Faculty of Physics and Institute of Applied Research, Vilnius University, Sauletekio Ave. 9 III, LT-10222 Vilnius, Lithuania²Singulus Technologies AG, Hanauer Landstrasse 103, 63796 Kahl am Main, Germany
andrius.sakavicius@ff.stud.vu.lt

Passivated emitter and rear (PERC) [1] solar cells are a very promising candidate for next-generation industrial-type screen-printed silicon solar cells. Excellent conversion efficiencies above 20.0% with record values up to 20.2% have been demonstrated by several companies and research institutes for large area, p-type PERC solar cells with screen-printed metal contacts [2]. Several production-type tools for the deposition of rear passivation layers are already available on the market [3] or under development. In particular, rear passivation layers consisting of aluminium oxide (AlO_x) have attracted considerable attention due to their excellent surface passivation properties.

However, in addition to excellent electrical properties, it is important that the AlO_x deposition process achieves high deposition rates and hence a high throughput which enables a low cost of ownership. Plasma-enhanced chemical vapour deposition (PECVD) processes applying an inductively coupled plasma (ICP) form a high-density plasma (HDP) with electron densities of around 10^{12} cm^{-3} [4] and hence allow high deposition rates of up to several nanometres per second. ICP PECVD processes have been intensively investigated for the deposition of dielectric insulation and encapsulation layers consisting of SiO_x or SiN_x [5, 6].

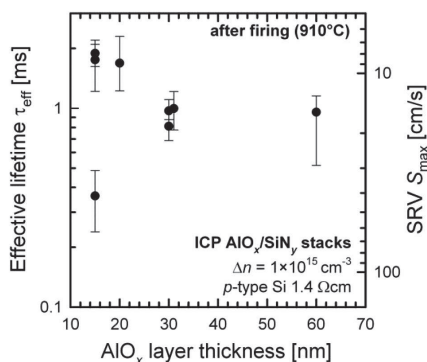


Fig. 1. Effective carrier lifetime and corresponding surface recombination velocity measured on 1.4 Ωcm float zone (FZ) wafers in dependence of the ICP AlO_x layer thickness showing lifetimes of up to 2 ms and surface recombination velocities below 10 cm/s for ICP AlO_x layers covered with a μW -PECVD SiN_x layer (SiN_x Roth und Rau) after firing [1].

In recent years, Singulus Technologies commercialized the ICP-PECVD process for the deposition of SiN_x antireflection layers of silicon solar cells using their SINGULAR tool platform. In this report, we investigate the application of the ICP-PECVD process for the deposition of AlO_x layers. We deposit the ICP AlO_x layers using a laboratory-type tool at Singulus and investigate the surface passivation properties. We apply ICP $\text{AlO}_x/\text{SiN}_x$ layer stacks as rear passivation to large-area PERC solar cells processed at Singulus as well as PERC cells processed at the Q-Cells Research Line.

- [1] T. Dullweber, M. Siebert, B. Veith, C. Kranz, J. Schmidt, R. Brendel B.F.P. Roos T. Dippell A. Schwabedissen, S. Peters, High-efficiency industrial-type PERC solar cells applying ICP AlO_x as rear passivation layer, 27th European Photovoltaic Solar Energy Conference, Frankfurt, Germany, 24-28 September 2012
- [2] B. Veith, T. Dullweber, M. Siebert, C. Kranz, F. Werner, N.-P. Harder, J. Schmidt, B.F.P. Roos, T. Dippell, R. Brendel, Energy Procedia **27**, 379-384 (2012).
- [3] H.-P. Sperlich, D. Decker, P. Saint-Cast, E. Erben and L. Peters, *Proceedings of the 25th European Photovoltaic Solar Energy Conference, Valencia, Spain* 1352 1357 (2010).
- [4] E. Kndler, G. Grahoff, K. Drescher, Surface and Coatings Technology **1**, 74-75 (1995).
- [5] J. W. Lee, K. D. Mackenzie, D. Johnson, J. N. Sasserath, S. J. Pearton, and F. Renc, J. Electrochem. Soc. **4**, 1481-1486 (2000).
- [6] J. Yota, J. Hander, and A. A. Saleh, J. Vac. Sci. Technol. **18**, 372 (2000).

APPLICATIONS OF HIGH-POWER LIGHT-EMITTING DIODES FOR SOLAR SIMULATORS

Artūras Baguckis¹, Algirdas Novičkovas^{1,2}, Algirdas Mekys^{1,2}, Vincas Tamošiūnas^{1,3}

¹ Faculty of Physics, Vilnius University, Saulėtekio al. 9, Bldg. III, LT-10222 Vilnius, Lithuania

² Institute of Applied Research, Vilnius University, Saulėtekio al. 9, Bldg. III, LT-10222 Vilnius, Lithuania

³ Center for Physical Sciences and Technology, A. Goštauto g. 11, LT-01108 Vilnius, Lithuania
baguckis.arturas@gmail.com

Solar simulators are devices that provide illumination for the controllable indoor testing of solar cells. Their primary purpose is to simulate so-called AM1.5G standardized conditions. Several types of light sources are used for solar simulators and the most common ones today are xenon arc lamps. This is due to their good match of the spectrum of the Sun and the ability to filter with ease the emitted light to meet A class criteria, defined in the international standard [1]. Such lamps, however, have the disadvantage of low luminous efficiency, high power consumption, decrease in performance quality with aging, complex control and thermal management issues.

In comparison with traditional lamps, light-emitting diodes (LEDs) have numerous advantages, such as high efficiency, lower thermal emission, long lifetime, low operating voltage, etc. Recently, 1.5W light emitting diodes were applied to simulate solar radiation with 90% of the required by the standard intensity [2]. Also, a hybrid light source with B class spectral match was demonstrated [3].

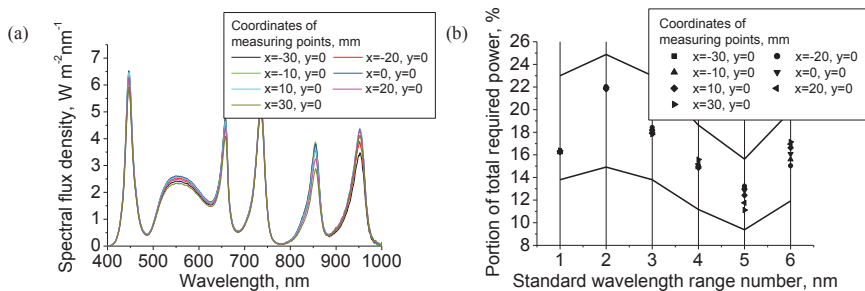


Fig. 1. Spectral irradiance distributions at 7 points of the test plane (a). Integrated spectral irradiance ratios to the total irradiance for six wavelengths intervals (every 100 nm between 400 nm and 900 nm and 900 – 1100nm) at 7 points of the test plane (b). Horizontal lines indicate upper and lower limits for A-class spectral match.

On this presentation, we report on the design and characterization of a solar simulator prototype based on high-power light-emitting diodes as light sources. Our goal is to demonstrate that compact array of only six types of LEDs (cool white, royal blue, deep red, far red and two types of infrared) can be sufficient for simulation of high (at least 100 mW/cm²) light flux density (see Fig. 1) with A-class spectral distribution match and A-class irradiance non-uniformity for the test area of several cm².

This study was supported by the Research Council of Lithuania (Grant No. MIP-099/2012). In addition, A. Baguckis would like to acknowledge support by project "Promotion of Student Scientific Activities" (VP1-3.1-ŠMM-01-V-02-003) from the Research Council of Lithuania. This project is funded by the Republic of Lithuania and European Social Fund under the 2007-2013 Human Resources Development Operational Programme's priority 3.

[1] International Electrotechnical Commission standard IEC 60904-9 Ed. 2.0.

[2] Jang, S.H., and Shin, M.W.: 'Fabrication and thermal optimization of LED solar cell simulator', *Curr. Appl. Phys.*, 2010, **10**, pp. S537–S539.

[3] Bliss, M., Betts, T.R., and Gottschalg, R.: 'An LED-based photovoltaic measurement system with variable spectrum and flash speed', *Solar Energy Materials & Solar Cells*, 2009, **93**, pp. 825–830.

MODELING OF DLTS RESPONSE FOR SILICON DIODES WITH DEFECT CLUSTERS

Elena Levchuk¹, Leonid Makarenko¹, Stanislav Lastovski²

¹ Department of Applied Mathematics and Computer Science, Belarusian State University, Minsk, Belarus

² Scientific-Practical Materials Research Centre of NAS of Belarus, Minsk, Belarus

liauchuk.alena@gmail.com

It is expected the formation of defect when high-energy Si knock-on atoms are created and cluster effects are likely to be quite important for radiation damage of silicon detectors in LHC experiments. However, the understanding of these effects in Si detectors irradiated with different particles is insufficient as compared to the knowledge on the role of isolated point defects.

DLTS is one of the main methods of defect characterization in semiconductor structures. At present two characteristic features of clustered defects are well established. First, it is temperature dependence of DLTS peak amplitude $S_{\max}(T)$ and closely related to this feature the inequivalent heights of divacancy peaks [1 – 3]. And second, the stretched kinetics for filling of clustered traps [3, 4]. This work focuses on studies of the first effect. Numerical simulation of cluster effect on DLTS signal has been performed.

To calculate temperature dependence of any DLTS peak related to a defect in a cluster it is necessary to calculate the distribution of electric potential and then to determine occupancy number of defects. To obtain electric potential ψ for the distribution of defects with axial symmetry the following problem should be solved:

$$\frac{1}{\rho} \frac{\partial}{\partial \rho} \left(\rho \frac{\partial \psi}{\partial \rho} \right) + \frac{\partial^2 \psi}{\partial z^2} = - \frac{\rho_c(\rho, z, \psi)}{\epsilon \epsilon_0}, \quad \rho > 0, -\infty < z < +\infty, \quad (1)$$

$$\left. \frac{\partial \psi}{\partial \rho} \right|_{\rho=0} = 0, \quad \psi \xrightarrow{\rho \rightarrow \infty} 0, \quad \psi \xrightarrow{|z| \rightarrow \infty} 0, \quad (2)$$

where charge density ρ_c is given by

$$\rho_c(\rho, z, \psi) = e(N_d - n(\psi) - N_{VV}(\rho, z)f_{VV}(\psi)), \quad (3)$$

carrier concentration n is related to electrical potential

as $n(\psi) = N_d \exp\left(\frac{e\psi}{k_B T}\right)$, f_{VV} is average charge of

divacancies. The distribution of defects in a cluster (N_{VV}) is characterized by the following function:

$$N_{VV}(\rho, z) = \frac{M_{VV}}{\sqrt{\pi^3} b a^2} \exp\left(-\frac{\rho^2}{a^2} - \frac{z^2}{b^2}\right), \quad (4)$$

where M_{VV} is number of divacancies in a cluster, $a = R\gamma^{-1/3}$, $b = R\gamma^{2/3}$, ($\gamma > 1$), hence, the cluster has the same characteristic volume as a spherical cluster with characteristic radius R .

The problem (1) – (2) was solved using finite element method. The results of the simulation were compared with experimental data obtained by DLTS method in order to identify unknown parameters of the cluster, particularly, number of divacancies in cluster. Fig. 1 represents this comparison for doubly charged divacancies.

As shown in Fig.1, peak amplitude demonstrates stronger dependence on temperature with increasing M_{VV} and decreasing γ . Since the value of M_{VV} , required to fit experimental data, is fewer than expected number of divacancies in a cluster, prolate clusters show better agreement with experimental data than spherical clusters.

We also considered clusters with distribution of defects characterized by sum of two functions of the kind (4) with different values of a and b and combinations of two close clusters.

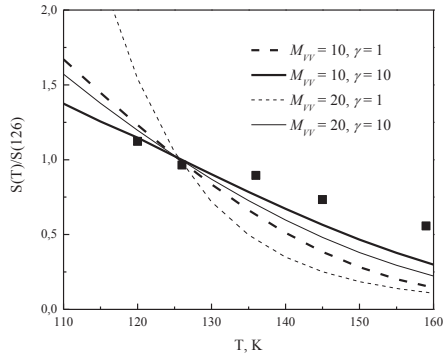


Fig. 1. Temperature dependencies of DLTS peak amplitude for doubly charged divacancies in prolate ($\gamma = 10$) and spherical ($\gamma = 1$) clusters for $M_{VV} = 10$ and $M_{VV} = 20$ (lines) and experimental data (markers). Peak amplitudes are normalized by the amplitude value at 126 K, $N_d = 2.55 \cdot 10^{13} \text{ cm}^{-3}$, $R = 10 \text{ nm}$.

[1] I.V. Antonova et al, Phys. Tekhn. Poluprovodn. **22**, 998 (1988).

[2] M. Kuhnke. ROSE/TN/2003-01.

[3] E. V. Monakhov et al, Phys. Rev. **B 65**, 245201 (2002).

[4] R. M. Fleming et al, J. Appl. Phys., **102**, 043711 (2007).

WITHDRAWED CONTRIBUTION

ELECTRICAL AND OPTICAL CHARACTERISTICS OF LIGHT-EMITTING DIODES WITH DOUBLE HETEROJUNCTION AS FUNCTION OF AGING DURATION

Laurynas Dabašinskas¹, Donatas Meškauskas¹, Artūras Žukauskas¹

¹ Institute of Applied Research, Vilnius University, Lithuania
Dabasinskas.laurynas@gmail.com

Since the first researches of semiconductors their unique light conversion property was observed which can be used for electromagnetic waves conversion to electric current and vice versa. Efficiency of this process is determined not only by light absorption or escape, but also by electric and thermal semiconductor properties. Most important of them are charge localization or separation realized in modern semiconductors with heterojunctions or thin layers. Series resistance also plays significant role in decreasing overall efficiency and increasing crystal temperature. Non-radiative recombination also increases crystal temperature which also have positive feedback.

Light-emitting diodes stands out with its relatively long life time, although catastrophic degradation is not intrinsic like of other luminaires. Degradation of LEDs is observed with light output gradual declination [1]. Defect generation in active or cladding layers, degradation of contacts and lens resin are responsible for light output variations [2].

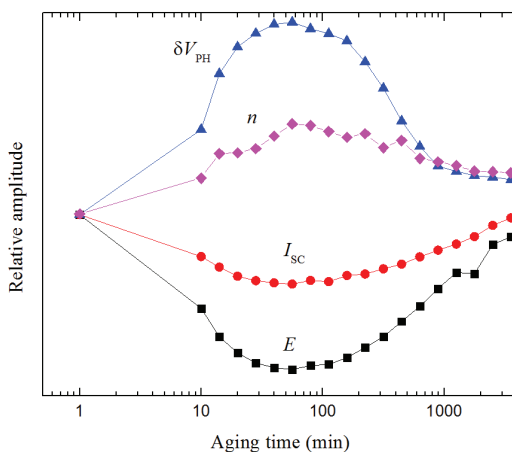


Fig. 1. LED under test differential photo-voltage, ideality factor, short circuit current and light output as function of aging duration.

The goal of this study was to prepare necessary equipment and methodology for electrical and optical parameters characterization of light-emitting diodes as function of aging duration. The mount was designed and custom made withstanding constant experimental condition and stabilized temperature for all devices under test. Automated LED aging current source with integrated stopwatch was made to ensure precise aging time constants. Methodology and automated operation of electrical and optical parameters characterization experiments was developed. Electrical parameters characterization consists of current-voltage, capacitance-voltage, differential photo-voltage versus current and short circuit current experiments. Optical parameters are investigated employing light-current experiment. Preliminary results (Figure 1) showed correlation between extreme point of differential photo-voltage, ideality factor, short circuit current and light flux as functions of aging time.

[1] O. Pursiainen, N. Linder, A. Jaeger, R. Oberschmid and K. Streubel, Identification of aging mechanisms in the optical and electrical characteristics of light-emitting diodes, *Appl. Phys. Lett.*, **79** (18), (2001).

[2] G. Meneghesso, M. Meneghini and E. Zanoni, Recent results on the degradation of white LEDs for lighting, *J. Phys. D: Appl. Phys.*, **43** (354007), (2010).

ANNEALING STUDIES ON DOFZ AND STFZ Si DIODES AFTER 3.5 MeV ELECTRON IRRADIATION

Dovilė Meškauskaitė

Vilnius University, Institute of Applied Research, Vilnius LT-10222, Lithuania
dovime@gmail.com

Dependence of the device electrical characteristics on fluence is essential in evaluation of the functionality of high-energy particle detectors under high fluence irradiation conditions. In this study, radiation damage in standard float zone (STFZ) and diffusion oxygenated float zone (DOFZ) Si detectors irradiated by electrons have been investigated by means of capacitance deep level transient spectroscopy (C-DLTS). DLTS is widely used method for studying deep level defects in semiconductors. DLTS method is used for the measurement of a deep-level activation energy, the concentration of the defects and the capture cross section. C-DLTS is based on measurements of the capacitance transient signals resulting from relaxation processes, following the abrupt changes of bias voltage and temperature [1].

The samples were irradiated with 3.5 MeV electrons. Irradiation fluence was 10^{12} e/cm². The irradiated samples were subjected to isothermal annealing at 250 °C temperature for different time intervals. The analysis of the C-DLTS spectra shows that the electron irradiation creates vacancy-oxygen, divacancies and carbon related defects. C_iC_s complex was detected only in STFZ Si sample, because the introduction of CiCs depends on the concentration of C_s and O_i. In oxygenated sample reaction channel C_i+O_i → C_iO_i is favoured. The annealing caused formation of unknown deep level (peak at 140 K) and VOH defect (Fig. 1). It was revealed that increasing in the concentration of VOH defect leads to the decreasing of the concentration of unknown defect level. The concentration of all electron traps decrease during annealing, and is less in DOFZ Si than in STFZ Si diode, while the concentration of all hole traps is increasing during annealing, and is higher in DOFZ sample.

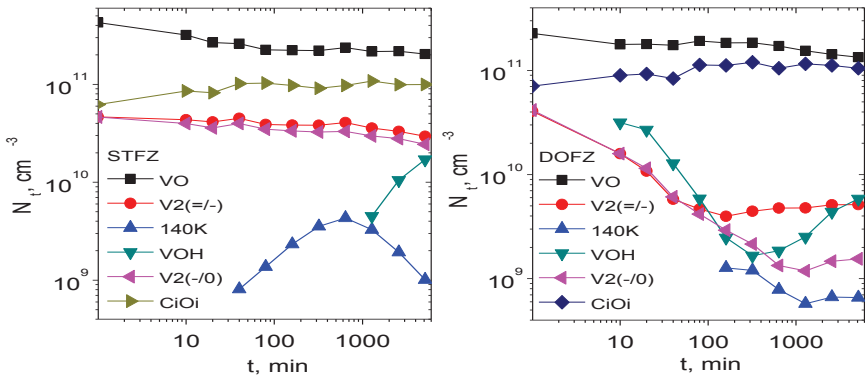


Fig. 1. Dependence of trap concentrations on the thermal annealing time.

[1] D. V. Lang, "Deep-level transient spectroscopy: A new method to characterize traps in semiconductors," in Journal of Applied Physics, vol. 45, pp. 3023-3032, (1974).

DIRECT LIGHT-INDUCED SURFACE PATTERNING IN a-As₂S₃ THIN FILMS

Ugis Gertners¹, Janis Teteris¹, Zanda Gertnere², Elina Potanina¹

¹ Institute of Solid State Physics, University of Latvia, Latvia

² Institute of Chemical Physics, University of Latvia, Latvia
gertners@gmail.com

The demand of lower cost surface-relief based optical instruments such as grating-based resonators or filters for waveguides, diffractometers, spectrometers, etc. is one of the main driving forces for the investigation of direct light-induced relief formation. The most common techniques for fabricating and investigating these surface-relief gratings involve an interferometric or holographic recording setup.

We have investigated that the light-induced mass transfer process strongly depends on the material itself and polarization of the light. The behavior of mass transfer and thus the resulting recording could be related to interaction between the polar photo-induced defects and the polarized electric field of recording beam. It has been shown that the mass transfer can be directed both ways – towards or away from the electric field intensity gradient. The evolution of surface relief in dependence from the recording time and polarization has been investigated in detail. The mechanism of the direct recording of surface relief on amorphous chalcogenide films based on the photo-induced plasticity has been discussed.

A direct recording technique is a comparatively new solution for lithography and, as shown in this report, provides new experimental techniques for better understanding of the interaction between the light and matter. The obtained gratings are very stable at room temperature, so this method can replace some of the chemical etching techniques and find a practical application in the applied physics.

MODELLING NANOSTRUCTURED TiO_2 CELLS FOR PLASMON-ENHANCED PHOTOCATALYSIS

Anton Yermalovich

Department of Micro- and Nanoelectronics, Belarusian State University of Informatics and Radioelectronics, Belarus
anton.yermalovich@gmail.com

Plasmonic energy conversion is known as a promising alternative to electron–hole separation in semiconductor devices [1]. This method is based on the generation of hot electrons in plasmonic nanostructures through electromagnetic decay of surface plasmons. Here are presented the fundamentals of using titanium oxide based nanostructures (TiO_2) and special attention is paid towards the possibility of mass-producing cheap and effective photovoltaic devices. This new method of using semiconductor nanoparticles on structured TiO_2 substrates offers a low cost method of fabrication with high conversion efficiencies. Thus, the modelling of nanostructured TiO_2 cells for plasmon-enhanced photocatalysis plays an important role for more efficient conversion of solar energy in photovoltaic and photocatalytic devices.

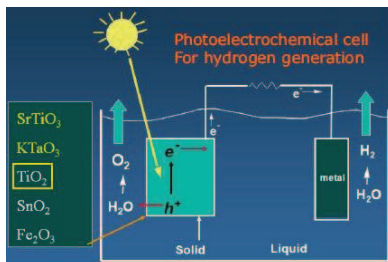


Fig. 1. Schematic illustration of photoelectrochemical cell for hydrogen generation [2]

Among the many investigated photocatalyst materials for the past decades, TiO_2 remains the most popular candidate for applications in solar cells, solar fuels, and environmental cleaning [3-5]. It is due to its outstanding and unique physicochemical properties. The properties of TiO_2 can be widely altered by introducing defects in the crystal lattice and by doping. TiO_2 is much cheaper than other photosensitive materials and its reserves are abundant. All these factors, so far, make TiO_2 superior for energy and environmental applications in comparison to other heterogeneous photocatalysts.

Nanostructures based on TiO_2 have received a great attention due to different physicochemical properties as compared to its bulk form [6]. It is reported that TiO_2 have enhanced photoactivity owing to its particle size and reduced recombination rate. The anatase phase is considered to be the active element in the mixed phase, whereas the rutile acts as an electron sink to reduce the recombination rate [7]. Overall, TiO_2 as nanostructures offers high surface to volume ratio and short path for charge carriers to the surface (especially for photogenerated holes).

Thus, operation of the catalytic system requires charge carrier transport to the surface, that is why the main problem still remain the charge carrier recombination. That problem can be successfully solved by the design, fabrication techniques. Modeling of TiO_2 based photocatalysts could greatly simplify this problem through the optimization of its their performance and further understandings of the mechanisms for enhanced photocatalytic activity.

- [1] C. Clavero. Plasmon-induced hot-electron generation at nanoparticle/metal-oxide interfaces for photovoltaic and photocatalytic devices // *Nature Photonics*. Vol. 8. P. 95–103 (2014).
- [2] Jiangtian Li, Scott Cushing, Peng Zheng, Nianqiang (Nick) Wu. Coupling of Semiconductor to Plasmonic Nanostructure for Solar Fuel Generation // Department of Mechanical & Aerospace Engineering, West Virginia University Morgantown, USA (2013).
- [3] M. Gratzel, Dye-sensitized solar cells, *J Photochem Photobiol C*, Vol. 4 145-153 (2003).
- [4] M. Ni, M.K.H. Leung, D.Y.C. Leung, K. Sumathy. A review and recent developments in photocatalytic water-splitting using TiO_2 for hydrogen production, *Renew Sust Energ Rev*, Vol 11. P. 401-425 (2007).
- [5] M.R. Hoffmann, S.T. Martin, W.Y. Choi, D.W. Bahnemann, *Environmental Applications of Semiconductor Photocatalysis*, *Chem Rev*, Vol. 95. P. 69-96(1995).
- [6] R. Sellappan. Mechanisms of Enhanced Activity of Model TiO_2 /Carbon and TiO_2 /Metal Nanocomposite Photocatalysts // PhD Thesis, Department of Applied Physics Chalmers University of Technology Göteborg, Sweden (2013).
- [7] D.C. Hurum, A.G. Agrios, K.A. Gray, T. Rajh, M.C. Thurnauer, Explaining the enhanced photocatalytic activity of Degussa P25 mixed-phase TiO_2 using EPR, *J Phys Chem B*, Vol. 107. P. 4545-4549 (2003).

WITHDRAWED CONTRIBUTION

EPOXY RESIN FILLED WITH CNT AND GNP: RHEOLOGY, DENSITY, AND ELASTIC MODULUS

Anna Borisova¹, Andrey Aniskevich¹, Mauro Zarrelli²

¹ Institute of Polymer Mechanics, University of Latvia, Riga, Latvia

² Institute for Composite and Biomedical Materials, National Research Council of Italy, Portici, Italy

Anna.Borisova@pmi.lu.lv

Nowadays, one of the important materials is often used in engineering, aerospace and other industries is epoxy resin which has highly competitive physical properties. Currently, new properties and improves of epoxy resins might be achieved by using different fillers where the most promising are carbon based nanofillers. Because of carbon nanotubes (CNT) and graphene nanoplatelets (GNP) exceptional characteristics they are considered as effective carbon nanofillers which would be capable to improve stiffness, conductivity, resistance to environmental conditions, etc. However, it is hard to predict theoretically particle behavior on NC properties. Therefore, physical properties of NC filled with carbon particles in different filler content should be experimentally investigated in order 1) to understand the mechanism how nanofillers impact the epoxy resin nanocomposite (NC) and 2) to determine the optimal CNT or GNP content which would maximally improve physical properties of NC, reduce production costs, and enhance multifunctionality and application possibilities.

The aim of the study is to investigate the impact of two different type carbon nanofillers on the density, rheological and mechanical behavior of epoxy resin.

To pursuit this objective, as a matrix were used mono-component thermosetting epoxy resin RTM6 employed in the aerospace industry. High aspect ratio carbon nanofillers, namely, CNT (1D) and GNP (2D) have been loaded into the hosting matrix by using a high-shear mixer at various weight contents, below and above the nominal percolation threshold.

In order to understand how carbon nanoparticles change the density of investigated nanocomposites hydrostatical weighting were performed. Results show quite insignificant but linear density increase with increasing the particle loading.

Rheological investigations showed that the nanocomposites' viscosity depends on nanofiller type and content. It is obtained that above critical filler content, the effect of nanoparticles on the neat resin viscosity abruptly change acting not longer as viscosity reducers. This critical content could be suitably regarded as a 'rheological percolation' behavior. Results reveal that above percolation threshold, CNT/epoxy nanocomposite are characterized by high viscosity due to the presence of a formed fully connected physical network among CNTs which will be broken up by increasing the shear rate. GNP suspensions, conversely, clearly show the effect of formation of a stable network over the whole considered shear rate sweep. At sub-percolation concentrations, the rheometric frequency sweep tests revealed, that both typology of nanoparticles act as viscosity reducer for the hosting system. To summarize the main found effect it can be stated that above percolation threshold CNT create a strong physical network which is destroyed by high shear rates, on the other hand GNP form weaker but stable network.

The quasistatic tensile tests were applied in order to determine mechanical properties of the NC. Both fillers increase elastic modulus by almost 10% at filler content below percolation threshold in comparison with neat epoxy resin. Results does not show significant improvement of tensile strength.

It is expected, that one of the most promising solutions is an attempt combining these two carbon fillers into a hybrid structure which could lead to a potentially new multifunctional material in research and application as the result of synergy effect of both fillers. It is considered that such hybrid NC besides high mechanical characteristics will provide electrical conductivity and thermal dissipation at lower filler content, that will minimize agglomeration ability and price of the NC.

GREEN SYNTHESIS OF SILVER NANOPARTICLES USING PLANT EXTRACTS

Alicja Szczepańska¹, Dorota Szczepańska², Dorota Kowalczyk¹

¹Gdansk University of Technology, Faculty of Applied Physics and Mathematics, Poland

²Gdansk University of Technology, Faculty of Chemistry, Poland
alicja2207@gmail.com

The size, shape and controlled dispersity of nanoparticles play a vital role in determining the physical, chemical, optical and electronic properties attributing its applications in environmental, biotechnological and biomedical fields. Various physical and chemical processes have been exploited in the synthesis of several metal nanoparticles by wet and dry approaches viz., ultraviolet irradiation, aerosol technologies, lithography, laser ablation, ultrasonic fields, and photochemical reduction techniques. However, these methods remain expensive and involve the use of hazardous chemicals. Therefore, there is a growing concern for the development of alternative environmentally friendly and sustainable methods. Increasing awareness towards green chemistry and biological processes has led to a necessity to develop simple, cost-effective and eco-friendly procedures.

The poster present the green synthesis of silver nanoparticles, using plant extracts with a subsequent investigation on the size distribution and surface structure of nanoparticles formed under various process conditions.

THERMAL BEHAVIOR AND MAGNETIC PROPERTIES OF ALGINIC ACID – Fe_3O_4 NANOCOMPOSITES

Małgorzata Kaźmierczak^{1,2*}, Katarzyna Pogorzelec-Glaser¹, Stefan Jurga²,
Bartłomiej Andrzejewski¹

¹Institute of Molecular Physics, Polish Academy of Sciences
M. Smoluchowskiego 17, 60-179 Poznań, Poland

²NanoBioMedical Centre, Adam Mickiewicz University, Umultowska 85, 61-614 Poznań, Poland
malgorzata.kazmierczak@ifmpan.poznan.pl

The interest in composites of polymers with magnetic nanoparticles stems from their unique physical properties and potential future applications for magnetic data storage [1], electronic devices and sensors [2], for biomedical applications in magnetic resonance imaging [3], drug delivery [4] and hyperthermia agents [5]. In this work we used magnetite (Fe_3O_4) nanoparticles embedded in alginic acid (AA). We obtained the magnetite (Fe_3O_4) nanoparticles by Pechini method from $\text{FeCl}_3 \cdot 6\text{H}_2\text{O}$, CH_3COONa and PEG with microwave activation (MARS-5 CEM) and prepared nanocomposites with alginic acid (AA). Aqueous dispersion of Fe_3O_4 nanopowder, AA and polyethylene glycol was casted and dried in the air at room temperature.

XRD studies verified the Fd-3m point group of the nanopowder with lattice parameters $a = 8.3641 \text{ \AA}$ and mean grain size 20 nm. Thermal behavior of alginic acid – Fe_3O_4 nanocomposites was examined by differential scanning calorimetry (DSC) and thermogravimetry analysis (TGA). The magnetic measurements were performed using the Quantum Design Physical Property Measurement System (PPMS) fitted with a Vibrating Sample Magnetometer (VSM) probe in the temperature range from 4 K to 300 K.

Acknowledgements

This work was supported by the National Science Centre in Poland (N N507 229040).

The project was supported through the European Union - European Social Fund and Human Capital - National Cohesion Strategy.

Authors would like to thank the Laboratory of Structural Studies at the Faculty of Physics, AMU for performing thermogravimetric experiments.

[1] D. Weller, A. Moser, Thermal effect limits in ultrahigh density magnetic recording, *IEEE Trans. Magn.* **35**, 4423 (1999).

[2] I. Koh, L. Josephson, Magnetic Nanoparticle Sensors, *Sensors* **9**, 8130-8145 (2009).

[3] C.W. Jung, P. Jacobs, Physical and chemical properties of superparamagnetic iron oxide MR contrast agents: ferumoxides, ferumoxtran, ferumoxsil, *Magn. Reson. Imaging* **13**, 661-674 (1995).

[4] S. Bucak, B. Yavuztürk, A.D. Sezer, Magnetic Nanoparticles: Synthesis, Surface Modifications and Application in Drug Delivery, chapter 7 in *Recent Advances in Novel Drug Carrier Systems*, ed. Ali Demir Sezer, InTech Publisher, October 2012

[5] P. Wunderbaldinger, L. Josephson, R. Weissleder, Tat peptide directs enhanced clearance and hepatic permeability of magnetic nanoparticles, *Bioconjugate Chem.* **13**, 264-268 (2002).

SURFACE ACOUSTIC WAVE PROPAGATION ON 36° ROTATED Y-X LiTaO₃

Justina Kalvelytė¹, Andrius Didžbalis¹, Romualdas Rimeika²

¹Faculty of Physics, Vilnius University, Lithuania

²Department of Radiophysics, Vilnius University, Lithuania

Justina.Kalvelyte@ff.stud.vu.lt

Andrius.Didzbalis@ff.stud.vu.lt

Surface acoustic waves (SAW) are widely used in many electronic devices like filters, converters, delay lines. SAW devices became popular when american scientists R. M.White and F.W. Volmer [1] suggested the interdigital trasducer (IDT) for SAW excitation and reception in piezoelectrical materials. Leaky surface acoustic waves (LSAW) are also popular for using in electronic devices. These waves has a shear horizontal polarization, which makes them especially interesting for sensor applications.

The objective of this research was to investigate the impact of surface metallization on the propagation of the LSAWs in piezoelectric 36° rot. Y-X LiTaO₃ crystals. Two experimental methods, the acousto-optic technique and the electroacoustic technique, were used.

The leaky SAWs of the LiTaO₃ crystals were generated using the interdigital transducers with a period of 50 μm and 33 electrode pairs.

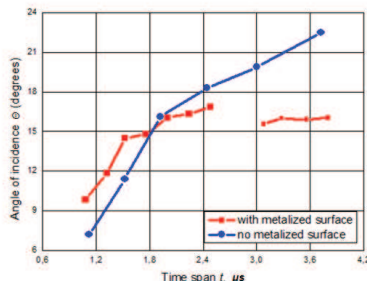


Fig. 1 Light incidence angle corresponding to the strongest diffraction as a function of probing beam position (in time-delay units) interaction to source of acoustic waves

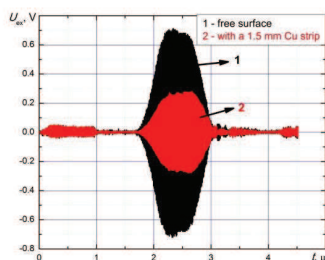


Fig.2. Signals on receiving IDT for LSAW propagation surface: 1) free; 2) with a 1.5 mm Cu strip.

When using the acousto-optic method, the He-Ne laser beam was pointed onto the crystal surface. The leaky SAW generates a bulk acoustic wave. Both waves cause the diffraction of light. During the experiment, we searched the angle of incident light corresponding to the strongest intensity of the diffracted light. The experiment revealed that coating the surface of lithium tantalate with a strip of metal causes changes both in the amplitude of the diffracted light signal and in the amplitude of the signal detected with interdigital transducers. Also, we have noticed the changes in the light incidence angle due to metallization. As seen in Figure 1, after coating the surface of lithium tantalate with a copper strip of 1 millimeter width, the angle of incident light behind that strip does not change the turning beam of light away from the source of acoustic waves.

When using the electroacoustic method, the leaky SAW was generated and detected with the interdigital transducer. We have observed strong changes in the wave amplitude due to crystal surface metallization. An example of strong signal decrease when the crystal was coated with a 1.5 mm Cu strip is shown in Figure 2.

[1] R.M. White, F.W. Voltmer, Direct piezoelectric coupling to surface elastic waves, Appl. , Phys. Lett., 7, 314 – 316 p., 1965.

Open Readings 2014. 57th Scientific Conference for Students of Physics and Natural Sciences
**INVESTIGATION OF COMPLEX GEOMETRIC SHAPE P-N JUNCTIONS
WITH SCANNING PROBE MICROSCOPY**

Mindaugas Kamarauskas^{1,2}, Virginijus Bukauskas¹, Arūnas Šetkus¹, Marius Treideris¹

¹Department of Physical Technologies, Center for physical sciences and technology, Lithuania

²Faculty of Physics, Vilnius University, Lithuania
kamarauskas.m@gmail.com

Formation of various nano structures on solar cell surface is becoming one of the most popular ways to improve them. This increased surface roughness allows us to improve some qualities of solar cell such as short circuit current [1].

While forming complicated nano structures on surface of solar cell we have to evaluate some geometrical properties of p-n junction, such as its depth from the surface and its steepness, to make it certain that solar cell is being used optimally. These properties are conveniently measured by Scanning probe microscopy (SPM). Because it allows us easily collect data about nanometric scale objects with p-n junctions in them and there are different types of atomic force microscopy which could be used depending on our needs [2].

In order to test physical parameters that can be extracted from the measurements of different types of microscopy, GaAs sample was selected as a reference sample. For the measurements we used three different modes of SPM, namely scanning Kelvin probe microscopy (SKPM), electrostatic force microscopy (EFM) and conductive atomic force microscopy (C-AFM). In all cases p and n regions can be identified. However precision of identified regions for different types of microscopy differs.

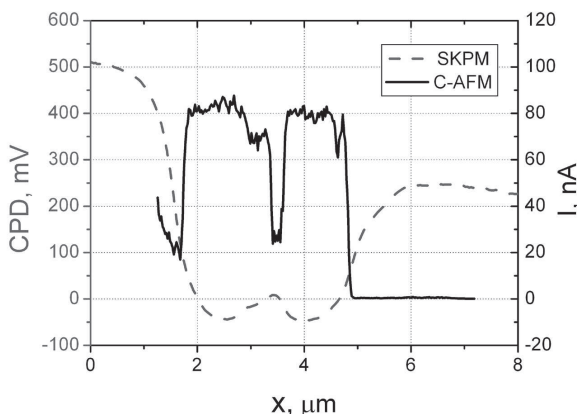


Fig. 1 SKPM and C-AFM measurements on GaAs sample

As it can be seen from the Fig.1, contact potential difference (CPD) between sample and microscope's tip measured by SKPM is the least precise due to interaction between sample's surface and cantilever on which tip is located, this causes some roundness in response signal. This roundness can be avoided by using EFM, as it measures variation of the local electric force gradients above the surface and influence of the cantilever in measured signal can be neglected in most cases. Alternative method, C-AFM measures sample's electrical current at any chosen surface point when external voltage is applied between tip and the sample. The major drawback of this type of microscopy is formation of oxide layer on some materials, which is caused by external voltage applied to the tip of a microscope. This oxide layer limits the repeatability of measurements, because every new measurement adds a new layer of oxide which weakens the response signal. This effect is a major problem for measurements on Si samples. Also naturally formed SiO₂ had a big impact on measurements made with SKPM. We discuss the measurement conditions that can improve evaluation of geometrical properties of p-n junction.

-
- [1] G. Dong, F. Liu, J. Liu, H. Zhang, M. Zhu, *Realization of radial p-n junction silicon nanowire solar cell based on low-temperature and shallow phosphorus doping*, *Nanoscale Research Letters* **8**, 544 (2013).
[2] S.B. Kuntze, D. Ban, E.H. Sargent, St.J. Dixon-Warren, J.K. White, K. Hinzer, *Electrical Scanning Probe Microscopy: Investigating the Inner Workings of Electronic and Optoelectronic Devices*, *Critical Reviews in Solid State and Materials Sciences* **30**, 71-124 (2005).

GRAPHITE SAMPLE PREPARATION FOR $\delta^{13}\text{C}$ MEASUREMENTEdmundas Bružas¹, Andrius Garbaras², Konstantinas Zakalskis³, Vidmantas Remeikis²¹ Department of Physics, Kaunas University of Technology, Lithuania² Department of Nuclear Research, Center for Physical Sciences and Technology, Lithuania³ Department of General Physics and Spectroscopy, Vilnius University, Lithuaniaedmundas.bruzas@ktu.edu

Isotope ratio mass spectrometry can be used as one of the experimental method which allows to evaluate total neutron flux through graphite stack of nuclear reactor [1].

Graphite was and still is an important material in Magnox, AGR, HTR and RBMK type nuclear reactors [1] in which it is used as neutron moderator. Nuclear graphite is a very pure material but it still contains some impurities of various elements which can be activated by (n, γ), (n, p), (n, α) reactions [1]. Therefore it is classified as long-lived radioactive wastes after the shutdown of a nuclear power plant. The evaluation of neutron flux can be used for the management of used nuclear graphite [1].

The objective of this work is to ascertain, how the $\delta^{13}\text{C}$ values of not activated nuclear reactor graphite (it was used as model of nuclear graphite) depend on sample preparation (graining, pulverizing, use of oxidator V_2O_5) and evaluate memory effect in elemental analyzer.

In our work was used natural, not irradiated, grained graphite from Poland. The measurements were made with the elemental analyzer *FlashEA 1112* connected to the stable isotope ratio mass spectrometer *ThermoFinnigan Delta Plus advantage*.

There were six samples prepared. There was used grained and pulverized (using manual grater) graphite, mixed with oxidator V_2O_5 and put into tin capsules.

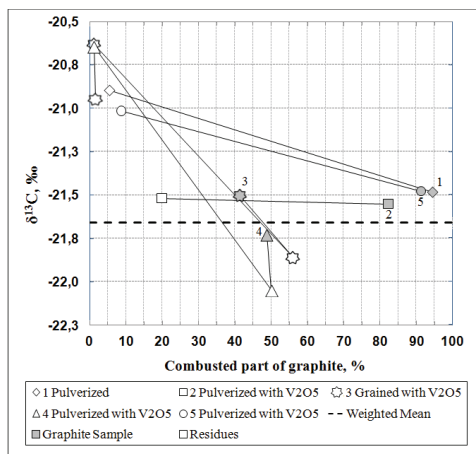


Fig. 1. $\delta^{13}\text{C}$ dependency on burnt part of graphite.

Fig. 1 shows graphite fractionation in the elemental analyzer. After each sample measurement, there were being made repeated measurements (delivering empty tin capsule into combustion furnace), until there were left no residues of graphite in the furnace.

When a sample needs more number of repeated measurements for complete combustion, it gives higher level of fractionation (samples 3, 4). It seems that during the first measurement usually burns the part of sample with lighter isotopes, giving greater $\delta^{13}\text{C}$ values of the residues. Though two measurements were needed for complete combustion of sample 2, but fractionation in this case is very small ($\delta^{13}\text{C}$ values of both measurements are almost identical). But possible effect of oxidator V_2O_5 was not confirmed by the measurements of sample 1 (without V_2O_5) and sample 5 (with V_2O_5) whose characters are very similar.

More researches must be done to determine the best graphite preparation for stable isotope ratio analysis.

Acknowledgements. Authors acknowledge support by project "Promotion of Student Scientific Activities" (VP1-3.1-ŠMM-01-V-02-003) from the Research Council of Lithuania. This project is funded by the Republic of Lithuania and European Social Fund under the 2007-2013 Human Resources Development Operational Programme's priority 3.

[1] V. Remeikis, A. Plukis, R. Plukienė, A. Garbaras, R. Barisevičiūtė, A. Gudelis, R. Gvozdaite, G. Duškesas, L. Juodis, Method based on isotope ratio mass spectrometry for evaluation of carbon activation in the reactor graphite, Nuclear Engineering and Design 240, 2697–2703 (2010).

Open Readings 2014. 57th Scientific Conference for Students of Physics and Natural Sciences
THE ENERGY SPECTRUM OF GRAPHENE QUANTUM DOTS
IN MAGNETIC FIELD AND WITH STAGGERED POTENTIAL.

Ludmila Szulakowska

Institute of Physics, Wrocław University of Technology, Poland
ludmila.szulakowska@gmail.com

We study the energy spectra obtained within tight-binding model for hexagonally-shaped graphene quantum dots (GQDs) subjected to external magnetic field. Energy spectra of periodic structures in the presence of magnetic field show recursive nature, if plotted as a function of magnetic flux and they are known as Hofstadter's butterflies [1].

We identify the self-similar gaps in subbands of the spectra and label them by two integers (t,s) satisfying the Diophantine equation. Therefore, we construct their linear trajectories in the form of the density-field diagram (Wannier diagram) [4]. In the spectra for relativistic carriers in graphene a special sequence of Landau levels can be identified. It is shown that their square root dependence on magnetic field is true for the nanostructures studied. Moreover, size effects and edge type influence on the Hofstadter spectra and electronic density are investigated.

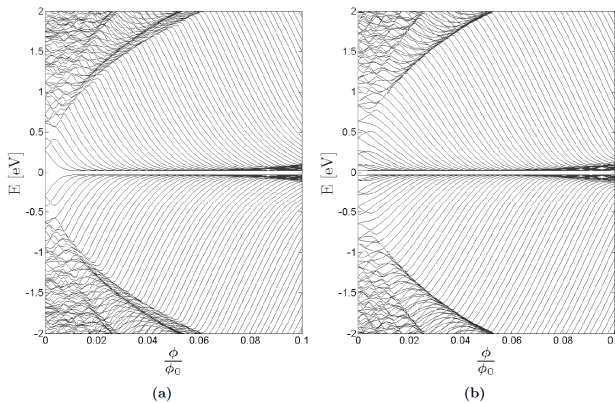


Fig. 1. Low-energy spectrum as a function of weak magnetic fields structures with edges of type armchair (a) and zigzag (b) are considered. Subbands shown as dark regions figures form Landau levels for relativistic particles.

Band gap induced by staggered potential appears in the zeroth Landau level for all values of magnetic flux.

Recently, in attempt to observe such fractal dependencies in experiment (with low magnetic fields), heterostructures of graphene coupled to hexagonal boron nitride and their spectra have been studied [2]. Superlattices arising in such structures have been predicted to break the A-B sublattice symmetry and, as a consequence, to open a band gap at the charge neutrality points [3].

The substrate effects for GQDs studied here are modelled with 'staggered' potential component of the Hamiltonian [5], which breaks the sublattice symmetry. This produces an energy gap in the zeroth Landau level persisting uninterrupted for the whole range of magnetic flux studied (fig. 1.)

-
- [1] D. R. Hofstadter, Energy levels and wave functions of Bloch electrons in rational and irrational magnetic fields, *Physical Review B* **14**, (1976).
 - [2] C. R. Dean, L. Wang, P. Maher, C. Forsythe, F. Ghahari, Y. Gao, J. Katoch, M. Ishigami, P. Moon, M. Koshino, T. Taniguchi, K. Watanabe, K. Shepard, J. Hone, P. Kim, Hofstadter's butterfly and the fractal quantum Hall effect in moire superlattices, *Nature* **497**, 598-602 (2013).
 - [3] B. Hunt, et al., Massive Dirac Fermions and Hofstadter Butterfly in a van der Waals Heterostructure, *Science* **340**, (2013).
 - [4] G. H. Wannier, A Result Not Dependent on Rationality for Bloch Electrons in a Magnetic Field, *Physica Status Solidi* **88**, 757 (1978).
 - [5] J. Cao, S.J. Xiong, Topological phase transition in a graphene system with a coexistence of Coulomb interaction, staggered potential, and intrinsic spin-orbit coupling, *Physical Review B* **88**, (2013).

MAGNONIC CRYSTALS

Filip Lisiecki^{1*}

¹Faculty of Technical Physics, Poznan University of Technology, Poland

^{*}lisiecki.filip@gmail.com

Propagation of different kinds of waves through the periodically modulated materials has been recently paid much attention. They are interesting, because it is possible to change their properties by controlling the geometry and the structure of used materials. For example, intensively studied are objects with modulated refractive index with a periodicity compared to the wavelength of electromagnetic waves – photonic crystals. One of their many interesting properties is photonic band gap. These are ranges of forbidden frequency for propagating electromagnetic waves. Photonic crystals have already found applications for example in optoelectronics.

Magnonic crystals are magnetic equivalents of photonic crystals. They consist of periodically modulated magnetic materials. The kinds of waves which are information carriers in them are spin waves. The quanta of them are called magnons. In the structures magnonic band gap is observed. These are frequency ranges for magnons, which cannot propagate through the structure. Magnonic devices have large potential in technological applications and can offer new, currently not available possibilities for example in photonic and electronic elements. Moreover, they offer better miniaturization compared to photonic devices, because of much shorter length of spin excitations than electromagnetic waves of the same frequency [1, 2].

[1] V. V. Kruglyak, S. O. Demokritov, and D. Grundler, Magnonics, Journal of Physics D: Applied Physics, vol. 43, no. 26, p. 264001 (2010).

[2] W. J. Hsueh, C. H. Chen, and R. Z. Qiu, Perfect transmission of spin waves in a one-dimensional magnonic quasicrystal, Physics Letters A, vol. 377, no. 19–20, pp. 1378–1385, (2013).

DIY Supercomputer

Michal Naskret

Department of Physics and Astronomy, University of Wrocław
mnaskret@gmail.com

One of the main difficulties that modern physics face is a barrier connected with finding analytic solutions to, sometimes seemingly easy, problems. Some of the problems we can analyze with a good accuracy numerically - using computers. High performance supercomputer is the best solution nowadays. It is a system with a massive number of processors connected into one computing grid. Unfortunately such a system is extremely expensive to create, maintain and repair.

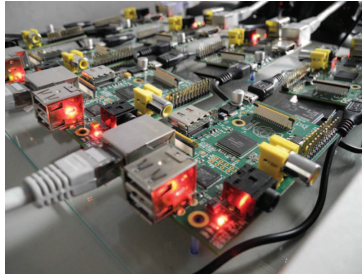


Fig. 1. Raspberry Pi based computer cluster

Using processors based on the ARM architecture(processors used in smartphones) can significantly decrease the total cost. Although the total performance also decrease, supercomputer based on the ARM architecture can be a great and affordable for students tool to simulate interesting problems and practice programming skills. In my lecture I will describe the process of building a low-cost supercomputer that can be done with basic IT and programming knowledge.

-
- [1] G.Moore, *Cramming more components onto integrated circuit*, Electronics magazine 38:3, (1965).
 - [2] J.Hall, *Foreword,[in:] T. Sterling: Beowulf Cluster Computing with Linux*, MIT Press, Cambridge, second edition, (2003).
 - [3] D.Eadline J.Radajewski, *Beowulf howto*, <http://ibiblio.org/pub/Linux/docs/HOWTO/archive/Beowulf-HOWTO.html>.

DFT CALCULATIONS OF THE FREQUENCIES AND INTENSITIES OF THE INVERSION VIBRATIONS IN THE AMMONIA MOLECULE.

Oksana Rudaya¹, George Pitsevich^{1*}

¹ Department of Physical Optics, Belarusian State University, Belarus.

rudaya_oksana@mail.ru

Ammonia molecule still attracts the attention of researchers. There are many approaches to the study of the inversion vibrations of this molecule. We propose another one approach to the analysis of the inversion vibrations of the nitrogen atom. If we freeze the stretching coordinates, the inversion vibration can be represented by a linear combination of the bending coordinates. If we use only bending coordinates the exact form of kinetic energy operator in the Hamiltonian for ammonia molecule can be represented as follows:

$$h_{\varphi} \frac{\partial}{\partial \varphi} + h_{\delta} \frac{\partial}{\partial \delta} + h_{\gamma} \frac{\partial}{\partial \gamma} + G_{\varphi\varphi} \frac{\partial^2}{\partial \varphi^2} + G_{\delta\delta} \frac{\partial^2}{\partial \delta^2} + G_{\gamma\gamma} \frac{\partial^2}{\partial \gamma^2} + G_{\varphi\delta} \frac{\partial^2}{\partial \varphi \partial \delta} + G_{\varphi\gamma} \frac{\partial^2}{\partial \varphi \partial \gamma} + G_{\gamma\delta} \frac{\partial^2}{\partial \gamma \partial \delta} \quad (1)$$

where φ, δ and γ represented on Figure 1.

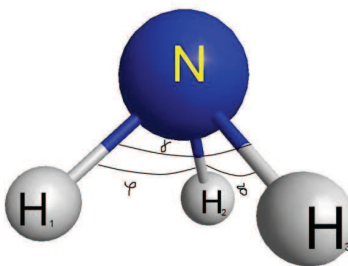


Fig. 1. Bending coordinates of the ammonia molecules.

The terms in (1) can be written as follows:

$$h_{\varphi} = -\frac{\hbar^2}{2M_H} \text{div}_{r_{H1}} (\vec{s}_{r_{H1}}^{\varphi}) - \frac{\hbar^2}{2M_N} \text{div}_{r_N} (\vec{s}_{r_N}^{\varphi}) - \frac{\hbar^2}{2M_H} \text{div}_{r_{H2}} (\vec{s}_{r_{H2}}^{\varphi}) \quad (2)$$

$$G_{\varphi\varphi} = -\frac{\hbar^2}{2M_H} (\vec{s}_{r_{H1}}^{\varphi})^2 - \frac{\hbar^2}{2M_N} (\vec{s}_{r_N}^{\varphi})^2 - \frac{\hbar^2}{2M_H} (\vec{s}_{r_{H2}}^{\varphi})^2 \quad (3)$$

$$G_{\varphi\delta} = -\frac{\hbar^2}{M_N} (\vec{s}_{r_N}^{\varphi} \cdot \vec{s}_{r_N}^{\delta}) - \frac{\hbar^2}{M_H} (\vec{s}_{r_{H2}}^{\varphi} \cdot \vec{s}_{r_{H2}}^{\delta}) \quad (4)$$

Formulas (2)-(4) contain Wilson \vec{s} vectors and mass of hydrogen (M_H) and nitrogen (M_N) atoms. Using this vectors one can get for example that:

$$G_{\varphi\varphi} = -\frac{\hbar^2}{\mu_{NH}} \frac{1}{l_{NH}^2} + \frac{\hbar^2}{2M_N} \frac{2 \cos \varphi}{l_{NH}^2} \quad (5)$$

It is possible to reduce this 3D task to 1D if we introduce follows symmetric coordinates:

$$\alpha = \varphi + \delta + \gamma$$

$$\beta = 2\varphi - \delta - \gamma \quad (6)$$

$$\chi = \delta - \gamma$$

It is clear that only α can describe the inversion vibration of nitrogen atom in ammonia molecule. Using α we have calculated potential energy surface were able to find wavenumbers of the inversion vibration and tunneling frequency.

THE APPLICATION OF THE LIGHT REFRACTION AND POLARIZATION IN MODERN ARCHITECTURE

Author: Joanna Symonowicz

Department of Physics, Wrocław University of Technology, Poland
198590@student.pwr.wroc.pl

Light is a very important factor in creating the architectural interiors. It shapes the character and decides about the functionality of a place. Most of the designs still include only plane glass windows transmitting the polychromatic rays. In my research I was trying to modify the solar spectrum using its specific properties, such as refraction and polarization, in order to obtain the aesthetic and functional resolutions in light provision for buildings.

As the result of constant change in taste of ornaments, modern architecture is dominated by the minimalistic approach. However, the *horror vacui* syndrom has not changed throughout the ages and the adoration of expressive colors is a natural state for humans. Such needs can be fulfilled by the system of prisms providing the breathtaking dispersion. [1] What is more, according the Malus' law, the intensity of the interior light can be regulated by two parallel polarizers. [2]

My aim was to create a small interior (that can be used for example as the meditation space) where I would apply the given light modifications. The main obstacles of the project were the dimensions and distances between certain elements of the system [3]. I would like to show them in my presentation along with the visualization of the final construction.

[1] B. E. Saleh, *Fundamentals of Photonics*, Wiley – Interscience, ISBN 978-0-471-358329, Hoboken, 2007.

[2] J. R. Meyer-Arendt, *Introduction to classical and modern optics (polish)*, (Trans. Państwowe Wydawnictwo Naukowe, Warszawa, 1977).

[3] E. Jagoszewski, *Introduction to optical engineering (polish)*, Oficyna Wydawnicza Politechniki Wrocławskiej, ISBN 978-83-7493-410-7, Wrocław 2008.

STUDENTS' SCIENTIFIC ASSOCIATION LABORATORY

Saulė Abbas, Vytautas Aukštikalnis, Darius Bagdonas, Milda Budreckaitė, Simona Barkauskaitė, Miglius Budriūnas, Justinas Girskis, Martynas Grybauskas, Nerijus Jurkūnas, Gintarė Kuksėnaitė, Mantas Kulnickas, Birutė Leiputė, Evaldas Paulauskas, Vytenis Pranculis, Maria Razgute, Deividas Sabonis, Edvnas Skliutas, Simona Streckaitė, Greta Striokaitė, Laura Šerkšnytė, Rūta Urbonavičiūtė, Rasa Valentinavičienė, Vytautas Butkus, Jonas Berzins

Students' Scientific Association of Physics Faculty, Vilnius University, Saulėtekio Ave. 9-III, Vilnius, Lithuania
jonasberzins@gmail.com

Students' scientific association is a voluntary organization consisting of students from Physics Faculty of Vilnius University. Our primary focus is to encourage society both inside and outside the university to follow the scientific path of life. The first day of the conference is important not only because of the conference' opening but it is the opening of so long waited laboratory, in which anyone will be able to work & experiment.



Fig. 1. Photos of the laboratory taken before (left) and after (right) repair.

Laboratory consists of 6 rooms including two workshops (one for mechanics and one for electronics) and two full rooms for specific projects. There is also a room for lectures or meetings and it was already successfully utilized in multiple meetings of Open Readings organizing committee. If you have many ideas but don't have the circumstances to put them into practice it is the place for you. Let's make something special!

WITHDRAWED CONTRIBUTION

Poster session 3

Biophysics, medical and environmental physics
Astrophysics and astronomy
Theoretical physics

TWO-PHOTON ABSORPTION CROSS SECTIONS MEASUREMENTS OF TOLUENE SOLUBLE CdSe/ZnS QUANTUM DOTS

Karolis Jurkus¹, Deividas Sabonis^{1,2}, Ignas Astrauskas^{1,2}, Gediminas Dauderis²

¹Faculty of Physics, Vilnius University, Sauletekio av. 9, Bld. III, LT-10222 Vilnius, Lithuania.

²Laboratory of Biomedical Physics, Institute of Oncology, Vilnius University, Baublio 3B, LT-08406, Vilnius, Lithuania

³Biophotonics group of Laser Research Center, Vilnius University, Sauletekio 9, c.3, LT-10222, Vilnius, Lithuania
Jurkus.K@gmail.com.

Near infrared excitation within the tissue transparency window in the region 650 - 1350 nm provides deeper penetration in tissues for imaging and sensitization applications. Biological molecules, photosensitizers, biomarkers and photo-drugs as a rule have no absorption in this spectral region, therefore, cannot be effectively excited. This can be overcome by the use of two photon excitation. In case of quantum dots (QDs) two photon absorption (TPA) cross sections are superior to those observed in conventional photosensitizers. However photophysical properties upon two-photon excitation of quantum dots are yet poorly understood.

The CdSe/ZnS core shell quantum dots of different size were used for the experiments. The two photon excitation of samples was performed by using home-made optical parametric amplifier ($\lambda = 650 - 2500$ nm) pumped by femtosecond "PHAROS" laser system. Two-photon absorption cross sections were evaluated by a comparative method with Rhodamine B as a reference compound [1]. The experiments were carried out in the Laboratory of Biomedical Physics, Institute of Oncology, Vilnius University with Deividas Sabonis as the head of the research.

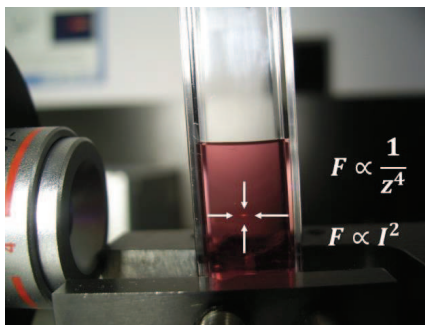


Fig. 1. Two photon excited fluorescence

Our results confirm that QDs have high enough TPA cross sections compared to organic dyes. This is paramount for applications and further optimization of two-photon properties of such nanoparticles. Such large TPA cross-sections make them efficient absorbers for multiphoton biological imaging and other nonlinear optical applications.

[1] Makarov, N.S., M. Drobizhev, and A. Rebane, *Two-photon absorption standards in the 550-1600 nm excitation wavelength range*. Optics Express, 2008. **16**(6): p. 4029-4047.

ALBUMIN COMPLEXES

Greta Jarockytė¹, Eleonora Žurauskienė², Ričardas Rotomskis²

¹Faculty of Natural Sciences, Vilnius University, M.K. Čiurlionio g. 21/27, LT-03101, Vilnius, Lithuania.

²Laboratory of Biomedical Physics, Institute of Oncology, Vilnius University, Baublio 3B, LT-08406, Vilnius, Lithuania

Greta.Jarockyte@gf.stud.vu.lt

Chlorin e₆ (Cle₆) is one of the most common photosensitizers used in photosensitized tumor therapy. It is believed that the tumor-localising property of Cle₆ may be related to its tendency to bind to serum albumins. As a model we used bovine serum albumin (BSA), whose properties and structure are similar to human serum albumin. The interaction of Cle₆ with BSA in aqueous solution has been investigated by means of a steady state absorption spectroscopy. By using a typical absorption difference spectra obtained for Cle₆ titration with BSA and a Scatchard plot the number of Cle₆ binding sites in BSA molecule was obtained. Also the affinity of Cle₆ to BSA was established by using the binding isotherm method and a Scatchard plot. The results of the study are discussed.

Addition of BSA to the solution of Cle₆ at molecular ratio of 1:1 shifts the absorption maximum to the longer wavelength about 10 nm. The same result was obtained for Cle₆ titration with HAS in previous studies [1]. Further increasing the amount of BSA no changes in absorption graph was observed.

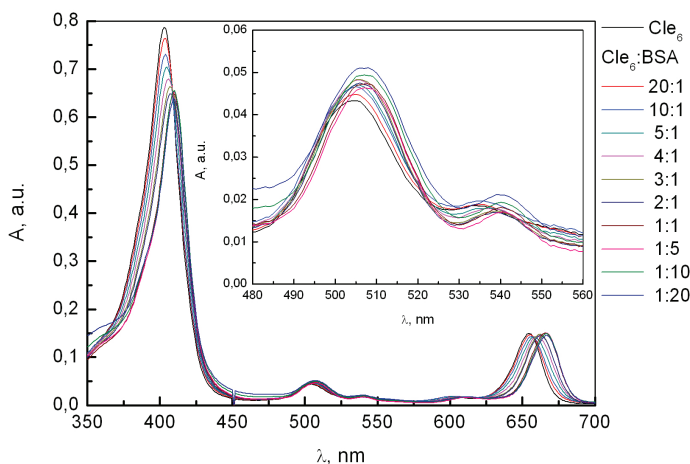


Fig. 1. Absorption spectra of Cle₆ titration of BSA.

The experiments were carried out in the Laboratory of Biomedical Physics, Institute of Oncology, Vilnius University using absorption spectrophotometer Cary 5E, Varian

[1] A. Jasaitis, G. Streckytė, R. Rotomskis; *Spectroscopic studies of photosensitizer-human serum albumin complexes and their photostability*; Proc. SPIE 2924, Photochemotherapy: Photodynamic Therapy and Other Modalities II, 91 (December 4, 1996); doi:10.1117/12.260770;

SPECTROSCOPIC STUDY OF HEMATOPORPHYRIN PHOTOTRANSFORMATION IN AQUEOUS MODEL MEDIUM: THE INFLUENCE OF ANTIOXIDANT

Tomas Biekša, Saulius Bagdonas

Quantum Electronics Department, Faculty of Physics, Vilnius University, Saulėtekio ave. 9, c. 3, LT-10222,

Vilnius, Lithuania

tombiekfol@gmail.com

Hematoporphyrin is a clinically approved photosensitizer of a first generation widely used in photodynamic therapy. A photosensitizer is a light-sensitive compound, which transfers the excitation energy to surrounding molecules inducing photochemical reactions and causing cellular damage. However, hematoporphyrin is unstable and its exposure to light leads to both photodegradation and phototransformation of porphyrin molecules [1].

Phototransformation studies are important to determine the photochemical activity of the photosensitizer. The formation of photoproducts also indicates the biological activity of photosensitizer proving a possibility of its application for diagnostics. However, the photochemical activity of photosensitizers is also affected by the amount of oxygen and acidity of the medium [2].

In some *in vivo* cases solid tumors possess oxygen-poor areas [3]. In these conditions the efficiency of photodynamic therapy (PDT) is limited. The goal of this study is to search for alternative methods to enhance the effect of PDT in such medium.

Using steady state methods of spectroscopy, photo-induced spectral changes were followed by comparing absorption and fluorescence spectra of hematoporphyrin in phosphate buffer solutions ($C = 10^{-4}$ mol/l) without or with added ascorbic acid, which is a water soluble antioxidant (concentrations up to 20 mmol/l). Absorption spectra (Fig. 1) were measured using a spectrophotometer AvaSpec-3648 (Avantes, The Netherlands), fluorescence spectra were measured using a fluorometer LS55 (PerkinElmer Inc., USA) in 1 cm quartz cuvettes.

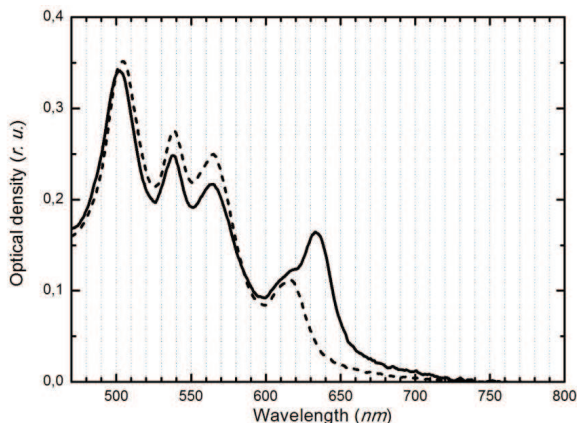


Fig. 1. Absorption spectra of hematoporphyrin in phosphate buffer solution ($C = 10^{-4}$ mol/l, pH = 6.9); (---) before irradiation, (—) after irradiation with diode pumped solid-state laser (50 min, 50 mW/cm²).

In normal conditions antioxidant acts by neutralizing reactive oxygen species, whereas protecting photosensitizer from auto-oxidation. Therefore, samples were irradiated by means of a diode pumped solid-state laser ($\lambda = 532$ nm) at different intensities seeking for a critical value of irradiation intensity, at which a lack of oxygen in solution is created. Since in oxygen-poor medium photosensitizing activity of hematoporphyrin becomes greatly reduced, further spectral changes emerge mainly because of interaction of photosensitizer with antioxidant. It has been found that under such conditions ascorbic acid provoked a new phototransformation pathway of hematoporphyrin.

[1] Bonnett, R., Martínez, G. Photobleaching of sensitizers used in photodynamic therapy. *Tetrahedron*. 2001, 57, 9513–47.

[2] Scolaro, L.M., Castriciano, M., Romeo, A., Patane, S., Cefali, E., Allegrini, M. Aggregation Behavior of Protoporphyrin IX in Aqueous Solutions: Clear Evidence of Vesicle Formation. *Phys. Chem.* 2002, 2453–9.

[3] Streckytė, G., Rotomskis, R., Bagdonas, S., Didžiapetriėnė, J., Kirvelienė, V. Fotosensibilizacija biosistemose: taikymas ir perspektyvos 2008.

INVESTIGATION OF METHYLATION STATUS OF LONG NON-CODING RNA H19 IN PROSTATE CANCER

Agnieška Mackoit¹, Sonata Jarmalaitė¹

¹ Human Genome Research Center, Vilnius University, Lithuania
agnieska.mackoit@stud.gmf.vu.lt

Prostate cancer is one of the most common cancer types in male population. Tumor genesis and progression in prostate is influenced by multiple genetic or epigenetic changes. Altered cellular epigenetic balance determines if cells become malignant and promotes the development of cancer [1].

Recent research on the human genome revealed big abundance of long non-coding RNA and its importance in the regulation of gene expression. H19 gene expresses a long non-coding RNA and functions as a tumor suppressor. It is located in an imprinted 11p15 locus near the insulin-like growth factor 2 (IGF2) gene and its promoter contains differentially methylated region (DMR), which is responsible for establishing paternal allele-specific methylation [2]. Epigenetic alterations in DMR sequences of H19/IGF2 gene cluster lead to the malignant diseases, such as Wilms tumor, bladder, cervix, prostate carcinomas and other types of cancer [3].

Prostate-specific antigen (PSA) test application is used in early detection of the disease, but it has low precision for prostate cancer, therefore the bigger part of the patients are misdiagnosed. It is vital to find a reliable molecular markers that are able to accurately distinguish cancerous alterations and identify early stages of the disease.

The main goal of our investigation was to evaluate appropriateness of H19 as epigenetic marker for prostate cancer detection. In this work we analyzed H19/IGF2 DMR methylation status in 54 samples of prostate carcinoma, compared them to 6 benign tissues and evaluated relations with clinical and demographic data.

DNA was extracted from tissues using phenol - chloroform method, then it was modified by bisulfite and amplified using methylation - sensitive PCR (MSP) method. Products of MSP reaction were analyzed on polyacrylamide and agarose gels after vertical and horizontal electrophoresis (Fig. 1).

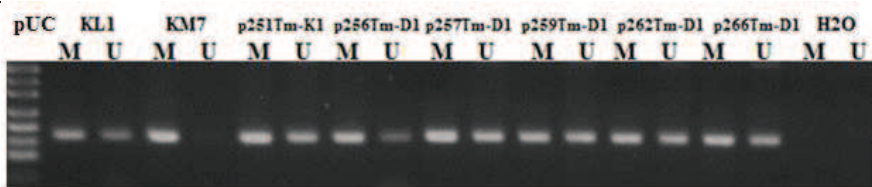


Fig. 1. H19 gene methylation status analysis using methylation sensitive polymerase chain reaction (MSP).

M – reaction with primers specific for methylated DNA sequences, U – reaction with primers specific for unmethylated DNA sequences. pUC – length marker, KL – leukocytes DNR (negative control), KM – in vitro methylated DNR (positive control), p251Tm-K1, p256Tm-D1, p257Tm-D1, p259Tm-D1, p262Tm-D1, p266Tm-D1 – different tumor DNR, H2O – pollution control

The results of MSP reactions showed 4 cases with hypermethylated DMR sequences. In all hypermethylation cases we observed second pT stage and Gleason score of 6 to 7. According to the data of progressive nature of tumor, 3 out of 4 cases were non-progressive tumors. We estimated the average age of patients with prostate carcinoma was about 65 ± 5.29 years and mean of PSA diagnostic concentration was 7.75 ± 3.6 ng/ml. Final examination revealed no significant correlation between the H19 promoter methylation status and patient age or clinical parameters.

[1] Li L.Ch., Carroll P.R., Dahiya R. *Epigenetic Changes in Prostate Cancer: Implication for Diagnosis and Treatment*, Journal of the National Cancer Institute, Vol. 97, No. 2, January 19, 2005.

[2] Paradowska A., Fenic I., Konrad L., Sturm K., Wagenlehner F., Weidner W., Steger K. *Aberrant epigenetic modifications in the CTCF binding domain of the IGF2/H19 gene in prostate cancer compared with benign prostate hyperplasia*, International Journal of Oncology, 2009, 35: 87-96.

[3] Matouk I., Raveh E., Ohana P., Lail R.A., Gershtain E., Gilon M., Groot N.D., Czerniak A., Hochberg A. *The increasing complexity of the Oncofetal H19 gene locus: functional dissection and therapeutic intervention*, International Journal of Molecular Sciences, 2013, 4310, 4291-4316.

NANOSYSTEMS BASED ON PHOSPHOLIPIDS AND SURFACTANTS AS INNOVATIVE DELIVERY SYSTEMS FOR GENE THERAPY – CIRCULAR DICHROISM STUDIES

Barbara Urban, Michalina Skupin, Paulina Egierska, Joanna Wolak, Maciej Kozak¹

¹ *Physics Department, Adam Mickiewicz University, Str. Umultowska 65, Poznań, Poland*

Barbaraurban2@gmail.com

Gene therapy is one of the most promising methods for treating a wide range of genetic diseases as well as cancer and neurodegenerative disorders. However the effectiveness of this method, requires the creation of effective and non-toxic methods for transferring the genetic material into a cell. Perfectly suitable for this purpose are delivery systems based on lipid-surfactant mixtures [1].

The aim of this study was to determine the possible use of amphoteric surfactants (zwitterionic alkyl derivatives of sulfobetaine [2]) and dicationic surfactants (as reference systems) as complexing agents of nucleic acids, with potential applications for gene delivery[3].

A series of measurements of the DNA conformation in selected DNA-zwitterionic surfactant and DNA-dicationic surfactant lipoplexes using the circular dichroism spectroscopy. CD spectra were recorded in the range 210-350 nm using J-815 spectrometer (Jasco). Based on the obtained results was confirmed the possibility of creating stable lipoplexes. The spectrum of the pure DNA solution exhibits a positive band near 277 nm, a negative band near 245 nm and a crossover point near 260 nm, indicating a right-handed B-DNA form (fully-hydrated). The increased surfactant concentration slightly shifted the bands towards higher wavelength. Surfactants were also shown in different kind of buffer and environment acidity.

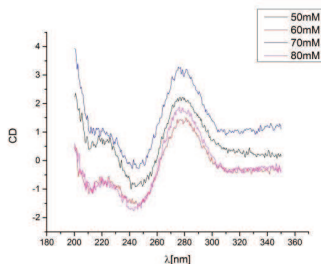


Fig. 1. Measured surfactant CD spectrum.

[1] M. Barańska, and J. Skretkiewicz. *Wiadomości lekarskie*. vol. LX, no. 60, pp. 305-311, 2007.

[2] Edited by Chunsheng Kang. *Gene Therapy - Developments and Future Perspectives*, July 2011, Croatia.

[3] Allay, J.A.; Galipeau, J.; Blakley, R.L. & Sorrentino, B.P. (1998a). *Retroviral vectors containing a variant dihydrofolate reductase gene for drug protection and in vivo selection of hematopoietic cells*. *Stem Cells*, Vol.16 (Suppl. 1), pp. 223–233, ISSN 1066-5099

[4] Shawn D. Wettig, Ronald E. Verrall and Marianna Foldvari, *Current gene therapy*, Gemini Surfactants: A New Family of Building Blocks for Non-Viral Gene Delivery Systems, vol. 8, pp. 9-23, 2011.

Searching of potential biocatalysts in metagenomic DNA libraries

Svetlana Šliachtīč, R. Šiekštelė, B. Pudžiuvytė, I. Matijošytė

Vilnius university Institute of Biotechnology, Sector of Applied Biocatalysis,

V.A. Graičiūno str. 8-255, LT-02241, Vilnius, Lithuania

E-mail: inga.matijosyte@vu.ibt.lt

Biocatalysis is a practical and environmentally friendly alternative to traditional metallo- and organocatalysis in chemical synthesis, both in the laboratory and on an industrial scale. Biocatalysts (enzymes) are characterised as high enantioselective, environmentally friendly tools, which operate under mild conditions in an aqueous environment and less waste is generated during the reactions. Nowadays, due to the wider application of biocatalysts the demand for enzymes with special or totally new characteristics is constantly increasing. Therefore, various commercial enzymes are being verified and modified for new catalytic activities and substrate specificities in order to design biocatalysts with novel functions. In addition, recent studies have shown, that various microorganisms living in unique environments can be considered as largest potential source of biocatalysts. Currently, in the laboratory is possible to cultivate less than 1 % of the microorganisms found in the nature, which is why only a small part of their genetic diversity can be covered by standard microbiological methods. Metagenomics is one of the modern method for searching and investigation of new enzymes, thus, reducing the cultivation problem [1]. This method is based on the direct extraction and analysis of total DNA in the environmental samples.

The aim of this work was to detect novel biocatalysts in metagenomic DNA library. Construction of the library resulted in more than 3400 recombinant clones. Functional and sequencing analysis of the recombinants revealed several clones with potential enzymatic activity of peroxidase, sulfatase, acylesterase and arylsulfatase genes. The results of functional analysis and DNA sequencing will be presented in more details during poster session.

References:

1. H.A Iqbal *et al.* Biocatalysts and small molecule products from metagenomic studies. *Cur Opin Chem Biol.* 2012; 16:109-116.

Open Readings 2014. 57th Scientific Conference for Students of Physics and Natural Sciences
ATOMIC FORCE MICROSCOPY OF COMPLEXES DNA WITH
CARBON NANOTUBE
Nadya Pleshko, Vladimir Krot

¹ Department of Physics, Belarusian State University, Minsk, Belarus
nadyavp@tut.by

Carbon nanotubes (CNTs) as one of the most perspective materials for future nanoelectronic devices have been acknowledged in the past decade. Unique electrical and optical properties of CNTs and their combination along with chemical functionalization by DNA promise a broad range of applications in medicine, molecular electronics and cancer therapy [1]. Some models of the DNA interaction with CNTs are known currently. Most popular model of the DNA wrapping around CNT by R. E. Smalley is proposed [2]. Wrapping of the DNA around of CNTs occurs when the aromatic hydrophobic DNA bases interact with the sidewall of the CNT via π -stacking.

In spite of existing mechanisms interpretation of complexing of DNA-CNT hybrids future progress in their studying is connected with methods subnanometer resolution on base of AFM.

The AFM image of DNA adsorbed onto mica in Figure 1 shows that diameter of molecules DNA is 1.8 ± 0.4 nm. That value agrees with diameter of DNA in aqueous solution.

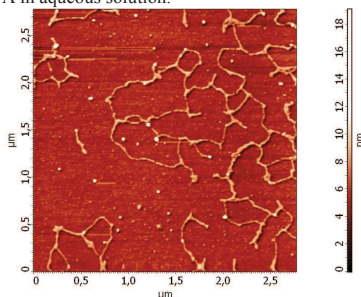


Fig. 1. AFM image of DNA.

Application of AFM allows the direct observation of DNA wrapping around a CNT. Investigation of hybrid system DNA-CNT is shown in Figure 2 (a). Figure 2 (b) represents the CNT-DNA hybrid profile variations in the direction of DNA coiling. Regular height modulations of the DNA-covered segments of the CNTs are also visible in the image. Profile emphasize the periodic nature of these modulations along the nanotube.

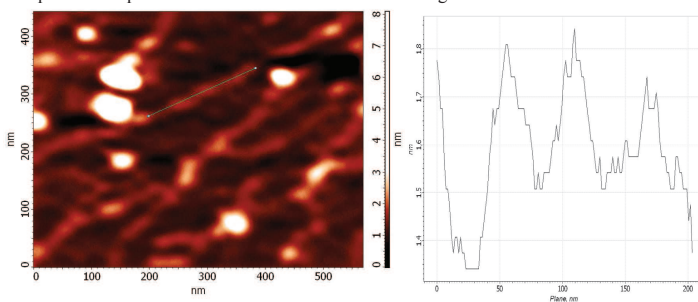


Fig. 2. AFM image of DNA-CNT hybrids (a), height profiles modulations of DNA along the nanotube (b).

Imaging of CNT-DNA have been hybrid geometry with subnanometer resolution. Results of investigation allow draw a conclusion about periodically spiral wrapped of the DNA strand around the nanotube. Also has been defined that structure of DNA destabilized consisting of hybrid system DNA-CNT.

-
- [1] K. Maehashi, K. Matsumoto et al., A Ultrasensitive detection of DNA hybridization using carbon nanotube field-effect, *Jpn. J. Appl. Phys* **43**, 1558-1560 (2004).
- [2] O'Connell M. J., Smalley R. E., Reversible water-solubilization of single-walled carbon nanotubes by polymer, *Chemical Physics Letters* **342**, 263-271 (2001).

NEW ALGORITHMS FOR IMAGE ANALYSIS IN NON-INVASIVE EXAMINATION METHODS OF CORNEAL AND CONTACT LENS TEAR FILM SURFACE

Piotr Szyperski¹

¹Faculty of Electronics, Wrocław University of Technology, Poland
piotr.szyperski@pwr.wroc.pl

The poster discusses the new robust algorithms for processing interferogram images. They are research subject intensively developed and analyzed in scientific institutions conducting studies in the field of physics (optics, optometry), bio-engineering and automation. In particular, they have been and are being studied by the poster author during his master thesis research and doctoral studies. The mentioned above research is carried out on the grounds of the high applicability potential of these methods to automate and increase the accuracy of the image processing and analysis in the non-invasive methods of empirical research and assessment of the quality index of the tear film. The contents of the poster considers the application of these algorithms in tear film examination and determining the temporal volatility course for quality measures of its structure on the optical surfaces of the human eye. Topics covered include, inter alia, opportunities to improve existing algorithms for the spectral-morphological analysis, used, e.g., for diagnosing the dry eye syndrome on the basis of the interferograms of the corneal surface. Another important aspect of the analysis described in the poster are the prospects to develop efficient and robust algorithms for the examination of strongly deteriorated mono-channel microscopic or biomedical images.

Developing the practical implementation of the introduced algorithms is desired by the medical industry. It is mainly due to the growing interest in designing and applying commercially a hardware system for automatic assessment of the biocompatibility degree of materials used in contact lenses manufacturing. Recently, as similar equipment was implemented successfully in the medical market for diagnosing the dry eye syndrome. Still, those devices make use of algorithms that are not sufficient for contact lens biocompatibility assessment. This issue and the problem accompanying its theoretical and engineering aspects was the main motivation of the author to undertake attempts in further development of this research field.

-
- [1] B. C. Primeau and J. E. Greivenkamp, "Interferometer for measuring the dynamic surface topography of a human tear film", in *Proceedings of SPIE Volume 8215, Design and Quality for Biomedical Technologies V*, San Francisco, 2012, pages.
 - [2] D. H. Szczesna, D. R. Iskander, and H. T. Kasprzak, "Evaluating the clinical utility of noninvasive methods for measuring tear film surface quality", *Photonics Letters of Poland*, vol. 3(1), pp. 35–37, 2011.
 - [3] D. H. Szczesna, D. Alonso-Caneiro, D. R. Iskander, S. A. Read, and M. J. Collins, "Lateral shearing interferometry, dynamic wavefront sensing, and high-speed videokeratoscopy for noninvasive assessment of tear film surface characteristics: a comparative study", *Journal of Biomedical Optics*, vol. 15, no. 3:037005, pages, 2010.
 - [4] D. H. Szczesna and D. R. Iskander, "Lateral shearing interferometry for analysis of tear film surface kinetics", *Optometry & Vision Science*, vol. 87, no. 7, pp. 513–517, 2010, ISSN: 1040-5488.
 - [5] R. Lopes and N. Betrouni, "Fractal and multifractal analysis: a review", *Medical Image Analysis*, vol. 13, no. 4, pp. 634–649, 2009, ISSN: 1361-8415.
 - [6] E. Skubalska-Rafajlowicz, "A new method of estimation of the box-counting dimension of multivariate objects using space-filling curves", *Nonlinear Analysis: Theory, Methods & Applications*, vol. 63, no. 5–7, e1281–e1287, 2005, Invited Talks from the Fourth World Congress of Nonlinear Analysts (WCNA 2004), ISSN: 0362-546X.
 - [7] A. Dubra-Suárez, "A shearing interferometer for the evaluation of human tear film topography", PhD thesis, Imperial College London, 2004.
 - [8] T. J. Licznarski, H. T. Kasprzak, and W. Kowalik, "Application of Twyman–Green interferometer for evaluation of in vivo breakup characteristic of the human tear film", *Journal of Biomedical Optics*, vol. 4, no. 1, pp. 176–182, 1999.
 - [9] M. Rottenkolber and H. Podbielska, "High precision Twyman–Green interferometer for the measurement of ophthalmic surfaces", *Acta Ophthalmologica Scandinavica*, vol. 74, no. 4, pp. 348–353, 1996, ISSN: 1600-0420.
 - [10] R. M. Goldstein, H. A. Zebker, and C. L. Werner, "Satellite radar interferometry: two-dimensional phase unwrapping", *Radio Science*, vol. 23, no. 4, pp. 713–720, 1988, ISSN: 1944-799X.
 - [11] M. Takeda, H. Ina, and S. Kobayashi, "Fourier-transform method of fringe-pattern analysis for computer-based topography and interferometry", *Journal of the Optical Society of America*, vol. 72, no. 1, pp. 156–160, Jan. 1982.

VISUAL ACUITY IN PERIPHERY IN TERMS WITH PERCEPTION AND ITS POSSIBLE CORRELATION WITH CENTRAL VISUAL ACUITY

Daiga Cerane, Anete Pausus, Peteris Cikmācs, Gunta Krumina

Department of Optometry and Vision Science, University of Latvia, Latvia

daiga.cerane@lu.lv

Visual acuity in periphery has a wide range in population. [1],[2]. However, if we look at the development of myopia (particularly, the axial myopia), then we see, that when the axial length of the eye increases, the distance between photoreceptors is increased, therefore the density of photoreceptor and retinal ganglion cells is lowered. It is remarked, that the retinal stretching happens mostly in foveola and near peripheral region in retina, while the rest of the retina is stretched less substantially, retaining non-uniform stretching. [3]

If axial myopia is corrected with spectacle lenses at constant vertex distance from the eye (lens placed in anterior plane of the eye), then by Knapp's law, the relationship between the object size and retinal image size is fixed. Therefore, it is possible to measure the relationship between visual acuity in both central and peripheral retina, and indirectly, to measure the photoreceptor density in retina (Fig. 1).

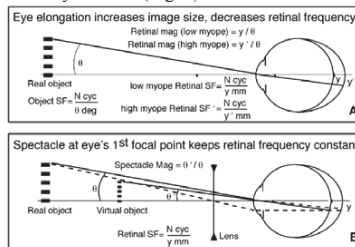


Fig. 1. Knapp's law [3].

In literature we can find many sources implying the term perceptual learning, in particular – peripheral and central visual acuity, however it is seen, that the actual perceptual learning rarely, if ever happens. [4].

It is shown that the perceptual learning happens while subjects are freshly introduced to the task, usually the measurements that are discarded due to subject's wide array of answers, are taken into account when speaking about learning, therefore these result tend to improve in time (when subject has learned how to properly perform the task). It is then observed, that peripheral visual acuity remains unchanged with perceptual training. [4]

The resolution acuity (highest spatial frequency that can be perceived veridically) is not perceptible to central visual defocus, however, the detection acuity (highest spatial frequency (luminance gratings) that can be detected on a uniform field) is susceptible to optical defocus, that implies that resolution acuity is dependent on neural sampling density, in contrast to detection acuity, that is contrast limited (both in peripheral and central vision). [5]

[1] Traquair, H.M. An introduction to clinical perimetry (appendix). *St Louis, MO. C.V. Mosby Company*, 1940.

[2] Low, F.N. The peripheral visual acuity of 100 subjects. *American Journal of Physiology*, 1943. 140, 83-88.

[3] Chui, T.Y.P., Yap, M.K.H., Chan, H.H.L., Thibos, L.N. Retinal stretching limits peripheral visual acuity in myopia. *Vision Research*, 2005. 45, 593-605.

[4] Westheimer, G. Is peripheral visual acuity susceptible to perceptual learning in the adult? *Vision Research*, 2001. 41, 47-52.

[5] Wang, Y., Thibos, L.N., Bradley, A. Effects of Refractive Error on Detection Acuity and Resolution Acuity in Peripheral Vision. *Investigative Ophthalmology & Visual Science*, 1997. 38, 2134-2143.

WITHDRAWN CONTRIBUTION

Open Readings 2014. 57th Scientific Conference for Students of Physics and Natural Sciences

ALTERATION IN CONFORMATIONAL STABILITY OF CYP7B1 ARG486CYS MUTANT IS A REASON OF NEURODEGENERATIVE DISORDER

Yaroslav Dichenko, Aleksei Yantsevich, Sergei Usanov

Institute of Bioorganic Chemistry, National Academy of Sciences, Republic of Belarus
dichenko@iboch.bas-net.by

Human cytochrome P450 (CYP7B1) is a microsomal enzyme that utilizes NADPH-cytochrome P450 reductase as an electron donor and catalyzes 7 α -hydroxylation of oxysterols [1]. CYP7B1 take part in several physiological functions depending on tissue localization, including bile acid biosynthesis [2], metabolism of steroid hormones (including neurosteroids) [3], regulation of immunoglobulin production [4] and metabolism of estrogen and androgen receptor ligands [5]. CYP7B1 dysfunctions are associated with a number of genetic disorders, such as liver failure in newborns neuropathy in adults. A list of point mutations in *cyp7b1* gene was found to be connected with neurodegenerative disorder – spastic paraplegia type 5 (SPG5). But up to date it was unknown what happens with the product of the modified gene.

So in order to cast light on the molecular reason of the disease we decided to get recombinant mutant forms and to compare its with recombinant wild type (WT) enzyme. Application of site directed mutagenesis and molecular cloning allowed us to construct *E. coli* expression system for C57R, F216S and R486C mutants, that was found in patients with SPG5 as it was earlier reported [6]. When performing heterologous expression of the proteins we realized that C57R and F216S enzymes form inclusion bodies and can't be expressed in native form neither under the same condition as WT nor any other conditions. Expression level of R486C mutant was significantly lower, comparing WT, and was substantially enhanced when expressing at the presence of substrate (DHEA). Analyzing data on expression we put forward a hypothesis: R486 mutant has low conformational stability which leads to decrease of native enzyme level in biological tissues. In order to check hypothesis we applied several approaches, that allowed to compare conformational stability of R486C mutant and WT enzyme. We compared tolerance of the enzymes to chaotropic agents, such as urea, GuHCl, SDS and determine thermodynamic stability of the native form. It was demonstrated that energy barrier for folded-unfolded transition is lower for R486C mutant. Also we demonstrated that ligand-bound forms of both enzymes are more stable than ligand-free form. Fluorescence quenching experiments, aimed to follow tryptophan residues availability to different types of quenchers (cesium and iodine ions, acrylamide), showed that tryptophan residues are more accessible for a quencher exactly in R486C mutant. This observation is an indirect, but typical sign of stability and structure changes, driven by mutation.

In silico analysis, performed in our work, showed that R486C substitution leads to significant changes of the polypeptide backbone, including modification of the active site geometry.

So, the data obtained indicate that R486C replacement significantly reduce CYP7B1 conformational stability in model *in vitro* system and this alteration may be the reason of disorder induced by mutation, when considering *in vivo* system.

-
- [1] A.R. Stiles et al, CYP7B1: one cytochrome P450, two human genetic diseases, and multiple physiological functions, J. Biol. Chem. **284**(42), 28485-28489 (2009).
[2] J.Y. Chiang, Regulation of bile acid synthesis, Front. Biosci. **3**, 176-193 (1998).
[3] S. Steckelbroeck et al, Characterization of the dehydroepiandrosterone (DHEA) metabolism via oxysterol 7 α -hydroxylase and 17-ketosteroid reductase activity in the human brain, J. Neurochem. **83**(3), 713-726 (2002).
[4] D.R. Bauman et al, 25-Hydroxycholesterol secreted by macrophages in response to Toll-like receptor activation suppresses immunoglobulin A production, Proc. Natl. Acad. Sci. USA **106**(39), 16764-16769 (2009).
[5] Y. Omoto et al, Early onset of puberty and early ovarian failure in CYP7B1 knockout mice, Proc. Natl Acad Sci USA **102**(8), 2814-2819 (2005).
[6] R. Schule et al, Analysis of CYP7B1 in non-consanguineous cases of hereditary spastic paraplegia, Neurogenetics **10**(2), 97-104 (2009).

CHARACTERIZATION OF MEMBRANE-BOUND CARBONIC ANHYDRASES ISOFORMS IV AND XIV

Sandra Bakšytė, Aurelija Mickevičiūtė, Vilma Michailovienė, Lina Baranauskienė,
Daumantas Matulis

Department of Biothermodynamics and Drug Design, Institute of Biotechnology, Vilnius University, Lithuania

baksyte@ibt.lt

Maintenance of extracellular pH, bicarbonate homeostasis and the buffer capacity of extracellular fluids are essential for cell survival. Brain functions are highly sensitive to small changes in pH but rapid alkaline shifts are generated during excitatory synaptic transmission. Since extracellular pH buffering is determined by the reversible hydration of carbonic dioxide, carbonic anhydrases (CA) are in a key position to govern the kinetics of neuronal activity-generated pH fluctuations. The membrane-bound CA isoforms IV and XIV which have their catalytic site located in the extracellular space are largely responsible for the CA activity detected on neuronal membranes and axons in both mouse and human brain [1,2]. Those isoforms show some overlap in distribution within the brain suggesting that CA XIV and CA IV may be functionally redundant. Inhibition of these isoforms may explain some neurological side effects of CA sulfonamide inhibitors which have been used as drugs to treat various diseases. Therefore, the development of more selective CA inhibitors shall improve the understanding of their function and treatment of disorders with less side-effects.

In our research, various physical properties such as stability profiles, protein-inhibitor interaction thermodynamics and enzyme kinetics were determined and compared for CA isoforms IV and XIV. Catalytic domains of human CA IV and CA XIV were expressed in mammalian and in *E. coli* cells. Isoforms were purified by affinity chromatography. Inhibitor binding to the CA isoforms was determined by isothermal titration calorimetry and thermal shift assay. Investigated properties can be exploited for finding purification conditions and most importantly for development of new compounds with improved affinity and selectivity.

[1] Shah, G. N. et al. (2005). Carbonic anhydrase IV and XIV knockout mice: roles of the respective carbonic anhydrases in buffering the extracellular space in brain. *Proceedings of the National Academy of Sciences of the United States of America*, 102(46), 16771–6;

[2] Svichar, N. et al. (2009). Carbonic anhydrases CA4 and CA14 both enhance AE3-mediated Cl⁻-HCO₃⁻ exchange in hippocampal neurons. *The Journal of Neuroscience : The Official Journal of the Society for Neuroscience*, 29(10).

DIFFERENCES IN THERMODYNAMICS OF INHIBITOR BINDING TO CARBONIC ANHYDRASE VI PURIFIED FROM *E. COLI*, MAMMALIAN CELLS AND HUMAN SALIVA

Justina Kazokaite, Goda Milinavičiūtė, Joana Gylytė, Virginija Dudutienė, Jurgita Matulienė, Daumantas Matulis

Department of Biothermodynamics and Drug Design, Institute of Biotechnology, Vilnius University, Lithuania

kazokaite@ibt.lt

The main function of carbonic anhydrases (CAs) is the maintenance of pH homeostasis catalyzing the reversible hydration of carbon dioxide. There are 12 human catalytic CA isoforms differing from each other in expression patterns, tissue localization and cellular distribution. CA inhibition has been exploited clinically for decades in various classes of diuretics, anti-glaucoma agents, anti-epileptics and anti-tumor drugs [1].

CA VI is the only secreted isoenzyme of the human CA family. This enzyme is found in saliva, tears and milk. It is responsible for antireflux defense, protection from carcinogens and taste function. Gene comparison tells that CA VI is closely related to membrane associated isoenzymes CA IV and CA IX. CA IV is a target for several pathologies, including glaucoma, retinitis pigmentosa and stroke. CA IX is a marker for hypoxic tumors. This association links CA VI with certain cancers which might be associated with salivary glands [2]. Therefore, it is important to analyze the affinity of sulfonamide inhibitors for CA VI.

Human recombinant CA VI was expressed in *E. coli* and in mammalian cells. Also, a half-liter of saliva was collected from twenty volunteers. CA VI from these sources was purified by affinity chromatography. Thermal stability of the protein and thermodynamics of interaction between the enzyme and inhibitors, were determined by the fluorescence thermal shift assay (TSA) and isothermal titration calorimetry (ITC). It was found that CA VI was most stable at pH 6. However, CA VI expressed in human saliva and mammalian cells were more stable than the *E. coli* form at all pHs. The affinity of commercial compounds and inhibitors designed and synthesized in our laboratory for CA VI from saliva was similar to the affinity for CA VI from *E. coli* and mammalian cells. This study shows that CA VI purified from bacteria is a perfect model to analyze reactions between human CA VI and inhibitors and the absence of glycosylation in *E. coli* has no significant effect on thermodynamics of inhibitor binding to this enzyme.

[1] R. McKenna et al. Insights towards sulfonamide drug specificity in α -carbonic anhydrases. *Bioorganic & Medicinal Chemistry* 21, 1526-33 (2013)

[2] W. Sly et al. Structure, function and applications of carbonic anhydrase isoenzymes. *Bioorganic & Medicinal Chemistry* 21, 1570-82 (2013)

EFFECTS OF STATIC MAGNETIC FIELD EXPOSURE ON PROKARYOTIC AND EUKARYOTIC CELL GROWTH

Piotr Stempiński¹, Emil Paluch², Izabela Konieczna³, Konrad Zabłocki⁴

¹ Department of Genetics, University of Wrocław, Poland

² Department of Microbiology, University of Wrocław

³ Department of Pathogen Biology and Immunology, University of Wrocław

⁴ Department of Biotechnology, University of Wrocław

zablockikonrad@gmail.com

The magnetic field and its effects on living organisms has been a particularly intriguing area of scientific research for decades. We believe this phenomenon is not fully fathomed and requires further research. There are still many questions that remains unanswered.

In this work we will evaluate the biological effects of a weak static magnetic field on the growth, frequency of cell divisions, quantity and morphology of the whole bacterial colonies as well as single cells of a prokaryotic and eukaryotic organisms. The results will be obtained with the spectrophotometric optical density analysis (OD 400-700 nm), which allows us to determine colony forming units (CFU) of the gram-negative bacterias: *Escherichia coli*, *Klebsiella pneumoniae*, *Proteus mirabilis* and a gram-positive: *Staphylococcus aureus* plus – as an eukaryotic model organism - *Saccharomyces cerevisiae*. Besides, earlier publications indicate that weak magnetic fields affect the synthesis of crucial molecules in photosynthesizing bacterias.[1] A decrease in lifespan and higher sensitivity to magnetic fields has been observed for *Escherichia coli*, in contrast to *Staphylococcus aureus* which remained unaffected.[2]

We resume the static magnetic field impact to be significantly higher on prokaryotic organisms, due to their less complex cell structure, rather than on eukaryotes. Verifying this could introduce the development of magnetic field techniques for the eradication of microorganisms and advances in antimicrobial therapy. [3]

[1] M. Peplar, Magnetic field benefits bacteria, Nature (2004), Published online, doi:10.1038/news041122-13.

[2] L. Fojt, L. Strašák, V. Vetterl, J. Šmarda, Comparison of the low-frequency magnetic field effects on bacteria *Escherichia coli*, *Leclercia adecarboxylata* and *Staphylococcus aureus*. Bioelectrochemistry 63 (2004) 337-341

[3] <http://www.fda.gov/Food/FoodScienceResearch/SafePracticesforFoodProcesses/ucm103131.htm>

Open Readings 2014. 57th Scientific Conference for Students of Physics and Natural Sciences
THE SURFACE-ENHANCED RAMAN SCATTERING FOR MERCURY
SULPHIDE MICROCRYSTALS

Hanna S. Matsukovich and Elena V. Shabunya-Klyachkovskaya

B. I. Stepanov Institute of Physics, NASB, Nezavisimosti Ave., 68, 220072 Minsk, Belarus

Ahnju@tut.by

This work shows the surface-enhanced Raman scattering for mercury sulphide microcrystals with two types of substrates. The first one were Si/Ge-nanostructures prepared by a chemical vapor deposition [1]. Afterwards gold nanoparticles were deposited on the Si/Ge-nanostructures surface. Substrates repared are three-dimensional arrays of coherently strained islands with a base of 200 nm and a height to 50 nm.

The second one was the gel-film of Ag nanoparticles on the glass. Silver sol was prepared by reduction of silver nitrate with sodium citrate as described in [2]. Polydispersed silver sol formed, average particle size is about 50 nm.

A He-Ne laser (632.8 nm) was used to excite the Raman spectra. Registration spectrum occurred range 200-800 cm^{-1} . For Raman measurments exposure time was 10 s.

Raman spectra for the mercury sulfide microcrystals on the glass surface and the silicon-germanium substrate are shown in (Fig. 1). We can see symmetric band A1 about 254 cm^{-1} , the transverse bands E(LO) at 286 and 344 cm^{-1} , a band at 202 cm^{-1} and the secondary bands about 432, 493, and 659 cm^{-1} , which are represented by the combined modes of the phonon oscillations $M_1 + M_1$, $M_1 + M_2$ and $M_2 + M_2$, respectively [3].

We can see selectively increasing intensity of the bands mentioned above in cases of using the substrates for surface-enhanced Raman scattering spectra. Also several new bands appear: the longitudinal E(LO) oscillations appear at 294 cm^{-1} (in the form of a shoulder at 286 cm^{-1}) and 353 cm^{-1} (in the form of a shoulder at 344 cm^{-1}) and the second order band $A_3 + A_3$ and $M_2 + M_2$ at 493 cm^{-1} , and 498 cm^{-1} , respectively. The maximum gain in both cases is for the band 344 cm^{-1} : 15.9 for the silicon-germanium substrate and 14.6 for the substrate with a silver gel-film.

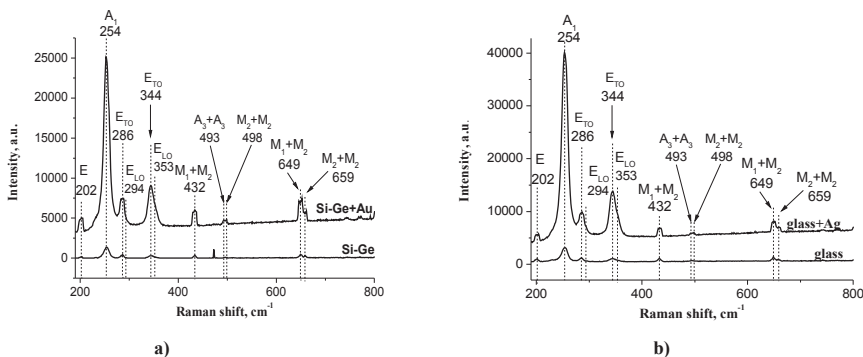


Fig. 1. Raman spectra of mercury sulphide microcrystals on the surface of the silicon-germanium substrate (a) and on the glass substrate (b).

[1] T. Stoica et al. Two-dimensional arrays of self-organized Ge islands obtained by chemical vapor deposition on pre-patterned silicon substrates, *Nanotechnology* 18, (2007), 455307.

[2] J.Fang et al., The study of deposited particulate films by simple method for efficient SERS, *Chem.Phys.Let.* 401, 271-275, (2005).

[3] M. A. Nusimovici and G. Gorre, Phonons in Cinnabar, *Phys. Rev. B.* 8, 1648-1656, (1973).

THE APPLICATION RAMAN SPECTROSCOPY IN MEDICINE

Sylvia Zięba¹, Martyna Stańczuk¹, Tomasz Buchwald²

¹ Poznan University of Technology, The Faculty of Technical Physics, 13a Nieszawska Str., 60-965 Poznan

² Poznan University of Technology, The Faculty of Technical Physics, Chair of Optical Spectroscopy,
13a Nieszawska Str., 60-965 Poznan

sylvia.zieba2@op.pl

Raman Spectroscopy is one of spectroscopy technique which measure Raman scattering ray. A Raman spectrum of a biological tissue can be treated as its “fingerprint”, which allows one to perform easy structural and chemical characterization and identification of such complex material. Medicine is one of science where we use Raman spectroscopy to examine biological materials. The main advantages of RS include a real-time analysis during medical examination or operation, precise results with low cost and minimal or no sample preparation.

Raman spectroscopy gets a possibility to examine teeth. We can use this method to compare the patients healthy place and find out a modification in surface of the teeth. The purpose of study is to compare the diagnostic effectiveness of Raman spectroscopy in detection of the early stages of tooth decay. In addition, studies with use of spectroscopic methods will help identify changes in the composition and structure of the enamel as a result of impact of caries. Raman spectroscopy can be used in vivo .

Raman spectroscopy in medicine gives us:

-possibility of examination in areas related to natural tissues and cell biology,

-opportunity to look for differences between cancerous, pre-cancerous and normal tissues.

On the other hand, this technique has disadvantages too. In vivo Raman spectroscopy is interfered with tissue fluorescence, which is several orders of magnitude greater than the Raman signal, and by the spectral contribution of the delivery and collection fiber optics.

These results of Raman Spectroscopy are a source of many valuable information about cells, teeth and tissues. This method is very helpful tool which gives us possibility to diagnosis a lot of diseases.

Acknowledgements:

We are very grateful for financial support from scientific group. Thanks to it we were able to take part in conference.

WITHDRAWN CONTRIBUTION

SYNTHESIS OF TETRACYCLINE-PROTEIN CONJUGATES TO GENERATE MONOCLONAL ANTIBODIES AGAINST TETRACYCLINE

Aliaksandr Krulik¹, Maksim Fomich¹, Svetlana Akalovich², Vadim Shmanai¹

¹Institute of Physical Organic Chemistry National Academy of Sciences, Minsk, Republic of Belarus,

²The Republic Research & Production Center for Transfusiology and Medical Biotechnologies, Minsk, Republic of Belarus

shmanai@ifoch.bas-net.by

Among numerous methods of analysis of biologically active substances [1], immunosorbent immune assay (ELISA) prevails as it allows one to avoid the drawbacks of traditional chromatographic methods [2]. However, the synthesis of reagents needed for ELISA of low-molecular weight is often accompanied by difficulties caused by the structure of the defined hapten.

ELISA-based test systems are the most popular methods for analysis of antibiotics and, in particular, tetracycline group. Antibodies against tetracyclines can only be obtained by animal immunization with macromolecular immunogens, which are mainly covalent conjugates of haptens with carrier proteins. The structure of immunogens in terms of binding site, length, rigidity, hydrophilicity, and steric configuration of the linker group is the critical factor for obtaining high avidity antibody.

We have developed several schemes of directed modification of the tetracycline molecule and obtained conjugates with bovine serum albumin (BSA). In order to improve the specificity and to exclude the effect of the linker and the carrier protein on the antibody, a range of immunogens with different structures has been synthesized. Modification was carried out via the amide group (2), the aromatic ring (3, 5, 6, 7), the hydroxyl group (4), and random multiple modification (1) via linkers of different structures and lengths (Fig. 1).

Balb/C mice have been immunized with the immunogens described before. According to the results of ELISA, plasma of the immunized mice contained antibodies that specifically interact with different conjugates of tetracycline and do not cross-react with the carrier protein.

Besides, tetracycline - horseradish peroxidase (HRP) conjugates have also been synthesized. The modification has been carried out via the aromatic ring (8, 9, 10).

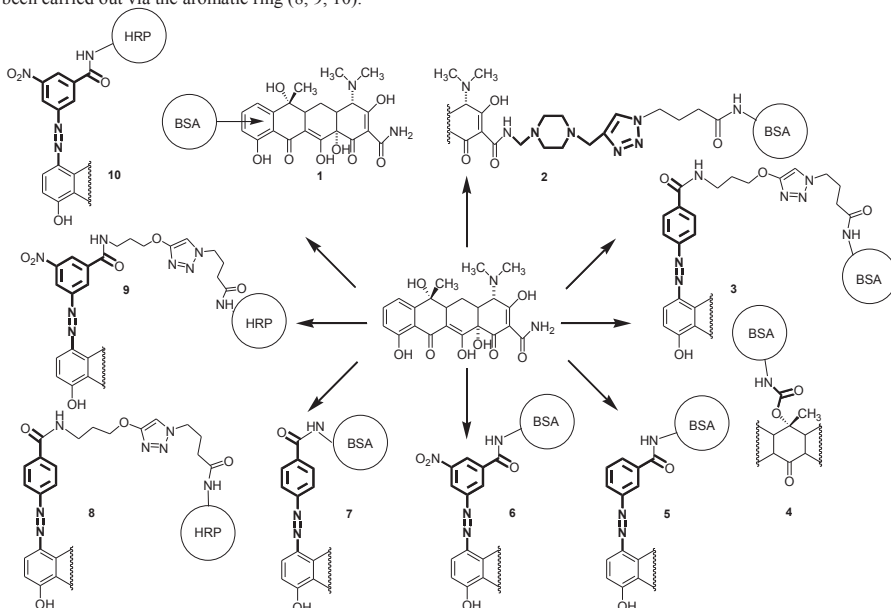


Fig. 1. Synthesis of tetracycline conjugates with protein

The methods developed allow one to obtain a range of tetracycline conjugates of desired structures.

[1] Koester C.J., Simonich S.L., Esser B.K. Environmental analysis. *Anal. Chem.*, 75(12), 2813-2829 (2003).

[2] Ahmed F.E. Analyses of pesticides and their metabolites in foods and drinks. *Trends Anal. Chem.*, 20(11), 649-661 (2001).

INTRINSIC STRUCTURE – THERMODYNAMICS CORRELATIONS OF FLUORINATED BENZENSULFONAMIDES AS INHIBITORS OF HUMAN CARBONIC ANHYDRASES

Joana Gylte¹, Asta Zubrine¹, Virginija Dudutiene¹, Alexey Smirnov^{1,2}, David D. Timm¹, Elena Manakova², Saulius Grazulis², Daumantas Matulis¹

¹Department of Biothermodynamics and Drug Design, Institute of Biotechnology, Vilnius University, Vilnius, Lithuania

²Department of Protein - DNA Interactions, Institute of Biotechnology, Vilnius University, Vilnius, Lithuania

gylte@ibt.lt

The carbonic anhydrases (CA) are established as therapeutic targets. There are 12 catalytically active CA isozymes in human body. At least 30 CA sulfonamide inhibitors have been used as drugs to treat glaucoma, epileptic seizures, altitude sickness, and as diuretics [1]. However, most of them exhibit poor selectivity towards target isozymes and result in various side effects.

In this work, a class of 4-substituted-benzensulfonamides and 4-substituted-2,3,5,6-tetrafluorobenzensulfonamides as inhibitors of CA is reported. The binding affinity to carbonic anhydrases I, II, VII, XII and XIII was measured by isothermal titration calorimetry and thermal shift assay, and inhibition was determined by stopped-flow CO₂ hydration assay. The combined use of these methods has provided a detailed picture of protein-ligand interactions. Experimentally obtained binding data usually depends on various factors including buffer and *pH*. In this study, intrinsic parameters of binding that are independent of these experimental conditions are presented. Structure–thermodynamics correlations were studied using intrinsic parameters. All used biophysical methods have confirmed that fluorinated sulfonamides bound stronger to CA than non-fluorinated, because the presence of electronegative substituents decrease the *pK_a* of sulfonamide group and this correlates with an increase in the CA inhibitory properties [2]. Furthermore, fluorinated compounds possessed nanomolar affinity for selected CAs and were selective towards CAI. One of the studied compounds exhibited exceptionally high-affinity and was selective inhibitor of CAI.

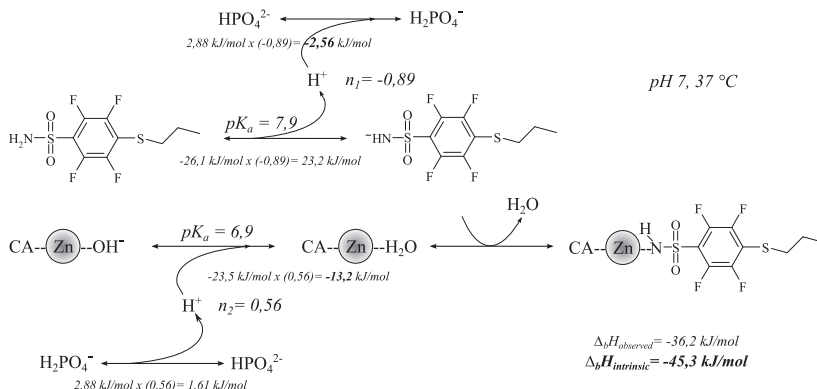


Fig. 1. Calculations of intrinsic parameters.

- [1] V. Alterio, A. D. Fiore, K. D'Ambrosio, C. T. Supuran, D. G. Simone, Multiple Binding Modes of Inhibitors to Carbonic Anhydrases: How to Design Specific Drugs Targeting 15 Different Isozyme, *Chemical Review* **112**, 4421–4468 (2012).
- [2] V. Dudutiene, A. Zubrine, A. Smirnov, J. Gylte, D. D. Timm, E. Manakova, S. Grazulis, D. Matulis, 4-Substituted-2,3,5,6-tetrafluorobenzensulfonamides as inhibitors of carbonic anhydrases I, II, VII, XII, and XIII, *Bioorganic Medicinal Chemistry* **21**, 2093–2106 (2013).

CLONING AND EXPRESSION OF THE RECOMBINANT FAB FRAGMENT OF A MONOCLONAL ANTIBODY TO THE HORMONE CORTISOL

Dmitri Dormeshkin, Vashkevich Irina, Sviridov Oleg, Andrei Gilep, Sergey Usanov

Institute of Bioorganic Chemistry NAS Belarus, Belarus
Dormeshkin@gmail.com

Cortisol is a steroid hormone, produced in human body by the zona fasciculata of the adrenal cortex. It plays a major role in response to stress and a low level of blood glucocorticoids [1]. Cortisol level measurement is important for pituitary and adrenal cortex functions monitoring. The majority of such diagnostic systems for cortisol quantitative measurement utilize the principle of cortisol affinity recognition by antibodies (immunoglobulins) IgG isotype.

The IgG molecule consists of four polypeptide chains, two heavy chains of approximately 50 kDa, divided into four structural domains (VH, CH1, CH2, CH3); and two light chains of approximately 25 kDa, divided into two structural domains (VL and CL). The heavy and light chain variable domains (VH and VL) associate to form antigen-binding site, and the minimal stable unit, possessing the antigen binding activity, is Fab fragment (Figure 1).

Hybridomas 5G-H2 synthesizes antibodies, which tightly bind steroid hormone cortisol. However, the use of hybridoma lines producing monoclonal antibodies has a number of disadvantages; among the others include the instability of cell lines and the high cost of their cultivation. Furthermore, the expanded hybridoma lines can lose their ability to produce a specific monoclonal antibody after prolonged growth in culture. Thus, immortalization of valuable clones by cloning antibody genes into bacterial system and sequencing them should be carried out. Moreover, recombinant antibodies and their fragments, like a Fab fragment give a unique opportunity for antibodies functions and properties manipulations [2].

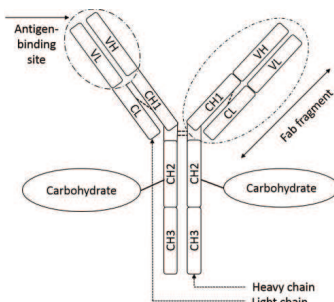


Fig. 1. Representation of the organization of protein chains of an IgG molecule

Using the hybridoma cell line 5G-H2, secreting monoclonal antibodies against steroid hormone cortisol as a source of mRNA and cDNA respectively, light and partially heavy chain gene fragments of Fab domain were amplified by the polymerase chain reaction (PCR). A set of degenerate oligonucleotide primers, covering all the family of mouse immunoglobulins IgG isotype was designed, according to the web-database IMGR.org alignment. Rare restriction sites were incorporated into VL and VH chains and used for cloning it into expression vector.

Expression of rFabs was carried out using bicistronic plasmid vector, which was constructed on the basis of pCWoRI-LIC plasmid and has two signal peptides pelB before N-terminal residues of VL and VH chains for protein transport into periplasmic space, and 6His amino acid tag fused to VH chain to facilitate rFab purification by IMAC [3]. Due to the appropriate redox potential in the bacteria periplasm recombinant protein folds correctly and could be isolated in soluble and active form. In order to express rFabs *Escherichia coli* BL21 expression strain was used.

Periplasmatic fraction was isolated by means of using cold osmotic shock. The protein of interest was isolated (and simultaneously purified) by metal affinity purification (IMAC) on Ni-IDA sepharose and then dialyzed.

Homogeneity of antibodies fragments was controlled by SDS-PAGE electrophoresis. The results indicates the presence of two amino acids chains with estimated molecular weight (25 kDa and 27 kDa for VL and VH chains respectively), confirming the effectiveness of the selected strategy and designed constructs. Binding activities of rFab and hybridoma secreted immunoglobulin were measured and no significant difference between them was revealed.

[1] Spironelli, C. Cortisol and ACTH plasma levels in maternal filicides and violent psychiatric women/ *Psychiatr Res.* **47**. 622– 627 (2013)

[2] Strebe, N. Cloning of Variable Domains from Mouse Hybridoma by PCR/ *Antibody Engineering.* **1**. 3-14 (2010)

[3] Wlad, H. Rapid two-step purification of recombinant mouse Fab fragment expressed in *E. coli*. *Protein Expr. Purif.* **22(2)**. 325-329 (2009).

THE MAGNETORHEOLOGICAL IMMERSION MEDIUM FOR ULTRASONIC THROMBOLYSIS

Yekelchyk Michail Dzmitryevich

Department of Physics, Belarusian State University, Belarus

yekelchyk@yahoo.com

Despite achievements in treatment of cardiovascular diseases, this pathology continues to remain the main reason of incidence and mortality in the world, annually carrying away 17 million lives. So, one of 8 men and one of 17 women in the world die of cardiovascular diseases to 65-year age. Thus in structure of diseases of system of blood circulation growth of an incidence by coronary heart disease and cerebrovascular pathology which in 91% of cases are the reasons of deadly outcomes from diseases of system of blood circulation among all population [1].

In the most perspective way of ultrasonic destruction of blood clots is ultrasonic thrombolysis which assumes introduction of an ultrasonic wave guide together with thrombolytic drugs (in particular, streptokinase) in a vessel with blood clot then, thanks to total influence of high-intensity ultrasound and preparation lysis, blood clot effectively collapses. And the ultrasound in this case, except mechanical cavitation influence, also considerably increases extent of penetration of a thrombolytic drug in blood clot [2].

Low-frequency high-intensity ultrasound causes changes in the structural and functional state of the blood cells and the vascular endothelium, as well as indicators of blood plasma coagulation, the severity of which depends on the parameters of ultrasonic treatment and head shape of the waveguide is used [3]. Among others, damage to vessel walls of the thrombus caused by the cavitation jet unfocused. In fact, damage to the vascular endothelium by ultrasound thrombolysis is one of the few remaining unsolved problems facing the widespread introduction of the method in clinical practice. The aim of this work is to develop a method of reducing damage to the vessel walls with ultrasound thrombolysis.

The study:

1) A modification of the method of ultrasound thrombolysis investigated: use of the magnetorheological fluid (colloidal solution containing fine particles (0.5 - 20 micron) oxide Fe (II, III) (magnetite), possessing the properties of the liquid and reacts to a magnetic field) as the immersion medium. The results of calorimetric experiments show that the cavitation threshold in magnetorheological fluid is lower than the cavitation threshold in blood, resulting in less energy needed for cavitation, which reduces damage to the vascular wall.

2) Three different magnetorheological fluid composition and the method of manufacture had developed (magnetorheological fluid based on saline, magnetorheological fluid based on dextran, magnetorheological fluid based on an aqueous solution of 10 % citric acid). Magnetorheological fluid showed an extremely high performance of bio neutrality: experiments *in vitro* on erythrocyte hemo neutrality and *in vivo* experiments on laboratory rats had conducted (intravenous injection of working volume of magnetorheological fluid (0.5 ml); blood tests and morphological studies of organs).

Currently studies destruction efficiency of fibrin clots *in vitro* by using a magnetorheological fluid as the immersion medium, further studies would be undertaken *in vivo*. Solution carrying fine particles of magnetite in the magnetorheological fluid is a great carrier for thrombolytic drugs. And thanks to the similarity of the size of cavitation bubbles formed and magnetite particles, the last transmitted more kinetic and thermal energy, which increases the degree of destruction of the fibrin clot net. Also, by the action of the toroidal magnetic field magnetorheological fluid, it is possible to change the shape of the immersion bridge between a thrombus and the waveguide so that the effect is realized for total internal reflection, i.e. almost all of the ultrasonic energy is directed into the thrombus, by which will be significantly reduced damage to the vascular wall. Among other things, when magnetite particles are in contact with the thrombus hyperthermia technique can be applied: the effects on the tissue with ferromagnetic particles of high-frequency magnetic field, the particles are heated by friction and break this tissue. When implementing the above described methods in this study, it is assumed optimal ultrasonic destruction of thrombus.

[1] Oganov. R.G. Prevention of cardiovascular disease - the real way to improve the demographic situation in Russia // *Cardiology*. - 2007. - № 1 - p. 4-7.

[2] Adzeriho, I.E. Ultrasound thrombolysis in the treatment of arterial thrombosis : MD PhD dissertation: 14.00.06 / I.E. Adzeriho. - Minsk 2004. - 322 p.

[3] Efimova N.N. "Effect of ultrasound on the efficiency and thrombolysis hemostasis using waveguides of different designs (experimental study)." MD PhD dissertation: 14.00.06. - Minsk, 2009. - 115 p.

WITHDRAWED CONTRIBUTION

INFARCTION QUALIFIED FOR CABG SURGERY

Sabina Brazevič¹, Magdalena Grajek¹, Tomasz Kopyciuk¹

¹Department of Physics, Adam Mickiewicz University in Poznań
sabinabrazevic@yahoo.com

Over the last thirty years cardiology was one of the fastest growing medical specialties. It is not known direct cause of coronary heart disease, only a few factors have been identified that increase risk of it occurrence [1].

So far, it is not known direct cause of coronary heart disease, only a few factors have been identified that increase risk of it occurrence. Obesity, diabetes, smoking, mental stress, lack of physical activity and eating high-energy foods contributes to a sharp increase in incidence of cardiovascular diseases, which are becoming more frequent.

Electrocardiography is the most commonly performed diagnostic test. Almost all patients treated at hospital are subjected to electrocardiographic examination. Much of ECGs recorded for life insurance, assessing ability to work and during other routine procedures.

Heart forming a time-varying electric dipole generates a variable electric potential. These changes spread throughout the body and reach the surface of the body, where they can be recorded using the appropriate equipment.

Electrocardiography is the "gold standard" in diagnosis of atrio-ventricular block, arrhythmias and others. Occurrence of pathological Q-waves, QRS complex, negative T-waves and depressions or elevations of ST segment strongly suggests a cause of coronary heart disease. To attenuate symptoms in patients with coronary artery disease a coronary artery bypass grafting (CABG) performs [2]. The main objective of this research was to determine whether there is a significant time has elapsed since heart attack until time of coronary artery bypass grafting surgery on the basis of results obtained from the ECG.

Furthermore, an additional goal was to determine statistically significant pathological changes in ECG and check if associated diseases, such as hypertension or diabetes, also have a negative impact on patient's condition. In order to compare changes in electrical potential of myocardial infarction and left ventricular ejection fraction caused by the surgery a group of 79 patients were subjected to a cycle of two studies: one performed before surgery and one after surgery.

There was a correlation between the presence of anterior myocardial infarction in patients whose past period of less than six months after infarction until the treatment, and the presence of elevated or depressed ST segment, the pathological Q-wave and left axis deviation (Table 1). Two-sided Fisher's exact test was equal $p = 0,054$, when the significance level was $\alpha = 0,05$. Obtained above values indicate a statistically significant relationship between the presence of elevated ST segment and patients with prior myocardial infarction, hypertension, and diabetes, in whom the disease entities occur over a period longer than six months as the time elapsed until surgery performed.

Table 1. Associative table for a group of people after a heart attack, hypertensive disease and diabetes for more than six months and elevated ST segment of ECG performed after surgery. 0 - means no, 1 - is YES.

MI + hypertension+ diabetes	Two-way summarizing table: incidence observed after surgery		
	ECG depressed ST 0	ECG depressed ST 1	Line Sum
0	71	19	90
% from line	78,89%	21,11%	
1	5	5	10
% from line	50,00%	50,00%	
Total	76	24	100

The time that has elapsed since the attack until the coronary artery bypass grafting surgery and location of attack is important statistically in myocardial regeneration after surgery.

[1] A. J. Camm, T. F. Lüscher, P. W. Serruys, *Choroby serca i naczyń*, Volume I, Poznań, Termedia Wydawnictwo Medyczne, 2006.

[2] A. Bayés de Luna J.M. Cino, S. Pujadas, "Concordance of Electrocardiographic Patterns and Healed Myocardial Infarction Location Detected by Cardiovascular Magnetic Resonance" [interactive], *The American Journal of Cardiology*, 2006, p. 443–451 [seen 2013-05-15], access via the Internet: <<http://www.sciencedirect.com/science/article/pii/S0002914905018898>>

FLAVONE-MEDIATED INSULIN FIBRILLATION

Akvilė Botyriūtė, Vytautas Smirnovas

Department of Biothermodynamics and Drug Design, Vilnius University Institute of Biotechnology, Vilnius, Lithuania

[Akville.Botyriute@chf.stud.vu.lt](mailto:Akvile.Botyriute@chf.stud.vu.lt)

Amyloid-like fibril formation is responsible for dozens of diseases such as Alzheimer's disease, Parkinson's disease, type-II diabetes and other. Misfolded proteins related to these disorders share resembling beta-sheet-rich secondary structure and fibril-like morphology of aggregates. In order to treat these diseases it is important to find efficient amyloid-like fibril formation inhibitors. Recent studies show that number of flavone derivatives affects amyloid-beta and transthyretin fibrillation.

We obtained over a hundred diverse flavone derivatives and checked their influence on recombinant human insulin fibril formation. Fibrillation process in presence and absence of flavones was monitored by Thioflavin T fluorescence at 520 nm (excitation 470 nm). Experimental data revealed that some of the flavone derivatives accelerate whereas others inhibit insulin fibril formation. Furthermore fibrils made in presence of these flavones were examined by FTIR and AFM. The differences in fibrils organization were observed.

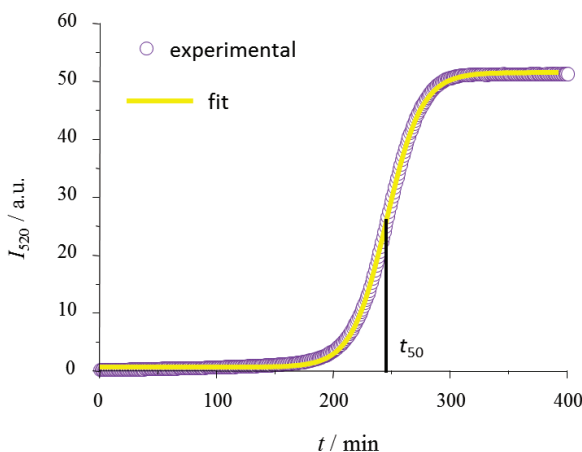


Fig. 1. Insulin amyloid-like fibril formation over time (experimental data of Thioflavin T fluorescence assay).

-
- [1] H. Kim, B. S. Park, et al., Effects of naturally occurring compounds on fibril formation and oxidative stress of beta-amyloid, *Journal of Agricultural and Food Chemistry* **53**, 8537-41, (2005).
 [2] M. G. Sharoar, A. Thapa, et al., Keampferol-3-O-rhamnoside abrogates amyloid beta toxicity by modulating monomers and remodeling oligomers and fibrils to non-toxic aggregates, *Journal of Biomedical Science* **19**, 104, (2012).
 [3] N. Ferreira, M. J. Saraiva, et al., Natural polyphenols inhibit different steps of the process of transthyretin (TTR) amyloid fibril formation, *FEBS Letters* **585**, 2424-30, (2011).

ELONGATION OF MOUSE PRION PROTEIN AMYLOID-LIKE FIBRILS: EFFECT OF TEMPERATURE AND DENATURANT CONCENTRATION

Katažyna Milto, Ksenija Michailova, Vytautas Smirnovas

Department of Biothermodynamics and Drug Design, Vilnius University Institute of Biotechnology, Vilnius, Lithuania
milto@ibt.lt

Prions are infectious proteins capable of causing such diseases as “mad cow” disease in cattle and Creutzfeld-Jakob disease in humans. These fatal neurodegenerative disorders arise when normal cellular form of prion protein (PrP^{C}) is converted into an aggregated, beta-sheet-rich isoform (PrP^{Sc}). One of the most surprising features of prions is their ability to self-replicate via the conversion of PrP^{C} into disease-associated isoform. One of the possible mechanisms of prion structure replication is elongation of amyloid-like fibrils.

Here we tried to gain an insight into elongation kinetics and thermodynamics of murine prion protein fibrils under different environmental conditions: several guanidine hydrochloride (GuHCl) concentrations. Quiescent conditions were used in order to avoid most of nucleation processes (such as primary nucleation and fragmentation of fibrils).

Using Arrhenius coordinates we were able to demonstrate differences in activation energies of fibril elongation when attaching folded versus unfolded PrP monomers (Fig. 1).

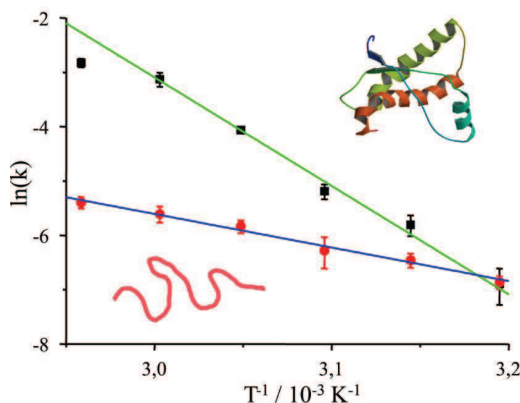


Fig. 1. Arrhenius plot in presence of 0,5 M (black squares) and 2,5 M (red squares) GuHCl.

SPECTRAL AND CORRELATION ANALYSIS OF FLUCTUATIONS OF CARDIOVASCULAR SYSTEM SIGNALS

Dovilė Čibiraitė¹, Sandra Pralgauskaitė¹, Jonas Matukas¹

¹ Department of Radiophysics, Faculty of Physics, Sauletekio Av. 9-III, LT-10222 Vilnius, Lithuania
dovile.cib@gmail.com

In Lithuania more than 50 % of human deaths are caused by cardiovascular diseases [1]. This trend continues to dominate in the EU countries as well. “Eurostat Database” data for 2010 shows that mortality from ischemic heart diseases was 76.5 deaths per 100,000 of population [2]. It is essential to discover more efficient tools for making more accurate and precise diagnosis as well as monitoring methods for cardiac and circulatory system diseases in order to observe their progress.

The aim of this research was to develop a program being able to process and analyse the fluctuations of signals generated by heart and circulatory system in purpose to discover a special testing methodology for human limb impedance signal.

The signal of cardiac and circulatory system is usually measured using electrodes [3]. In this work an optical method is used to investigate signals generated by blood flow. A light emitting diode and a photodiode were placed in a light-tight chamber, a human limb (in this case – a finger) is placed in-between. The signal is acquired by measuring the fluctuations of transmitted light through the finger.

The program was built using this algorithm:

- Scanning of digitized signal.
- Eliminating of 50 Hz and more than 100 Hz frequency components.
- Centring of the signal.
- Processing by the method of moving averages.
- Subtracting centred signal from the primary measured signal.
- Computing a correlation function and a power spectrum.
- Entering data into text documents.

The test run showed that all the subjects had heart rate variations between 1.37 Hz and 1.63 Hz (Fig. 1).

Apparent respiratory frequency can also be obtained from measured signals – it corresponds to 0.1 Hz - 0.5 Hz frequency. The respiratory signal cannot be seen in the measured spectrum, because its spectral power is much lower than the heart rate signal power.

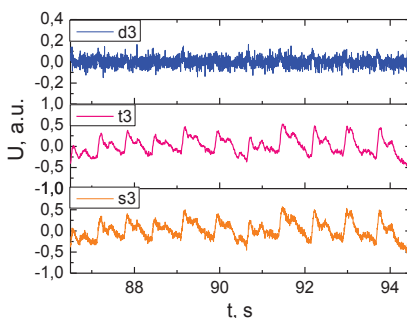


Fig. 1. Measured and processed signal of cardiac and circulatory system over time (d3 – fluctuations, t3 – signal after moving average filter, s3 – initial measured signal).

In conclusion it is notable that this program, based on spectral and correlation analysis method, enables monitoring of cardiovascular system parameters.

[1] http://epp.eurostat.ec.europa.eu/cache/ITY_OFFPUB/KS-NK-06-010/EN/KS-NK-06-010-EN.PDF (last checked 2014-02-14).

[2] <http://data.euro.who.int/hfad/> (last checked 2014-02-14).

[3] P. Jurak et al., Elimination of the Respiratory Effect on the Thoracic Impedance Signal with Whole-body Impedance Cardiography, Computing in Cardiology 2010, 37, p. 1051 – 1054.

THE FLUORESCENCE SPECTROSCOPY OF MEDICAL SAMPLES AND THE ANALYSIS OF SPECTRA USING MULTI-CURVE RESOLUTION METHODS

Jurgita Stankevičiūtė¹, Vilmantas Gėgžna^{2,3}, Aurelija Vaitkuvienė³

¹ Faculty of Physics, Vilnius University, Lithuania

² Faculty of Natural Sciences, Vilnius University, Lithuania

³ Institute of Applied Research, Vilnius University, Lithuania

jurgita.stankeviciute@ff.stud.vu.lt

In the medical practice the evaluation of indistinct premalignant cervical lesions is based on examination of cytological smear samples. Although the examination is performed in laboratory the accuracy of it is influenced by the human factor. The sensitivity of such tests ranges from 50% to 80%, while specificity – from 70% to 90% [1]. Methods of fluorescence spectroscopy have huge potential as an alternative to non-invasive clinical detection of changes in cells. Until now only preliminary researches of cervical smear auto-fluorescence has been made comparing low-grade squamous intraepithelial lesions (LSIL) group to one without pathological changes (Normal) and the number of samples investigated was very low. Thus the goal established for this work is to investigate a larger quantity of Normal and LSIL group samples for purposes of medical diagnostics using autofluorescence based measurements and spectra decomposition methods.

The tasks of this research were to:

1) examine investigate a larger quantity of fluorescence spectra;

2) improve data analysis system involving spectra decomposition algorithms called principal component analysis (PCA), mutual information least-dependent component analysis (MILCA), multi curve resolution – alternating least squares (MCR-ALS);

3) calculate the accuracy of cervical Normal and LSIL group autofluorescence-based identification in comparison to cytology-based evaluation.

Methods. 37 samples of Normal, 33 samples of LSIL group were investigated registering 5 spectra per undried specimen. Spectra were preprocessed, divided to 2 subsets (for classification model creation and for model validation). The components were extracted combining PCA, MILCA, MCR-ALS algorithms and statistical Mann-Whitney and receiver operating characteristic (ROC) methodologies.

The best results of Normal and LSIL group classification were received using PCA method: the Mann-Whitney test showed statistically reliable difference ($p < 0.05$), the accuracy measure called AUC (area under the ROC curve) = 0.64(0.56÷0.72), sensitivity = 58.8% (51.2÷66.0), specificity = 62.1% (54.6÷69.2), positive predictive value = 58.1%(50.6÷65.4), negative predictive value = 62.8% (55.2÷69.8), overall accuracy = 60.6% (53.0÷67.7). All measures indicated with their 95% confidence intervals in brackets.

Resume. Mann-Whitney test indicates statistically reliable differences between spectra of cytological Normal and LSIL groups. Unfortunately these differences are not sufficient to fulfill requirements for medical diagnostics, i.e. $AUC > 0.75$ [2]. It should be mentioned that the “golden standard” in medicine is histological evaluation. Due to medical rules, the histological evaluation is not available for both cytological Normal and LSIL cases. Thus the next step of analysis should be the development of auto-fluorescence based classification algorithm to distinguish between cytological Normal/LSIL group and histologically evaluated group of cytological HSIL (high-grade squamous intraepithelial lesions) cases.

[1] A. Vaitkuvienė, V. Gėgžna, R. Kurtinaitienė, and J. V. Vaitkus, Cervical smear photodiagnosis by fluorescence, Photomed and Laser Surg, 30, 268-274, 2012.

[2] J. Fan, S. Upadhye, and A. Worster, Understanding receiver operating characteristic (ROC) curves. CJEM8(1), 19–20, 2006.

Open Readings 2014. 57th Scientific Conference for Students of Physics and Natural Sciences

CHITOSAN AEROSOL NANOPARTICLE PRODUCTION BY ELECTROSPRAYING

Vadimas Dudoitis, Vidmantas Ulevičius, Genrik Mordas

State Research Institute Center for Physical Sciences and Technology, Vilnius, LT-02300, Lithuania

vadimas.dudoitis@ftmc.lt

Chitosan is a deacylated by-product of chitin, which is one of the most abundant polymeric material on the planet. It has good sorption ability in aqueous solution for heavy metals [1], though there are the limitations of chitosan application as sorbent in practise due to its lower sorption rate than other sorbents. One way of improving chitosan's sorption rate is by altering its physical properties. The nano sized chitosan granules increase the sorption dramatically due to a high surface area per unit mass and a porous structure [2].

Special case of liquid atomisation is electrospraying. This technique is used for generation of liquid droplet spray, strongly influenced by an electrical field. This process consists of liquid capillarity, a droplet breakdown in the electric field, a working mode of the spray selection and aerosol particle neutralisation in the chamber [3].

In order to determine aerosol particle formation, chitosan was diluted in the citric acid with palladium salt ($\text{Pd}_2\text{Cl}_3\cdot\text{H}_2\text{O}$) and ejected by an electrospray generator (EAG; TSI 3480). For generated chitosan particle evaluation data from a scanning electrical mobility particle sizer (SMPS; TSI 3936) was used to measure particle size distributions. SMPS was measuring particles in the range from 6 nm to 294 nm, each scan composed of an up-scan duration 120 s and a retrac - 15 s.

The most efficient way to generate aerosol nanoparticles is then the EAG is operating in the cone-jet mode. For chitosan aqueous solution the high voltage (HV) was varying in the range from 1.5 kV to 3.5 kV. In (Fig. 1) shows dependence of HV affects particle size distribution at fixed chitosan-palladium complex concentration of chitosan 1.5 g/L. The generated aerosol particles were observed in the nucleation mode cluster. Difference in particle distributions, can be explained by the operating modes of EAG, which are controlled based on HV and liquid property.

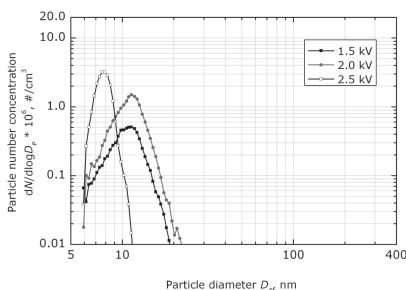


Fig. 1. Chitosan nanoparticle generation from the solution of citric acid and palladium using electrospray generator. Dependency of high voltage on particle size distribution is depicted.

-
- [1] S. E. Bailey, T. J. Olin, R. M. Bricka, D. D. Adrian, A review of potentially low-cost sorbents for heavy metals. *Water Research* **33**(11), 2469–2479 (1999).
- [2] O. Gylinė, V. Ulevičius, V. Dudoitis, K. Plauškaitė, R. Butkienė, Z. Kuodis, I. Vitėnienė, Heavy metal sorption onto chitosan and chitosan-citrate derivatives. *Chemija* **24**(2), 118-127 (2013).
- [3] D.-R. Chen, D. Y. Pui, S. L. Kaufman, Electrospraying of conducting liquids for monodisperse aerosol generation in the 4 nm to 1.8 μm diameter range. *Journal of Aerosol Science* **26**(6), 963–977 (1995).

CROSS-SHORE AND LONGSHORE HEAVY-MINERAL CONCENTRATIONS DISTRIBUTION ON THE BALTIC SEA MAINLAND COAST, LITHUANIA

Julija Fedorovič¹, Donatas Pupienis², Ilya Buynevich³, Darius Jarmalavičius⁴, Gintautas Žilinskas⁵

^{1,4,5} Institute of Geology and Geography, Nature Research Centre, Lithuania,

² Faculty of Natural Sciences, Vilnius University, Lithuania,

³ Department of Earth and Environmental Science, Temple University, USA

julijafed@inbox.lt

The sandy beaches of the Baltic Sea along the mainland coast of Lithuania are mainly composed of quartz sands. Heavy minerals are locally important accessory components. Heavy-mineral concentrations (HMCs) in coastal sands serve as important indicators of hydrometeorological and sedimentological conditions [1], [2].

To examine the patterns in HMC distribution, a total of 221 surface sand samples were collected from the middle of the beach, foredune toe, and stoss slope at 500 m intervals along the mainland coast from the northern part of the Port of Klaipėda to Lithuania–Latvia border. To characterize the relative concentrations of heavy minerals, a Bartington MS3 field scanning sensor was used for rapid and effective measurements of low-field volume magnetic susceptibility (MS). Along the Baltic Sea beach, in-situ MS values of $\kappa < 50 \mu\text{SI}$ of background quartz-rich sands contrast with $\kappa > 150 \mu\text{SI}$ in surface HMCs.

The highest value of MS was found near cliffs, where mean grain size reach 0.5 mm. Heavy mineral concentration depends on grain size [3]. As the distance of the cliff increase, mean grain size and MS value is going to decrease (Fig. 1). The highest MS values were found in the middle of the beach, the lowest – on the slope.

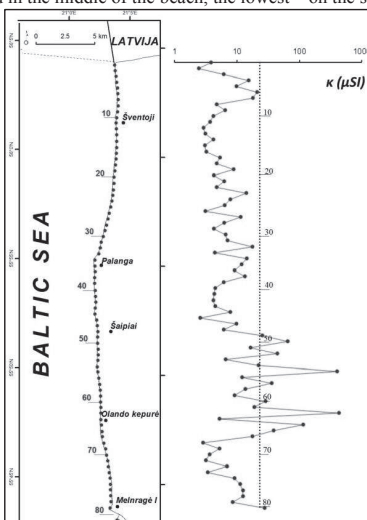


Fig. 1. Magnetic susceptibility (MS) of surface layer along the Baltic Sea mainland coast

At cross-section of the coast with foredune maximum average MS values are on foredune toe and less on the middle of the beach and stoss slope.

The main factor that controls heavy mineral concentration grading longshore and cross-shore the coast is the source area of the sediments, erosional and/or accretional beach processes and human activity.

[1] O. E. Frihy, M. F. Lotfy, P. D. Komar. Spatial variations in heavy minerals and patterns of sediment sorting along the Nile Delta, Egypt. *Sedimentary Geology* 97. 33–41(1995).

[2] P. D. Komar, C. Wang. Processes of selective grain transport and the formation of placers on beaches. *Journal of Geology* 92. 637–655 (1984).

[3] R. N. Dubois. Inverse relation between foreshore slope and mean grain size as a function of the heavy mineral content. *Geological Society of America Bulletin* 83. 871–876 (1972).

Sources of wintertime black carbon aerosols in an atmosphere in Vilnius

Steigvilė Byčėnienė¹, Julija Pauraitė^{1,2}, Vadimas Dudoitis¹ and Vidmantas Ulevičius¹¹ Institute of Physics, Center for Physical Sciences and Technology, Lithuania² Faculty of Physics, Vilnius University, Lithuaniajulijapauraitė@yahoo.com

Black carbon (BC) is a primary aerosol emitted directly at the source from incomplete combustion processes such as fossil fuel and biomass burning and therefore much atmospheric BC is of anthropogenic origin. BC aerosols contribute significantly to climate change, health, water and food resources, seasonal weather patterns, and livelihoods. The aim of this experimental study was to investigate BC aerosol sources, optical properties and their dynamics in the urban environment.

Continuous real-time measurements of aerosol light attenuation properties were investigated at Vilnius, an urban region for the period of January 2014. A Magee Scientific Company AethalometerTM, Model AE31 Spectrum, manufactured by Aerosol d.o.o., Slovenia, was deployed at the site and provided real-time, continuous measurements of the BC mass concentration. The optical transmission of carbonaceous aerosol particles was measured sequentially at 7 wavelengths ($\lambda = 70, 450, 520, 590, 660, 880$ and 950 nm). The concentration of BC corresponds to the 880 nm.

Discernible influence of the residential heating during January 2014 can be seen in Figure 1, where the daily evolution of (A, B) aerosol BC mass concentration at 520 nm are depicted. This is a strong indication that the aerosol particles over the site containing the different composition and depend on the source. Figure 1 shows values of aerosol BC mass concentration during the study period as a function of local time.

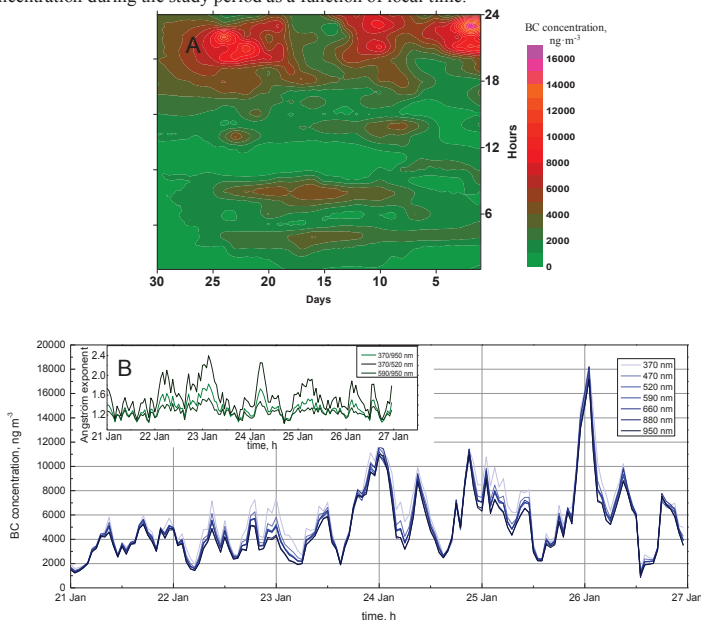


Fig. 1. Diurnal variations in BC concentration and Angström exponent of the absorption coefficient in Vilnius during the study period.

There were clear diurnal variations for all the variables. During the night, when the height of the planetary boundary layer decreased, emissions were entrapped in the lower levels of the atmosphere and caused high concentrations of aerosols at the surface, while during the daytime, as the planetary boundary layer developed, the turbulent mixing led to a lower concentration of BC (Fig. 1(A)). The mean concentration of BC for the entire period were 6500 ng m^{-3} . The mean values of Angström exponent of the absorption coefficient $a_{370-520}$ and $a_{590-950}$ were 1.57 and 1.28 .

[1] S. Byčėnienė, V. Ulevičius, V. Dudoitis, J. Pauraitė, Identification and Characterization of Black Carbon Aerosol Sources in the East Baltic Region, *Advances in Meteorology*, (2013).

ADSORPTION OF TARGET ORGANIC COMPOUNDS ON ACTIVATED CARBON

Inga Rumskaitė^{1,2} and Vytautas Abromaitis^{1,2}

¹ Department of Environmental Engineering, Kaunas university of technology, Radvilėnų pl. 19, LT-50254, Kaunas, Lithuania

² Wetsus, Centre of excellence for sustainable water technology, P.O. Box 1113, 8900 CC Leeuwarden, the Netherlands
inga.rumskaitė@gmail.com

Water pollution due to organic compounds is a serious problem because of toxicities and carcinogenic nature of the pollutants. Adsorption on carbon is inexpensive, universal and easy operational method to remove organic pollutants from water. The goal of this project is to investigate the effect of activated carbon (AC) of adsorption phenomenon of organic pollutants and evaluate adsorption constants. Three main classes of organic pollutants were used for experiments: easily biodegradable (acetate), slowly biodegradable (metoprolol) and non-biodegradable organic matter (BTEX – benzene, toluene, ethyl benzene and xylenes).

The batches tests were used to estimate Freundlich and Langmuir isotherms constants [1] for target compounds adsorption on AC. Tests were carried out with a whole group of BTEX and each compound separately to evaluate the influence of other compounds. The adequate tests and calculations were performed with metoprolol, acetate and bisolute (metoprolol and acetate mixture).

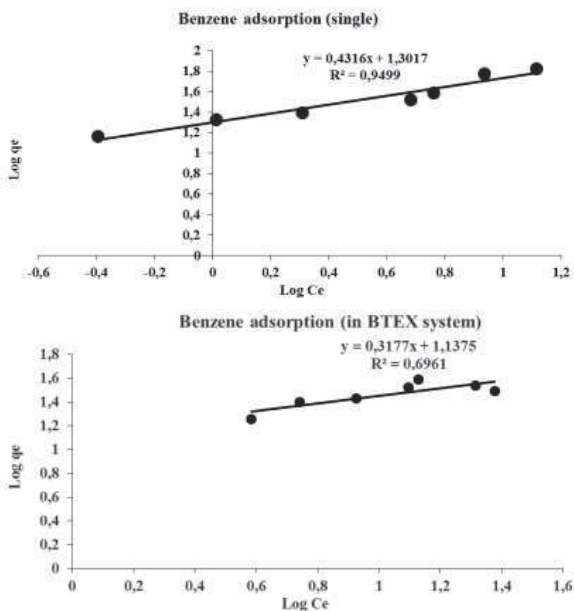


Fig. 1. Freundlich isotherms of benzene adsorption in single solute (above) and BTEX system (below).

The results shows that in the case of BTEX Freundlich isotherm model for adsorptive capacity of AC is more reliable than Langmuir model because of variability of Langmuir constants. However, both models confirm that BTEX compounds are better adsorbed in the case of single solution (Fig. 1). In the case of metoprolol and acetate, adsorption capacity of AC in bisolute is 23 % less than in single solute according to metoprolol adsorption in Freundlich model. The calculated constants also shows the lowest adsorption capacity of AC on acetate than metoprolol.

The present study offers data which can be used for the modeling of biological activated carbon systems to treat pharmaceuticals (metoprolol) or aromatic compounds (BTEX).

[1] O. Hamdaoui, E. Naffrechoux. Modeling of adsorption isotherms of phenol and chlorophenols onto granular activated carbon: Part I. Journal of Hazardous Materials. 147 (2007), 381–394

DECOMPOSITION OF 2-NAPHTHOL IN SIMULATED WASTEWATER SOLUTION USING DBD PLASMA

Inga Rumskaitė¹, Edvinas Krugly¹, Jolanta Sedlina², Dainius Martuzevičius¹, Martynas Tichonovas¹, Dalia Jankūnaitė¹, Viktoras Račys¹ and Jonas Baltrušaitis^{3,4}

¹ Department of Environmental Engineering, Kaunas university of technology, Radvilėnų pl. 19, LT-50254, Kaunas, Lithuania

² Institute of Physical Energetics, Riga Technical University, Aizkraukles 21, LV-1006 Riga, Latvia

³ Department of Occupational and Environmental Health, College of Public Health, University of Iowa, Iowa City, USA

⁴ PhotoCatalytic Synthesis Group, MESA+ Institute for Nanotechnology, Faculty of Science and Technology, University of Twente, Meander 225, P.O. Box 217, 7500 AE Enschede, the Netherlands
inga.rumskaitė@gmail.com

2-naphthol forms as a secondary product of many industrial activities, such chemical, paper and paint, pesticide industries,¹ and is known as a hazardous substance for human beings and the environment. DBD methods are advantageous over advanced oxidation procedures (AOP) when reactive oxidative species generation is considered.

The degradation of 2-naphthol was examined in a pilot dielectric barrier discharge (DBD) pilot setup.² Plasma was generated in a quartz tube with ambient air used as a feed gas for the reactor. The performance of the reactor was evaluated according to the ozone amount produced, both in gas and liquid phase, as well as the overall decomposition efficiency of 2-naphthol.

A screening experiment was performed to find the most important process parameters, followed by the 2-naphthol decomposition kinetics experiment. The largest negative response was obtained for the initial concentration of 2-naphthol with the decomposition efficiency decreasing when increasing 2-naphthol concentration. The increasing power and higher aeration intensity resulted in a positive significance towards 2-naphthol decomposition efficiency.

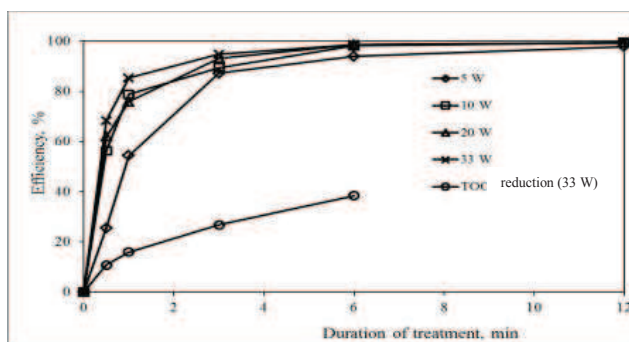


Fig. 1. 2-naphthol decomposition efficiency using different DBD power (TOC reduction curve at 33W DBD power is also shown).

The greatest decomposition efficiency was achieved when using 20W and 33W of power (Fig. 1). The major amount of 2-naphthol (about 90%) was decomposed after the first 2 minutes (2.6 and 1.95 min, respectively). These data are in a good agreement with the measured TOC values, where after 6 min at 33 W DBD power 38.4 % mineralization degree was achieved.

The intermediary reactive products of 2-naphthol decomposition were determined using a combination of FTIR and GC/MS analyses. The degradation intermediates consisted mostly of oxygen containing functional groups: carboxylic acids, as well as amides and amines.

DBD plasma can be successfully applied for decomposition of 2-naphthol in water. This technology is quite universal, efficient and suitable for decomposition of most chemical compounds, including most stable chemicals. Also DBD can be used in combination with a secondary method, capable to decontaminate low resulting concentration products.

[1] R. Srekanth, K. P. Prasanthkumar, M. M. Sunil Paul, U. K. Aravind and C. T. Aravindakumar, The Journal of Physical Chemistry A, 2013, 117, 11261-11270

[2] M. Tichonovas, E. Krugly, V. Račys, R. Hippler, V. Kauneliene, I. Stasiulaitiene and D. Martuzevicius, Chemical Engineering Journal, 2013, 229, 9-19

SHIELDING AND ACTIVATION STUDIES TO ESTIMATE THE RADIOACTIVE WASTES ARISING FROM THE OPERATION OF THE ESS BEAM DUMP.

Benjaminas Marcinkevičius¹, Daniela Ene², Artūras Plukis¹

¹Center for Physical Sciences and Technology, Lithuania

²European Spallation Source, Sweden

benjaminas.marcinkevicius@ftmc.lt

The European Spallation Source (ESS) is the European common effort in designing and building a next generation large-scale user facility in Lund, Sweden, for studies of the structure and dynamics of materials. The proposed schematic layout of the ESS facility is based on a linear driver (Linac) directing the proton beam (5 MW of 2.5 GeV) of 2.8 ms long pulses with a 20 Hz on a tungsten target where neutrons are produced via spallation reactions. Further the neutrons will be moderated to thermal and subthermal energies in a couple of moderators placed around the target. The moderators feed 22 beamlines guiding the neutrons to the scattering instruments, mainly for neutron scattering research.

This work studies the radiological status of the shielding of the tune-up dump of the facility. This device will be placed in the lower room of the accelerator to target (A2T) section and will be used to tune the linac when the proton beam is not being sent to the target wheel.

The dump design and its associated planned irradiation history were taken from ESS Technical Design Report [1], but using copper as active zone of the dump. In the geometry model used in calculations the shielding around the dump was built as concentric cylindrical layers of iron and ordinary concrete.

As criterion for optimization limit of 1 $\mu\text{Sv/h}$ was used at the end of the shielding.

It was found that an optimum shielding configuration consists in 3 m of iron followed by 2 m of concrete.

In order to derive the ground and water activation of the shielding foundations for selected optimum configuration an additional layer of five meters of soil was added to the geometry model.

Activation calculations were performed for various locations within the dump device, shielding and soil. Calculations were performed using MCNPX2.6.0, Monte Carlo program [2] based on CEM3k nuclear reaction model coupled with CINDER'90 activation code [4]. For validation purpose the code FLUKA [3] was used as well.

The obtained results were used to characterized and classify the waste arising from the facility and to derive the source term needed for environmental impact analysis.

Through the comparison of the results obtained via the two methods used in the work it was found the difference within one order of magnitude.

[1] S. Peggs, R. Kreier, *ESS Technical Design Report*, ESS-doc-274, (2013)

[2] D. B. Pelowitz, *MCNPX User's Manual*. Version 2.6.0, LA-CP-07-1473, Los Alamos National Laboratory (LANL) (2008).

[3] A. Ferrari, P.R. Sala, A. Fasso', and J. Ranft, *FLUKA: a multi-particle transport code*, CERN-2005-10 (2005), INFN/TC_05/11, SLAC-R-773

[4] W. B. Wilson, S. T. Cowell, T. R. England, A. C. Hayes & P. Moller, *A Manual for CINDER'90 Version 07.4 Codes and Data*. (2007).

LOW COST COMPUTER CONTROLLED SAMPLE POSITIONING SYSTEM

Bartosz Dziedzic

Institute of Physics, Cracow University of Technology, Poland
bd13.01.89@gmail.com

Experimenters from all fields have the same problem. Costs of experiments are many times higher than their budget. Many times they are buying just essential parts of measurement systems to cut costs. Sometimes there's no problem, but often it's bad idea, because reduced measurement system can increase uncertainties, increase time of measurements or worse – decrease life of measuring apparatus.

In my occurrence I'll show the situation in Solid State Physics Laboratory in Cracow, and then I'll show the Sample Positioning System of my design and made.

Sample Positioning System has four degrees of freedom – three degrees along cartesian coordinate system axis with about $5\text{ }\mu\text{m}$ resolution and forth – rotation around Z-axis with 0.1 degree resolution. Modular structure of device allows to increase resolution, add more degrees of freedom, and many more features limited by experimenter's imagination and creativity.

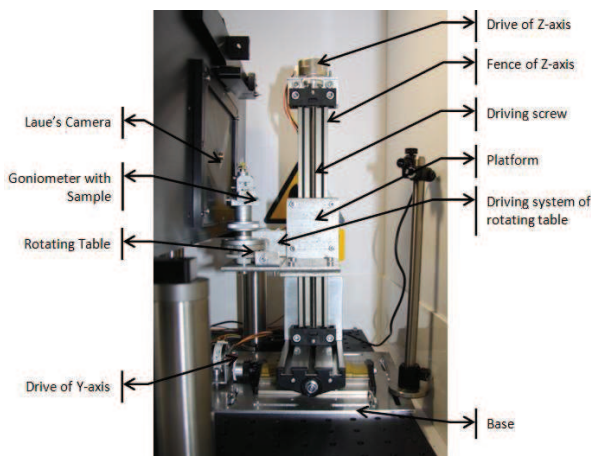


Fig. 1. Sample Positioning System in Laue's diffraction chamber in Solid State Physics Laboratory

Open Readings 2014. 57th Scientific Conference for Students of Physics and Natural Sciences
ENTANGLEMENT DETECTION WITH ENTANGLEMENT WITNESS
OPERATOR IN TWO QUBIT SYSTEMS

Piotr Rożek¹

¹ Poznan University of Technology, Faculty of Technical Physics, Institute of Physics, Poland

piotrozek91@gmail.com

Entanglement is one of the fundamental consequences of quantum mechanics postulates. It caused lot of discussions about quantum mechanics itself [1,2]. Experiments show that [3] entanglement is, despite of philosophical difficulties, real physical phenomena and can be observed. It's not only interesting phenomena from fundamental research point of view, but also interesting applications. For example, there are computational problems that can't be solved in reasonable time using classical computer [4], to name a few: simulation of quantum system, factorization of large numbers.

First idea of quantum computer was introduced in 80s by Feynman [5]. Later, this concept was extended by many researchers. What is interesting, and related to this problems, it was shown that information is a physical quantity.

Basic tool of all algorithms used in quantum computing are entangled states. For example, in two qubit system entangled states are given by:

$$\begin{aligned} |\psi_{\pm}\rangle &= \frac{1}{\sqrt{2}}(|1_A 0_B\rangle \pm |0_A 1_B\rangle) \neq |x_A\rangle \otimes |y_B\rangle \\ |\phi_{\pm}\rangle &= \frac{1}{\sqrt{2}}(|1_A 1_B\rangle \pm |0_A 0_B\rangle) \neq |x_A\rangle \otimes |y_B\rangle \end{aligned} \quad (1)$$

It is clear, that state can be separated into product of two states.

In this work, methods of detecting entanglement in two qubit system (and some generalizations for many-qubit systems) will be presented. Entanglement witness [6,7] method will be discussed and compared to CHSH inequalities check. Application of this methods in solid state systems [8,9] will be presented.

[1] John S Bell et al. Physics, 1(3), 195200 (1964).

[2] John F. Clauser, Michael A. Horne, Abner Shimony, and Richard A. Holt. Physical Review Letters 23, 880 (1969).

[3] A. Aspect, P. Grangier, and G. Roger, Physical Review Letters 49, 91 (1982).

[4] Peter W. Shor. SIAM J. Comput. 26, 1484 (1997).

[5] R. P. Feynman, International Journal of Theoretical Physics 21, 467 (1982).

[6] Otfried Gühne and Géza Tóth. Entanglement detection. Physics Reports 75, 474 (2009).

[7] M. Horodecki, P. Horodecki, and R. Horodecki, Physics Letters A 223, 1 (1996).

[8] M. Governale, M. G. Pala, and J. König, Phys. Rev. B 77, 134513 (2008).

[9] L. Faoro and F. Taddei, Phys. Rev. B 75, 165327 (2007).

LEVY FLIGHTS IN NON-HOMOGENEOUS MEDIA AND $1/f$ NOISERytis Kazakevičius¹, Julius Ruseckas^{1,2}¹Institute of Theoretical Physics and Astronomy, University of Vilnius, Lithuania
rytis.kazakevicius@gmail.com

The Lévy α -stable distributions, characterized by the index of stability $0 < \alpha \leq 2$, constitute the most general class of stable processes. The Gaussian distribution is their special case, corresponding to $\alpha = 2$. If $\alpha < 2$, the Lévy distributions have power-law tails $\sim 1/x^{1+\alpha}$. There are many systems exhibiting Lévy α -stable distributions: distribution function of turbulent magnetized plasma emitters and step-size distribution of photons in hot vapours of atoms have Lévy tails; theoretical models suggest that velocity distribution of particles in fractal turbulence is Lévy distribution [1] or at least has Lévy tails. If system behavior depends only on large noise fluctuations, such noise intensity distributions can be approximated by Lévy distribution, leading to Lévy flights. Lévy flights can be found in many physical systems: as an example we can point out anomalous diffusion of Na adatoms on solid Cu surface and anomalous diffusion in optical lattices. Lévy flights can be modeled by fractional Fokker-Planck equations or Langevin equations with Lévy noise.

One of the characteristics of the signal is the power spectral density (PSD). Signals having the PSD at low frequencies f of the form $S(f) \sim 1/f^\beta$ with β close to 1 are commonly referred to as “ $1/f$ noise”. Power-law distributions of spectra of signals with $0.5 < \beta < 1.5$, as well as scaling behavior are ubiquitous in physics and in many other fields. Despite the numerous models and theories proposed since its discovery, the subject of $1/f$ noise remains still open for new discoveries. The nonlinear stochastic differential equations generating signals with $1/f$ noise were obtained in Refs. [2], starting from the point process model of $1/f$ noise. Such nonlinear SDEs were used to describe signals in social systems. We generalized this nonlinear stochastic differential equations Eq. (2) by changing Gaussian noise into Lévy noise.

$$dx = a(x)dt + b(x)dL_t^\alpha, \quad (1)$$

$$dx = \sigma^\alpha \gamma x^{\alpha(\eta-1)+1} dt + x^\eta dL_t^\alpha. \quad (2)$$

Here x is a signal (velocity of diffusing particle) and L_t^α is α -stable Lévy process ($0 < \alpha \leq 2$). If $\alpha = 2$ it reduce to standard Wiener process (the Brownian motion). α is stability index of α -stable Lévy distribution, η is multiplicativity of noise, σ and γ are normalization constants. We solved Eq. (2) by using numerical methods results are presented in Fig. 1. During calculations we restricted signal value in interval $x \in [x_{\min}, x_{\max}]$. The drift term $a(x)$ in Eq. (2) represent subharmonic external force effecting particle. Lévy flights in subharmonic potentials lead to various interesting phenomena such as stochastic resonance in single well potential. The power law dependence of diffusion coefficient $b^2(x)$ can be traced to existence of energy flux due temperature gradient in a bath. Long jumps, which leads to Lévy noise dL_t^α , can arise from complex scale free structure of a bath as in the case of enzyme diffusion on an a polymer.

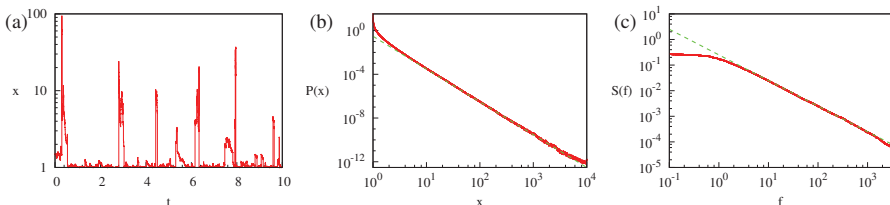


Fig. 1. (a) Signal generated by SDE with Lévy noise (2) with reflective boundaries at $x = x_{\min}$ and $x = x_{\max}$. (b) Steady state of probability density function $P_0(x)$ of the signal. The dashed line shows the slope x^{-3} . (c) Power spectral density $S(f)$ of the signal. The dashed line shows the slope $1/f$. Parameters used are $\alpha = 1$, $x_{\min} = 1$, $x_{\max} = 10^4$, $\sigma = 1$.

In conclusions, a class of nonlinear stochastic differential equations providing the power-law behavior of spectra, including $1/f$ noise, and the power-law distributions of the probability density has been analyzed. Usually such equations are driven by white Gaussian noise. We have generalized the nonlinear stochastic differential equations to be driven by Lévy noise instead of Gaussian noise. To preserve statistical properties of the generated signal we have changed the drift term in the equations. This model can be used to model Lévy flights in non-equilibrium and nonhomogeneous environments, like porous media and some cases of polymer chains. If specific conditions are satisfied our model generated Lévy flights which leads to $1/f$ noise.

[1] H. Takayasu, Stable Distribution and Lévy Process in Fractal Turbulence, Prog. Theor. Phys. **72**, 471 (1984).

[2] B. Kaulakys and J. Ruseckas, Stochastic nonlinear differential equation generating $1/f$ noise, Phys. Rev. E **70**, 020101(R) (2004).

WITHDRAWED CONTRIBUTION

A REVIEW OF CONTEMPORARY MODELS OF INFLATION THEORY

Michał Bogdan

Department of Physics and Astronomy, University of Wrocław, Poland

bogdan490@gmail.com

The current scientific view on the history of the Universe is that it expanded from a very small area to its present shape. This expansion was governed by Friedmann's equation, which is derived from the principles of classical gravity, according to Einstein's general theory of relativity. We do not have insight from this theory to the earliest moments of the universe, because the very high density of matter-energy at this time warrants a quantum gravity theory, which we currently lack.

The dynamics of the Universe described by Friedmann's equation suggests that some parts of the Universe were never in causal contact, that is, light did not have enough time to travel between these parts. However, the temperature in the entire Universe is virtually the same, which suggests the contrary. Inflation was proposed to solve this paradox- it posits that the Universe underwent a period of very rapid expansion at the beginning of its history, which pushed previously causally interacting parts of it so far away, that they became causally disconnected- as the Friedmann equation suggests.

Inflation also explains why the Universe is flat and why no magnetic monopoles, predicted by unification theories, are measured.

There have been various attempts by theorists to explain the occurrence of inflation. Most of them focus on describing how inflation could occur, develop and stop in a regime governed by an effective scalar field- usually without answering, what elementary physical mechanism is responsible for the emergence of the scalar field (it may stem in some way from quantum gravity). This approach is partly justified by developments in other areas of physics, where effective scalar fields are successfully used to treat various phenomena in areas from condensed matter to particle physics.

The first model was developed by Alan Guth. It suggests that the Universe started in a high-energetic value of the scalar field, which caused the rapid expansion of the Universe. This state was separated from the ground state of zero energy by a wall of potential, which was crossed in different places at different times via quantum tunnelling, therefore stopping the inflation. However, this model was abandoned, as it did not provide a mechanism for the ending of inflation- the expanding part of the Universe would always remain much larger than the non-expanding part; the Universe would consist of a very large expanding area with only small non-expanding bubbles.

Many new models followed; most approaches can be broadly classified as the so-called chaotic inflation and slow-roll inflation models. These models give different predictions about the fluctuations of temperature of the cosmic microwave background. New observational data from Planck's satellite has falsified chaotic inflation models and, at present, mostly slow-roll inflation models remain on the market.

Attempts are made to provide some physical justification for the proposed shape and features of the scalar field, even though this remains a very speculative area of physics- for example, by physically motivating the proposed shape of the scalar field by effective approaches to quantum gravity.

MODELING OF ACTIVE GALACTIC NUCLEI WINDS

Rokas Naujalis^{1,2}, Kastytis Zubovas²¹Faculty of Physics, Vilnius University, Lithuania²Center for Physical Sciences and Technology, Vilnius, Lithuaniarokasn@yahoo.com

Active galactic nuclei (AGN) are some of the most luminous sources in the Universe. Their characteristic light spectrum is different from stars and it is believed that their energy source is accretion of gas on to a supermassive black hole (SMBH) instead of nuclear fusion. Gas forms a disc around the SMBH in which it slowly spirals in towards the center due to viscosity. Strong gravity of the black hole forces gas to move at high speeds and heats up the gas. Inside the disc temperatures can reach more than $\sim 10^6$ K resulting in strong thermal radiation with a peak at X-ray wavelengths. This radiation can have enough pressure to create line-driven winds by pushing out part of the gas from the disc. Such winds produce massive outflows which can influence further evolution of parent galaxy by either blowing out and heating the surrounding gas and thus stopping further star formation or enveloping and compressing dense molecular cloud thus accelerating star formation. In this work, we model accretion discs with different feeding rates and calculate the resulting mass loss rate due to wind.

We calculate accretion disc evolution around a $10^8 M_\odot$ SMBH. We use a 1D code which integrates the disc evolution equations derived in [1]. We use the α disc prescription in which viscosity is equal to $\nu = \alpha c_s H$ [2], where c_s is the sound speed inside the gas, H – disc height and α – proportionality parameter which is equal to 0.1 [3]. The disc is modeled from 3 to $1000 R_{\text{Schw}}$ (Schwarzschild radius – radius of the black hole's event horizon), because orbits at smaller radius are unstable and at larger radius gas self-gravity might occur which is not accounted for, might become important. During its evolution the accretion disc is being supplied with gas at a constant rate from an external source at a distance $500 - 600 R_{\text{Schw}}$. Gas supply rates vary from $0.0022 M_\odot \text{ yr}^{-1}$ to $22 M_\odot \text{ yr}^{-1}$ (or 0.001 to 10 times the Eddington accretion rate, which for $10^8 M_\odot$ black hole is equal to $2.2 M_\odot \text{ yr}^{-1}$, at the Eddington accretion rate, radiation pressure becomes equal to the force of gravity) in different models.

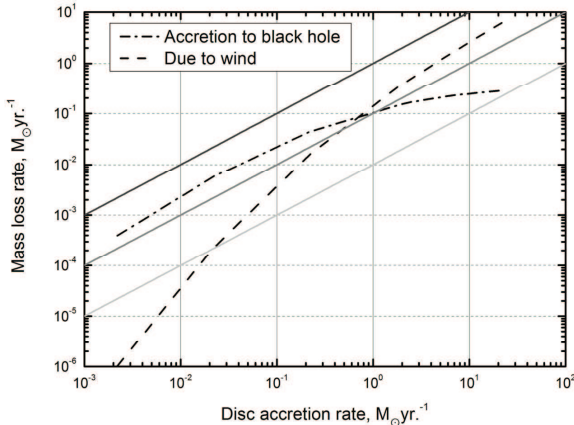


Fig.1. Maximum accretion rate to black hole (dash dotted line) and mass loss rate due to wind (dashed line) dependence from accretion rate onto a disc. Solid lines represent 0.01, 0.1 and 1 loss to gain ratios respectively.

The dependence of both maximum mass loss rates due to wind and accretion rates on to the SMBH on the disc feeding rate is shown in Figure 1. When the feeding rate is much smaller than the Eddington accretion rate, the wind is negligible and most of the gas falls on to the SMBH. When the feeding rate increases the wind becomes progressively more important and exceeds the SMBH accretion rate at feeding rate of $\sim 0.8 M_\odot \text{ yr}^{-1}$. At the highest feeding rate mass loss due to wind is equal to $\sim 30\%$ (or $\sim 6.5 M_\odot \text{ yr}^{-1}$) of the feeding rate thus creating massive outflows. At the same time accretion on to the SMBH starts to reach saturation at $\sim 0.55 M_\odot \text{ yr}^{-1}$ because most of the gas gets blown away before it is able to reach the centre of the disc. This saturation means that SMBH accretion does not reach the Eddington accretion rate. Also due to limited radius of the modeled disc most of the gas ($\sim 70\%$) escapes through the outer edge. Expanding the radius at which disc properties are being calculated is our future goal.

[1]Pringle J. E., 1981, ARAA, 19, 137

[2]Shakura N.I., Sunyaev R.A., 1973, A&A, 24, 337

[3]King A. R., Pringle J. E., Livio M., 2007, MNRAS, 376, 1740

WITHDRAWED CONTRIBUTION

Leadership phenomenon in the agent-based herding model

Aleksejus Kononovicius¹, Vygintas Gontis¹

¹Institute of Theoretical Physics and Astronomy, Vilnius University, Lithuania
aleksejus.kononovicius@gmail.com

It is often thought that endogenous interactions are behind many big spontaneous events observed in the complex socio-economic systems. Social cooperation, spontaneous emergence, formation of financial bubbles, financial flash-crashes and even mass panic may be caused by the endogenous dynamics and certain general similarities of human psychology [1, 2]. The tendency to rely on others, importance of social interactions, tight coupling suggests that it might be possible to influence the collective behavior of the complex socio-economic systems.

One of the suitable frameworks to test this idea is known as agent-based modeling [3, 4]. In this framework a generalized entity, known as agent, is used in place of real-life interacting parts of the modeled system. While the real-life interactions might be very complex, agents are frequently assumed to interact by following very simple rules. Despite the underlying simplification the complex collective behavior emerges as a result of the interactions between these agents.

In this contribution we consider agent-based herding model proposed by Alan Kirman [5], which explains herding behavior in ant colonies and is also successfully applied to other socio-economic scenarios [6]. Leadership can be introduced into this model rather simply by assuming that some of the agents occupy fixed states and may interact with every other agent in the system. In this case one agent transition probability (from state i to state j) takes the following form:

$$\mu(i \rightarrow j) = \left[\sigma_j + \frac{h}{N} X_j + h M_j \right] \Delta t,$$

here σ_j is the individual transition rate to state j , h is responsible for herding behavior transitions, M_j is a number of leaders in the j state. Note that Δt in the above should be small enough for only one transition to be probable.

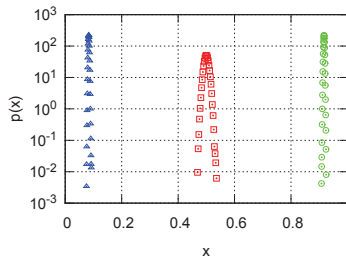


Fig. 1. Influence of the leaders on the stationary opinion distribution of the system (squares - $M_1 = M_2 = 0$, circles - $M_1 = 20, M_2 = 0$, triangles - $M_1 = 0, M_2 = 20$). There are 10^4 agents in the system. Other model parameters: $\sigma_1 = \sigma_2 = 2$, $h = 1$.

As you can see in the figure above the leaders, despite being only in a small number, are able to significantly impact the output of a large system. This result suggests some of the possible applications - one may facilitate spread of a new technology or product by donating it to influential individuals (e.g., government, journalists), central banks and market regulators could stop financial bubbles and crashes by initiating trades based on the economic fundamentals rather than plain speculation.

-
- [1] G. Akerlof, J. Shiller, *Animal Spirits: How Human Psychology Drives the Economy, and Why It Matters for Global Capitalism* (Princeton University Press, 2009).
 - [2] J. P. Bouchaud, Crises and collective socio-economic phenomena: Simple models and challenges, *Journal of Statistical Physics* **151**, 567-606 (2013).
 - [3] R. Conte et al., Manifesto of computational social science, *European Physics Journal Special Topics* **214**, 325-346 (2012).
 - [4] M. Cristelli, L. Pietronero, A. Zaccaria, Critical Overview of Agent-Based Models for Economics, *Proceedings of the School of Physics "E. Fermi"* **CLXXVI**, 235 - 282 (2012).
 - [5] A. P. Kirman. Ants, rationality and recruitment, *Quarterly Journal of Economics* **108**, 137-156 (1993).
 - [6] A. Kononovicius, V. Daniunas, Agent-based and macroscopic modeling of the complex socio-economic systems, *Social Technologies* **3**, 85-103 (2013).

INVESTIGANION ON HASH-ROUTING SCHEMES IN INFORMATION-CENTRIC NETWORKS

Petras Paulauskas

Department of General Physics and Spectroscopy, Vilnius University, Lithuania

petras.paulauskas@ff.stud.vu.lt

Information-centric networks (ICN) are overlay networks, where content is found not by the traditional addressing, but by the naming of the content. It forms a new approach of identification, addressing and caching of such content in the network. It is important how to search and transfer the content, but not how to connect clients to the network. When planning information-centric networks these three main questions occur: 1) the design of the new architecture of the network, 2) the distribution and caching of content in the network, 3) the mechanisms of request routing.

The main scope of this work was to construct the ICN with different caching properties and to investigate how the caches are used.

When designing placement of caches the main focus was the mechanism of request routing. There are two main routing and caching strategies in this setting: on-path and off-path. According to the on-path strategy, contents are cached as they travel through the network by any on-path cache or a subset of traversed caches [1]. Content requests are forwarded towards the content source, but are stopped at the first cache. When using the off-path strategy, content placement and request-to-cache routing operate according to predefined rules that assign contents to the caches. It could be implemented by *hash-routing*.

In this work, an information-centric network based on LITNET network topology and parameters was generated. *Icarus* program [2] was used to simulate this ICN. Five different routing schemes of off-path strategy and tree – on-path schemes were investigated in three different network scenarios to analyze hash-routing schemes in information-centric networks and compare the results of on-path to off-path strategies. Two main attributes were varied in the study: *cache to content population ratio* (C) (size of the network caches) and *content popularity distribution skewness* (α) (represented by the Zipf parameter). The impact of these variables on the cache-hit-ratio (number of requests for content, which reached the caches) and on the average link load (Fig. 1) was analyzed.

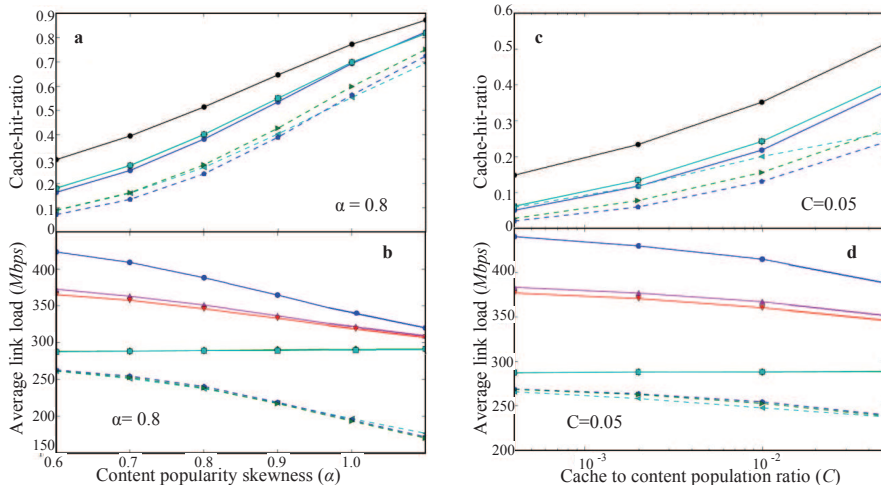


Fig. 1. The dependencies of cache-hit-ratio (a, c) and average link load (b, d) on α and C parameters. The marking of off-path schemes: \bullet HR Symm, \blacktriangle HR Multicast, \blacklozenge HR Asymm, \blacksquare HR Hybrid AM, \blacktriangledown HR Hybrid SM. The marking of on-path schemes: \blacktriangleleft ProbCache, \bullet Ubiquitous, \blacktriangleright CL4M.

The results (a, c) show that off-path routing schemes reach higher cache-hit-ratio than reached using on-path routing schemes. It means that using hash-routing schemes the caches were used more efficiently. However, the results (b, d) illustrate that the network load increases when using hash-routing schemes.

[1] L. Saino, I. Psaras, G. Pavlou, Hash-routing schemes for information centric networking, Proceedings of the 3rd ACM SIGCOMM workshop on Information-centric networking - ICN '13, Hong Kong, 27-32 (2013).

[2] Lorenzaino / icarus, <https://github.com/lorenzaino/icarus/> (2014-01-15).

INVESTIGATION OF ABSORPTION IN A FINITE SET OF CYLINDERS

Giedrius Tušinskis

Department of Theoretical Physics, Vilnius University, Lithuania

giedrius.tusinskis@ff.stud.vu.lt

The array of parallel cylinders is a convenient object while investigating complex structures, which possess properties that can be used in electronics. Structures from periodic cylinders - photonic crystals - are used in optics as elements of objects which control a beam. Photonic crystals of macroscopic elements are convenient because one can easily manipulate them without any special equipment and the requirements for the precision of processing of the surfaces are lower [1]. The problem of electromagnetic wave scattering by a finite cylinder set is once again interesting due to the possibility of modeling different type structures [2]. These structures should have perspective properties for their application in electronics and be made from materials with high absorption. Also further development should be made for the problems arising in the range of THz waves [3]. Absorption is important because it is highly affected by changes in the density and mobility of charge carriers inside a structural element of a photonic crystal. The main advantage is that the concentration of charge carriers and their mobility can be changed by altering the illumination, temperature, direct magnetic field. By doing this one can change the electrodynamical properties of the structure. Calculating techniques allow us to solve boundary problems of complex two-dimensional structures made from cylinders [4]. Another reason, which caused the renewed interest in scattering problems, is the creation of metamaterials and problems arising from their application in electronics.

After solving the boundary problem we find magnitudes of cylindrical waves. With a set of field values one can characterize the system with the required accuracy. It isn't convenient because we have to operate with large amounts of data. Here we investigate the energy absorbed and scattered per length unit per period of an array of cylinders placed equidistantly along axis x . While studying these parameters, with different electric properties of the cylinders, distance between the cylinders, the polarization and frequency of the wave, we try to deepen our knowledge of the phenomenon and hopefully find some kind of patterns.

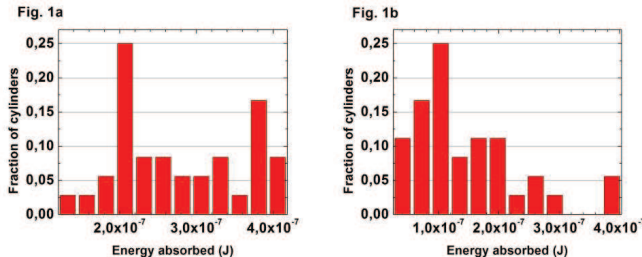


Fig. 1. Energy absorbed by fraction of cylinders per period per unit length with different polarization of the wave perpendicular (a) parallel (b).

Here we present the dependencies of the fraction of number of cylinders on absorbed energy per period per unit length for a set of $N=36$ identical cylinders placed along the direction of propagation of incident wave with perpendicular (a) and parallel (b) polarization of wave. The distance between centers of cylinders is 4.2 mm. One can see the close absorbed energy values can have different number of cylinders and an energy gap can occur (see Fig. 1b). The incident wave is a monochromatic linearly polarized plane wave. The cylinders under investigation are made from silicon, which has the permittivity $\epsilon_{Si}=11.8-i(\omega\epsilon_0\rho)$, here $\omega=2\pi f$, $f=12\text{GHz}$ (frequency of the incident wave), ρ - specific resistivity, $\rho=10\Omega\text{m}$. The radius of cylinder $R=2\text{mm}$.

- [1] F. J. Valdivia-Valero and M. Nieto-Vesperinas, Resonance excitations and light concentration in sets of dielectric nanocylinders in front of a subwavelength aperture. Effects on extraordinary transmission. Optics Express, Vol. 18, No 7, 6740 (2010).
- [2] J. D. Joannopoulos, S. G. Johnson, J. N. Winn, R. D. Meade. Photonic Crystals, Princeton university press (2008).
- [3] H. Toyama and K. Yasumoto, Electromagnetic scattering from periodic arrays of composite circular cylinder with internal cylindrical scatterers. Progress in Electromagnetics Research, PIER 52, 321-333 (2005).
- [4] A. K. Ozturk and R. Paknys Analysis of Propagation Between Rows of Conducting Cylinders That Model Solid Surfaces Using the Same Surface Area Rule. IEEE Transactions on Antennas Propagation, VOL. 60, NO. 5, 2602-2606, (2012).

MODELLING ELECTRONIC DENSITY OF STATES IN CARBON NANOTUBES

Jonas Narkeliūnas, Jevgenij Chmeliiov, Stepas Toliautas

Department of Theoretical Physics, Faculty of Physics, Vilnius University, Lithuania
Jonas.Narkeliunas@ff.stud.vu.lt

Carbon nanotubes are large molecular systems made entirely of carbon atoms. Structurally, they can be viewed as a graphene sheet rolled-up in some particular direction to make a tube. Since their discovery few decades ago, they have inspired a lot of theoretical and experimental studies as they show better electrical and mechanical properties than other ordinary materials [1]. One special feature that attracted a lot of attention was the dependence of the energy gap on the nanotube's diameter and geometry, which led to speculations that one day carbon nanotubes could replace silicon transistors. In this research, we performed various calculations concerning the density of states in carbon nanotubes, from which the energy gap can be calculated.

The goal was to check whether or not including additional neighbouring atoms in the tight-binding model increases accuracy of energy dispersion relations. Our work was based on the fifth-nearest-neighbour tight-binding (5NNTB) description of electronic structure of graphene [2] which proved to be more accurate than previous models. We expected to see similar improvements when applied to carbon nanotubes, though we ignored curvature effects on σ bonds and relative position of atoms. Using zone-folding method [3], we obtained energy dispersion relations for carbon nanotubes, which were compared with results obtained by Density Functional Theory (DFT) implemented in *Vienna Ab-initio Simulation Package* [4, 5]. The results showed great improvements when the influence of more distant atoms was taken into account. As shown in Fig. 1, in this case the form and position of van Hove singularities resembles those obtained from DFT calculations.

Moreover, after analyzing carbon nanotubes of different diameters, we concluded that all carbon nanotubes with diameter less than 8 Å have a degeneracy point between the conduction and valence bands due to distortion of the σ bonds. Also, we found that the energy gap is inversely proportional to nanotube's diameter. Hence the new tight-binding model is good improvement from earlier models and is a good approximation for those carbon nanotubes that have small curvature.

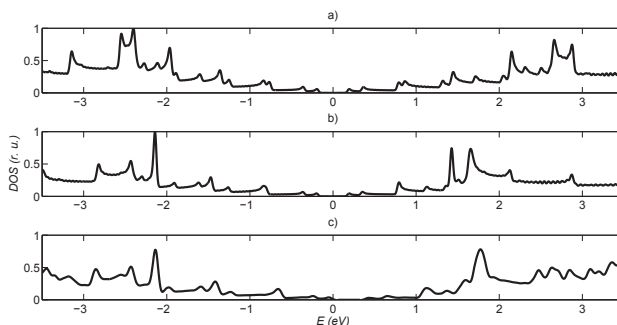


Fig. 1. Electronic density of states of carbon nanotube (27,0). Calculated using: a) 3NNTB model; b) 5NNTB model; c) DFT.

-
- [1] A. Jorio, G. Dresselhaus, M.S. Dresselhaus, *Carbon Nanotubes: Advanced Topics in the Synthesis, Structure, Properties and Applications* (Springer, 2007).
 - [2] Y. Jing-Han, J. Wei-Wei, L. Er-Qiang, P. Tian-Song, Z. Yuan-Yuan, W. Hui, Fifth-nearest-neighbor tight-binding description of electronic structure of graphene, *Commun. Theor. Phys* **53**, 1172-1176 (2010).
 - [3] S. Reich, C. Thimsen, J. Maultzsch, *Carbon Nanotubes* (WILEY-VCH, 2004).
 - [4] G. Kresse, J. Hafner, Norm-Conserving and ultrasoft pseudopotentials for first-row and transition-elements, *J. Phys.: Condens. Matter* **6**, 15 (1996).
 - [5] G. Kresse, J. Hafner, Efficient iterative schemes for ab initio total-energy calculations using a plane-wave basis set, *Phys. Rev. B* **54**, 11169 (1996).

Open Readings 2014. 57th Scientific Conference for Students of Physics and Natural Sciences

MOLECULAR DYNAMICS SIMULATIONS OF ATOMIC IONS IN AQUEOUS SOLUTION

Kristina Jakubavičiūtė, Kęstutis Aidas

Dept. of General Physics and Spectroscopy, Faculty of Physics, Vilnius University, Lithuania
kristina.jakubaviciute@ff.stud.vu.lt

Molecular dynamics simulation is one of the most detailed molecular simulation methods for calculating the movement of each individual particle in a complex system. Newton's equations of motion along with periodic boundary conditions are solved for a very high number of particles in order to obtain information about systems' structural changes and the dynamic and thermodynamic properties. The advantage of this method is that it provides a detailed evolution of the chemical system in a cost effective manner. We have used MOLSIM software for molecular dynamics simulations in this work.

Classical molecular dynamics simulations of Na^+ , Li^+ , Mg^{+2} , Al^{+3} and Cl^- ions in aqueous solution were considered to investigate the distribution and dynamics of water molecules in the near-ions environment. In addition, we have studied the dependence of the structure of distribution of water molecules on the type of the applied force field. Two types of potentials were considered: (i) Coulomb's and Lennard-Jones and (ii) Coulomb's and Lennard-Jones polarizable potential. Following force fields for the water were selected: non-polarizable TIP3P [1], TIP4PEw [2], TIP5P [3] and polarizable Ahlstrom [4], POL3 [5] and modified Ahlstrom force fields.

During molecular dynamics simulations radial distribution functions and coordination numbers were computed. Simulated coordination numbers of Na^+ and Li^+ cations are in good agreement with experimental data. The coordination number of sodium is between 5-6. In lithium case, the water molecules of the first solvation layer tend to distribute in a tetrahedral shape, and the coordination number of Li^+ is 4. The intensity of the first peak in radial distribution function depends on the choice of the force field, although radial distribution function is found to have similar shape in all cases, see Fig. 1.

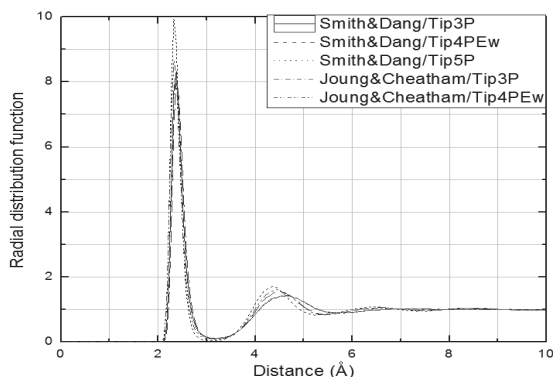


Fig. 1. Simulated Na-O radial distribution function for the different force fields applied.

Distribution of water molecules is more structured in the cases of magnesium and aluminum than in the cases of monovalent Na^+ and Li^+ ions. This is due to the higher cationic charge. Water molecules in the solutions of Mg^{+2} and Al^{+3} migrate from the first solvation layer to the second (and vice versa) less frequently. Coordination numbers of both magnesium and aluminum were found to be 6. The best agreement with the experimental data for magnesium was obtained by using the TIP5P water potential of Allner et al. [6].

The coordination number of Cl^- anion was found to be 6,7. It slightly varies depending on the chosen type of the force field.

[1] Jorgensen W. J. Am. Chem. Soc, 1981, **103**, 335-340.

[2] Horn H., Swope W., Pitera J., Madura J., Dick T., Hura G. Head-Gordon T. J. Chem. Phys, 2004, **120**, 9665-9678.

[3] Mahoney M., Jorgensen W., J. Chem. Phys, 2000, **112**, 8910-8922.

[4] Ahlstrom P., Wallqvist A., Engstrom S., Johnsson B. Molecular Physics, 1989, **68**, No. 3, 563-581.

[5] Caldwell J., Kollman P. J. Phys. Chem, 1995, **99**, 6208-6219.

[6] Allner O., Nilsson L., Villa A. J. Chem. Theory Comput, 2012, **8**, 1493-1502.

TUNABLE LIEB AND KAGOME LATTICES FOR ULTRA-COLD YTTERBIUM ATOMS

Mantas Račiūnas^{1,2}, Giedrius Žlabys^{1,2}, Egidijus Anisimovas^{1,2}

¹Faculty of Physics, Vilnius University, Lithuania

²Institute of Theoretical Physics and Astronomy, Vilnius University, Lithuania
mantas.raciunas@tfai.vu.lt

By combining multiple laser beams a standing wave pattern of laser intensities can be created, which, when filled with ultra-cold atoms acts as a periodic potential. This potential can be easily tuned by changing the corresponding intensities of laser beams. In this work we are studying Lieb and Kagome lattices.

Formerly the Lieb lattice has been constructed by using laser beams with 12 different wave vectors [1] in our work a new way to create optical Lieb lattice was proposed by superimposing two square lattices (with in-plane and normal polarizations) with 4 wave vectors each, thus simplifying the experimental setup (Fig 1). The resulting potential consists of corner sites at minimum and line-center sites at maximum.

Ytterbium atoms feel different potential sign according to their internal state, thus an antimagic wavelength is chosen so that the atoms in ground and excited states would be trapped in line-center and corner sites of the primitive cell respectively.

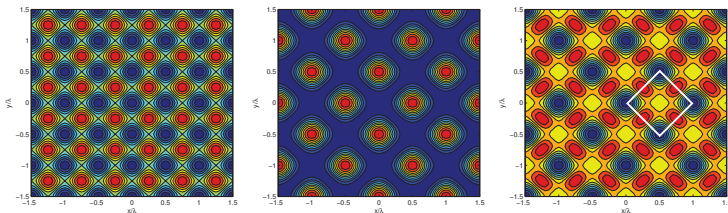


Fig. 1. Superimposing the interference patterns obtained from the in-plane (a) and normal (b) polarization channels one produces the Lieb lattice (c) trapping different internal states in corner and line-center sites. Blue (red) color corresponds to low (high) intensity.

In order to analyse these periodic systems it is useful to employ the Wannier representation. It provides essentially a real-space picture of localized orbitals which can be applied for studying chemical bonds, local and global dielectric properties and developing model Hamiltonians [2]. Here we concentrate on the latter - using maximally-localized Wannier functions[3] the hopping parameters for the Lieb lattice are calculated from first principles with different laser intensities. These parameters are then used to determine the optimal conditions for constructing the Kagome lattice and to check if the tight-binding approximation is valid. Band structure can be obtained by solving the eigenvalue equation for the model Hamiltonian with parameters of our choice.

-
- [1] J. C. Everts, *Topological phases and fermionic superfluidity on the Lieb lattice*, Faculty of Science, Utrecht University (2012).
 - [2] N. Marzari et al., *Maximally localized Wannier functions: Theory and applications*, Rev. Mod. Phys. **84**, 1419-1475 (2012).
 - [3] R. Walters et al., *Ab initio derivation of Hubbard models for cold atoms in optical lattices*, Phys. Rev. A **87**, 043613 (2013).

SIMULATION OF THE INTENSITY SPECTRUM OF AUTOIONIZING STATES OF RUBIDIUM ATOM EXCITED BY ELECTRON IMPACT

Gintaras Kerevičius

Department of Theoretical Physics, Faculty of Physics, Vilnius University, Saulėtekio Ave. 9, LT-10222, Vilnius, Lithuania
gintaras.kerevicius@ff.stud.vu.lt

The autoionizing states (AS) of Rb atom are located between lowest $4p^6\ ^1S_0$ and first excited $4p^5(4d, 5s)$ states of Rb ion [1]. For Rb atom this corresponds to the energy interval (15 – 21) eV and the distance between AS is of the order (10 – 100) meV. This fact makes the analysis of AS difficult in general and the identification of the respective experimental spectra [2] should be taken with great care based on the expected unambiguous classification of the respective theoretical spectra [3]. The experimental spectra of the AS of alkali metal atoms excited by electron impact are measured by registering the so called Auger electrons.

Commonly the experiment is performed by setting the initial electrons and atoms unpolarized. But after the collision of atoms with electrons, the core excited states (AS) of atoms become polarized. This polarization is described by alignment parameters A_K [4], which determine a different probability for atomic electron to occupy AS magnetic states defined by the absolute value of magnetic quantum number. The alignment parameters A_K are the main part which determine the asymmetry of Auger electrons ejected from AS [5].

The lifetime of the AS is finite, therefore the atom will decay to a lower energy state. The atom has two significant decay channels, i. e. ejecting an Auger electron or emitting a photon. Based on our calculations the radiative decay of AS of Rb is highly improbable with a probability 3 to 4 orders of magnitude lower compared to autoionization. The Auger decay of AS of Rb is energetically possible only to the lowest energy ion state $4p^6\ ^1S_0$. Then absolute values of parameters describing the angular distribution asymmetry of Auger electrons – α_K [4] are approximately equal to 1 [3]. All in all, the parameter which describes the angular distribution of Auger electrons ejected from AS is as follows [4]:

$$\beta_K = A_K \cdot \alpha_K. \quad (1)$$

In order to simulate a proper intensity spectrum of AS of alkali metal atoms excited by electron impact one needs to calculate the atomic structure parameters described further. These parameters were calculated in previous work [3]. The energy spectra of AS of Rb atom was used to determine the peak positions of spectral lines, excitation cross sections of AS were used to determine maximum intensity values of respective spectral lines and autoionization probabilities were needed to determine the width of these lines. Radiative decay probability was not needed for the reasons mentioned above. To account for the asymmetry of the angular distribution of Auger electrons ejected from the electron impact excited AS, alignment and asymmetry parameters were used also.

Using all these as a part of input parameters a program 'Spectrum' was written with 'Python' programming language. Another part of input parameters was a digitized experimental spectra [2]. This program calculates theoretical and draws theoretical and experimental spectra of atomic states in general. A theoretical intensity spectra of the AS of Rb atom excited by 27 eV electrons and observed at 75° polar angle will be calculated and plotted. The intensity spectrum with and without the asymmetry of angular distribution of Auger electrons ejected from AS will be plotted together with a digitized experimental spectra [2] for comparison (output of the program 'Spectrum').

-
- [1] O. Laporte, G. R. Miller and R. A. Sawyer, The First Spark Spectrum of Rubidium (Rb II), *Phys. Rev.* **38**, 843–853 (1931).
 - [2] V. Pejcev, D. Rassi, K. J. Ross and T. W. Ottley, High-resolution ejected-electron spectrum of rubidium vapour autoionising levels excited by electrons with kinetic energies in the range 27 to 400 eV, *J. Phys. B: At. Mol. Phys.* **10**, 1653–1659 (1977).
 - [3] A. Kupliauskienė and G. Kerevičius, Theoretical study of the $4p^5nl'n'l'$ autoionizing states of Rb excited by electron impact, *Phys. Scr.* **88**, 065305(7pp) (2013).
 - [4] A. Kupliauskienė and V. Tutlys, Properties of Auger electrons following excitation of polarized atoms by polarized electrons, *Nucl. Instr. and Meth. B* **267**, 263–265 (2009).
 - [5] S. Kaur and R. Srivastava, Excitation of the lowest autoionizing $np^5(n+1)s^2$, $^2P_{3/2,1/2}$ states of Na($n=2$), K($n=3$), Rb($n=4$) and Cs($n=5$) by electron impact, *J. Phys. B: At. Mol. Opt. Phys.* **32**, 2323–2342 (1999).

STUDY OF THE SPECTRAL MANIFESTATIONS OF INTRAMOLECULAR HYDROGEN BOND FORMATION IN THE MALONALDEHYDE MOLECULE.

Ol'ga Novichenok, Alena Mel'nikova, George Pitseвич

Department of Physical Optics, Belarusian State University, Belarus.

one-heartbeat@bk.ru

Malonaldehyde molecule is a toughie for experimental methods for determining the frequency of the stretching vibrations of the hydroxyl group involved in the formation of an intramolecular hydrogen bond. That is why the theoretical methods of investigations are very important in this case.

We have found the equilibrium geometry and calculated IR spectra of this molecule using B3LYP/cc-pVDZ, B3LYP/cc-pVTZ and B3LYP/cc-pVQZ approximations. In all cases IR spectra were calculated in harmonic and unharmonic approach. It was found that there is strong interaction between stretching O-H bond and one of C-H bond vibrations. Due to this fact the harmonic wavenumber for $\tilde{\nu}_{OH}$ is 3118.2 cm^{-1} . In potential energy distribution (PED) of this mode there are two terms - $71.0\% q_{OH} + 26.6\% q_{CH}$. On the other hand harmonic wavenumber for $\tilde{\nu}_{CH}$ is 3174.0 cm^{-1} . As kinematic interaction between this internal coordinates is absent we have to assume that there is force interaction in this case. Really, we have found that off-diagonal force constant, describing this interaction was found to be -0.066 mdyn/\AA . In PED of this mode there are two terms too - $26.3\% q_{OH} + 70.1\% q_{CH}$. To find the harmonic wavenumber for $\tilde{\nu}_{OH}$ without force interaction we slightly changed Hessian removing interaction between hydroxyl and C-H hydrogen atoms. This decreased off-diagonal force constant $k_{OH/CH}$ up to 0.003 mdyn/\AA . So unperturbed wavenumber and PED of $\tilde{\nu}_{OH}$ are 3130.8 cm^{-1} and $97.4\% q_{OH} + 0.2\% q_{CH}$. So, one can see that interaction between stretching O-H bond and one of C-H bond vibrations leads to red shift of $\tilde{\nu}_{OH}$.

Using B3LYP/cc-pVQZ approximations 1D and 2D potential energy surfaces were calculated (Fig.1).

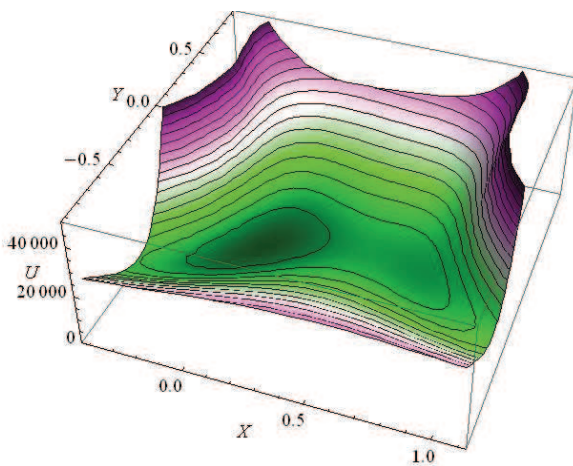


Fig. 1. 2D PES for malonaldehyde molecule.

We were able to calculate wavenumbers of O-H group vibrations using PES by numerical solving of the Schrödinger equation. They were compared with results of unharmonic calculations of malonaldehyde IR spectra in the same approximation.

WITHDRAWED CONTRIBUTION

THE QUANTUM MECHANICAL MODELING OF INTERACTION BETWEEN FRAGMENT OF BACTERIAL CELL WALL AND SILICON SURFACE

Veranika Burko¹, Yana Douhaya², Anastasiya Berezhnaya³

¹Belarusian State University of Informatics and Radioelectronics, Minsk, Belarus

²Belarusian National Technical University, Minsk, Belarus

³Institute of Microbiology of National Academy of Science, Belarus
veranika.burko@gmail.com

For applying with the most efficiency biological preparations must meet the strict storage conditions. This problem can be solved by using as a "container" for the storage and transport of bacteria porous materials such as porous silicon. The advantage of porous material is the ability to provide a relatively constant conditions within the pores, allowing bacteria in such a pore to be isolated from the environment. This allows to extend the shelf life of the drug and to exclude fermentation process.

Bacillus subtilis are a group of Gram positive, spore-forming, aerobic bacteria. Morphological features: the vegetative cells of culture represent sticks bacillary form of a size $0,6-0,7 \times 1,0-1,3$ microns with rounded ends. Experimental studies showed that using of porous materials as carriers for inoculum leads to concentration of spores in obtained in this way biopreparation $1,3 \times 10^9/\text{ml}$, which is 32% higher than with conventional inoculum.

For theoretical investigation of the interactions mechanism *B. subtilis* with porous silicon, the structure of the cell wall of Gram-positive bacteria, consisting mainly of murein chains, is considered. Chemically active fragments was determined given the orientation of the biomolecules to the substrate. Special attention evokes the presence of oxygen in these fragments having a double bond to the carbon. Because a π -bond is weaker than σ -bond, it may take part in the interaction with the substrate. In this case, we can assume the presence of the following most probable formation mechanisms of a new bond between oxygen and substrate: direct interaction of oxygen with silicon (C-O-Si); interaction of oxygen with hydrogen bonded to silicon substrate (C-O-H-Si) (Fig. 1). Important to note that in the second case the hydrogen bond formation is possible.

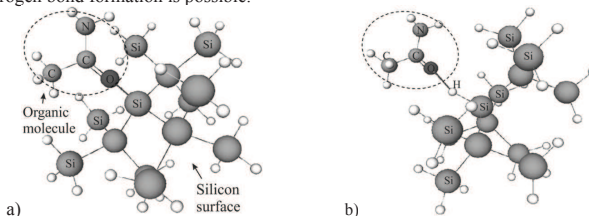


Fig. 1. Interaction mechanisms: a) C-O-Si; b) C-O-H-Si.

To carry out quantum mechanical modeling using SCF (self-consistent field theory) was applied the program NWChem, which operates within the graphical environment ECCE. For atoms directly interacting in the reaction was used the basis 6-31G *, for the rest - 3-21G.

Simulation results showed that in the case of directly interaction between the substrate and molecule minimum of the binding energy is observed when the distance between them is about 0,168 nm (Fig. 2, a). This means that in this case bond formation takes place. In the case of interaction through hydrogen atom, the interaction energy decreases when the distance between the molecules increases. (Fig. 2, b). This means that interaction mechanism C-O-H-Si does not lead to formation of any covalent or hydrogen bonds. Thus, these results allow the conclusion that the bacterium is immobilized by the formation of chemical bonds on the silicon substrate, provided that the surface of the substrate free from hydrogen.

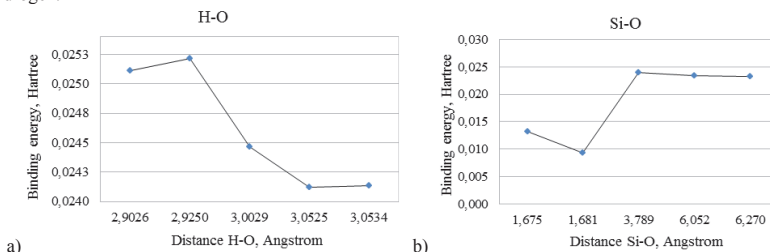


Fig. 2. Dependencies binding energy a) Si-O (mechanism C-O-Si), b) HO (mechanism C-O-H-Si) of distance.

Author index

A

Abbas, Saulė.....158
 Abramavičius, Darius91
 Abromaitis, Vytautas191
 Adomėnas, Povilas.....26
 Adomėnienė, Ona.....26
 Aidas, Kęstutis.....81, 205
 Akalovich, Svetlana178
 Aleknavičius, Justinas.....30
 Aleksa, Valdemaras.....85, 86, 87, 106
 Aleksiejūnas, Ramūnas124
 Alster, Jan91
 Andrijauskas, Tomas54
 Andrzejewska, Weronika165
 Andrzejewski, Bartłomiej149
 Andzane, Jana38
 Anisimovas, Egidijus.....206
 Aniskevich, Andrey147
 Arbačiauskienė, Eglė97
 Astrauskas, Ignas161

B

Babrauskas, Giedrius87
 Bagdonas, Darius158
 Bagdonas, Saulius46, 163
 Baguckis, Artūras139
 Bakšytė, Sandra172
 Balčiūnas, Ignas.....62, 63
 Baltmiškytė, Ingrida106
 Baltrušaitis, Jonas192
 Banys, Jūras114, 115
 Baranauskienė, Lina.....172
 Baranska, Małgorzata90
 Barkauskas, Jurgis104
 Barre, Maud41
 Bašinskaitė, Eglė91
 Belko, Nikita.....45
 Bellucci, Stefano114
 Berezhnaya, Anastasiya210
 Bergamini, Silvia54
 Bertašius, Valentas56
 Berzinš, Jonas.....72, 73, 158
 Beterov, Ilya I.54
 Biekša, Tomas163
 Bieliauskas, Aurimas97
 Bieniek, Maciej.....34
 Błazyk, Małgorzata33
 Blaževič, Dominyka89
 Bogdan, Michal198
 Borisova, Anna.....147
 Botyriūtė, Aklvilė184

Brazevič, Sabina183
 Brazilius, Gediminas.....102
 Bričkus, Dominykas16
 Bružas, Edmudas.....152
 Buchwald, Tomasz28, 176
 Budriūnas, Miglius158
 Budriūnas, Rimantas.....62, 63, 64
 Bukauskas, Virginijus32, 151
 Bulai, Pavel200
 Burko, Veranika210
 Burokas, Raimundas97, 99
 Burov, Leonid.....17
 Buscaglia, Vincenzo115
 Butkus, Vytautas.....2, 91, 158
 Butkutė, Renata31
 Butsen, Andrei23
 Buynevich, Ilya189
 Byčenkienė, Steigvilė190

C

Čapkauskaite, Edita.....44
 Celzard, Alain114
 Čeponis, Tomas.....118, 119
 Cerane, Daiga.....169
 Čerkauskaitė, Aušra70
 Černiukė, Irina132
 Cesiulis, Henrikas105
 Chmeliov, Jevgenij204
 Chruszcz-Lipska, Katarzyna90
 Čibiraitė, Dovilė186
 Cikmács, Peteris169
 Cojocar, Crina67

D

Dabašinskas, Laurynas142
 Dagys, Laurynas80
 Danielius, Romualdas59
 Dapkute, Dominyka47
 Dargis, Donatas.....120
 Dargis, Rytis117
 Dauderis, Gediminas.....161
 Dementev, Alexander16
 Dichenko, Yaroslav.....171
 Didžbalis, Andrius150
 Dmitrochenko, Alesya.....182
 Dmukauskas, Mantas.....129
 Dormeshkin, Dmitri180
 Douhaya, Yana210
 Dovgal, Darya107
 Dudoitis, Vadimas188, 190
 Dudutiene, Virginija179
 Dudutienė, Virginija173

Dudutis, Juozas74
 Dūsing, Jan76
 Duškesas, Grigorijus.....83
 Dzedzic, Bartosz194
 Dzmitryevich, Yekelchik Michail ...181

E

Egierska, Paulina165
 Eidikas, Paulius141
 Eikevičius, Adomas113
 Ene, Daniela193
 Entin, Vasilii M.54
 Erts, Donats38

F

Fedorovič, Julija189
 Fomich, Maksim.....178

G

Gabrytė, Eglė59
 Gailevičius, Darius67
 Garbaras, Andrius83, 152
 Garliauskas, Mantas83
 Gaubas, Eugenijus.....118, 119
 Gavutis, Martynas.....49
 Gawarecki, Krzysztof.....137
 Gečys, Paulius74, 75
 Gedvilas, Mindaugas.....72
 Gėgžna, Vilmantas.....187
 Gertnere, Zanda.....144
 Gertners, Ugis144
 Getautis, Vytautas97
 Gilep, Andrei.....180
 Girsks, Justinas.....158
 Gontis, Vyngintas.....201
 Gorbatevič, Alexander17
 Grajek, Magdalena183
 Grazulis, Saulius179
 Gričius, Žygimantas.....101
 Grigalaitis, Robertas115
 Grigalevičius, Saulius93
 Grigaliūnaitė-Vonsevičienė, Gražina....132
 Grill, Roman116
 Grinys, Tomas117
 Gruodis, Alytis.....25
 Grybauskas, Martynas158
 Grześkiewicz, Bartłomiej.....24
 Gudelis, Arūnas.....83
 Gunes, Veyis41
 Gustainyte, Ausra95

Gylyte, Joana.....	179
Gylytė, Joana.....	173

H

Heintzmann, Rainer	21
Hliatsevich, Maryna	200
Holmes, Justin D.	38
Hovorun, Dmytro M.	209

I

Ignatjev, Ilja	87
Imbrasas, Paulius	25
Irina, Vashkevich	180
Ivanov, Maksim.....	40

J

Jakubavičiūtė, Kristina	205
Jankauskas, Vygtintas.....	25, 26
Jankūnaitė, Dalia	192
Janonis, Vytautas	121
Janulevičius, Gytautas.....	103
Jarmalaitė, Sonata	164
Jarmalavičius, Darius.....	189
Jarockytė, Greta	162
Jarockytė, Rimantė	63
Jasiūnas, Arnoldas	118, 119
Jonušauskas, Linas	20
Jovaišaitė, Justina	98
Jurga, Stefan	149
Jurkūnas, Nerijus.....	158
Jurkus, Karolis	161
Juršėnas, Saulius	25, 26, 27, 97, 98
Juškevičius, Kęstutis.....	78

K

Kačėnauskaitė, Laura	96
Kaczor, Agnieszka.....	90
Kadys, Arūnas	129
Kalnaitytė, Agnė	46
Kalpakovaitė, Agnė	117
Kalvelytė, Justina	150
Kamarauskas, Mindaugas	151
Karpavičius, Linas	65
Karpicz, Renata	93
Kašalynas, Irmantas	123
Kavalenka, Alena	48, 170
Kavalenka, Sophy	45, 48
Kazakevičius, Rytis	196
Kazbekova, Ainagul	177
Kazlauskas, Karolis	26, 97
Kaźmierczak, Małgorzata	149
Kazokaitė, Justina	173
Kerevičius, Gintaras	207
Kišonaitė, Miglė	44
Komar, Olga	133, 134
Komskis, Regimantas	26

Konieczna, Izabela	174
Kononovicius, Aleksejus.....	52, 201
Kopyciuk, Tomasz	183
Kościński, Łukasz	33
Kosmaca, Jelena.....	38
Kotkowiak, Michał	24, 146
Kowalczyk, Dorota	148
Kozadaev, Konstantin	79
Kozak, Maciej.....	165
Kozlova, Olga	135, 136
Kozlovskaya, Ekaterina	108
Kranauskaitė, Ieva.....	114
Kravicov, Oleg	127
Kreiza, Gediminas	97
Krot, Vladimir.....	167
Krugly, Edvinas.....	192
Kruhlik, Aliaksandr	178
Krumina, Gunta.....	169
Kryuchkov, Nikita	197
Kučinskas, Dainius.....	64
Kudaibergen, Marzhan	177
Kuksėnaitė, Gintarė	158
Kulnickas, Mantas	158
Kunakova, Gunta	38
Kuokštis, Edmundas	127

L

Lastovski, Stanislav	140
Laužadis, Justas	123
Ławniczak, Paweł.....	110
Lengvinaitė, Dovilė	81
Levchuk, Elena	140
Lewandowski, Mikołaj	33
Liaugaudas, Gediminas	120
Lisiecki, Filip	154
Loban, Valeriy	48
Łuciński, Tadeusz	33
Łukawski, Damian	33
Lukenskas, Adomas	39
Lukoševičius, Laurynas.....	69

M

Machnikowski, Paweł	137
Mackevičiūtė, Dovilė.....	68
Mackoit, Agnieszka.....	164
Mackoit, Mažena	125
Macutkevič, Jan	114
Madeikis, Karolis	112
Mahilny, Vladimir	21
Maigyte, Lina	67
Makarenko, Leonid	140
Makauskas, Benas.....	60
Malevich, Alex.....	108, 109
Malinauskas, Mangirdas	20, 67, 68, 69
Malinauskas, Tadas	130
Manakova, Elena	179
Maneikis, Andrius	132

Marcinkevicius, Benjaminas	193
Marcinkevičiūtė, Agnė	58
Markauskas, Edgaras	18
Maršalka, Arūnas	82
Martuzevičius, Dainius.....	192
Matijošytė, I.....	166
Matsukovich, Hanna S.	175
Matukas, Jonas	186
Matulienė, Jurgita	173
Matulis, Daumantas. 44, 172, 173, 179	
Mažulė, Lina.....	77
Mekys, Algirdas.....	139
Melnikova, Alena	208
Meškauskaitė, Dovilė.....	118, 143
Meškauskas, Donatas	142
Miasojedovas, Arūnas	99
Michailova, Ksenija	185
Michailovienė, Vilma	172
Michalak, Natalia	33
Mickevičius, Jūras	124
Mickevičiūtė, Aurelija	172
Mielnik-Pyszcorski, Adam	137
Mikitichuk, Alena	79
Miliniavičiūtė, Goda.....	173
Miłos, Zygmunt	33
Miłos, Katažyna	185
Minkevičius, Linas	112
Minko, Anatolij	107
Mironas, Audružis.....	32
Mitoseriy, Liliana	115
Mituś, Antoni	53
Mordas, Genrik	188
Muravitskaya, Alina	94
Musiienko, Artem	116

N

Nanni, Paolo	115
Narkeliūnas, Jonas	204
Narmontas, Andrius.....	61
Naskret, Michal	155
Naujalis, Rokas.....	199
Navikas, Vytautas	49
Nazarov, Sergey	21
Nevedomskaitė, Ugnė	158
Nguyen, Thi Dieu Lien	170
Nomeika, Kazimieras	126
Nordström, Birgitta.....	56
Norkūnas, Algirdas.....	131
Novichenok, Olga	208
Novičkovas, Algirdas	139

O

Oginskis, Antanas Kleopas	132
Oleg, Sviridov	180
Ozerenskis, Domantas	85, 86

P

Pačebutas, Vaidas	31
Paipulas, Domas	70, 71, 77
Paluch, Emil	174
Pankiewicz, Radosław	110
Paulauskas, Evaldas	158
Paulauskas, Petras	202
Pauraitė, Julija	190
Paurazaitė, Simona	122
Pausas, Anete	169
Pavlov, Jevgenij	119
Pawlik, Grzegorz	53
Peckus, Martynas	67
Petersons, Gvido	38
Petris, Adrian	19
Pitlik, Taras	200
Pitsevich, George	107, 108,
.....	109, 156, 208
Pleshko, Nadya	167
Plukis, Artūras	193
Podlipskas, Žydrūnas	124
Pogorzelec-Glaser, Katarzyna	110, 149
Popescu, Silviu T.	19
Popov, Vladislav	48, 66
Potanina, Elina	144
Pralgauskaitė, Sandra	186
Protsenko, Iryna O.	209
Ptaszyński, Krzysztof	24
Pučetaitė, Milda	82, 89
Pudžiuvytė, B.	166
Puišys, Audrius	71
Puodžiūnas, Tomas	77
Pupienis, Donatas	189
Purlys, Vytautas	67

R

Rachocki, Adam	110
Račiukaitis, Gediminas	72
Račiūnas, Mantas	206
Račys, Viktoras	192
Radiūnas, Edvinas	92
Radosz, Wojciech	53
Raišys, Steponas	92, 99
Ramanenka, Andrey	94
Razgute, Maria	158
Reklaitis, Ignas	77
Rekštytė, Sima	68
Remeikis, Vidmantas	152
Rimeika, Romualdas	150
Rimkus, Renaldas	25
Robak, Elzbieta	146
Rodin, Aleksej	16
Romero, Elisa Gonzalez	95
Rotomskis, Ricardas	47
Rotomskis, Ričardas	46, 96, 162
Rožek, Piotr	195
Rudaya, Oksana	156

Rumskaitė, Inga	191, 192
Ruseckas, Julius	52, 196
Ryabtsev, Igor I.	54

S

Sabirovaitė, Reda	106
Šablinskas, Valdas	89
Sabonis, Deividas	158, 161
Sabulis, Kostas	55
Šačkus, Algirdas	97
Sakanas, Aurimas	115
Sakavičius, Andrius	138
Šalkus, Tomas	41
Santos, Isabel Pastoriza	95
Sasnauskas, Kasperas	16
Šatas, Laurynas	41
Sedlina, Jolanta	192
Seitebmetov, Talgat	177
Serevičius, Tomas	25, 26
Šerkšnytė, Laura	158
Šetkus, Arūnas	32, 151
Shabunya-Klyachkovskaya, Elena V.	175
Shmanai, Vadim	178
Šiekštelė, R.	166
Sirutkaitis, Valdas	77
Skaigiris, Rokas	27
Skardžiūtė, Lina	98
Šikūnaitė, Evelina	104
Skliutas, Edvinas	158
Skupin, Michalina	165
Šlėkaitė, Akvilė	96
Šliachtich, Svetlana	166
Sliaptso, Yauheni	109
Smirnov, Alexey	179
Smirnovas, Vytautas	184, 185
Smolarkiewicz, Iga	110
Sokolov, Eugene	17
Staliūnas, Kestutis	67
Stańczuk, Martyna	28, 176
Stanionytė, Sandra	130
Stanislauskas, Tomas	62
Stanislauskas, Tomas	65
Stanislovaitis, Paulius	61
Stankevičiūtė, Jurgita	187
Stankevičiūtė, Karolina	58
Stankevičiūtė, Rūta	42
Stašys, Karolis	31
Stempiński, Piotr	174
Stempitsky, Viktor	135
Steponkevičius, Kęstutis	60
Steponkienė, Simona	47
Stonkutė, Edita	56
Straigis, Šarūnas	63, 65
Streckaitė, Simona	93, 158
Striokaitė, Greta	158
Subačius, Andrius	78
Šuminas, Rosvaldas	58

Sutkaitis, Mindaugas	82
Symonowicz, Joanna	157
Szczepańska, Alicja	148
Szczepańska, Dorota	148
Szulakowska, Ludmiła	153
Szyperski, Piotr	168

T

Tamaševičiūtė, Elena	51
Tamošiūnas, Vincas	139
Tarasenka, Natalie	23
Tarasov, Dmitry	45
Tautvaišienė, Gražina	56
Teteris, Janis	144
Tichonovas, Martynas	192
Timm, David D.	179
Toliautas, Stepas	204
Tolstik, Alexei	21
Tolstik, Elen	21
Tomašiūnas, Rolandas	77
Treideris, Marius	151
Tretjakov, Denis B.	54
Trimailovas, Justas	35
Tritt-Goc, Jadwiga	110
Trull, Jose	67
Tumėnas, Saulius	113, 122
Tumkevičius, Sigitas	98
Tušinskis, Giedrius	203

U

Ulevicius, Vidmantas	190
Ulevičius, Vidmantas	188
Urban, Barbara	165
Urbanavičiūtė, Rūta	158
Usanov, Sergei	171
Usanov, Sergey	180

V

Vaitekoniš, Šarūnas	49
Vaitkevičius, Augustas	128
Vaitkuvienė, Aurelija	187
Valentinavičienė, Rasa	158
Valiokas, Ramūnas	49
Valkūnas, Leonas	91
Valušis, Gintaras	112
Varanavičius, Arūnas	62, 63, 64, 65
Vaškėlis, Šarūnas	32
Velička, Martynas	88
Venckevičius, Rimvydas	123
Vengalis, Bonifacas	132
Vengelis, Julius	58
Vengris, Mikas	59
Vernickaitė, Edita	105
Vinčiūnas, Antanas	75, 76
Vitta, Pranciškus	35
Vlad, Valentin I.	19
Vorobel, Vit	37

W

Wolak, Joanna.....	165
Wozniak, Tomasz	159

Y

Yakshina, Elena A.	54
Yantsevich, Aleksei	171
Yantsevich, Alexei	182
Yasunas, Aleksandr	133
Yavkin, Nikita	84
Yermalovich, Anton	145

Z

Zabłocki, Konrad	174
Zajac, Grzegorz	90
Zakalskis, Konstantinas	83, 152
Žalga, Artūras.....	42, 100, 101, 102, 103, 131
Zarrelli, Mauro	147
Žeimys, Ernestas	60
Zelenina, Maria.....	135
Ženovienė, Renata	56
Zięba, Sylwia	28, 176
Zigmantas, Donatas	91

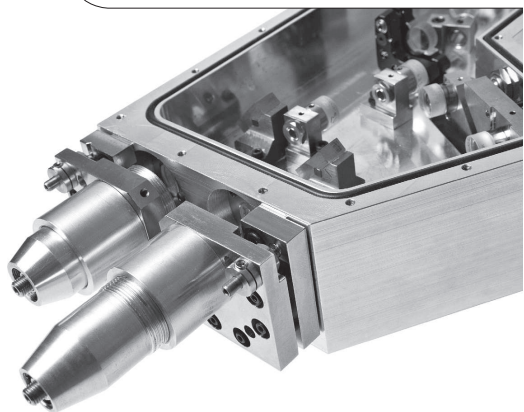
Žilinskas, Gintautas	189
Zimmerer, Cordelia	88
Žlabys, Giedrius.....	206
Zubovas, Kastytis	55, 199
Zubrienė, Asta.....	44
Zubrine, Asta.....	179
Žukauskas, Alvaras.....	37
Žukauskas, Artūras.....	141, 142
Žulonas, Žygimantas	100
Žurauskienė, Eleonora	162

UAB Altechna is a laser technology company operating in the fields of photonics and laser research since 1996.

Altechna is a reliable supplier of laser products: laser optics, crystals, lasers and optomechanics.

Our products:

- Lasers and laser equipment
- Spectroscopy equipment
- CCD cameras
- Positioning systems
- Laser crystals and optics
- Other laboratory equipment



Altechna represents:



www.aerotech.com



www.innolas.com



www.miyachi.com



www.andor.com



www.laserquantum.com



www.oceanoptics.com



Photonic Cleaning Technologies
www.photoniccleaning.com



For worldwide photonics
www.lasos.com



www.semrock.com

A place to implement new tech ideas

The Baltic Institute of Advanced Technology (BPTI) is a private, high quality research-oriented institute, creating and developing new technologies. Our aim is to offer an informal research space without bureaucratic constraints for scientists and researchers who are willing to take up challenges and to turn their ideas into concrete results.

BPTI gathers interdisciplinary research teams, able to provide efficient solutions to technological and social problems. We assume social responsibility and invite any enterprise, university, institute or other partner in Lithuania or abroad to co-operate in realizing interesting ideas. BPTI is an institute which develops, stores, and disseminates scientific knowledge and expertise in the field of technology and innovation.

Our values: freedom, scientific novelty / technological (societal) relevance, quality, responsibility, mutual trust and openness. Main research directions are data mining and its application in systems control, medicine, robotics, financial analysis and political science; data and information visualization; (formal) modeling and analysis of complex systems, statistical analysis, social network analysis; language technologies and text analytics; mechanical systems stability and control; computer vision systems (processing, correction, compression, quality control, video analytics); modeling and analysis of stochastic systems; analysis of biophysical signals; research of ligand-protein binding in silico, effect of ligand binding on protein stability - development of pressure shift model.

We provide diverse research services from companies and agencies of different sizes and with different needs: from simple advice on the right technologies and research needs, to the development of a complete system, from an idea to its design and / or prototype.

Contacts

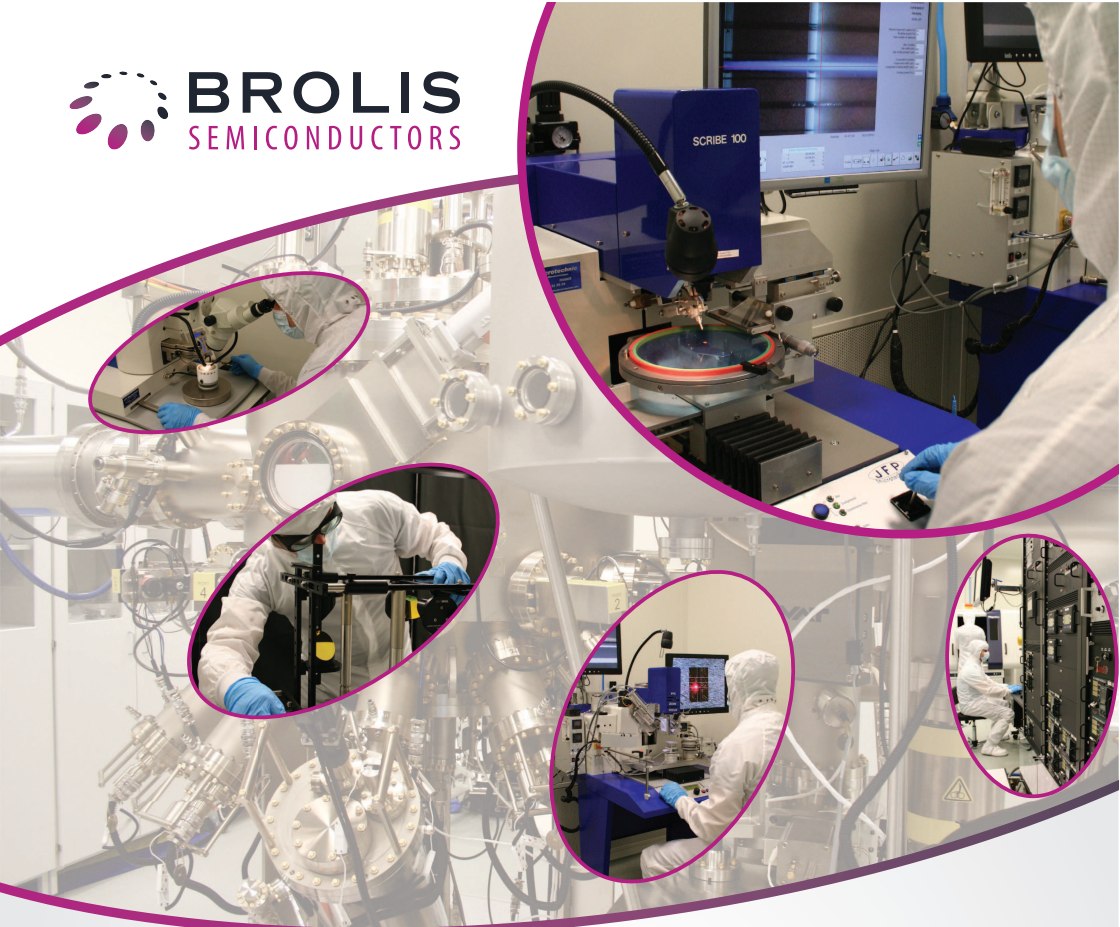
Baltic institute of advanced technology

Saulėtekio av. 15, LT-10224, Vilnius, Lithuania

Tel: +370 683 87737

E-mail: info@bpti.lt

www.bpti.eu



MBE FOUNDRY SERVICE

Your epi-wafer supplier for:

- Infrared thermal imaging FPA wafers: type-II superlattice, InSb, InAs.
- High-speed GaAs, InAs and InSb MMIC
- Thermo-photovoltaics
- Any custom structure from AlGaInAsSb

MID-INFRARED LASER DIODES

Brolis Semiconductors is a world leader in type-I GaSb laser diode technology:

- Wavelengths covered: 1800 nm – 4000 nm
- Room-temperature operation
- Continuous wave operation
- Ultra low input powers
- Die, bar, TO-can.
- Facet coating on request

**BEYOND STATE-OF-THE-ART TECHNOLOGY
FOR INFRARED APPLICATIONS**



A manufacturer and Your partner for Laser and Photonics components

- Nd:YAG LaserLine components
- FEMTOLine components
- Pockels cells for Q-switching and pulse picking
- Laser Optics for high power lasers
- Frequency conversion and laser media crystals
- Opto-mechanics mounts and optical positioners

Reliable supplier
for R&D and OEM customers
for more than 30 years!

Visit our website
www.eksmaoptics.com



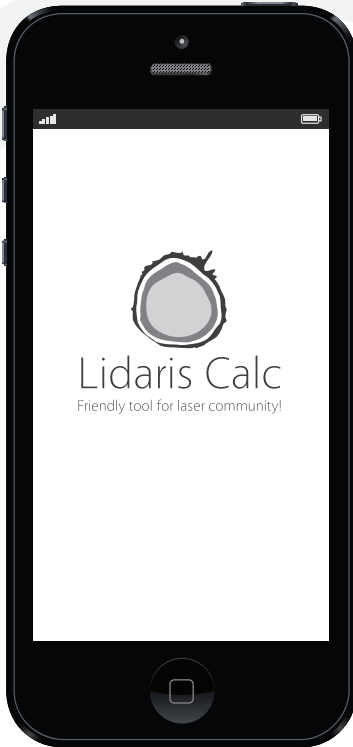


EKSPLA

Advanced Scientific Lasers and Systems

Working with lasers?

Get **free** app from LIDARIS!



Lidaris Calc - is a free software tool for smartphones equipped with laser related calculators that are frequently required in practice.

- estimates laser peak- fluence and power;
- scales damage threshold of dielectrics with pulse duration;
- performs conversions between popular photonic units;
- estimates spot size of focused Gaussian beams;
- calculates diffraction angles of diffraction gratings.

Calculations can be done by providing intuitive parameters such as laser beam diameter, laser pulse energy or average power, wavelength, repetition rate ect. It can save a lot time when adjusting laser systems in front of optical table.

LIDARIS LTD
www.lidaris.com

Email info@lidaris.com
Phone +370 609 09233
Skype lidt-service
Address: Sauletekio Avenue 10,
LT-10223 Vilnius, Lithuania

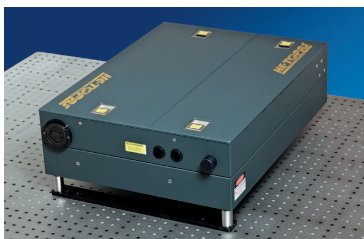


TOPAS

SERIES MODELS



TOPAS white
Optical Parametric Amplifier



HE-TOPAS
Optical Parametric Amplifier



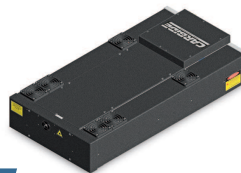
TOPAS-C
Optical Parametric Amplifier

PHAROS

SERIES PRODUCTS



PHAROS
High-Power Femtosecond Lasers



CARBIDE
Femtosecond Laser for Industrial & Medical Applications



ORPHEUS
Collinear Optical Parametric Amplifier



HARPIA
Off-the-Shelf Pump-Probe Spectrometer

1
GPS MONITORING
PLATFORM IN 24 LANGUAGES

8
HIGH ADDED VALUE
SOLUTIONS

5
GPS TRACKING DEVICES

0
LOST
CUSTOMERS

24x7
TECHNICAL
SUPPORT



PARTNERS IN
87 COUNTRIES



EUROPEAN EXPORT
CHAMPIONS AWARD



40 367
OBJECTS ON
TRUSTTRACK

TRUST
US



7 YEAR
EXPERIENCE



IN 5 LANGUAGES

LT
RU
PL
EN
ES
FR
AR
DE
HI
UR
IT
PA

OFFICE
SPEAKS IN 12
LANGUAGES

RESULTS IN
2013

AWARDS

TOP 5 TECHNOLOGY
COMPANY



IN CENTRAL-EASTERN
EUROPE,
NO. 1 IN THE BALTICS
BY DELOITTE

THE MOST
PROMISING COMPANY



BY "LITHUANIAN
TRANSPORT LEADERS
2013"

10TH FASTEST
GROWING
COMPANY



IN LITHUANIA
BY "GAZELLE 2012"

AMONG FINANCIALLY
MOST STABLE
COMPANIES



IN LITHUANIA BY
CREDITINFO

ECO-DRIVE -
THE BEST SERVICE



FOR TRANSPORT
INDUSTRY BY ICC
LITHUANIA

Photonics Tools

- Optomechanics
- Motion Controls
- Tunable Lasers
- Advanced Imaging
- OCT Systems
- Optics
- Fibers



You Speak, We Listen.....



THORLABS

www.thorlabs.com
scandinavia@thorlabs.com

LEMONA electronics

Lemona is one of the largest companies in the Baltic States selling electronic parts and components.

We offer more than 5,000,000 brand-name goods, such as electronic components, spare parts and accessories for domestic appliances, lead accumulators, power supplies, industrial automation components, tools and materials, sound and lighting equipment, car audio system and multimedia, home and vehicle security systems, solar and wind energy sources.

Thanks to advanced business and work management program we supply goods to our customers from various electronic components manufacturers and procurement agents world wide.

UAB Lemona, Lithuanian capital company, was founded in 1992. Thanks to purposeful work and consistency of highly qualified employees and smart business solutions, our company achieved strong market position. Today, our customers and suppliers acknowledge us as a partner that professionally, reliably and quickly meets their needs.

